

THE GROWTH OF SHORT FATIGUE CRACKS  
IN TITANIUM AND ALUMINIUM ALLOYS

BY

RICHARD KENDALL BOLINGBROKE

Thesis submitted to the University of Nottingham  
for the degree of Doctor of Philosophy

February 1988

## ABSTRACT

An investigation has been made of the growth of short fatigue cracks in aluminium and titanium alloys, with special emphasis on the effects of microstructure.

For the commercial aluminum alloys examined (7010 and 2014A) a degradation in short fatigue crack resistance accompanied an increase in the degree of ageing, as is commonly reported for long, through thickness cracks. The short cracks however, were seen to propagate at substantially faster rates than conventional, long cracks at the same apparent applied  $\Delta K$  and R - ratio. The similar, faceted fracture produced for both types of crack suggests that the same propagation mechanism was operative, despite the differences in growth rate. Discontinuous growth was observed for microstructurally short cracks, associated with the crack tip being held up over large numbers of cycles at grain boundaries both at the surface and in the interior of the specimen. The discontinuous nature of propagation and the anomalously fast growth continued until the maximum plastic zone size ahead of the crack tip approximated to the grain size of the material. At greater crack depths propagation rates, at equivalent  $\Delta K$ s, for long, through thickness cracks and short cracks showed reasonable agreement, small discrepancies being explained in terms of the variation in closure contribution for the two types of crack.

Similar propagation characteristics were observed for the two titanium alloys studied (IMI 318 and IMI 550) with substantially faster propagation for microstructurally short cracks than for long cracks at equivalent  $\Delta K_s$ . In contrast to long crack behaviour however, an increase in grain size resulted in a deterioration in short crack propagation resistance. The microstructure which was found to be the most resistant to the growth of short cracks consisted of fine primary  $\alpha$  and transformed  $\beta$  grains with the volume fraction of each type of  $\alpha$  approximately equal. The grain boundaries between the two distinct  $\alpha$ -morphologies were seen to be particularly effective in reducing the propagation rate. In contrast, a coarse, aligned, Widmanstätten  $\alpha$ -morphology exhibited the worst resistance to short crack growth. Even though colony and prior  $\beta$  grain boundaries were useful in retarding crack growth, propagation across packets of Widmanstätten laths was very rapid.

Crack shape effects were considered to be important. A study was made to assess the variation in crack shape and the effect on crack propagation, particularly in non-equiaxed microstructures. Cracks with depths approximating to the grain size were seen to vary significantly in shape, though they all eventually took a semi-elliptical form, with half surface length/depth ( $a/c$ ) ratios between 1.0 and 0.8, at greater crack depths. It is suggested that a better correlating parameter for short crack growth is crack area rather than surface crack length which is commonly used at present. In this way, the effects of crack

x shape can be accommodated.

## CONTENTS

<u>CHAPTER</u>	<u>Page</u>
1. <u>INTRODUCTION</u>	1
2. <u>FATIGUE CRACK GROWTH IN ALUMINIUM &amp; TITANIUM ALLOYS</u>	4
2.1 <u>Introduction</u>	4
2.2 <u>Long, through thickness fatigue crack behaviour</u>	8
2.2.1 <u>Introduction</u>	8
2.2.2 <u>Environmental affects on near-threshold crack growth</u>	10
2.2.2.1 <u>Aluminium alloys</u>	12
2.2.2.2 <u>Titanium alloys</u>	15
2.2.3 <u>Roughness induced crack closure</u>	17
2.2.4 <u>Microstructural effects on near-threshold crack growth</u>	22
2.2.4.1 <u>Grain size</u>	22
2.2.4.1.1 <u>Titanium alloys</u>	27
2.2.4.1.2 <u>Aluminium alloys</u>	31
2.2.4.2 <u>Precipitate type in age hardenable alloys</u>	33
2.2.4.3 <u>Copper content in high strength aluminium alloys</u>	37
2.2.4.4 <u>Dispersoid type in high strength aluminium alloys</u>	38
2.2.5 <u>Crack path</u>	39
2.2.5.1 <u>Effect of microstructural barriers</u>	39
2.2.5.2 <u>Fatigue fracture planes in aluminium alloys</u>	43
2.2.5.3 <u>Dual phase microstructures</u>	47
2.3 <u>Initiation of fatigue cracks</u>	48
2.3.1 <u>Introduction</u>	48
2.3.2 <u>Initiation in aluminium alloys</u>	51
2.3.3 <u>Initiation in titanium alloys</u>	53
2.4 <u>Microstructurally short fatigue cracks</u>	57
2.4.1 <u>Introduction</u>	57
2.4.2 <u>Grain size effects on short crack behaviour</u>	66
2.4.3 <u>Crystallographic texture</u>	75
2.4.4 <u>Dual phase microstructures</u>	76
2.4.5 <u>Environmental effects</u>	77
2.4.6 <u>The effect of crack length</u>	79
2.4.7 <u>Crack shape</u>	83
2.5 <u>Other types of short fatigue cracks</u>	86
2.6 <u>The effects of short fatigue crack testing procedures</u>	91
3. <u>EXPERIMENTAL TECHNIQUES</u>	94
3.1 <u>Introduction</u>	94
3.2 <u>Tensile testing</u>	94
3.3 <u>Long, through thickness fatigue crack testing</u>	95
3.4 <u>Short fatigue crack testing</u>	100
3.4.1 <u>General testing technique</u>	100
3.4.2 <u>Determination of crack shape</u>	104
3.4.3 <u>Stress intensity solutions</u>	105

	<u>Page</u>
4. <u>ALUMINIUM ALLOYS - MATERIALS</u>	108
4.1 <u>Introduction</u>	108
4.2 <u>Alloy development</u>	108
4.3 <u>Strengthening mechanisms</u>	110
4.3.1 2xxx series alloys	110
4.3.2 7xxx series alloys	111
4.4 <u>Microstructural evaluation</u>	115
4.4.1 7010	115
4.4.2 2014A	117
5. <u>ALUMINIUM ALLOYS - RESULTS</u>	120
5.1 <u>Long, through thickness fatigue crack behaviour in 7010</u>	120
5.2 <u>Aspects of short crack growth</u>	122
5.3 <u>Effect of ageing condition on short crack propagation behaviour</u>	125
5.4 <u>Effect of grain orientation on short crack propagation behaviour</u>	126
5.5 <u>Effect of testing conditions on short crack propagation behaviour</u>	127
5.6 <u>Behaviour of short cracks in 2014A</u>	128
6. <u>ALUMINIUM ALLOYS - DISCUSSION</u>	130
6.1 <u>Behaviour of long, through thickness cracks</u>	130
6.2 <u>Aspects of short crack growth</u>	137
6.3 <u>Effect of ageing condition on short crack propagation behaviour</u>	139
6.4 <u>Comparison of long &amp; short crack behaviour</u>	143
6.4.1 The anomalously rapid growth of short cracks	143
6.4.2 The transition from short to long crack growth	148
6.5 <u>Effect of grain orientation on short crack propagation behaviour</u>	150
6.6 <u>Effect of testing conditions on short crack propagation behaviour</u>	152
7. <u>TITANIUM ALLOYS - MATERIALS</u>	155
7.1 <u>Introduction</u>	155
7.2 <u>Alloy classification</u>	156
7.3 <u>Texture</u>	159
7.4 <u>Alloy development</u>	160
7.5 <u>Microstructural evaluation</u>	162

	<u>Page</u>
8. <u>TITANIUM ALLOYS - RESULTS</u>	167
8.1 <u>Introduction</u>	167
8.2 <u>Long, through thickness crack behaviour</u>	167
8.3 <u>Short fatigue crack behaviour</u>	169
8.3.1 $\alpha + \beta$ heat treated microstructures	169
8.3.1.1 318A	170
8.3.1.2 318B	172
8.3.1.3 318C	172
8.3.1.4 550A	174
8.3.2 $\beta$ heat treated microstructures	175
8.3.2.1 318D	175
8.3.2.2 318E	177
8.3.2.3 550B	179
9. <u>TITANIUM ALLOYS - DISCUSSION</u>	180
9.1 <u>Long, through thickness fatigue crack behaviour</u>	180
9.2 <u>Aspects of short crack growth - <math>\alpha + \beta</math> heat treated microstructures</u>	184
9.3 <u>Aspects of short crack growth - <math>\beta</math> heat treated microstructures</u>	190
9.4 <u>Comparison of long &amp; short crack behaviour</u>	195
10. <u>CRACK SHAPE</u>	199
10.1 <u>The effect of grain shape on crack shape</u>	199
10.2 <u>The effect of grain size on crack shape</u>	204
 <u>CONCLUSIONS</u>	 207
 <u>FURTHER WORK</u>	 211
 <u>ACKNOWLEDGEMENTS</u>	 213
 <u>REFERENCES</u>	 214
 <u>APPENDIX 1</u>	

## CHAPTER 1

### INTRODUCTION

Over the past ten years much effort has been directed towards establishing an understanding of short fatigue crack behaviour. This, in part, has been due to the introduction of a defect tolerant approach to component lifing in many parts of the aerospace industry, which can highlight the problems associated with short cracks. Using linear elastic fracture mechanics, fatigue life prediction is carried out by the integration of expressions based on the Paris equation, relating the crack growth rate ( $da/dN$ ) to the stress intensity factor range ( $\Delta K$ ), i.e.:

$$da/dN = C \Delta K^m \dots\dots\dots (1.1)$$

where  $C$  and  $m$  are constants obtained from laboratory tests on standard fatigue crack propagation specimens.

Recently, concern has arisen about this approach in situations where components are operating at high stress and thus to achieve reasonable fatigue lifes, the initial defect sizes considered may be small in relation to the microstructural scale of the material. Such 'microstructurally' short cracks have been observed to propagate significantly faster, at the same apparent  $\Delta K$ , than conventional, long, through thickness cracks, of the type used to determine the data on which lifing predictions are made.

If this anomalous behaviour is not taken into account the Paris equation integration will lead to overestimates of fatigue life and consequently increase the likelihood of in service component failure. It is towards these high stress, small initial defect situations that the aerospace industry is moving in order to reduce both component weight and cost. Thus, particular interest is now being shown in short fatigue cracks.

Although a number of studies of short crack propagation have been made, more information is required in certain areas. The intention of this work has been to examine some of the effects of microstructure, stress level and load ratio on the short crack propagation behaviour of commercial aluminium (7010 and 2014A) and titanium (IMI 318 and IMI 550) alloys. Both families of alloys are extensively employed in airframe and aero-engine construction and are thus used in applications to which the short crack problem relates. The use of these two alloy systems has meant that, via appropriate heat treatments, an extensive range of microstructures could be generated. In the aluminium alloys different ageing conditions have been studied, thereby assessing the effects of slip distribution through change in precipitate coherency. Underaged and overaged microstructures have been obtained with similar monotonic yield strength levels, thus eliminating one of the variables often regarded as important in crack propagation studies. In contrast, for the commercial titanium alloys, which are not precipitation hardenable, the size, shape and distribution of phases has been studied.

Previous studies have highlighted the importance of grain size effects for microstructurally short cracks, hence titanium alloys are good candidates for this type of investigation as the effective grain size can be changed by an order of magnitude by heat treatments above and below the  $\beta$  transus.

In common with the majority of previous studies a surface replication technique has been used to monitor the growth of short cracks embedded in smooth specimens. Although this is a non continuous recording method, it provides an accurate measure of crack dimensions down to very short crack lengths ( $\sim 1\mu\text{m}$ ). The data recorded however, only relate to the surface crack length and provide limited information on growth at the mid point of the semi-elliptical crack, in the interior of the specimen. Such data are considered important and therefore a further aim of this study was to examine the effects of crack shape on the propagation of short cracks.

## CHAPTER 2

### FATIGUE CRACK GROWTH IN ALUMINIUM & TITANIUM ALLOYS

#### 2.1 INTRODUCTION

Traditionally, fatigue lifeing of components has been determined using S-N type data, where an alternating stress range less than the fatigue limit, or at higher stress ranges, a 'safe' fatigue life is specified. However, as this information is usually determined from testing small, smooth specimens, a proportion of the fatigue life is taken up with initiation. If features are present in a large component that reduce the initiation time such as inherent, microstructural defects or stress concentrators, fatigue lives may, in practice, be severely overestimated. Consequently large safety factors need to be employed when using such data in design. It also means that many components reach the end of their design lives whilst still in a satisfactory condition. Therefore, an approach to fatigue life prediction, which uses a large fraction of the available life of many components, whilst still maintaining safety standards, has a strong economic appeal, particularly for aerospace applications. Such a defect tolerant approach has more recently been introduced, incorporating fracture mechanics theories. In this approach, fatigue life assessment is made assuming defects just smaller than can be detected using non-destructive inspection techniques are present in the structure. The number of fatigue cycles for the crack to grow from this length, to the largest permissable size for component integrity, is calculated and suitable inspection intervals determined in order to find any cracks before failure.

The application of fracture mechanics concepts to fatigue crack propagation is based on the work carried out by Paris et al (1). They assumed that the nominal value for the crack tip driving force ( $\Delta K$ , stress intensity factor range) characterising the crack tip stress and strain fields, could be used as a correlator for fatigue crack growth. This was expressed in an empirical formula now known as the Paris equation.

$$da/dN = C (\Delta K)^m \quad \dots\dots\dots 2.1$$

where  $da/dN$  is the crack propagation rate and  $C$  and  $m$  are scaling constants determined experimentally for individual materials. By substituting the relationship between stress intensity factor range ( $\Delta K$ ) and the crack length ( $a$ ), i.e.:

$$\Delta K = \Delta\sigma\sqrt{\pi a} \quad \dots\dots\dots 2.2$$

where  $\Delta\sigma$  is the alternating stress range, and integrating between the initial, undetectable crack size and the final permissible crack size, fatigue life prediction can be made.

More recent experimental studies have shown that apart from some structural steels (2), where the Paris equation adequately describes growth over a wide range of growth rates, the premise upon which this equation is based may lead to both underestimates and overestimates of fatigue lines depending on the propagation rate. This behaviour is best described by a plot of crack growth rate vs stress intensity factor range which can be subdivided into three distinct regions (figure 2.1). This schematic plot, produced by Ritchie and Suresh (3) illustrates three sections of propagation behaviour and their corresponding mechanisms. In the central region (B) the Paris equation adequately describes growth behaviour, which is little

influenced by microstructure and specimen thickness. At higher propagation rates (C) the Paris equation underestimates crack growth rates as growth becomes unstable and the cyclic fracture toughness is approached. Here the influences of microstructure, mean stress and specimen thickness are significant. In the third regime (A), the Paris equation leads to underestimates of fatigue life. Propagation rates are reduced and eventually a stress intensity factor is reached below which no further growth is detected (threshold stress intensity factor range,  $\Delta K_{th}$ .) At these propagation rates, growth is no longer continuous along the crack front and is influenced strongly by microstructure, mean stress and environment.

Fatigue thresholds are usually measured using specimens containing through thickness cracks greater than about 5mm in length. It is assumed that crack length does not affect growth behaviour, i.e. that a similitude concept applies and cracks propagate under identical conditions independent of length. However, Pearson (4) has shown that short, surface cracks, less than about 1mm in length, can grow at rates greater than corresponding long cracks under identical nominal driving forces. Such observations suggest that fatigue lifeing based on conventional test piece data may lead to overestimates of life where initiation from small defects is involved. Figure 2.2 (5) shows typical short crack growth behaviour in relation to long, through thickness crack data, on a  $da/dN$  vs  $\Delta K$  diagram.

There are several ways of defining short fatigue cracks:

- (i) Microstructurally short cracks. Cracks which are of a length comparable to the scale of the local microstructure (usually the grain size).
- (ii) Mechanically short cracks. Cracks which are of a length comparable to the scale of local plasticity. This includes cracks that are either embedded in the plastic zone of a notch or of a length comparable to the size of their own crack tip plasticity.
- (iii) Physically short cracks. Cracks which are physically small typically 0.5→1.0mm .

Case (ii) represents a limitation to the linear elastic fracture mechanics approach and a breakdown in the similitude concept. In assuming that the controlling parameter,  $\Delta K$  (or  $\Delta J$  for EPFM), adequately describes the stress state at the crack tip, the fracture mechanics approach also assumes that for two cracks of different lengths growing under the same conditions, the plastic zone sizes and stress and strain distribution around the zones will be identical. However, when cracks are short, compared to the size of the local microstructure or plasticity, the concept of similitude is violated and the local driving forces at the crack tip may be changed to an extent that differences in both long and short crack growth characteristics are observed.

## 2.2 LONG, THROUGH THICKNESS FATIGUE CRACK BEHAVIOUR

### 2.2.1 Introduction

The defect tolerant approach to fatigue life prediction uses data from the Paris and near-threshold regimes of the  $da/dn$  vs  $\Delta K$  diagram (figure 2.1). The fact that changes in micro-structure, mean-stress and environment can strongly influence near-threshold crack propagation behaviour has recently been attributed to the phenomenon of crack closure.

Early work on crack closure was conducted by Endo et al (6). They suggested that the lower propagation rates observed for cracks, in a low strength steel, growing in water compared to in air, were due to the formation of corrosive deposits on the crack faces in the former environment. These wedged them open and reduced the driving forces at the crack tip. Later, Elber (7, 8), interpreted crack closure in terms of fracture mechanics concepts. From compliance measurements made during crack propagation in 2024-T3 aluminium sheet, under both constant and variable amplitude loading, he proposed that closure due to plasticity effectively reduced crack tip driving forces. Plastic zones generated in front of the growing crack tip produced permanent residual displacements in the wake of the crack once it had grown further and passed through the plastically deformed material. These displacements caused premature contact between opposing crack faces during unloading, effectively closing the crack even though a tensile stress was still applied. (Figure 2.3b).

Since propagation cannot occur when a crack is closed, the stress intensity factor range ( $\Delta K$ ) experienced at the crack tip has to be modified to incorporate the value of stress intensity

at which the crack closes ( $K_{cl}$ ) even though the load is non-zero. Thus if;

$$\Delta K_{app} = K_{max} - K_{min} \dots\dots\dots 2.3$$

where  $\Delta K_{app}$  is the applied value of  $\Delta K$  and  $K_{max}$  and  $K_{min}$  the applied maximum and minimum stress intensity factors respectively, the effective stress intensity factor range at the crack tip ( $\Delta K_{eff}$ ) can be expressed:

$$\Delta K_{eff} = K_{max} - K_{cl} \dots\dots\dots 2.4$$

As the propagation rate is governed by the effective stress intensity factor range, Elber proposed that the Paris equation could be modified to;

$$da/dN = C(\Delta K_{eff})^m = C(U\Delta K)^m \dots\dots\dots 2.5$$

Where  $U$  = ratio of effective to applied stress intensity factor ranges. From further testing varying crack length, load ratio ( $R = K_{min}/K_{max}$ ) and stress intensity, Elber devised a linear expression relating  $U$  and  $R$  for the 2024-T3 alloy.

$$U = 0.5 + 0.4R \dots\dots\dots 2.6$$

Where  $-0.1 < R < 0.7$ . A good fit was found between this expression and ready published data on the alloy (9).

Elber's testing was carried out on sheet material at intermediate growth rates. Here, plane stress conditions prevailed, especially at high  $R$  - ratios. More recent experimental studies have shown that plasticity induced crack closure cannot account for all the closure observed in the near-threshold stress intensity regime (10). Where; plane strain deformation conditions exist and plastic zone sizes are much smaller.

Moreover, Newman (11) has shown that plasticity induced crack closure, modelled for plane strain conditions, could not account for the marked role of load ratio on near-threshold crack growth. At these low propagation rates, the influence of changes in microstructure, load ratio and environment has been attributed to other closure mechanisms, in particular oxide-induced and roughness-induced crack closure.

### 2.2.2 Environmental effects on near-threshold crack growth

Since Endo et al (6) first illustrated the concept of oxide-induced crack closure, the role of corrosion deposits in influencing near-threshold fatigue crack propagation behaviour has been examined in some detail. At low load ratios, the presence of a moist atmosphere can promote the thickening of corrosion products on crack faces. This can provide a mechanism for enhanced crack closure if the oxide layers can attain a thickness comparable to the crack tip opening displacement, such that the crack can be wedged open on unloading (figure 2.3c). Oxide thickening is a result of fretting oxidation, whereby oxide layers are continually broken up and new ones reformed on the clean fracture surfaces, by the repeated contact of the crack faces. This requires a combination of plasticity induced crack closure and significant Mode II displacements.

In a review of the subject, Suresh and Ritchie (12) noted that the formation of corrosion products and the promotion of oxide induced closure were dependent on:

- (i) a small crack tip opening displacement, comparable in size to the thickness of oxide formation, such as occurs in the near-threshold regime,

(ii) a highly oxidising medium where oxide formation is possible even without fretting,

(iii) low load ratios, which promote plasticity induced closure and the repeated contact between crack faces close to the crack tip,

(iv) rough fracture surfaces, which through Mode II displacements provide contact between crack faces, and

(v) lower strength materials where plasticity induced closure mechanisms are dominant and where considerable fretting damage can occur due to the soft matrix material.

The behaviour of low strength steels in inert and moist atmospheres can highlight the effect of these particular influencing parameters. (13-15). At low load ratios, threshold stress intensity values appeared to be higher in moist air than in inert, dry hydrogen or dry helium environments. However, at higher R - ratios, such differences disappeared. Figure 2.4 shows typical results for a 2.5%Cr - 1% Mo steel in terms of  $da/dN$  vs  $\Delta K$  diagram (13). Auger Spectroscopy analysis of the corrosion products on the near-threshold fracture surfaces in this study, revealed that oxide thicknesses were much greater (typically 20 times) than for any other atmosphere/load ratio combination studied. It was concluded that the enhanced oxide formation shielded the crack tip from experiencing the whole range of the applied stress intensity, thereby promoting higher value of measured threshold. By operating the tests at high R - ratio or in dry atmospheres, oxide formation at, or close to, the crack tip was severely reduced and lower threshold stress intensities resulted.

A number of studies (14-18) have also shown that strength level can influence the amount of oxide formation and thus near-threshold behaviour. Ultra high strength steels ( $\sigma_y > 1000$  MPa) (17, 18) were shown to have a lower resistance to crack propagation than low strength steels (13-16), due to harder substrate reducing abrasion of oxide debris and to less plasticity induced closure. However, differences in propagation behaviour are further exaggerated as high strength steels are more susceptible to hydrogen embrittlement (19).

#### 2.2.2.1 Aluminium Alloys

The effect of environment on the crack propagation behaviour of aluminium alloys is inherently more complex than that of steels. Whereas for steels it is generally observed that an increase in strength is accompanied by a reduction in the contribution of oxide induced crack closure to the overall fatigue behaviour, the same cannot be said for aluminium alloys. Factors such as alloy processing, composition and microstructure need to be considered in relation to environmental conditions.

Vasudévan and Suresh (20) investigated the effect of environment on the near-threshold behaviour of a 7075-T7 alloy. Considerably enhanced near-threshold propagation rates were associated with growth in moist air, compared to those in a vacuum environment. Although principally attributed to the embrittling effect of hydrogen in the moist air, significant excess corrosion debris found near the crack tip, was thought to have contributed to crack arrest. Oxide thicknesses were comparable to the maximum crack tip opening displacement (CTOD) at threshold (0.1 $\mu$ m). The authors concluded that crack growth for this alloy

was accompanied by two mutually competitive mechanistic processes which had opposite effects on near-threshold growth. The formation of excess corrosion debris tended to slow crack growth, while at the same time hydrogen embrittlement considerably enhanced propagation.

Vasudévan and Suresh (20,21) also made comparisons between the near-threshold behaviour of overaged (T7), peakaged and underaged microstructures of the 7075 alloy. Estimations of oxide thickness on crack faces were made using secondary ion mass spectrometry and scanning Auger Spectroscopy. While oxide thicknesses comparable to the CTOD were generated for the overaged material, very little oxide formation was associated with the other two ageing conditions. In fact, for the latter microstructures oxide thicknesses were approximately equal to thicknesses of naturally formed oxide deposits on freshly polished surfaces ( $\sim 0.01\mu\text{m}$ ) and were insignificant in comparison to the scale of crack tip opening displacement. Although this would suggest that a greater contribution to closure through oxide formation would be expected for the overaged material, the authors noted that greater fatigue crack propagation resistance was associated with the underaged, and to a lesser extent the peak aged, microstructures. In addition, hydrogen embrittlement of aluminium alloys in general becomes less pronounced with increasing ageing (22,23) and therefore would be expected to enhance propagation of the underaged alloy. Vasudévan and Suresh (20, 21) concluded that other factors, namely roughness-induced closure and slip reversibility, influenced near-threshold growth and combined to reduce propagation resistance with increased ageing. It was also noted that although the

overaged material was less prone to hydrogen embrittlement, cathodic hydrogen production at the same time as oxide formation at the crack tip may have been a significant source of embrittlement, which would have been absent in the peak aged and underaged materials.

The beneficial effect of eliminating embrittling and corroding atmospheres by operating fatigue tests in vacuum, had been noted as early as 1932. Gough & Sopwith (24) reported that for a wide range of non-ferrous metals, fatigue lives were extended significantly in vacuum compared to air. Similar effects have been noted more recently for 7075 and 7475 (21, 23). Figure 2.5 shows some results of Suresh et al (2.1) for 7075. At low load ratios, the increase in threshold stress intensity factor range with operating the tests in vacuum for each ageing condition, was attributed to the absence of environmental embrittlement. Carter et al (23) experimenting with the 7475 alloy, thought that additional benefits also arose from the rewelding of clean metal surfaces and from allowing easier slip reversibility as modelled by Pelloux (25).

At higher R - ratios, a reduction in  $\Delta K_{th}$  for all ageing conditions, in moist air was attributed partly to the absence of oxide induced closure effects, (figure 2.5). However, similar reductions in  $\Delta K_{th}$  in tests operated in vacuum were not observed. Suresh et al (21) concluded that this was caused by a combination of the absence of hydrogen embrittlement in the vacuum atmosphere and more prominent crack tip deflection in this environment, which enhanced propagation resistance through both crack closure and deflection mechanisms.

Finally, the effect of changing test frequency on crack growth has also been studied (26, 27). Vasudévan and Bretz (26) showed that for a 7075-T7351 alloy, an increase in frequency from 25 to 200 Hz produced substantially more oxide build up near the crack tip and a corresponding increase in propagation resistance. Oxide layers were enlarged by 50% to 0.15  $\mu\text{m}$  when the frequency was increased. At the higher frequency it was proposed that fretting was induced at an equal rate to oxide formation, producing the thicker oxide film and hence making a greater contribution to propagation resistance through oxide induced crack closure.

#### 2.2.2.2 Titanium Alloys

Studies into the effect of environment on the fatigue properties of titanium alloys have been wide and varying (28-37). Irving and Beevers (28) for example, have compared the fatigue behaviour of Ti-6Al-4V in various heat treated conditions in both air and vacuum environments. Figure 2.6 reports their data for an  $\alpha_p$  and transformed  $\beta$  microstructure which was typical of all the microstructural conditions studied and shows a considerable enhancement in propagation resistance in the vacuum atmosphere. This behaviour was explained (28, 30) in terms of a  $K_{\text{max}}$  controlled, structure sensitive, facet linkage growth mechanism which promoted faster growth in air at low stress intensities, but which was absent in vacuum. Further, discontinuous growth continued in vacuum at propagation rates  $< 10^{-8}$  mm/cycle. On fractographic examination this was found to have occurred in a structure sensitive mode, similar to growth in air, and was ascribed to weak environmental

interactions with the crack tip. No indication of the nature of these interactions in either environment was given.

Recent studies (33, 34) have highlighted the importance of embrittling mechanisms at the crack tip in titanium alloys, due to the presence of hydrogen in air. Similar behaviour to that observed by Beevers (28, 30) shown in figure 2.6, was thought to be due to the formation of hydrides at the crack tip in air which impeded the reversibility of slip and reduced the local fracture stresses ahead of the crack tip (33). The hydrogen induced reduction in basal plane fracture stress (34) in Ti-6Al-4V fatigued in air, as compared to in vacuum, resulted in an increase in cleavage-like fracture of the  $\alpha$  phase, a decrease in secondary cracking and in less crack tip deviation, all of which augmented propagation rates. Moody and Gerberich (35, 36), working with a Ti-6Al-6V-2 Sn alloy, reported that hydride precipitation from the internal hydrogen concentration was responsible for the cleavage of  $\alpha$  grains during slow fatigue crack growth. At threshold, the fracture surface was reported to consist of cleavage through the  $\alpha$  phase separated by ductile rupture of  $\beta$  ligaments. As cleavage of whole grains is unlikely in fatigue, it is possible that fracture through the  $\alpha$  phase actually occurred in a fatigue facet, 'cleavage-like', mode in this case.

In hydrogen environments, the hydride habit plane has been reported to be close to (10 $\bar{1}$ 0) (37). In air environments, however, Meyn (38) observed fast, substained load fracture on (0001) planes or on planes  $\sim 15^\circ$  from (0001) in a Ti-8Al-1Mo-1V

was the prominent fracture mechanism. Later, however, Paton and Spurling (39) demonstrated that when hydrogen concentrations were low, such as in air or conversely from internal concentrations, the most common hydride habit planes were (0001) and  $(10\bar{1}7)$  which are  $\sim 15^\circ$  from (0001). Hence it is possible that the rate of fatigue fracture of titanium alloys in air can be enhanced by the hydrogen embrittlement mechanisms, causing cleavage-like fracture close to the basal planes, as reported by Gray & Lütjering (34).

The observations and arguments presented in this section suggest that the role of a specific environment on the fatigue properties of a specific microstructure, will be comprised of contributions from crack advance mechanisms, such as hydrogen embrittlement, coupled with the retarding influence of closure phenomena. A detailed understanding of the resulting behaviour will be further complicated by considerations of other extrinsic and intrinsic material characteristics. These will be discussed in detail in the following sections.

### 2.2.3 Roughness induced crack closure

Substantial closure can result through uneven, irregular fracture surfaces generated at the crack tip. If during the unloading portion of a fatigue cycle, the fracture surfaces can make contact at discrete points behind the crack tip before the minimum load is reached, premature crack arrest can occur through a reduction in the effective stress intensity factor range. Figure 2.3d schematically depicts this type of closure termed roughness induced closure.

To understand why roughness induced crack closure is more prominent in the near-threshold regime, the crack path has to be analysed. At intermediate growth rates, in the Paris regime, crack advance in many materials often occurs by a striation mechanism termed Stage II growth by Forsyth (40). Ductile striations are formed at the crack tip as a result of concurrent or alternating crack tip shear on two or more operative slip systems. A relative smooth fracture surface results, macroscopically perpendicular to the applied stress axis, and Mode I displacements predominate (3). At lower growth rates, the scale of plasticity ahead of the crack tip is of a comparable dimension to the grain size of the material. Here, growth often occurs in only one shear direction, along one primary slip band. Designated Stage I growth by Forsyth (40), propagation under mixed Mode I and Mode II displacements results and a rougher fracture path is produced. For an ideally elastic crack such displacements would not lead to the development of roughness induced closure, as crack faces would fit together perfectly on unloading. However, as fatigue cracks growing at near-threshold growth rates involve assymetrical plastic deformation, a slight mismatch between opposing crack faces occurs, which can lead to fracture surface contact at loads above the minimum applied load and the premature arrest of the crack.

The transition from Stage II to Stage I type growth as propagation rates were reduced, was shown by the work on steels by Otsuka et al (41). Later Minakawa and McEvily (42) interpreted their data in terms of roughness induced closure using a simple model based on the differences between pure Mode I and mixed ~~Mode I~~ Mode II opening (figure 2.7).

The combination of a planar fracture surface and only Mode I opening (figure 2.7a) lead to a perfect match between crack faces at the end of every cycle. However, due to a more serrated fracture surface, coupled with Mode II displacements, surface mismatch was shown to occur, leading to crack face contact during unloading (figure 2.7b).

Direct evidence that fracture surface contact at discrete points behind the crack tip contributed to closure was given by Walker and Beevers (43) working on pure titanium. From crack tip opening displacement measurements and by studying replicas of the sides of their SEN specimens in the region of the crack tip, they found that the effective stress intensity calculated by Elber's technique (7, 8) for plasticity induced closure could not account for all the closure that they observed. They concluded that due to a small amount of in plane shear on unloading, fracture surface contact tended to wedge the crack open and prevent the stress intensity falling to the applied minimum load. They went on to show that the crack propagation rate could be better described by the term  $\Delta\theta$ , the change in angle subtended by the crack faces. When no closure was apparent  $\Delta\theta$  was directly proportional to  $\Delta K$ .

The first quantitative model for roughness induced crack closure, derived by Purushothaman and Tien (44), did not consider any Mode II displacement. By equating the asperity height to values of crack tip opening displacement, values of the closure stress intensity could be calculated. The asperity height was simply defined as  $\alpha(h-h_0)$  where  $h$  and  $h_0$  were the

dimensions of the final and initial fracture surface roughness respectively and  $\alpha$  was a constant of less than unity.

Suresh and Ritchie (45) later devised a model to account for the combination of Mode I and Mode II displacements characteristic of near-threshold crack growth. They idealised fracture surface roughness in terms of triangular cross-sectioned asperities of height  $h$  and assumed that cracks unloaded with a combination of Mode I displacement ( $u_I$ ) and Mode II displacement ( $u_{II}$ ) where  $u_{II} = Xu_I$  ( $X$  = fraction of Mode I displacement). An expression relating the closure and maximum stress intensities was formulated:

$$\frac{K_{cl}}{K_{max}} = \left\{ \frac{2\alpha X}{1+2\alpha X} \right\}^{\frac{1}{2}} \dots\dots\dots 2.7$$

where  $\alpha$  was a non dimensional fracture surface roughness factor equal to  $h/d\omega$  ( $d$  = grain size of material and  $\omega$  = length of the base of the asperity). Hence the magnitude of closure was dependent on the extent of fracture surface roughness and the proportion of Mode II displacement. The authors showed that even with low values of fracture surface roughness up to 35% reduction in effective stress intensity could arise if Mode II displacements equalled only 30% of the Mode I displacement.

A more recent model proposed by Beevers et al (46) tried to account for the distance of an asperity from the crack tip on the closure contribution. The stress intensity above which the crack could be assumed to be fully open ( $K_{op}$ ) was given as:

$$K_{op} = \frac{LG}{2(1-\nu)} \left( \frac{2\pi}{C} \right)^{\frac{1}{2}} \dots\dots\dots 2.8$$

Where  $L$  = asperity height,  $G$  = shear modulus,  $\nu$  = Poisson's ratio and  $C$  = distance of the asperity from the crack tip. Beevers and al argued that as  $L$  &  $C$  were proportional to the grain size of the material if transgranular failure occurred, the stress intensity at which the crack became fully open was proportional to the square root of the grain size, (i.e.  $K_{op} \propto d^{1/2}$ ). However, King and co-workers (47, 48) working on fine and coarse grained Astroloy have shown considerable difference between experimental data and values predicted by this model.

Both the Beevers model and the one proposed by Suresh and Ritchie include terms connected with the microstructural dimensions of the material. Changes in grain size, for example, may significantly affect the amount of roughness induced closure and therefore near-threshold propagation behaviour. Effects of changing microstructural features are considered in the following section.

The location of roughness induced closure in relation to the crack tip has recently been examined (49, 53). Duggan (49, 50) found for Waspaloy that a hole drilled through the thickness of a CT type specimen close to the crack tip at threshold, so removing the wake of the crack, resulted in no change in closure. In fact an increase in stress intensity was required for further propagation to occur. In complete contrast, studies by Minakawa et al (51) and by Zaiken & Ritchie (52, 53) have both found that on removing the wake behind the crack tip in 7xxx series aluminium alloys, the closure contribution was steadily reduced.

The largest closure contribution was found to occur within 1mm of the crack tip. In the latter studies (52, 53) approximately 50% of closure was thought to occur within 0.5 mm of the crack tip (figure 2.8). The relationship shown in figure 2.8 has some similarities to the model formulated by Beevers et al (46). The model proposed that the stress intensity at which the crack could be assumed to be fully open ( $K_{op}$ ) was related to the distance of the asperity behind the crack tip (C) by the expression  $K_{op} \propto C^{-\frac{1}{2}}$ . Hence a proportionally high degree of closure would be found close to the crack tip which diminishes as the distance between the crack tip and the asperity causing closure increases. Although exhibiting similar features to Zaiken and Ritchie's work (52, 53) the Beever's model predicts that virtually all the closure occurs very close to the crack tip. Zaiken and Ritchie's work suggests, however, that a significant closure contribution still exists at an appreciable distance behind the crack tip, thereby restricting the universal applicability of the model.

#### 2.2.4 Microstructural effects on near-threshold crack growth

##### 2.2.4.1 Grain size

Numerous studies have shown that changes in grain size can markedly affect near-threshold growth behaviour. In particular an enhancement in propagation resistance accompanies an increase in microstructural unit size. This type of behaviour has been noted in a wide range of materials, for instance, in steels (54-62), titanium alloys (28, 32, 63-68), nickel base superalloys (47) and aluminium alloys (23, 69-72) and in general has been attributed to an increased contribution from closure mechanisms and a reduction in driving forces through crack deflection processes.

A good example of this influence of grain size was shown by Gray et al (55, 55, 56) working with a fully pearlitic steel. At a low R - ratio an increase in prior austenite grain size, and to a lesser extent the pearlite interlamellar spacing, produced significant improvements in propagation resistance and higher threshold stress intensity factor ranges. The fact that at higher R - ratios growth characteristics for different grain sizes and interlammellar spacings were very much alike, was taken as evidence that the more irregular fracture surfaces generated by the coarser grained materials promoted additional closure, specifically roughness and oxide induced.

Differences in crack path for coarse grained and fined grained materials were considered by Masounave and Bailon (60, 61). They proposed that a longer overall crack length would result for the coarse grained material and propagation rates would therefore be lower at a specific stress intensity factor. Figure 2.9 schematically shows their argument. Although the length  $AB = A'B'$ , the crack path  $ACDEFB$  would be longer than  $A'C'D'E'F'G'H'B'$  and under the same driving force the propagation rate perpendicular to the applied stress would be lower.

The greater angle of crack tip deflection at grain boundaries for coarser grained materials not only leads to a rougher fracture surface and to a longer overall crack length, but can also significantly reduce crack tip driving forces. Suresh (73, 74) has recently tried to quantitatively model such behaviour. He developed a model for a single kinked crack by

Bilby et al (75), to describe the behaviour of a double kinked crack, firstly under purely elastic loading conditions and then under similar loading but with a fracture surface mismatch producing premature asperity contact. Figure 2.10 shows the profile of idealised crack studied in each case. The crack was assumed to be tilted by an angle  $\theta$ , over a distance  $D$  before growth again occurred perpendicular to the stress axis for a distance  $S$ . The deflection was repeated, though reversed, in adjoining segments. The extent of deflection could be described by the ratio  $\frac{D}{(D + S)}$ . It was assumed that the effects of prior deflections in crack path became negligible, as the crack grew along the segment  $S$  and that the effective driving force in each segment could be described by the weighted average of the effective stress intensity values for the deflected span  $D$  and the straight span  $S$ .

From the previous model by Bilby et al (75), Suresh proposed that the average stress intensity factor range for each span ( $\overline{\Delta K_I}$ ) could be defined by:

$$\overline{\Delta K_I} = \frac{\Delta K_I [D \cos^2 (\theta/2) + S]}{(D + S)} \dots\dots\dots 2.9$$

where  $\Delta K_I$  was the applied stress intensity factor range.

In a similar geometric manner the crack propagation rate of the deflected crack ( $\overline{da}/dN$ ) could be described in terms of the growth rate of an undeflected crack ( $da/dN$ ) growing under the same value of  $K_{eff}$ , i.e:

$$\overline{da}/dN = \left\{ \frac{(D \cos \theta) + S}{D + S} \right\} da/dN \dots\dots\dots 2.10$$

Suresh (73) illustrated the model for a crack deflected by  $60^\circ$  with  $D/D + S = 0.5$ . He proposed that the deflected crack had an apparent driving force 1.14 times greater than an undeflected crack, at equal growth rates, and propagated at ~25% slower rate in a direction perpendicular to the stress axis, at equal values of effective stress intensity factor range.

In a later paper (74) Suresh further developed the model to account for closure contributions due to fracture surface contact. In a similar fashion to that used previously by Suresh and Ritchie (45), the ratio ( $X$ ) of in-plane displacement ( $U_{II}$ ) to normal displacement ( $U_I$ ) was used, where  $X = U_{II}/U_I$ . An expression was derived comparing the reductions in driving forces due to the tilted nature of the crack and due to the fracture surface contact, such that;

$$\frac{\Delta K_I}{\Delta K_{eff}} = \left\{ \frac{D \cos^2(\theta/2) + S}{D + S} \right\}^{-1} \left\{ 1 - \frac{X \tan \theta}{1 + X \tan \theta} \right\}^{\frac{1}{2}}^{-1} \dots 2.11$$

As the expressions on the right hand side of the equation will always be greater than unity for a deflected crack, the nominal stress intensity factor ( $\Delta K_I$ ) to propagate a deflected crack will be greater than for an undeflected crack at the same growth rate. Suresh demonstrated that for a fairly realistic crack with  $\theta = 45^\circ$  and  $D/D+S = 0.25$ , even a 25% mismatch would lead to an increase of approximately 80% in the apparent stress intensity factor range compared to a linear crack.

In addition to their observations on crack path in coarse and fine grained materials, Masounave and Bailon (60) derived a relationship between the threshold stress intensity factor range ( $\Delta K_{th}$ ) and the grain size (d) of the ferritic steel under examination. The relationship took an analogous form to that of the Hall-Petch equation, i.e.:

$$\Delta K_{th} = \Delta K_o + K_f d^{\frac{1}{2}} \quad \dots\dots\dots 2.12$$

where  $\Delta K_o$  and  $K_f$  were material constants. By combining equation 2.12 with the Hall-Petch equation, a relationship was established between the yield strength ( $\sigma_y$ ) and  $\Delta K_{th}$ :

$$\Delta K_{th} = \Delta K_o + K_f K_y (\sigma_y - \sigma_o)^{-1} \quad \dots\dots\dots 2.13$$

where  $K_o$ ,  $K_f$ ,  $K_y$  and  $\sigma_o$  were all material constants. Masounave and Bailon concluded that there was a trade off between good fatigue crack propagation resistance and strength. The increase in propagation resistance with increasing grain size however, was attributed wholly to grain size effects and not to any decrease in yield strength of the material. Furthermore, the applicability of equation 2.13 to other materials will be limited to those simple alloys, like ferritic steels, which behave according to the Hall-Petch equation. The simple relationship proposed in equation 2.12 has some similarity to the characteristics of the Beevers crack closure model discussed previously (46) (equation 2.8). In this model it was proposed that the stress intensity above which a crack was assumed to be fully open ( $K_{op}$ ) was proportional to the square root of the grain size. Hence  $\Delta K_{th}$  would also be proportional to  $d^{\frac{1}{2}}$  as  $K_{op} \propto \Delta K_{th}$ .

Although the majority of experimental evidence is in agreement with the principles of these models, a number of studies have suggested that an increase in grain size does not automatically lead to greater propagation resistance (62, 76, 77). Carlson and Ritchie (76, 77) for example, used a very high strength steel with different prior austenite grain sizes, ranging from 30  $\mu\text{m}$  to 180  $\mu\text{m}$ . The yield strengths of all the microstructures studied were almost identical to each other. They reported a very similar fatigue behaviour for all microstructures, with a small increase in  $\Delta K_{\text{th}}$  with decreasing prior austenite grain size. Carlson and Ritchie argued that in addition to the effect of grain size, any effects due to a change in the yield strength have to be considered, which may alter fatigue behaviour through a change in flow properties, crack closure stresses or possibly environmental influences.

#### 2.2.4.1.1 Titanium Alloys

Due to the allotropic transformation at the  $\beta$ transus temperature, alloys based on titanium provide good systems in which to show the effects of grain size on long, through thickness crack propagation behaviour. Typical grain sizes can increase by an order of magnitude across the  $\alpha+\beta$  transformation, with the microstructural unit size changing from the primary  $\alpha$  ( $\alpha_p$ ) or transformed  $\beta$  grain size to the prior  $\beta$  grain or colony size. A number of studies (34, 63, 65-68, 78-81) have highlighted the substantial improvements in crack propagation resistance of  $\beta$  processed alloys compared to  $\alpha+\beta$  processed. The fact that at high R - ratios the beneficial effects of the Widmanstätten

microstructure all but disappear (63), is an indication of the importance of closure mechanisms in a manner similar to those described previously for steels. Yoder et al (66) have reported however, that for a range of  $\alpha+\beta$  and  $\beta$  processed Ti-8Al-1Mo-1V structures, the coarse, transformed  $\beta$ , Widmanstätten microstructures still exhibited slightly improved crack propagation resistance at an R - ratio of 0.7 compared to the finer, equiaxed  $\alpha$ /transformed  $\beta$  morphologies. They concluded that although changes in grain size could markedly influence the near threshold growth behaviour, other intrinsic material properties should be considered as well. Gray and Lütjering (34) have considered that not only do  $\beta$  heat treated microstructures have larger grain sizes so leading to a more tortuous crack path, but also their tendency for secondary cracking or crack branching to occur further enhances propagation resistance through the generation of additional crack surface area. This latter effect would still be apparent at closure free R - ratios and so may help to explain some of the results reported by Yoder et al (66).

It has been observed by Eylon and Bania (82) that propagation through both equiaxed  $\alpha$ /transformed  $\beta$  and aligned Widmanstätten microstructures in Ti-11 (Ti-6Al-2Sn-1.5Zr-1Mo-0.4Bi) can occur at corresponding rates under certain conditions. Peters et al (79) have extended this view slightly further by developing a semi-quantitative model which accounts for the effects of crack closure, crack tip deflection and crack surface area. It showed that when all these factors were considered, the data on a  $da/dN$  vs  $\Delta K$  diagram for  $\alpha+\beta$  and  $\beta$  processed

Ti-6Al-4V microstructures lay close to each other between stress intensity factor ranges of 3 to 9  $\text{Mpa}\sqrt{\text{m}}$ . Their qualitative view did not, however, include the effects of factors such as secondary cracking, slip reversibility, strength and textural effects.

Changes in the heat treatment process of  $\beta$ -annealed microstructures, such as temperature, time at temperatures and cooling rate, have also been seen to affect near threshold growth behaviour. For example, Hicks et al (68) have shown for the near  $\alpha$  alloy IMI685 (Ti-6Al-5Zr-0.5Mo-0.3Si) that an improvement in propagation resistance, accompanied an increase in prior  $\beta$  grain size and transformed  $\beta$  colony size. At higher R - ratios the effects were again diminished. From crack opening stress intensity measurements the authors concluded that an increase in microstructural unit size promoted crack path tortuosity and therefore crack closure mechanisms. Yoder et al have reported similar behaviour on increasing the packet size in  $\beta$  processed Ti-6Al-4V (83) and on increasing the colony and prior  $\beta$  grain size by increasing the oxygen content in a similar alloy (84).

The analysis of propagation behaviour based on colony size in  $\beta$  processed alloys can sometimes be misleading. As Eylon (85) has shown, cracks can propagate from one colony to another without deviation. He concludes that this is due to the inter-relationship between the crystallographic orientations of transformed  $\alpha$  platelets within a prior  $\beta$  grain, through one of the 12 variants of the Burger's relation:

$$\begin{aligned} (110)_{\beta} / (0001)_{\alpha} \\ \langle 111 \rangle_{\beta} / \langle \bar{1}1\bar{2}0 \rangle_{\alpha} \end{aligned}$$

This can have the effect of increasing the effective grain size and therefore promoting greater propagation resistance. In an earlier paper (82), Eylon reported the opposite effect of colony size. For a Ti-11 (Ti-6Al-2Sn-1.5Zr-1Mo-0.4Bi),  $\beta$  processed microstructure he observed a beneficial effect on propagation resistance by decreasing the grain size, which was attributed to the crack tip arresting effect of the colony boundaries. However, his experiments were carried out on thin specimens (of the order of the prior  $\beta$  grain size) and the cracks studied were relatively short (again of the order of the prior  $\beta$  grain size) (86). Hence the manner of propagation was not analogous to long, through thickness crack, near-threshold behaviour, but rather more akin to short crack behaviour which will be considered in more detail in section 2.4.

A further mechanism to explain the beneficial effect of a coarse grain size on propagation resistance has been proposed by Robinson and Beevers (32). Studies on  $\alpha$  titanium at low R ratios showed the near-threshold fatigue fracture surfaces to consist of two distinct regions, namely faceted fracture and "torn" fracture. The crack path was interpreted in terms of a two stage fracture mechanism model, whereby favourably orientated grains would fracture through a  $\Delta K$  controlled faceted fracture mechanism. Other grains, unfavourably orientated, would be bypassed and would restrain propagation until fractured in a tensile manner. An increase in grain size, it was proposed, would lead to greater restraint on propagation as larger ligaments would remain unbroken. Such a model relies on the effectiveness of

the relative misorientations of grains to resist fatigue fracture. More recent understanding has shown that although relative grain misorientations can effectively stop a propagating crack tip, the effect would not be great enough to leave whole grains unfractured behind the crack front.

#### 2.2.4.1.2 Aluminium Alloys

Grain size effects on the near-threshold fatigue crack propagation resistance of aluminium alloys has also been studied in some detail (e.g. 23, 26, 69-72, 87, 88). For example, Asaro et al (69) have shown that the beneficial effects of coarser grained microstructures on fatigue crack growth resistance is associated with a greater closure contribution at low growth rates. Crack closure measurements on a 2048 aluminium alloy subjected to a constant  $K_{max}$ , revealed a transition from a region of high closure to one of low closure as the crack length increased. By varying the grain size of the alloy, it was demonstrated that this transition occurred when the maximum plastic zone size ahead of the crack tip approximately equalled the grain size of the material.

Earlier work by Lindigkeit et al (70, 71) also demonstrated the improvement in near-threshold crack growth resistance with coarsening grain structure. Their work on a laboratory produced 7075 alloy and Ti-8.6Al, fatigued in vacuum and in a 3.5% Na Cl solution, was interpreted to indicate that the amount of reversible slip of dislocations per cycle close to the crack tip was important. Slower propagation rates for coarser grained materials were ascribed to the greater number of dislocations

able to move back along original slip planes during unloading and therefore not contributing to crack advance. It was argued that in finer grained structures, more grain boundary/dislocation interactions would occur during the loading portion of the fatigue cycle, inducing greater cross slip. This is shown schematically in figure 2.11. These dislocations would not be available for reverse slip on their original slip planes during unloading and enhanced crack propagation rates would result. The effect of slip distribution will be more extensively reviewed in section 2.2.4.2.

These observations, plus those of Carter et al (23) and Bretz and co workers (26, 87, 88), indicate that grain size effects affect propagation resistance basically through two mechanisms. Firstly by extrinsic resistance, such as crack closure, which is greater for coarse grained materials through rougher fracture surfaces and increased crack tip deflection. As Bretz and co workers (26, 87, 88) have shown, these effects significantly enhance propagation resistance of coarse grained materials at low R ratio and are virtually absent at high R ratios. Secondly, beneficial influences on propagation resistance can also result through inherent material characteristics, such as slip distribution. These inherent material properties are still operative at high R ratios, where contributions from crack closure mechanisms are absent, and help to account for differences in propagation behaviour between coarse and fine grained microstructures during closure free growth.

Davidson & Lankford (89) have recently suggested that dispersoid mean free path is the important microstructural element in fatigue crack growth, rather than grain size. From direct observation of near-threshold propagation in an SEM of two 7XXX series alloys (7075-T651) and the powder metallurgy alloy, 7091-T7E69), they concluded that slip line length was controlled by dispersoid size and volume fraction. Both alloys exhibited similar propagation behaviour and threshold stress intensity factor ranges despite having grain sizes which differed by over an order of magnitude. As the slip line lengths between dispersoids were comparable for the two alloys, this was thought to be the controlling influence over propagation behaviour.

#### 2.2.4.2 Precipitate type in age-hardenable alloys

The degree of ageing and therefore the type and size of second phase precipitation, is an important parameter in influencing near-threshold fatigue crack growth. In general a worsening of crack propagation resistance accompanies increased ageing where slip is more homogeneously distributed. A good example of this type of behaviour comes from the recent work by Zaiken and Ritchie (90, 91), who studied the near-threshold behaviour of under-peak and over-aged 7150. Figure 2.12 shows their results on a  $da/dN$  vs  $\Delta K$  plot. At both  $R = 0.1$  and  $0.75$  there was a definite trend of decreasing threshold stress intensity factor range with increasing ageing, though the differences between the various microstructures were somewhat diminished at the higher, closure free load ratio. This suggested that intrinsic material factors were responsible for the behaviour.

Some years earlier, Hornbogen and Zum Gahr (92) had presented a model to account for such observations. They proposed that at low growth rates the inhomogeneous, trans-crystalline slip associated with underaged microstructures severely retarded crack growth, compared to more aged structures that deformed homogeneously. Working with an age-hardenable Fe-36Ni-12Al-0.02C alloy, Hornbogen and Zum Gahr produced different microstructures, through heat treatment. Two contained predominantly  $\gamma'$  precipitates (Ni<sub>3</sub>Al) which were coherent with the matrix and the third contained much coarser  $\gamma'$  precipitates as well as incoherent, bcc  $\alpha'$  (Fe<sub>3</sub>Al). Fatigue testing down to  $10^{-6}$  mm/cycle produced similar trends to those observed by Zaiken and Ritchie (90, 91), figure 2.12.

Hornbogen and Zum Gahr's model was based upon the number of dislocations able to reverse, during the unloading portion of the fatigue cycle, along the same slip plane that they moved away from the crack tip during loading. In quantitative terms, the crack growth rate ( $da/dN$ ) was equal to the difference in this number multiplied by the Burger's vector ( $b$ ), i.e.:

$$da/dN = (N_O - N_R)b \quad \dots\dots\dots 2.14$$

where  $N_O$  and  $N_R$  were the number of dislocations moving away from and back towards the crack tip during a fatigue cycle respectively. For the more underaged microstructures, which contained the coherent  $\gamma'$  preceipitates, slip was assumed to occur only on a few parallel slip planes within a particular grain. Due to the heterogeneous nature of deformation only a few dislocations were removed from the slip system by cross slip and

the proportion able to move back along the same slip plane during unloading (i.e.  $N_R/N_O$ ) was high. The result was little overall crack tip damage per cycle. However, for the overaged microstructure, the coarse, incoherent precipitates promoted easy cross-slip out of the original slip plane and as the number of slip systems was much larger than for the previous case, fewer dislocations were able to reverse, on unloading, to the crack tip. Therefore, a larger proportion of dislocations contributed to crack growth, enhancing propagation rates.

The fact that these differences were more pronounced at low growth rates was explained in terms of dislocation/grain boundary interactions. The reverse plastic zone size at near-threshold propagation rates was generally smaller than the grain size and dislocation: grain boundary interactions were infrequent. But at higher propagation rates where these interactions were more numerous, slip could be activated in neighbouring grains, so reducing the number of dislocations able to reverse during unloading. Thus, even for heterogeneously deforming microstructures, the strain became more homogeneous and propagation rates for all ageing conditions were similar at the same value of stress intensity factor range.

More recent work supporting Hornbogen and Zum Gahr's model has come mainly from studies on high strength aluminium alloys (13, 20, 21, 23, 64, 91, 93-98). In certain studies (20, 21, 23, 90, 91) changes in slip characteristics caused changes in fracture mode. For example, Suresh et al (21) reported for a 7075 alloy, that transgranular, crystallographic

growth was associated with an underaged temper, while a much flatter crack path was produced in an overaged microstructure. Hence greater crack tip deflection and enhanced crack closure would result for the underaged condition. These observations were in keeping with the Hornbogen and Zum Gahr model, as the heterogeneous deformation of an underaged structure would produce a rough, crystallographic crack path. For the homogeneously deformable, overaged microstructure, where many slip systems were available and cross-slip relatively easy, a smoother fracture surface results due to the larger number of finer slip steps.

Further evidence that underaged microstructures are more effective in retarding crack advance in the near-threshold region at low load rates was provided by Zaiken and Ritchie (91) working with a 7150 alloy. After producing cracks in compact tension (CT) specimens growing at near-threshold propagation rates in under-peak and over-aged tempers and  $R = 0.1$ , a single compressive overload of magnitude five times the tensile peak load was applied. Further cycling at the previous threshold stress intensities produced an immediate reinitiation of growth, which in all cases progressively decelerated until rearrest occurred. Deceleration and rearrest occurred after far less crack extension for the underaged temper, which was interpreted in terms of the more efficient redevelopment of roughness induced closure. Planar slip in the underaged microstructure produced more pronounced fracture surface asperities after the overload, which had effectively flattened all previous surface roughness. Hence crack rearrest took place much sooner.

Lindigeit et al.(94) reported similar behaviour to the work of Hornbogen and Zum Gahr for a high purity 7075 alloy fatigued in vacuum and  $R = 0.1$ . At low growth rates greater propagation resistance was reported for less heavily aged structures. However, for three underaged microstructures aged at  $100^{\circ}\text{C}$  for 0.5, 10 and 100 hours, they thought the Hornbogen and Zum Gahr model was invalid. Even though the fatigue crack propagation resistance decreased with increasing ageing, the 0.5 hour aged material showed the most homogeneous slip distribution. This was indicated by the high tensile ductility and from fine slip steps on the fracture surface. However, no microstructural evidence from TEM observations were presented. Lindigeit et al (94) postulated that if this temper had the most homogeneous slip of the three, then according to Hornbogen and Zum Gahr's model it should have shown the least resistance to propagation. The anomaly was explained in terms of the difference in ductility of the tempers rather than using slip reversibility concepts.

#### 2.2.4.3 Copper content in high strength aluminium alloys

Copper, added to most age hardenable alloys to increase strength, is also added to the 7XXX series alloys to improve stress corrosion cracking resistance. The effect of copper content on near-threshold crack growth is therefore of some importance, as has been revealed by Lin and Starke (99-101) and Vasudévan and Bretz (26).

Lin and Starke, in altering the copper content in a 7XXX series alloy with nominal composition Al-6Zn-2Mg-XCu, found that copper rich alloys tended to deform more homogeneously, due to an increased volume fraction of strengthening precipitates and number of semi-coherent and incoherent precipitates. An increase in copper content in peak-aged microstructures (T651) (99, 100), lead to a reduction in propagation resistance as slip behaviour changed from one of precipitation shearing and strain localisation in the copper lean alloys, to one of precipitate by-passing in the copper rich alloys. Propagation rates down to only  $10^{-6}$  mm/cycle were studied, however, discernable differences in behaviour would be expected to be apparent at near-threshold growth rates. In a later study Lin and Starke (101) reported near-threshold behaviour for similar alloys in the T7351 condition. Little or no difference in propagation rates were observed for all the various alloys (copper content 0.01%+2.1%). This was explained by the fact that in the more overaged condition, the strengthening precipitates were mostly semi-coherent or incoherent anyway. Any deformation was therefore homogeneous, independent of copper content.

#### 2.2.4.4 Dispersoid type in high strength aluminium alloys

Recent developments in improving the mechanical properties of high strength aluminium alloys have been concerned with reducing impurity concentrations and grain refining. The former, by using high purity aluminium charge and the latter, by the addition of chromium or zirconium which precipitate as small, intermetallic dispersoids.

The effect that this latter operation has on near threshold crack growth has been studied by Zedalis et al (102). They compared two high purity 7XXX series alloys (7475-T6) and (7075-T6). The 7475-T6 alloy contained chromium as a grain refiner, which formed incoherent  $\text{Al}_2\text{Mg}_2\text{Cr}$  dispersoids,  $0.02 \rightarrow 0.5 \mu\text{m}$  in diameter. The dispersoids in the 7050-T6 alloy, where zirconium was the grain refiner, were semi-coherent, tetragonal,  $\text{ZrAl}_2$ , which were typically  $0.01 \mu\text{m}$  in diameter. Despite the fact that the grain size of the 7475-T6 alloy was the larger of the two, a higher threshold stress intensity factor range was reported for the 7050-T6 alloy at  $R = 0.05$  in a dry argon atmosphere. This was attributed to greater coherency of the  $\text{ZrAl}_2$  dispersoids with the lattice. The incoherent  $\text{Al}_2\text{Mg}_2\text{Cr}$  intermetallics were thought to remain virtually underformed in the crack tip plastic zone leading to stress concentrations and the possibility of debonding and cracking.

#### 2.2.5 Crack Path

##### 2.2.5.1 Effect of Microstructural Barriers

As crack growth rates are reduced, the onset of near-threshold type propagation appears to coincide with a change in fracture surface appearance from one of structure-insensitive to a structure-sensitive mode. Numerous studies (28, 32, 63, 64, 83, 103-108) have indicated that this transition from smooth flat to rough, cleavage-like fracture, occurs when the cyclic plastic zone size roughly corresponds to the material grain size.

Some of these studies (83, 103-107) have shown on  $da/dN$  vs  $\Delta K$  diagrams, that a bilinear relationship exists with a definite transition in slope occurring at a point  $\Delta K_T$ , corresponding to the cyclic plastic zone size and grain size being equal.

A model proposed by Yoder et al (83, 103-107) and based on the size of the cyclic plastic zone size, considered the type of fatigue propagation (either structure-sensitive or structure-insensitive) to depend solely on the material yield strength ( $\sigma_y$ ) and the mean free path between microstructural barriers to slip band transmission ( $\bar{l}$ ). In most materials  $\bar{l}$  was equal to the grain size. Using Rice's derivation of the cyclic plastic zone size under plane strain conditions  $r_y^c$  (109) i.e.

$$r_y^c = 0.033 (\Delta K / \sigma_y)^2 \dots\dots\dots 2.15$$

Yoder et al assumed that when  $r_y^c$  became the same order as  $\bar{l}$  a transition in the  $da/dN$  vs  $\Delta K$  slope would occur. The stress intensity factor range at the transition point ( $\Delta K_T$ ) could thus be described:

$$\Delta K_T = 5.5 \sigma_y (\bar{l})^{1/2} \dots\dots\dots 2.16$$

For the two titanium alloys under consideration (Ti-6Al-4V and Ti-8Al-1Mo-1V) (83, 84, 104) which were in a  $\beta$  annealed condition, the model fairly accurately predicted the transition points over a change in Widmanstätten packet size from 20  $\mu m$  to 60  $\mu m$ . For these microstructures  $\bar{l}$  was assumed to be the packet size rather than the prior  $\beta$  grain size. Considerable crack bifurcation was observed at stress intensities below the transition point ( $\Delta K_T$ ).

It was concluded that this transgranular, crystallographic bifurcation caused a reduction in the effective stress intensity range and consequently crack propagation rates.

In a later study, Yoder et al (106), working with a  $\beta$  annealed, CORONA 5 alloy (Ti-4.5Al-5Mo-1.5Cr), found that crack bifurcation only occurred above the transition stress intensity factor, in contrast to their earlier observations. However, as before, propagation rates were rapidly reduced below  $\Delta K_T$ , down to threshold. Compositional differences were examined to account for the contrasting behaviour. For the CORONA 5 alloy, primary  $\alpha$ -platelets constituted approximately 50% of the microstructure, the rest being regions of retained  $\beta$ . The Ti-6Al-4V and Ti-8Al-1Mo-1V alloys however consisted of a greater proportion of primary  $\alpha$  with barely enough retained  $\beta$  to surround the  $\alpha$ -platelets. The authors proposed that for the CORONA 5 alloy, when the cyclic plastic zone size roughly exceeded the length of the  $\alpha$ -platelets, a critical stress intensity level was exceeded and interfacial cracking of  $\alpha/\beta$  boundaries was induced.

Yoder et al (107) have also used their cyclic plastic zone model to interpret changes in the slopes of  $da/dN$  vs  $\Delta K$  diagrams of 7XXX series aluminium alloys. Using data obtained by Bucci et al (110) for a 7075-T6 alloy, three transitions were identified and related to  $\bar{l}$ . The transitions are shown on a  $da/dN$  as  $\Delta K$  diagram in figure 2.13. According to equation 2.16, the transition  $T_3$  was controlled by the grain size of the material ( $r_y^c = 4.4 \mu\text{m}$ ) in accordance with the transition from structure-insensitive to structure-sensitive growth observed in other materials (103-106, 108).

The cyclic plastic zone sizes of the transitions  $T_1$  and  $T_2$  at lower stress intensities were calculated to be 0.76  $\mu\text{m}$  and 1.91  $\mu\text{m}$  which seemed to correlate with the dispersoid spacing and subgrain size respectively for the alloy. Evidence to support this theory was presented by using Bucci et al's data (110) for a 7050-T6 alloy. Transitions for this alloy corresponded to cyclic plastic zone sizes equal to the dispersoid spacing (0.71  $\mu\text{m}$ ) and the grain size (4.0  $\mu\text{m}$ ). No transition coinciding to the subgrain size was observed. It was argued that as zirconium replaced chromium as the grain refiner in the 7050 alloy compared to the 7075 alloy, the formation of subgrains was partly suppressed and consequently the transition  $T_2$  was absent. Yoder et al's cyclic plastic zone model assumes that definite transitions occur at specific stress intensities. In many cases the exact position of such transitions, if they are present at all, can vary through experimental scatter and interpretation. The reproducibility of results produced by the model must therefore be open to speculation.

Yoder et al (83, 103) have further conjectured that the sharpness of such transitions is dependent on the grain or packet size distribution about the mean value. An alloy exhibiting a fairly constant microstructural size, would show a sharper transition at  $\Delta K_T$  than one displaying a wide variation in grain diameter.

As discussed in Section 2.2.4.1.2, Davidson and Lankford (89) doubted that grain size was the microstructural dimension controlling near-threshold propagation behaviour in 7XXX series alloys. From their direct observations of growth in a SEM they proposed that dispersoid size and volume fraction controlled slip line length and therefore near-threshold behaviour.

#### 2.2.5.2 Fatigue fracture planes in aluminium alloys

Stubbington and Forsyth (111), during the 1960's, first suggested, from metallographic examination of fracture surfaces, that fatigue fracture occurred crystallographically on {111} planes in a  $\langle 1\bar{1}0 \rangle$  direction in two aluminium alloys, (Al-7.5 Zn-2.5Mg and Al-2.5Cu-1.5Mg). Confirmation was made using a Laue back reflection X-ray technique. Metallographically, it was revealed that in some planes intersecting {111} planes produced parallel lamellae running in the  $\langle 1\bar{1}0 \rangle$  direction, while elsewhere the fracture was essentially planar running along {111} planes. Later Pelloux (25) and Knott and co-workers (112, 113) demonstrated that fracture facets in Stage II growth and at lower growth rates, were close to a {100} orientation and propagation occurred in a  $\langle 110 \rangle$  direction. Pelloux (25) used an etching method to produce specifically shaped etch pits on fracture surfaces which helped to identify facet fracture orientations. A solution of  $50\text{H}_2\text{O} : 50\text{HNO}_3 : 32\text{HCl} : 2\text{HF}$  applied for approximately three seconds was found to produce such pits. Etch pit orientations were determined by etching a polished and plastically deformed specimen and by using the slip line traces as reference orientation markers.

For both a 2024-T3 and an overaged 7075 alloy, square based pyramidal pits were formed (figure 2.14a). Pelloux proposed that the side faces of such pits were {111} planes, the base a {100} plane and that the edges of the basal plane were parallel to <110> directions. He concluded that on the basis of a large number of observations, striations formed at low growth rates ( $10^{-6}$  mm/cycle) were parallel to a <110> direction with  $\pm 10\%$  and the fracture plane was close to a {100} orientation.

Knott and co-workers first working with pure Al-Cu alloys (112) and later with more complex Cu-Al based alloys (113) also reported propagation in a <110> direction and on a {100} plane. Garrett and Knott (112) determined, from X-ray diffraction studies, that fracture on {100} planes occurred in Al-Cu alloys, but reported that cleavage mechanisms were not responsible as had been previously thought. Instead, a restricted slip mechanism was proposed in terms of the emission of n pairs of slip dislocations from the crack tip according to

$$\frac{a}{2} [101]_{(11\bar{1})} + \frac{a}{2} [101]_{(111)} + a[001]_{(001)} \dots 2.17$$

where the (111) and (111) planes intersect the crack front along [110] as observed. The resulting opening, a [001], was normal to the (001) plane.

Higo, Pickard and Knott (113) used a similar etch pit method to that developed by Pelloux (25) to reveal the fracture orientation of various Cu-Al alloys. The etching solution in this case was 2.5g FeCl<sub>3</sub> + 10cm<sup>3</sup> HCl in 150cm<sup>3</sup> ethanol.

Similar, square based pyramidal etch pits to those seen by Pelloux were observed. The authors also noted that on a microscopic scale the (100) planes seen macroscopically could be ridged along  $(1\bar{1}1)$  and (111) planes if the slip was uneven or sequential, rather than continuous. This may help to account for the differences between the work of Pelloux and Knott and co-workers and that of Stubbington and Forsyth.

Albrecht and Lütjering (93), however, have indicated that fracture occurred in {111} slip planes in an underaged, high purity 7075 alloy. Pelloux's etch pit method was again used to identify the fracture orientation of small, sharp slip steps on the surface. The triangular based pyramidal pits formed had faces of {100} planes and a basal plane parallel to the fracture surface which was a {111} plane. (figure 2.14b).

Other researchers have reported growth not on {100} or {111} planes, but on {110} planes with propagation in a variety of directions. Electron microscopy replica studies by Bowles and Broek (114) revealed that fracture of a 7075-T6 alloy occurred on {110} planes. However, an etch pit technique on similar fracture surfaces produced mainly cubic shaped pits (figure 2.14c) and a few triangular based pyramidal shaped pits (figure 2.14b) indicating fracture on {100} or {111} planes respectively. In many cases irregular shaped pits were created indicating that fracture was not on a low index plane. Crack growth directions were seen to vary from grain to grain but were confined to  $\langle 110 \rangle$  or  $\langle 100 \rangle$  directions.

To explain the variations in crack path, Bowles and Broek (114) considered the deformation mechanisms which would satisfy slip on {111} planes in fcc metals. Two were thought to be possible:

(i) (001) crack plane [110] crack tip direction and (111) slip planes. The slip planes make an angle of  $54^{\circ}44'$  with the crack plane, and

(ii) (0 $\bar{1}$ 1) crack plane, [011] crack tip direction and (111) and ( $\bar{1}$ 11) slip planes. The slip planes make an angle of  $35^{\circ}16'$  with the crack plane.

Pelloux (25) had suggested that fracture on [001] type planes was observed as the angle of the slip planes were closer to the planes of maximum elastic shear stresses ( $\sim 70^{\circ}$  to the crack plane in Mode I crack opening). Bowles and Broek (114) proposed a model based on Pelloux's work, showing that propagation was equally possible on [110] planes as on [100] planes, assuming that the resolved shear stresses for the two slip systems in randomly orientated grains were not very different. They also noted that according to Laird (115), [100] planes in aluminium alloys were often orientated normal to the tensile axis due to textural effects and this may have contributed to the fact that fracture along (100) planes was more commonly reported. The small, triangular based pyramidal pits seen in a few places on fracture surfaces indicated, according to Bowles and Broek (114), that on a microscopic scale striations consisted of parts of (111) planes, though the overall fracture was either on (100) or (110) planes.

Nix and Flower (116) have also reported fracture on  $\{110\}$  planes in preference to  $\{100\}$  planes in a 7010-T76 alloy. They suggested that striation formation occurred by cleavage on  $\{110\}$  planes coupled with plastic deformation during blunting and closing of the crack. Scanning transmission electron microscope thin foil studies and etch pit techniques were used to determine fracture planes. 'Roof top' shaped pits (figure 2.14d) were produced indicating  $\{110\}$  fracture planes. They proposed that the differences between their observations and those of others, who reported  $\{100\}$  fracture planes (25, 112), 113) may have been due to incorrect observations being made during the previous work. Without stereo-imaging, which Nix and Flower had used, they thought that 'roof top' shaped etch pits may have been mistaken for cubic shaped pits. Nix and Flower's material was also strongly textured, producing higher tensile stresses in  $\{110\}$  planes than on  $\{100\}$  planes. This may have promoted fracture on  $\{110\}$  planes if slip was equally possible on  $\{110\}$  and  $\{100\}$  planes. The likelihood of cleavage-like fracture on planes that are not close packed in fcc metals, (e.g.  $\{110\}$ ) is however questionable. More often fracture would be expected to occur on  $\{111\}$  or  $\{100\}$  planes.

#### 2.2.5.3 Dual phase microstructures

Advantageous near-threshold crack propagation behaviour has recently been demonstrated for microstructures consisting of two distinct phases (12, 108, 117-120). For steels, a combination of a martensitic phase for strength and a ferritic phase for increased ductility can, through careful

heat treatment, significantly increase threshold stress intensity factor ranges. McEvily and co-workers (108, 117) for example, produced a microstructure containing ferrite islands totally encapsulated by martensite. The beneficial fatigue properties associated with such a microstructure at low R-ratios was attributed to the preferred fracture through the ferrite, which produced a tortuous crack path and led to considerable crack tip deflection and closure contributions. Tzou and Ritchie (119) reported a threshold stress intensity factor range greater than  $20 \text{ MPa}\sqrt{\text{m}}$  at  $R = 0.05$  for a plain carbon steel with a microstructure consisting of fine, fibrous martensite dispersions in a coarse ferrite matrix. The steel, which had been intercritically annealed and brine quenched, exhibited a 50% improvement in threshold over conventionally heat treated material. The relevance to this study concerns the two phase titanium microstructures. The fine, transformed  $\beta$  phase and primary  $\alpha$  phase may be analogous to the martensite/ferrite phases in steels.

### 2.3 INITIATION OF FATIGUE CRACKS

#### 2.3.1 Introduction

The initiation of fatigue cracks, at or near the surface of a cyclically deforming structure, generally occurs close to singularities such as inclusions, scratches and pits. These can all act as local stress concentrators.

For a surface, free from such features, initiation from persistent slip bands (PSBs) may be observed. Ewing and Humphrey (121) observed initiation from slip bands in  $\alpha$  iron as early as 1903. By repeatedly interrupting the load cycles and polishing and etching the test pieces, they observed the formation of a few slip bands. These bands slowly widened and were finally seen to be the cause of crack initiation. The term: persistent slip band was defined by Thompson et al (122) some years later. Their experiments, fatiguing high purity, polycrystalline copper specimens, showed that on periodic inspection throughout the fatigue life, a few slip bands were visible and that they remained visible even after electro-polishing. On restarting cycling, slip again occurred along these persistent slip bands eventually leading to crack initiation. Forsyth and Stubbington (123) later reported the presence of intrusion/extrusion pairs associated with bands of intense slip in an age-hardened Al-Cu alloy. Small visible extrusions, about  $0.1\mu\text{m}$  thick and  $10\mu\text{m}$  long were found in accentuated slip lines. Cracks were sometimes seen to originate from crevices in the specimen surface, left by the formation of an extrusion.

Cottrell and Hull (124) have proposed a model to account for the formation of these intrusion/extrusion pairs, assuming slip to occur on two intersecting slip bands sequentially during a fatigue cycle. Figure 2.15 schematically presents the model. During the loading portion of a fatigue cycle, slip first occurs along one slip band (figure 2.15b) and then along a second, resulting in two slip steps on the surface (figure 2.15c).

On unloading, sequential slip again occurs, producing an extrusion at one end of a slip band and an intrusion at the other (figure 2.15e).

Another established model for crack initiation from a clean surface (125) does not require the formation of an extrusion/intrusion pair. Although, as Fine and Ritchie (126) have highlighted, surface roughening would extenuate the process by increasing local stresses. Neumann's model (125), depicted schematically in figure 2.16 can be explained in the following manner. During the tensile part of a fatigue cycle a slip step can be formed at the specimen surface along a favourable orientated slip plane (figure 2.16a). If the stress amplitude is large enough, slip could be activated on a second slip plane, as the first becomes inactive due to work hardening (figure 2.16b). Decreasing the stress, during the unloading part of the fatigue cycle, leads to the formation of a crack, as the excess dislocations on the active slip planes run out. (Figure 2.16c).

The point at which a coarse slip band actually forms into a fatigue crack is still unclear. Miller (127, 128) has suggested that crack growth can be considered to start from the first cycle, though with current experimental techniques such a hypothesis is impossible to prove.

The remainder of this section considers the types of initiation commonly observed for aluminium and titanium alloys.

### 2.3.2 Initiation in aluminium alloys

The type of initiation observed in commercial aluminium alloys can vary markedly depending on composition and processing techniques. Factors which promote local stress concentrations or create inhomogeneous structures, such as inclusions, coarse intermetallics and wide precipitate free zones, can markedly reduce initiation resistance.

In the previous chapter (section 2.2.4.2) examples were presented to show that by increasing the length of ageing in precipitation hardenable aluminium alloys, crack propagation resistance decreased. Sanders and Starke (129) however, have highlighted the opposite effect in terms of initiation. Such behaviour has been attributed to the degree of homogeneity in the microstructure. For an underaged 7075-T6 alloy, it was suggested that as the shearable precipitates tended to localise strain, large slip offsets would occur at a specimen surface and low initiation resistance would result. The more incoherent precipitates in an overaged microstructure would promote a more homogeneous strain distribution and hence smaller slip offsets at a specimen surface.

Initiation resistance has also been seen to be improved by controlling the grain size. For example, Lütjering et al (130), investigating the fatigue behaviour of a high purity, 7XXX series alloy, showed a significant improvement in initiation resistance to accompany a decrease in grain size. This was attributed to the reduction in slip band length, which reduced the number of dislocations in a pile up.

A study by Kung and Fine (131) into the initiation behaviour of 2024-T4 and the high purity version of the same alloy, 2124-T4, revealed that the type of initiation was dependent on the stress amplitude. At high stress amplitudes initiation in both alloys occurred in slip bands. The slightly better initiation resistance of 2024-T4 over 2124-T4 was ascribed to the smaller grain size of the former alloy. However, at lower stress amplitudes, initiation in 2024-T4 was almost exclusively from constituent particles, while only half those in 2124-T4 were from the same source. A small improvement in initiation resistance was observed for the high purity version of the alloy, presumably as few constituent particles were present in the microstructure. Examination of the area around the constituent particle disclosed that initiation had occurred along slip bands impinging on them. It was thought that intrusion and extrusions could form more readily at low stress amplitudes on slip bands that initiated at the second phase particles. It is possible, however, that these constituent particles could also act as stress concentrators. An earlier study by Grosskreutz and Shaw (132) on a similar alloy also reported initiation from particles. The authors suggested that this was due to interface debonding between the matrix and the second phase particles and not to slip band cracking, although a heavy concentration of slip bands around the particles was observed.

### 2.3.3 Initiation in titanium alloys

Studies of the initiation behaviour of  $\alpha$  titanium (e.g. 133) have highlighted that both slip band formation and mechanical twinning can lead to crack nucleation. In the latter case, the dislocation debris produced by a moving  $[11\bar{2}1]$  twin interface can induce the growth of whiskers of material at the interfaces, leading to initiation in a similar manner to that of extrusion formation by slip bands. Correspondingly, nucleation can occur at twin interfaces which produce intrusions.

In  $\alpha+\beta$  titanium alloys, the presence of the  $\alpha$  stabiliser aluminium, helps to facilitate slip on the pyramidal planes in the  $\alpha$  phase. This competes with mechanical twinning and basal plane slip as a means of accommodating strain and twinning related initiation is less frequently observed. A number of studies have reported initiation to have occurred by slip band formation in the  $\alpha$  phase or at  $\alpha/\beta$  grain boundaries (134 - 141). Some research (135 - 136) has shown however, that although slip band nucleation, early in the fatigue life, is prevalent at high stress amplitudes,  $\alpha/\beta$  interface cracking, later in the fatigue life, predominates at stress levels close to the fatigue limit. Benson et al (135) for example, observed that interface cracking occurred without the prior formation of visible slip bands at the  $\alpha/\beta$  interface. This was explained in terms of the cyclic stress level. Close to the fatigue limit, stresses did not exceed a critical value required to cause softening and the formation of coarse slip bands in the  $\alpha$  phase.

An unknown mechanism was assumed to continue at the  $\alpha/\beta$  interface however, and eventually initiation was caused by this mechanism.

Steel and McEvily (137) have also observed initiation in Ti-6Al-4V at low stress levels, fairly late in the fatigue life, from points on the specimen surface that showed no signs of slip band formation. Rather than explaining this in terms of  $\alpha/\beta$  interface cracking, Steel and McEvily attributed it to an internal stress intensification process that caused initiation to occur slightly subsurface in some cases. Similar observations have been made by Neal and Blenkinsop (142) and Ruppen et al (143).

Neal and Blenkinsop (142) reported internal initiation in  $\alpha$  transformed  $\beta$  microstructures of Ti-6Al-4V and Ti-4Al-4Mo-2Sn-0.5Si, usually when the stress levels were low. Examination of fracture surfaces revealed that at every crack origin a flat facet was present, which from X-ray analysis was identified as an  $\alpha$  grain. Furthermore X-ray diffraction techniques disclosed that the facet was inclined at about  $14^\circ$  to the basal plane. This was correlated with the cleavage plane  $(10\bar{1}7)$ . A mechanism was proposed whereby, due to restricted slip on the prismatic slip planes, dislocations built up at grain boundaries. This induced a stress large enough to produce cleavage on  $(10\bar{1}7)$  planes before the critical resolved shear stresses on the  $(10\bar{1}1)$  and  $[0001]$  planes could be reached. Conversely, Ruppen et al (143) have proposed that initiation occurred subsurface at  $\alpha/\beta$  interfaces in various morphologies in Ti-6Al-4V.

Their model considered that dislocations on  $\{10\bar{1}0\}_\alpha$  planes in the  $\alpha$  phase piled up at  $\alpha/\beta$  interfaces. To accommodate the strains in the  $\beta$  phase, two slip systems became operative, whose  $\langle 111 \rangle_\beta$  were coplanar with the  $\langle 11\bar{2}0 \rangle_\alpha$  Burger's vector of the  $\alpha$  phase. During the fatigue cycle the relative movement of these two slip systems produced a resultant displacement perpendicular to the  $\{100\}_\beta$  cleavage plane. Cleavage resulted along this plane causing cracking in the  $\beta$  phase, starting at the  $\alpha/\beta$  interface. The mechanism was only expected to be operative in transformed  $\beta$  colonies where the prismatic plane was orientated close to the maximum shear stress. Hence subsurface initiation was more likely to occur as the probability of finding a suitably orientated colony in the specimen interior would be higher than on the surface.

The observation of internal initiation, particularly at low stress amplitudes, in Ti-6Al-4V has also been noted by Brown and Smith (144). They attributed this to environmental effects on slip band formation in the  $\alpha$  phase.

At the specimen surface, local plastic deformation will expose clean metal to the environment in the slip bands. Reaction with any oxygen and/or nitrogen in the testing atmosphere was thought to produce local hardening, slowing down the initiation process.

Hence the possibility of failure occurring from a sub surface origin was increased. Such a process would be favoured at low stress amplitudes, as more time would be available for the surface hardening process to occur.

In a similar manner to that previously reviewed for aluminium alloys (130), a reduction<sup>m</sup> the grain size of titanium alloys has led to an improvement in initiation resistance. Lucas (145, 146), for example, has shown an increase in the fatigue life to result from the reduction in primary  $\alpha$  grain size, in an  $\alpha$  + transformed  $\beta$  microstructure in Ti-6Al-4V. This was attributed to a shortening of the slip band length. Stubbington and Bowen (136) produced a highly initiation resistant microstructure in the same alloy, through a suitable thermo-mechanical route. This not only reduced the primary  $\alpha$  grain size, but also spherodised the transformed  $\beta$  grains, so diminishing the number and length of  $\alpha/\beta$  interfaces available as initiation sites. A good example of grain size effects was presented by Lin et al (139). They noticed a worsening of fatigue lives in Ti-6Al-4V when the alloy was cold rolled prior to testing. Metallographic inspection found that this process sheared some transformed  $\beta$  grains, which in effect increased the primary  $\alpha$  grain size with regard to the mean free path available for slip band formation. Consequently, initiation resistance diminished.

In contrast to the significant effects of primary  $\alpha$  grain size on initiation resistance, Lucas (145) reported only a small increase in fatigue strength, at low stress amplitudes, due to the refinement in prior  $\beta$  grain size.

Bowen and Stubbington (140, 141) however, have attributed the increase in low cycle fatigue strength of  $\alpha + \beta$  worked,  $\beta$  annealed Ti-6Al-4V, in part to the reduction in the prior  $\beta$  grain size. They considered that this had the effect of decreasing the mean free slip path. The fact that these studies were conducted at significantly different stress levels may contribute to the variation in the observed behaviours.

Bowen (141) also reported the effect of texture in Ti-6Al-4V on initiation resistance. Lower fatigue lives, which were taken to imply worse initiation resistance, were observed when specimens were oriented so that the basal planes in the primary  $\alpha$  phase were normal to the stress axis. This was as compared to specimens oriented so that the basal planes were parallel to the stress axis. Differences in the elastic and plastic Poisson's ratio with crystallographic orientation were thought to be responsible for these observations. A strain applied parallel to the basal plane resulted in smaller strain changes normal to the stress axis, due to the higher values of Poisson's ratio. This constraining influence was thought to be responsible for the enhancement in initiation resistance.

## 2.4 MICROSTRUCTURALLY SHORT FATIGUE CRACKS

### 2.4.1 Introduction

Since the early studies of de Lange (147) and Pearson (4), the propagation behaviour of microstructurally short cracks has become a topic of considerable research effort. Much of this work has been directed towards identifying the effects which make these microstructurally short cracks grow at faster rates than long, through thickness cracks.

Such behaviour implies that fatigue life prediction based on conventional LEFM analysis can lead to severe over-estimates where small initial defects are observed. The early work by de Lange (147), who used a replication technique to monitor the growth of naturally initiated cracks from smooth surface steel and aluminium alloy specimens, yielded no propagation rate data. He did notice, however, that soon after initiation, the cracks entered a long stage of "hesitating" growth which corresponded to crack lengths between 5 and 10 grain diameter. This was followed by a period of rapid growth to failure, which appeared to be insensitive to the local crack tip microstructure. The later study by Pearson (4) on two precipitation hardenable aluminium alloys, involved growth rate measurements and demonstrated that short surface cracks, typically less than 0.5mm deep, could propagate at faster rates than would have been predicted from long crack tests (figure 2.17). Only when the crack depths were greater than approximately 130 $\mu$ m did the growth rates of the short cracks tend towards those of the long cracks.

More recently, a number of studies (e.g. 48) have confirmed both de Lange's and Pearson's observations. Figure 2.18 schematically displays results of Lankford (148) and shows the anomalously rapid growth seen by Pearson and the 'hesitating' growth, of crack lengths approximately 2 to 3 times the grain size, reported by de Lange. It is now recognised that it is the relative size of the crack to the microstructure in which it is contained, which can affect the growth characteristics of short cracks.

In particular, crack tip: microstructure interactions can significantly alter local crack tip driving forces. In addition, the absence of crack closure phenomena and the breakdown in LEFM similitude concepts are contributory factors to the apparent differences in long and short crack growth characteristics.

The  $da/dN$  vs  $\Delta K$  diagram shown in figure 2.18 can be divided into three distinct regions to describe aspects of short crack growth. Firstly, there is an area where cracks may be able to initiate but are arrested soon thereafter and fail to propagate any further. This is indicated by the hatched region on the left hand side of figure 2.18 and can be explained in terms of the crack tip driving force being below the threshold for short cracks (the endurance limit). This will be discussed in more detail below. Secondly, cracks that are able to propagate further are affected by the local microstructure in front of the crack tip. This can result in the appearance of "dips" on the  $da/dN$  vs  $\Delta K$  diagram caused by temporary deceleration in the crack growth rate. In the majority of cases the position of the deceleration dips has been shown to be microstructurally sensitive, in that they coincide with crack tip or crack tip plastic zone interactions with grain boundaries. Hence their position on the  $\Delta K$  axis is grain size dependent. As Lankford (148, 149) has confirmed, it is not the grain boundaries that are the cause of intermittent growth, but the fact that a crack tip may have to grow into a grain whose relative crystallographic orientation may be significantly different to the one that it has just grown through.

In the third region on the right hand side of figure 2.18 data from a number of cracks come together and eventually join the line corresponding to long, through thickness crack, LEFM behaviour. It is typical that at this point the crack depths of the short cracks are many times the grain size of the material.

The critical crack depth, below which short crack effects are apparent, was first reported by Kitagawa and Takahashi (150). They presented crack growth data for a HT-80 steel in terms a threshold stress range below which failure does not occur vs crack depth diagram (a) (figure 2.19). They postulated that if LEFM was applicable to any crack, independent of length, the diagram should just consist of two lines. A horizontal line representing the fatigue endurance limit of a smooth specimen and a line, of slope  $-\frac{1}{2}$ , representing the threshold stress intensity factor range ( $\Delta K_{th} a^{-\frac{1}{2}}$ ). The two lines should cross at a critical crack depth,  $a_0$  (figure 2.19). The authors, however, noticed that at short crack depths the threshold stress intensity factor range fell away from the predicted behaviour, i.e. it was dependent on crack depth. Later, Taylor and Knott (151) defined the crack depths,  $a_1$  and  $a_2$  (figure 2.19), between which short cracks would be expected to grow, against LEFM predictions. A crack with a depth less than  $a_1$  would become non propagating, as described earlier by Lankford (148, 149) and shown on figure 2.18. The crack depth defined by  $a_2$  has considerable importance in engineering terms, as cracks larger than this depth can be modelled using existing LEFM techniques.

Typical experimental data (e.g. 152 - 155) demonstrating the decline in threshold stress intensity ranges below  $a_2$  are shown in figure 2.20 (154). Here, the critical crack depth,  $a_2$  was found to be modelled well by continuous mechanics arguments (156) and that;

$$a_2 = \left( \frac{1}{\pi \alpha^2} \right) \left( \frac{\Delta K_{th}}{\Delta \sigma_{th}} \right)^2 \dots\dots\dots 2.18$$

where  $\Delta K_{th}$  and  $\Delta \sigma_{th}$  were the threshold stress intensity factor range for long cracks and the endurance limit respectively and  $\alpha$  was a geometric factor.

The microstructural significance of  $a_2$  has not been determined, though Taylor and Knott (151) simply defined this crack length as ten times the characteristic microstructural size. Even though this is a very simplistic approach, it does indicate the approximate dimensions in many cases.

Tanaka et al (157) attempted to model the decline in threshold stress with crack length below  $a_2$ , in terms of a two-dimensional, blocked slip band model. It was based on the premise that a slip band formed at a crack tip would be blocked at a grain boundary, unless a critical value of stress intensity was reached. Further growth into the adjoining grain would not occur until this condition was satisfied. If the length  $b$  was defined as:

$$b = a + \omega_0 \dots\dots\dots 2.19$$

where  $a$  was the crack length and  $\omega_0$  the size of the blocked slip band zone, the threshold stress ( $\sigma_{th}$ ) could be determined as:

$$\sigma_{th} = K_C^m / \sqrt{\pi b} + (2/\pi) \sigma_{fr} \cos^{-1} (a/b) \dots\dots 2.20$$

where  $K_c^m$  was the critical value of stress intensity for propagation to occur and  $\sigma_{fr}$  the frictional stress for dislocation motion.

Using already published data Tanaka et al (157) showed that their model adequately predicted threshold behaviour, particularly for softer materials. They concluded that the reduction in threshold stress intensity factor range below that predicted by LEFM for cracks with lengths less than  $a_2$ , was due to the stress strain environment of the plastic zone, which the stress intensity factor could not adequately describe.

The models discussed to date, such as Tanaka et al's, have only considered the application of fracture mechanics to the prediction of a threshold for short crack growth and have not examined the rate of propagation once the threshold has been exceeded. Thus, even though LEFM predictions can be modified to account for very short cracks, it can not be expected accurately to model crack growth rates, which have been shown to depend on microstructural influences and micromechanisms.

The breakdown in LEFM in predicting the growth of short cracks stems from factors such as the loss of similitude between long and short cracks, any changes in stress state due to surface effects for very short surface cracks and to the inability to model the effects of microstructure on crack tip driving forces.

A study by El Haddad et al (158) considered this inability of LEFM and EPFM to describe short crack growth behaviour. By introducing an effective crack length parameter (defined as the actual crack length (l) plus an additional crack length ( $l_0$ ) into fracture mechanics arguments, they derived stress intensity solutions that closely fitted experimental data. Their modified stress intensity factor range ( $\Delta K$ ) equation took the form;

$$\Delta K = \Delta\sigma\sqrt{\pi(l + l_0)} \quad \dots\dots\dots 2.21$$

where  $\Delta\sigma$  was the applied stress range. The term  $l_0$ , which was a constant for a given material, could be determined by considering the case at the fatigue endurance unit, where the crack length l was virtually zero. The authors considered the term  $l_0$  to be a measure of the reduced flow resistance of surface grains due to their lack of constraint. However, the use of an arbitrary parameter, such as  $l_0$ , which happens to give a good empirical fit to experimental data and has no real, physical basis, can not be considered to be a practical solution to the problem.

A model, derived from crack tip strain principles, to try to account for the rapid growth of short cracks, as well as the retardation effect of microstructural boundaries, has been proposed by Chan and Lankford (159). Whereas LEFM analysis is based on cracks growing under plane strain conditions, Chan and Lankford considered that short cracks would grow under plane stress conditions.

This was based on their observations that crack tip opening displacements (CTOD) were larger for short cracks and that consequently, the plastic strain range ( $\Delta\epsilon_p$ ) for these cracks would be higher, leading to increased crack growth rates under nominally identical driving forces. In the model it was assumed that the plastic strain range ( $\Delta\epsilon_p$ ) for short cracks could be related to the stress intensity factor range ( $\Delta K$ ) through a power-law formulation;

$$\Delta\epsilon_p = c\Delta K^n \quad \dots\dots\dots 2.22$$

where c and n were constants.

The retardation effects of grain boundaries were thought to be dependent on the distance of the crack tip from the grain boundary (X) and the relative crystallographic orientation of the adjoining grains. The latter relationship was described by the function  $K(\phi)$ , which was a measure of resolved shear stresses on particular slip systems in the cracked grain ( $\tau_A$ ) and the uncracked grain ( $\tau_B$ ). Hence;

$$K(\phi) = 1 - \tau_B/\tau_A \quad \dots\dots\dots 2.23$$

and  $\tau_B/\tau_A$  could be used as a measure of the ease with which slip could propagate into the next grain.

In developing equation 2.22, Chan and Lankford derived an expression relating crack growth rate (da/dN) to  $\Delta K$  which included the retarding effects of microstructure.

If D was the grain diameter, then

$$da/dN = C_1 \Delta K^n [1 - K(\phi) (\frac{D-2x}{D})^m] \quad \dots\dots\dots 2.24$$

$C_1$ ,  $n$  and  $m$  are constants. . Figure 2.21 demonstrates the behaviour of the model for a crack tip approaching a grain boundary. As  $K(\phi)$  approaches unity (i.e. the number of propagating slip bands in the uncracked grain are few), complete crack arrest can occur. The form of the curves closely resembled that of experimental data (e.g. figure 2.18 (148)) and the model appears to suitably represent the propagation characteristics of microstructurally short cracks.

Suresh (73, 150) has also considered the affect of the relative crystallographic orientation of adjoining grains on the crack tip driving forces of a short crack propagating through them. He showed for a crack emanating in a grain at an angle of  $45^\circ$  to the surface of a specimen and then being deflected by  $-90^\circ$  at the first grain boundary, that the 'effective' driving force was reduced to 0.78 of the applied driving force purely through crack deflection considerations. Thus, if the deflection is large enough, the effective cyclic stress may be reduced to less than the critical value for propagation (the endurance limit) and complete arrest may occur.

In the following sections a more detailed examination of effects of microstructural parameters on short crack growth behaviour is presented.

#### 2.4.2 Grain size effects on short crack behaviour

If, as has been highlighted in the previous section, the presence of grain boundaries can significantly affect short fatigue crack propagation behaviour, the characterisation of grain size effects may be of considerable importance in understanding the mechanisms of growth. Two of the models discussed previously, those of Tanaka et al (157) and Chan and Lankford (159), predict that an increase in the microstructure unit size will result in decrease in short crack propagation resistance. The formers' blocked slip band model (151) predicts this through a reduction in the fatigue endurance limit. The model also predicts the commonly observed behaviour of an increase in propagation resistance with grain size for long, through thickness cracks. This has been discussed in detail in section 2.2.4.1 and has been attributed mainly to the development of a greater degree of crack closure at near-threshold growth rates, through the generation of rougher fracture surfaces.

In complete contrast to these models, Morris et al (161-163) have argued that an increase in grain size tends to reduce crack propagation rates, due to a greater contribution to plasticity, rather than roughness, induced crack closure. Their models (161-163) are based on crack closure stresses, which were seen to retard crack growth depending on the location of the crack tip relative to the grain boundary towards which it is growing.

In studying crack opening displacements of small surface cracks in an aluminium 2219-T851 alloy, Morris (161) concluded that crack tip opening displacements (CTOD) were proportional to the distance of crack tip to the next grain boundary ( $Z_o$ ). Furthermore, crack tip closure stresses ( $\sigma_{cc}$ ) were found to be greatest for those crack tips with large CTODS (i.e. when  $Z_o$  was large). This was later (164) expressed as:

$$\frac{\sigma_{cc}}{\sigma_{max}} = \alpha \left( \frac{Z_o}{2c} \right)^{\frac{1}{2}} \dots\dots\dots 2.25$$

where  $\sigma_{max}$  was the maximum applied stress,  $\alpha$  a constant and  $2c$  the crack length. Morris (164) found that this expression adequately described his experimental data except when the crack tip was virtually at the grain boundary (i.e.  $Z_o \sim 0$ ). It was assumed that this slight discrepancy in the model arose from slip nucleating across the grain boundary in front of it.

More recently Morris et al (162, 163) have extended this crack closure stress model to predict growth rates. Even for microcracks in 2219-T851 (162), Morris et al showed that crack opening displacements in the centre of the crack were linearly elastic and therefore they assumed that LEFM could adequately describe crack growth, hence;

$$da/dN = A \Delta K_{eff}^m \dots\dots\dots 2.26$$

where  $A$  and  $m$  were constants and  $\Delta K_{eff}$  the effective stress intensity factor of the crack tip which could be reduced by the crack tip closure stress ( $\sigma_{cc}$ ) such that:

$$\Delta K_{eff} = 1.12 (\sigma_{max} - \sigma_{cc}) \sqrt{2c} \dots\dots\dots 2.27$$

Hence, propagation rates could be calculated using the relationships described in equations 2.25, 2.26 and 2.27.

$$da/dN = A \Delta K^n (1 - \alpha Z_o (\frac{1.12\sigma_{max}}{\Delta K})^2)^n \dots\dots\dots 2.28$$

where A,  $\alpha$  and n were constants.

From equations 2.25 and 2.28 it was shown that when a crack entered a new grain and  $Z_o$  was at its maximum value, crack closure stresses would take their largest value and crack propagation rates would be of a minimum. Additionally, as the grain size was increased, crack closure stresses would also increase leading to greater propagation resistance. Figure 2.22 shows Morris et al's experimental data for a 7075-T6 aluminium alloy with the solid lines in the figure representing predicted propagation behaviour from the model described by equation 2.28.

The increase in crack growth rate as the crack tip approaches the grain boundary proposed in Morris et al's model contrasts with the behaviour modelled, more recently, by Eastabrook (165). This model, based upon the distribution of dislocations in a slip band ahead of a microcrack tip, suggested that a maximum value of  $da/dN$  would be attained at a point near the centre of a grain and would thereafter decline to a minimum value as the grain boundary was approached.

The majority of experimental data available describing the propagation behaviour of microstructurally short cracks, suggest that the crack closure stress model can not be universally applied.

Furthermore, the experimental data indicates that crack tip propagation up to grain boundaries is more similar to that proposed by Eastabrook, with propagation rates diminishing as the crack tip approached the grain boundary. The effect that this has on propagation rates been shown by Gerdes et al (166), who examined the growth of short microcracks in a Ti-8-6Al alloy with two different grain sizes (20  $\mu\text{m}$  and 100  $\mu\text{m}$ ). Growth, in vacuum, was monitored at various points throughout the fatigue lives in a SEM. Figure 2.23 shows Gerdes et al's data for short surface cracks growing at  $R = 0.1$ . Also shown are the corresponding long crack curves at  $R = 0.2$  and  $R = 0.6$ . The fact that the finer grained material exhibited better short crack propagation resistance across the range of stress intensity factor ranges studied, was attributed to the greater number of crack tip/grain boundary interactions for this microstructure. Such interactions were thought to lower crack tip driving forces through a greater number of crack tip deflections.

The unexpected feature of this work, however, was that for both grain sizes, the minima in propagation rates occurred at around a crack depth of 50  $\mu\text{m}$ . Although this can be explained for the 100  $\mu\text{m}$  grain sized microstructure in terms of the crack tip interacting with the first grain boundary, as has been reported by Lankford (148, 149), no such account can be readily given for the finer microstructure. However, Gerdes et al, did notice that up until the first minima in propagation rates, cracks in both microstructures appeared to be straight and inclined at approximately  $45^\circ$  to the stress axis.

Thereafter, considerable crack tip deflection occurred, which was accompanied by a change in the fracture mode, from one occurring due to planar slip, to one operating through multiple slip.

Although no solution to this problem can be suggested from Gerdes et al's results, it is noted that their fatigue testing was carried out at different stress levels for each microstructure. It is possible that a mean or maximum stress effect may promote the observed behaviour. In addition, it can be noted from figure 2.23, that no data was collected for the finer microstructure at crack depths below the grain size. Any grain boundary effects on crack propagation behaviour may therefore have been missed.

In other titanium alloys, similar grain size effects on short crack propagation behaviour have been observed. In the work by Hicks and Brown (167), the long and short crack propagation behaviour of the alloys IMI 318 (Ti-6Al-4V) and IMI 685 (Ti-6Al-5Zr-0.5Mo-0.25Si) were studied. Short, surface cracks growing in the  $\alpha + \beta$  heat treated Ti-6Al-4V alloy, with an average primary  $\alpha$  grain size of 12  $\mu\text{m}$ , exhibited propagation rates approximately five times slower at corresponding stress intensity factor ranges, than those growing in IMI 685. The latter alloy had a coarse, aligned  $-\alpha$  microstructure with a prior  $\beta$  grain size of 3.5 mm, resulting from heat treatment above the  $\beta$  transus. The inverse relationship between grain size and short fatigue crack propagation resistance was found to be in complete contrast to that found for the long, through thickness cracks in the same alloys.

Later work by Hicks and Brown (168, 169) on the Ti-6Al-5Zr-0.5Mo-0.25Si (IMI 685) alloy showed that short crack characteristics could persist up to crack depths of several millimetres and hence highlighted the fact that behaviour was strongly microstructurally dependent and not just an effect of physical crack size. For these particular studies the prior  $\beta$  grain size was of the order of 5mm and the microstructure contained large, discrete colonies of aligned  $\alpha$  platlets, approximately 1mm across. Within each colony, crack propagation rates were seen to be dependent on the crack path, which was termed either crystallographic or noncrystallographic. For both types of cracks significant periods of arrest occurred at the prior  $\beta$  grain boundaries. However, for the crystallographic cracks, propagation within individual prior  $\beta$  grains resulted in fracture along favourably orientated slip bands extending across many  $\alpha$ -platlets, giving a cleavage-like appearance. The associated propagation rates were considerably higher than those for the noncrystallographic cracks where colony boundaries caused crack arrest, significant crack tip deviation and the promotion of crack path tortuosity.

In the same study (169), another near  $\alpha$  titanium alloy, IMI 829 (Ti-5Al-3Zr-3Mo-1Sn-0.5Si) was examined. This alloy had a much finer prior  $\beta$  grain size than IMI 685 ( $\sim$  1mm) and a high proportion of basketweave, Widmanstätten  $\alpha$ , achieved by fast cooling from above the  $\beta$ -transus. No discernable difference was observed between the long, through thickness and short crack behaviour.

This was attributed to the considerable misorientation of the  $\alpha$ -platlets in the basketweave structure, effectively reducing the microstructural dimension to a size much smaller than the crack depths studied. Hence, although the cracks studied were physically short (i.e. less than about 1mm), they could not be described as microstructurally short and propagation behaviour approximated to the long crack situation.

Brown and Taylor (138, 170), noted no such grain size dependence on short crack growth behaviour in  $\alpha + \beta$  heat treated Ti-6Al-4V. Alterations in heat treatment temperature and time, resulted in two primary  $\alpha$  and transformed  $\beta$  microstructures with average primary  $\alpha$  grain sizes of 4.7 and 11.7  $\mu\text{m}$ . Whereas the long, through thickness propagation resistance was increased with grain size, no differences in short crack behaviour between the two microstructures could be discerned. One suggestion to account for this short crack behaviour was, that a quicker build up of roughness induced crack closure would occur in the coarser grained material, through a more tortuous crack path, and that this would mask any grain size effects on propagation rates. Re-examination of both microstructures under polarised light showed areas of identical contrast (approximately 300 $\mu\text{m}$  across) much larger than the individual primary  $\alpha$  grain size and suggested that similar crystallographic orientations existed between groups of primary  $\alpha$  grains within each prior  $\beta$  grain. This observation led to the explanation that the only really effective boundaries to short crack propagation were those at the prior  $\beta$  grains.

Hence little difference in growth characteristics would be expected between the two relatively fine grained alloys. An alternative explanation for these observations was recently given by Brown and King (171), who suggested that the variation in grain size between 4.7 and 11.7  $\mu\text{m}$  was not large enough to produce any observable grain size effect, given the large degree of scatter usually associated with short crack growth data.

Similar grain size effects to those seen in titanium alloys have been noticed for steels (172), nickel-base superalloys (167, 47), and aluminium alloys (167, 174). Tokaji et al (172) reported increased short crack propagation resistance in a low alloy Cr-Mo steel when the prior austenite grain size was reduced from 91 to 15  $\mu\text{m}$ . They attributed this to the deceleration of the crack tip on the surface when a surface, or sometimes even a bulk grain boundary, was approached. In Astroloy (167, 47), a decrease of approximately a factor of two in short crack propagation rate was recorded on decreasing the grain size from 50  $\mu\text{m}$  to between 5-12  $\mu\text{m}$ . Interestingly, in the latter study, Brown, King and Hicks (47) found the best short crack propagation resistance to occur in a 'necklace' microstructure consisting of 40  $\mu\text{m}$  grains surrounded by a necklace of 5  $\mu\text{m}$  grains.

In contrast to the amount of research that has been directed to grain size effects in titanium alloys, very little work has been carried out on aluminium alloys.

Hicks and Brown (167) have examined the short crack behaviour of two aluminium alloys with different grain sizes, however, their data cannot be used to define grain size effects, as two distinctly different alloys were used, which resulted in changes in fracture mode, yield strengths and modulus.

The overwhelming majority of data described in this section indicates that, contrary to the results of Morris et al (162, 163) an increase in grain size will have a deleterious effect on short crack propagation resistance. Recently, Brown and King (171) have suggested an explanation for the contradictory effects shown by Morris et al. The cracks modelled in the Al 2219-T851 alloy were Mode I cracks, greater than 25  $\mu\text{m}$  deep, growing virtually perpendicular to the stress axis. Brown and King argued that the plasticity induced closure effects, proposed to account for Morris et al's observations, may give rise to contrasting behaviour when compared to the highly crystallographic, slip band cracks reported by other investigators, particularly in Ni-base and Ti alloys. Whereas slip band cracks may have to undergo distinct changes in crack tip direction on crossing grain boundaries, Mode I cracks would not, and are associated with more homogeneous deformation and thus, the operation of several independent slip systems within a grain.

### 2.4.3 Crystallographic Texture

The influence of crystallographic texture on short crack growth characteristics has been examined by Brown and Taylor in an  $\alpha+\beta$  processed Ti-6Al-4V alloy (138, 170). Short crack propagation resistance was reported to be noticeably improved when the smooth bar test specimens were machined from the LT orientation of the plate rather than the TL orientation. This was consistent with the crack direction being aligned to the basal planes in the hexagonal primary  $\alpha$  grains in the latter orientation, which has been reported to allow an easier path for crack propagation through a reduction in Modulus and Poisson's ratio (141). Significantly, this behaviour was in contrast to that for long cracks in the same microstructure, where the increase in faceted growth in the TL oriented material promoted greater roughness induced crack closure.

In a similar study on an extruded 7475 aluminium alloy, Gregory et al (176) have shown considerable textural effects on microcrack growth. Here, smooth test specimens were machined parallel to ( $0^\circ$ ) and at  $45^\circ$  to the extrusion direction. Initial propagation behaviour was similar for the two orientations with crack tip declaration and arrest occurring at low values of stress intensity factor range. While propagation rates increased for the  $0^\circ$  orientated specimens at slightly higher  $\Delta K_S$ , cracks in the  $45^\circ$  orientated specimens continued to grow intermittently. Examination of the fatigue fracture surfaces identified growth on  $\{111\}$  slip planes in the  $\langle 110 \rangle$  direction for the  $0^\circ$  orientated specimens.

Cracks, inclined at an angle of approximately  $30^\circ$  to the stress axis grew to failure with little crack tip deviation. However, in specimens orientated at  $45^\circ$  to the extrusion direction cracks were observed to change propagation direction at a surface crack length of approximately  $100\ \mu\text{m}$ , from lying perpendicular to the stress axis to  $45^\circ$  to it. This change in crack plane orientation was thought to promote considerable crack arrest, even for cracks only  $50\ \mu\text{m}$  in depth. Textural studies indicated that initial growth occurred on two intersecting  $\{111\}$  slip planes, but on propagation into the specimen interior, grains of another textural component were encountered. As these grains exhibited only one favourably orientated slip system, crack tip re-orientation was necessary leading to continued crack tip arrest.

#### 2.4.4 Dual Phase Microstructures

Whereas much of the previous discussion has considered the interaction between a crack tip and a grain boundary, these boundaries have been between grains of similar nature and composition. Where the boundary is also an interface between different phases, a considerable influence can be exerted on propagation behaviour. Kunio and Yamada (177) showed for a 0.37%C, ferritic/martensitic steel, that small cracks nucleated in the softer, ferrite matrix could be substantially retarded on reaching the harder, martensitic second phase. Further propagation was observed only to occur when the stress was increased to above the fatigue limit.

Similar observations by De los Rios et al (128, 178) on ferritic/pearlitic structures suggest that the fatigue limit for these materials is not a measure of the stress to avoid crack nucleation, but rather a measure of the stress required to overcome the retardation effects of the second phase. The beneficial behaviour to crack growth offered by the pearlite appeared to be the fine banding of ferrite/cementite plates in the structure, which severely reduced slip length.

In  $\alpha+\beta$  heat treated titanium alloys (166, 167), similar behaviour has been reported, with initiation and early initial growth occurring along slip bands in primary  $\alpha$  grains, analogous to the ferrite matrix in steels. Crack tip deflection has been seen to occur at  $\alpha_p$ /transformed  $\beta$  boundaries, although no direct evidence was given in either study of the cracks becoming non-propagating.

#### 2.4.5 Environmental effects

The difficulties associated with monitoring short crack growth in environments other than laboratory air, has been the predominant reason why only limited data has been obtained. The relevant studies (149, 166) have both involved the use of an SEM, with specially modified loading rigs, to examine short cracks at various stages through their fatigue lives. The cracks being grown in inert environments between insertion into the SEM. In the first study, by Lankford (149), short cracks in a 7075-T6 aluminium alloy were grown in a  $N_2$  environment and the behaviour compared to that in laboratory air.

Lankford's findings, summarised in the  $da/dN$  vs  $2a$  diagram shown in figure 2.24, revealed that although the nitrogen atmosphere appeared to promote slightly better propagation resistance, similar fracture modes were observed in each environment. Crack paths however, were found to be quite distinct. Whereas cracks grown in air were all within  $10^\circ$  normal to the stress axis, cracks in the inert atmosphere were typically orientated at  $45^\circ$  to the loading direction. Similar findings were reported by Gerdes et al (166) for short cracks growing in a Ti-8.6Al alloy in both laboratory air and under vacuum.

Lankford (149) used a stereoimaging technique to examine the shear bands at the loaded crack tips in both environments. For the air grown cracks, one or two shear bands were usually detected emanating from crack tips at approximately  $80^\circ$  to the propagation direction. All crack tip opening was seen to be in Mode I. Conversely, the nitrogen environment produced plastic deformation ahead of the crack tip in only one shear band, lying in the plane of the crack propagation direction. In this case, the material ahead of the crack tip yielded under Mode II opening. Furthermore, Lankford considered that if the increased crack path tortuosity of the  $N_2$  grown short cracks was taken into account (i.e. the actual crack length projected onto the plane normal to the stress axis), propagation rates for the two environments would be comparable. This was somewhat dissimilar to the case for long, through thickness cracks where the inert atmosphere was seen to promote propagation resistance (figure 2.24), even though crack opening modes did not differ significantly between environments.

This contradictory behaviour was explained in terms of the efficiency of crack extension in the plastic zone ahead of the crack tip. This was thought to be easier when the shear bands lay in the plane of the crack tip ( $N_2$  atmosphere) which led to a decrease in short fatigue crack propagation resistance.

#### 2.4.6 The effect of crack length

One of the most important criterion from the point of view of the engineer, is what is the crack depth at which short crack propagation behaviour can no longer be distinguished from that of long cracks and hence the lower limit to which conventional LEFM can be utilised in design? Considering the Kitagawa plot (figure 2.19) this critical crack depth was defined as  $a_2$ , the point below which the short crack data deviated from the line describing the relationship between stress intensity factor range and crack depth. From the available data in the literature, including their own results on aluminium bronze, Taylor and Knott (151, 179) suggested that  $a_2$  could simply be defined as approximately ten times the grain size of the material. Cracks shorter than this did not satisfy the condition that the surrounding material deformed homogeneously, due to the constraint of the local microstructure ahead of the crack tip. In engineering design terms, Taylor and Knott hypothesized that there was no real need to perform short crack tests. From conventional long crack propagation data, the crack depth  $a_0$  (figure 2.19) could be determined and the critical depth  $a_2$  could be calculated, assuming  $a_2 = 4a_0$ .

Fatigue lives could then be computed using existing fracture mechanics procedures, with  $a_2$  as the critical defect size.

Tokaji et al (172), examining the short crack propagation characteristics of a steel with two different prior austenite grain sizes, also found that the shortest crack depth, that LEFM could be applied, was microstructurally dependent. For the two grain sizes ( $d$ ) evaluated, 15  $\mu\text{m}$  and 91  $\mu\text{m}$ , the critical crack depth ( $a_2$ ) was found to be 13 $d$  and 5 $d$  respectively. It was also noted however, that the effects of local microstructure on growth characteristics virtually disappeared when cracks became deeper than about 3 times the grain size for both microstructures. The fact that cracks deeper than this continued to grow at faster rates than predicted by LEFM, was attributed to the build up of crack closure with increasing crack depth. The authors concluded that such 'mechanically' short cracks could be evaluated by LEFM, if crack closure for short cracks could be experimentally measured. Furthermore, the real limit of LEFM corresponded to a crack depth of about 3 x grain size.

Blom et al (174) have also considered that an LEFM approach, in describing short crack behaviour, is valid down to crack depths below the divergence of long and short crack propagation data, if the analysis is based upon the effective stress intensity factor range ( $\Delta K_{\text{eff}}$ ). For the two aluminium alloys evaluated (2024-T3 and 7475-T6), the critical crack depth ( $a_1$ ) below which 'real' short crack behaviour was observed and could not be predicted by  $\Delta K_{\text{eff}}$  could be determined from a

modified Kitagawa plot (2.25). The critical crack depth ( $a_1$ ) was at the point of intersection between the line describing the fatigue limit (for a particular R - ratio) and the sloping line showing the dependence of crack depth on  $\Delta K_{eff}$ . This crack depth is consistent with that characterised by Taylor and Knott (151, 179) and shown in figure 2.19 as  $a_1$ . A change in fracture mode around the depth  $a_1$  was also observed. Cracking was initially in a crystallographic, Stage I type mode through entire grains and a change was seen at  $a_1$  to a zig<sup>^</sup>zag, transcrystalline stage II mode. Blom and co-workers interpreted their results to indicate that there was a slow increase in crack closure contributions with crack depth above the critical depth  $a_1$ . Such behaviour is consistent with that previously described by Tokaji et al (171).

A similar view was taken by Gerdes et al (166) from their results on a Ti-8.6Al alloy, which showed that short crack propagation data at a low R-ratio tended towards the long crack data at an R-ratio of 0.6 as the crack extended. Hence short crack propagation could be better described by  $\Delta K_{eff}$ , as proposed by Blom et al (174). However, short crack testing carried out at the higher R-ratio revealed that propagation resistance deteriorated still further with respect to the R = 0.1 data (figure 2.26). If crack closure contributions are absent or small, for microstructurally short cracks, as has been suggested (172, 174), any differences in propagation behaviour between tests at high and low R-ratios should also be small. Clearly, Gerdes et al's results do not verify this conjecture, unless the describing parameter ( $\Delta K$ ) is inadequate for the present purpose.

Indeed, Gerdes et al found that the data from the two R-ratio short crack tests were virtually identical when plotted in terms of  $K_{max}$ . It appears that short cracks may therefore be controlled by  $K_{max}$ , or  $\sigma_{max}$ , rather than by  $\Delta K$ . The fact that at both high and low R-ratios, the crack propagation rate was seen to decelerate at identical crack depths ( $\sim 45 \mu m$ ) and that fractographic examination revealed similar crack paths, supports this view.

In an attempt to characterise the parameters distinguishing long and short crack behaviour, Lankford (180) has recently considered the relationship between the maximum plastic zone size ahead of a crack tip ( $r_{mpz}$ ) to the crack depth (a) and the microstructural unit size (d). From a correlation of the available literature and from his own data for a 7075-T6 aluminium alloy, Lankford determined two interdependences between these parameters. The information implied that for short cracks to grow at faster propagation rates than long, through thickness cracks, the ratio of plastic zone size to crack depth should exceed about 0.05. However, it was shown that this relationship could not be applied universally in predicting whether a crack will exhibit anomalously rapid growth, as some materials did not show short crack propagation characteristics, even though this ratio was exceeded. The parameter that did manage to predict the type of growth expected was the ratio between the plastic zone size corresponding to the minimum crack depth studied ( $r_p^{min}$ ) and the size of the local microstructural unit, usually the grain size (d).

$r_p^{\min}/d$  was found to be less than 1 for all the materials that experienced rapid growth of short cracks. A further appealing aspect of this ratio was that it should equal 1 when the long and short crack propagation data merged. Taking Taylor and Knott's suggestion that this occurred when the crack depth was about 10 x the grain size (151, 179), Lankford showed that  $r_p^{\min}/d = 0.84$  for his 7075-T6 alloy, which is close to unity.

#### 2.4.7 Crack Shape

If, as has been discussed above, the local microstructure at a crack tip can significantly influence short crack propagation behaviour, it can be assumed that the shape of the crack may be distorted by these microstructural interactions. Under simple tensile loading conditions, a crack surface should take a half penny appearance if driven by  $K$  assuming that initiation also occurred from a similarly shaped source and that microstructural influences were absent. An  $a/c$  ratio of 1.0 (where  $a$  and  $c$  are the crack depth and half the surface crack length respectively) should be maintained throughout the crack life if surface effects are ignored. It has been observed however, that the effect of the local microstructure at the crack tip produces an irregular crack front (172, 181, 182). Additionally, the choice of initiation site, whether it be from an inclusion or through slip band formation, can control the initial crack shape. The determination of the crack shape is important, in that short crack growth models are normally based on the crack tip propagating into the material bulk, while experimental observations are almost exclusively founded upon measurements of surface crack length.

The majority of crack growth rate studies assume a constant  $a/c$  ratio is maintained throughout (148, 149, 166-169, 176). The ratio is usually determined from the crack shape at the end of testing, when the crack depth is large with respect to the microstructure. Furthermore, Lankford (148) has shown that a fairly constant, half penny crack shape ( $a/c = 1.0$ ) is preserved even at crack depths of the same order as the grain size, in a 7075-T6 aluminium alloy. Conversely, Tokaji et al (172) have shown for a large grained Cr-Mo steel ( $d = 91 \mu\text{m}$ ), that below crack depths of about  $3d$  crack aspect ratios varied between 0 and 1.5. The diversity being a result of the nature of the crack tip: grain boundary interactions. At greater crack depths a constant  $a/c$  ratio of about 0.8 was reported. The reason why no deviation from an  $a/c$  ratio of about 0.8 was seen for a finer grain size material, was attributed to little data being obtained below crack depths of  $3d$ . Hence any variation due to microstructure had been missed.

In a  $100 \mu\text{m}$  grain sized, Ti-8.6Al alloy, that exhibited planar slip, Wagner et al (181) have examined the change in crack shape as a crack lengthened. This was achieved through grinding back through short surface cracks and measuring the crack length of various crack depths. They showed that the cracks were able to propagate faster along the specimen surface than into the material bulk and suggested that this was probably due to free surface effects. The aspect ratio was seen to change continuously depending on the location of the surface and interior crack tips, and was always below unity.

Qualitatively, a shallow profile was observed when the surface crack was able to accelerate after being held at a grain boundary, as shown schematically in figure 2.27 a/c/e. In contrast, a near semi-circular profile occurred when surface grains were arrested by grain boundaries (figure 2.27 b/d).

Cox and Morris (182) have employed a statistical method to predict the evolution of crack shape in a 7075-T6 aluminium alloy. Monte Carlo simulations were carried out, based on stress intensity solutions around an irregular crack front coupled with the laws governing crack growth through the influence of microstructure, founded upon an established plasticity induced crack closure model (163). Furthermore, experimental evidence was presented to substantiate the model. Results based on predictions and experiments are shown in figure 2.28 in terms of the aspect ratio vs the normalised crack depth. Initially, very shallow cracks were formed ( $a/c < 0.1$ ) due to crack formation from slip bands. Thereafter, the aspect ratio increased to a maximum between crack depths of  $50-100 \mu\text{m}$  before becoming constant at around 0.8 at greater depths. The peak in aspect ratio had been predicted by Zurek et al's model (163), which is based upon the parameter  $z$ , the distance of the crack tip to the next grain boundary towards which it is growing. Due to the non equiaxed grain shape being assessed ( $\sim 120 \mu\text{m}$  in length and only  $20 \mu\text{m}$  deep),  $z$  would take a much smaller value for cracks growing into the specimen interior and this, according to Zurek et al, will increase propagation rates in that direction, so leading to a greater aspect ratio.

## 2.5 OTHER TYPES OF SHORT FATIGUE CRACKS

The second definition of a short crack, as described in section 2.1, is when the crack length is small compared to the scale of local plasticity. Although this definition is usually applicable to cracks embedded in the plastic zone generated by a notch, it can also be assigned to the case where the plastic zone produced ahead of a crack tip, is of the order of the crack length (i.e. the crack length is usually small and the stress field containing it, very large, typically approaching the yield stress).

The latter situation can be identical to that of microstructurally short cracks, as discussed in section 2.4. The rapid growth of such cracks has been partly attributed to the breakdown in LEFM in adequately describing the crack driving forces. Smith (156) for example, has shown that for LEFM to be applicable, the ratio of plastic zone size to crack length should be less than 0.02. Clearly, if the crack length is small and the stresses applied to it large, this criterion can be invalidated. Dowling (183) has attempted to use elastic-plastic fracture mechanics (EPFM) to describe the growth of this type of crack in a steel subjected to completely reversed strain cycling. Although the use of the J-integral produced a closer correlation of short crack data with those for long, through thickness cracks, cracks with lengths less than about 189 $\mu$ m still exhibited faster than expected propagation rates. A further improvement in equivalence was obtained when El Haddad et al (158) reanalysed Dowling's data in terms of their  $l_0$  concept (described in section 2.4.1).

The ability of the  $l_0$  characterisation to correlate long and short crack data is significant, however, as it is devised empirically, with no established physical meaning, current application in developing an understanding of the short crack problem is limited.

Similarly, for cracks embedded in the plastic zone generated by a notch, the premise that plastic yielding in front of the crack tip is small compared to the crack length, is violated. For this type of crack, similar growth characteristics to microstructurally short cracks have been observed. Initially, propagation rates are high, well below the long crack threshold. Subsequently, they are reduced and crack arrest can occur. Using arguments based on the J-integral, Hammouda and Miller (184) have explained this behaviour in terms of a notch plasticity theory. Here, crack propagation rates were determined by the sum of the shear displacement in the material caused by the presence of the notch and that generated by the plastic zone ahead of the crack tip. When the crack was completely embedded in the plastic zone of the notch, the contribution of the latter to the total shear displacement was minimal. Crack growth rates were decreased until arrest occurred or the crack grew out of the notch plastic zone. In the latter case, the short crack propagation data would merge with that of long cracks, as the plastic zone ahead of the crack tip would dominate and growth would be determined by LEFM considerations.

Other arguments have been presented based on crack closure concepts. For instance, Tanaka and Nakai (185) have used a compliance technique to measure crack closure for small cracks embedded in notches in a low carbon steel. Their data showed that little closure was associated with these cracks, which led them to present their results in terms of the effective stress intensity factor range ( $\Delta K_{eff}$ ). The anomalously fast growth rates of the short cracks fell into the line associated with  $\Delta K_{eff}$  for long, through thickness cracks. Analytical studies by Newman (186) have supported this view. He showed that as a crack increased in length, while still embedded in the notch plastic zone, the permanent residual plastic strains associated with the zone, increase with the length of wake behind the crack tip. The effective driving force at the crack tip is continually reduced, slowing the crack propagation rates until crack arrest occurs or the crack grows out of the notch plastic zone field.

The final definition of a short crack mentioned in the introduction (2.1), was when a crack is considered to be long compared to the scale of both the local microstructure and the local plasticity, but is physically short (generally less than 1mm). Although characterisations based on LFM and continuum mechanics should be applicable, anomalously fast propagation rates can occur compared to long cracks growing under nominally identical driving forces.

Behaviour of this type has been highlighted by McCarver and Ritchie (187) working with a nickel base superalloy. Precracked, bend specimens had their top surface ground away to leave small, surface cracks, 0.01 to 0.2mm deep. After the application of a stress relieving heat treatment, the cracks were fatigued at  $R = 0.1$  at various initial stress intensity factor ranges ( $\Delta K$ ) and the number of cycles to failure was noted. Threshold stress intensity factor ranges ( $\Delta K_{th}$ ) were defined in terms of the initial  $\Delta K$  that failed to cause any detectable crack extension in  $5 \times 10^7$  cycles.  $\Delta K_{th}$  values were reported to be over 60% smaller than measured  $\Delta K_{th}$  for long, through thickness cracks. There was a similarity, however, between the threshold values for these short cracks and the threshold values for long cracks growing at an  $R$  ratio = 0.8. The authors concluded that although LEFM was valid in that the maximum plastic zone sizes were less than 0.067 of the crack length, the lower threshold associated with the physically short cracks was due to the absence of crack closure contributions. Since a crack of small dimensions will have limited fracture surface area, it would be expected to grow at a faster rate than a long crack at the same low  $R$  ratio which would be subjected to considerable crack closure.

Support for McCarver and Ritchie's theory has more recently been given (53, 188, 189). James and Morris (188) have measured the crack opening displacements (COD), at minimum load, on a function of crack length, for cracks up to 500  $\mu\text{m}$  deep in a Ti-6Al-2Sn-4Zr-6Mo alloy.

Some of their results, depicted in figure 2.29, show that an increase in crack closure was seen up to crack lengths of about 150  $\mu\text{m}$ . Thereafter, no increase in COD and, hence closure, was apparent. Even though the crack length was over an order of magnitude greater than either the primary  $\alpha$  or transformed  $\beta$  grain size, crack propagation rates were higher than predicted by LEFM up to 150  $\mu\text{m}$ .

Zaiken and Ritchie (53) and Bu & Stephens (189) have both shown for 7XXX series aluminium alloys, that by machining away the wake of a long crack behind a crack tip that had previously been grown down to threshold, growth could recommence at low R ratio. This was despite the fact that the nominal stress intensity factor ranges did not exceed threshold values. Similar experiments performed at higher R ratios (0.8) by Zaiken and Ritchie revealed that cracks remained dormant after the removal of the wake and the loads reapplied.

In-situ crack closure measurements made by Zaiken and Ritchie (53) during the removal of the wake behind the crack tip in the R = 0.1 tests, showed that only about 50% of the closure was within 500  $\mu\text{m}$  of the crack tip. This is in some agreement with the crack closure model proposed by Beevers (46), in section 2.2.3, in that both consider that closure builds up quickly behind the crack tip. The Beevers model though, considers that the wake immediately behind the crack tip is important as it is here that the majority of the closure is generated.

The effect on short fatigue crack behaviour of the replication technique, commonly used for monitoring the initiation and growth of short fatigue cracks, has recently been studied (138, 144, 190). Brown (144), for example, working with a number of microstructural variations of a Ti-6Al-4V alloy, noticed increased fatigue lives of specimens subjected to interrupted cycling and replication, as compared to those which were cycled continuously to failure. What needs to be ascertained is whether it is the interruption in cycling or the application of the replicating medium that is responsible for the beneficial extension of the fatigue life.

Earlier work in a similar field by Evans and Gostelow (191) on an aligned, Widmanstätten Ti-6Al-5Zr-0.5Mo-0.25Si alloy (IMI 685), showed that a five minute dwell at maximum load after each fatigue cycle was detrimental to the fatigue life. An increase in the number of crystallographic facets on the fracture surfaces and other similarities to creep behaviour, prompted the authors to propose a model for dwell sensitivity based as a combination of creep and a hydrogen assisted dislocation locking mechanism.

The work of Evans and Gostelow was in agreement with that of Stubbington and Pearson (192, 193) which was concerned with dwell at maximum load in  $\alpha$  and transformed  $\beta$  microstructures of two highly textured titanium alloys (Ti-6Al-4V and Ti-4Al-4Mo-2Sn-0.5Si). Significantly higher growth rates were reported where dwell was introduced, especially when the stressing

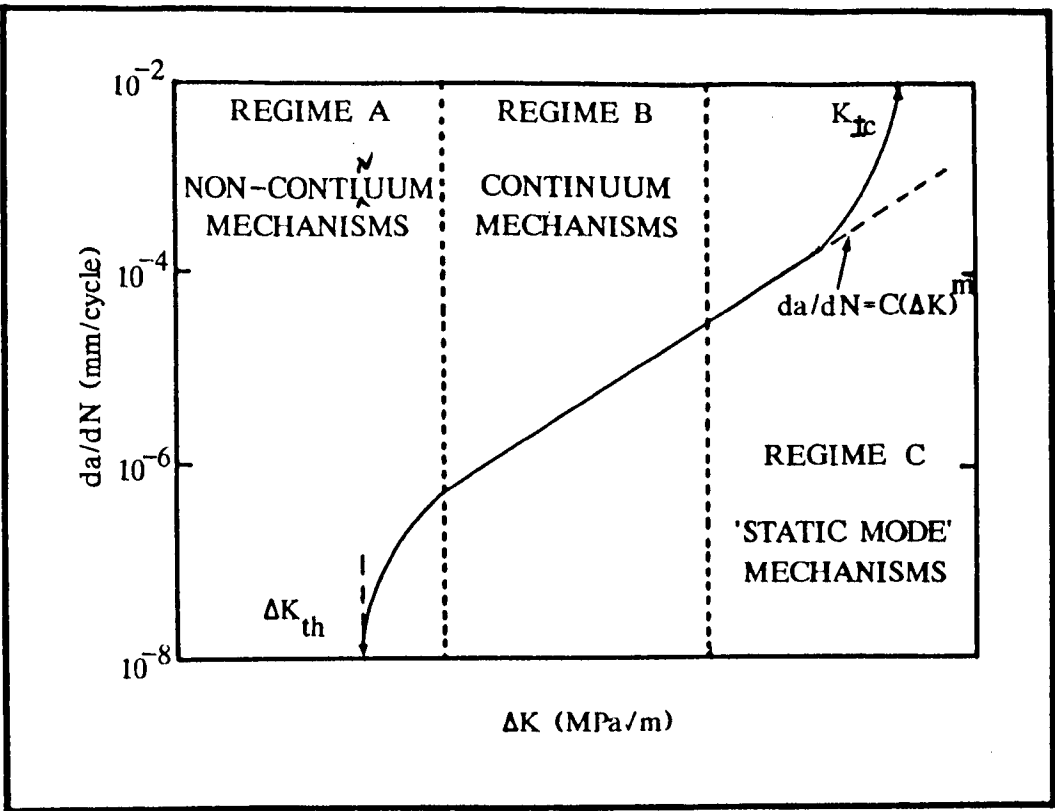
direction was approximately normal to the basal planes of the primary  $\alpha$  grains. Dwell effects were worse for microstructures which contained the greatest proportion of primary  $\alpha$ , but negligible for predominantly transformed  $\beta$  structures, even though these were still highly textured. The observed behaviour was attributed to strain-induced hydrogen embrittlement at, or immediately ahead of, a crack tip in the  $\alpha$  phase.

Conversely, Eylon (194, 195) has found no detrimental effects on propagation rates due to dwell at maximum load in various Ti-6Al-4V microstructures. Indeed, in some cases increased propagation resistance accompanied the dwell tests, which was thought to be due to a more tortuous crack path and the associated increase in crack closure contributions. In the later study (195) Eylon recorded no detrimental effects due to dwell, even though the alloy he was evaluating was strongly textured and contained over twice the hydrogen content of the material used by Stubbington and Pearson (192, 193).

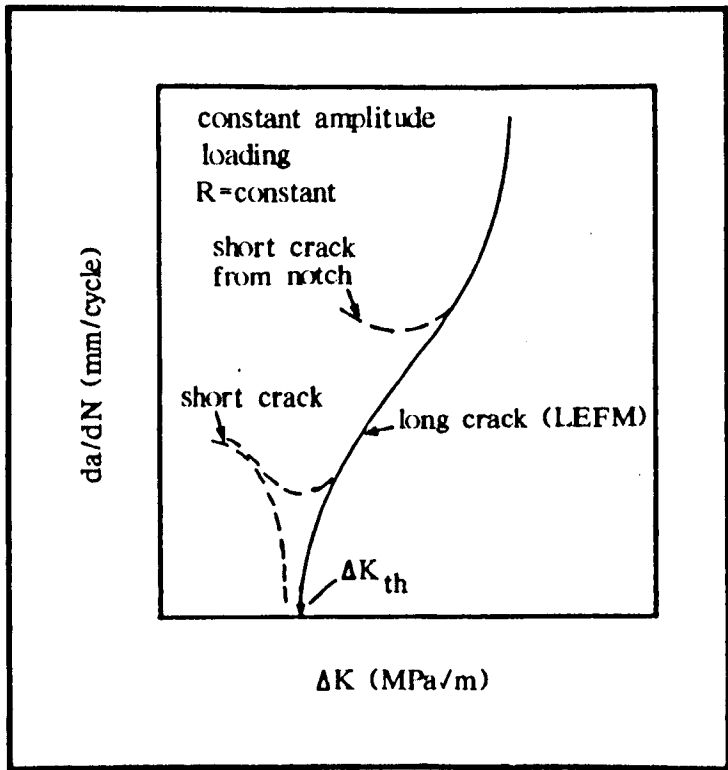
Stubbington and Pearson (192, 193) had also noted a more tortuous crack path in tests where dwells had been applied, even though faster propagation rates were observed. It should be noted that in these studies, propagation rates down to only about  $10^{-4}$  mm/cycle were examined. The effects of crack closure on growth rates would have been more apparent at lower growth rates. In addition, Eylon (195) concluded, that microstructure, hydrogen content and texture did not directly influence dwell effects and that specimen design and testing procedure could not be ignored as possible causes of the conflicting dwell test results.

Brown and Smith (144) have shown, for both Ti-6Al-4V and pure Ti, that an increase in the fatigue life resulted from the repeated use of the replication technique used to monitor short crack growth behaviour, with the greatest enhancement occurring at lower stresses. It was suggested that these observations could be attributed to strain ageing effects, either in the bulk of the specimen or at the surface. Hence both initiation and propagation would be retarded. At the lower stress levels, the strain ageing was more effective as a strengthening mechanism, as the local plastic strain would be smaller. Brown (138, 190) has shown similar behaviour for a Ti-6Al-4V microstructure containing predominantly primary  $\alpha$ . Data plotted in figure 2.30 shows this beneficial effect on fatigue life when the cycling is interrupted for replication, compared to that for continuous cycling.

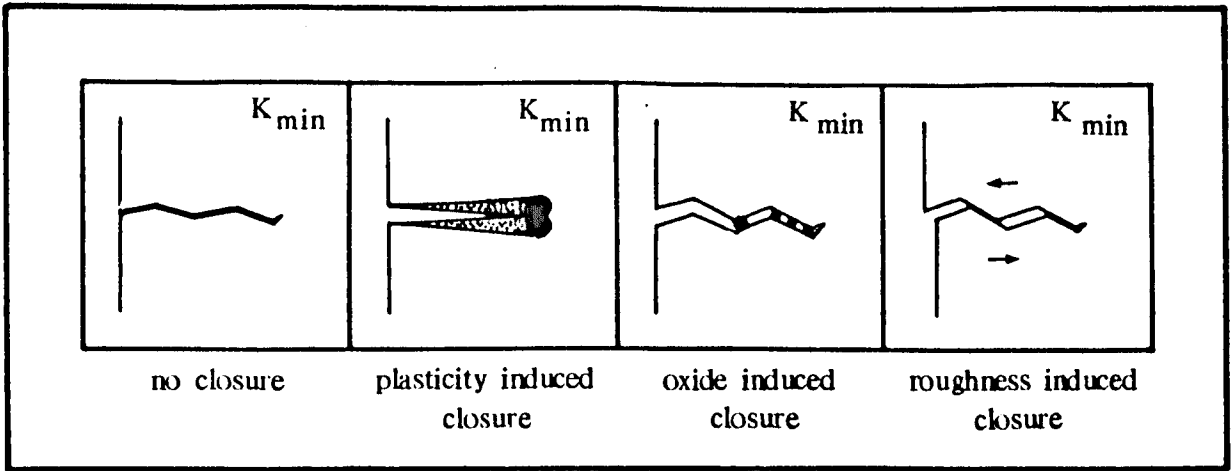
In the same study, Brown (191) evaluated the effects of the acetone impregnated replicating material. Testing showed that when replicas were taken more frequently, the fatigue life was reduced (figure 2.30). It was suggested that the acetone used to soften the replicating material may have caused changes in the ease of cracking, either through a reduction in surface energy or due to a reaction producing hydrogen at the crack tip. In titanium alloys therefore, the measured fatigue lives using the replication technique, will be determined by the competing processes during the rest periods, of strengthening due to strain ageing and changes due to the presence of acetone.



2.1 Schematic illustration of the three regimes of fatigue crack propagation behaviour. (3)



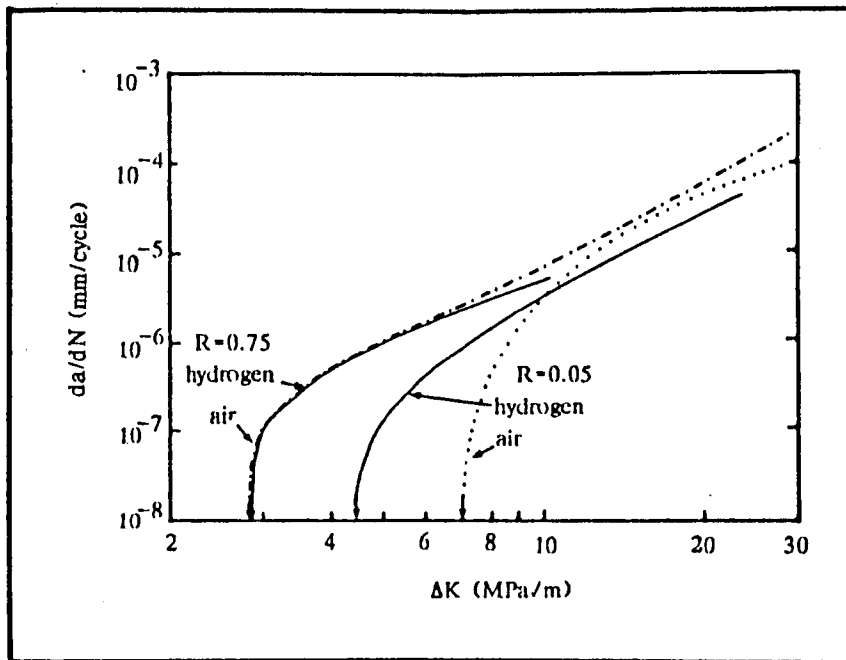
2.2 Typical fatigue crack propagation rates ( $da/dN$ ) for long and short cracks as a function of stress intensity factor range ( $\Delta K$ ) (5)



2.3

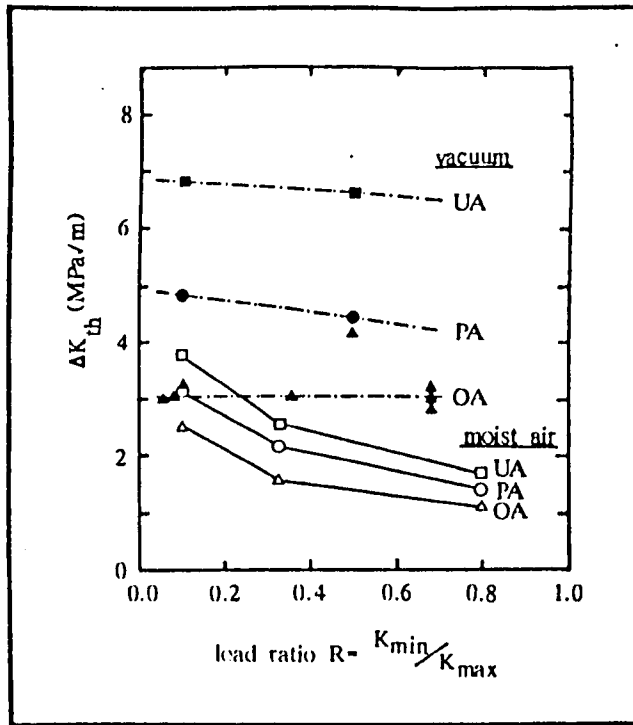
Schematic illustration of possible mechanisms of fatigue crack closure

- (a) no closure (b) plasticity induced crack closure  
 (c) oxide induced crack closure  
 (d) roughness induced crack closure

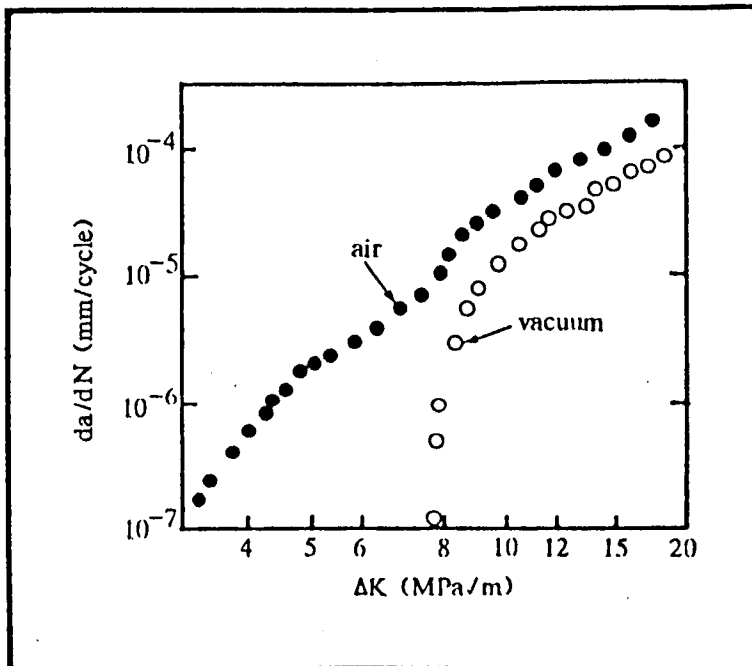


2.4

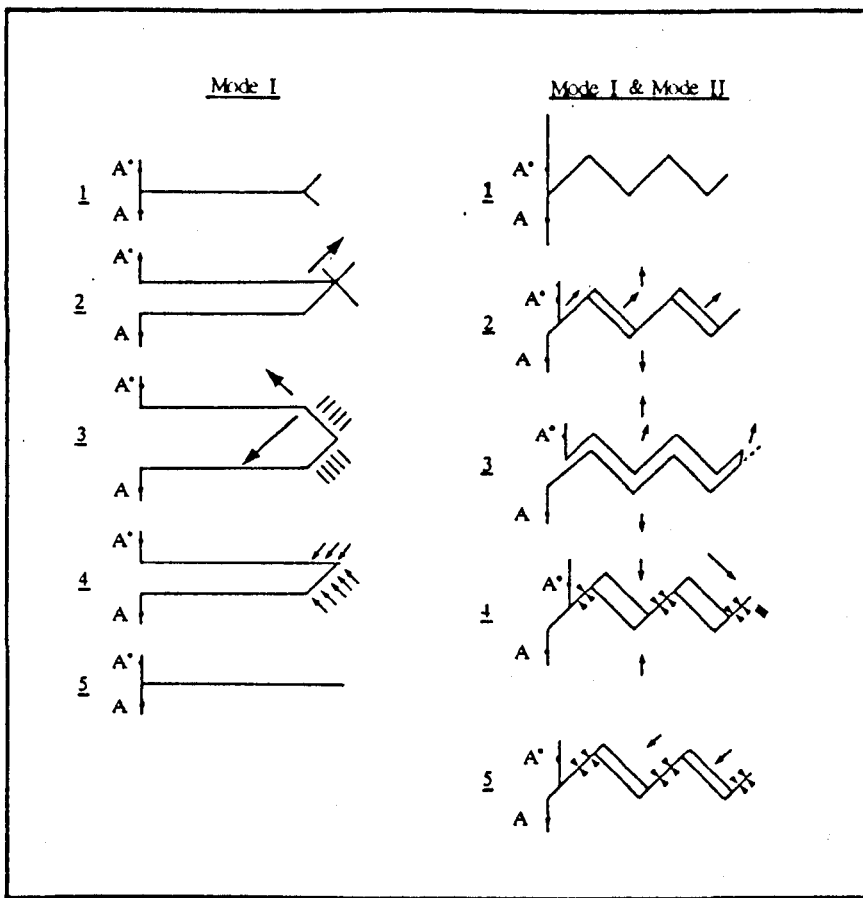
Fatigue crack propagation of martensitic 2.5% Cr - 1% Mo steel tested at  $R = 0.05$  and  $R = 0.75$  in moist air and dry hydrogen gas (13)



2.5 Variation in threshold stress intensity factor range ( $\Delta K_{th}$ ) with load ratio  $R$  for 7010 underaged (UA), peakaged (PA) and overaged (OA) conditions tested in moist air and in vacuo (21)



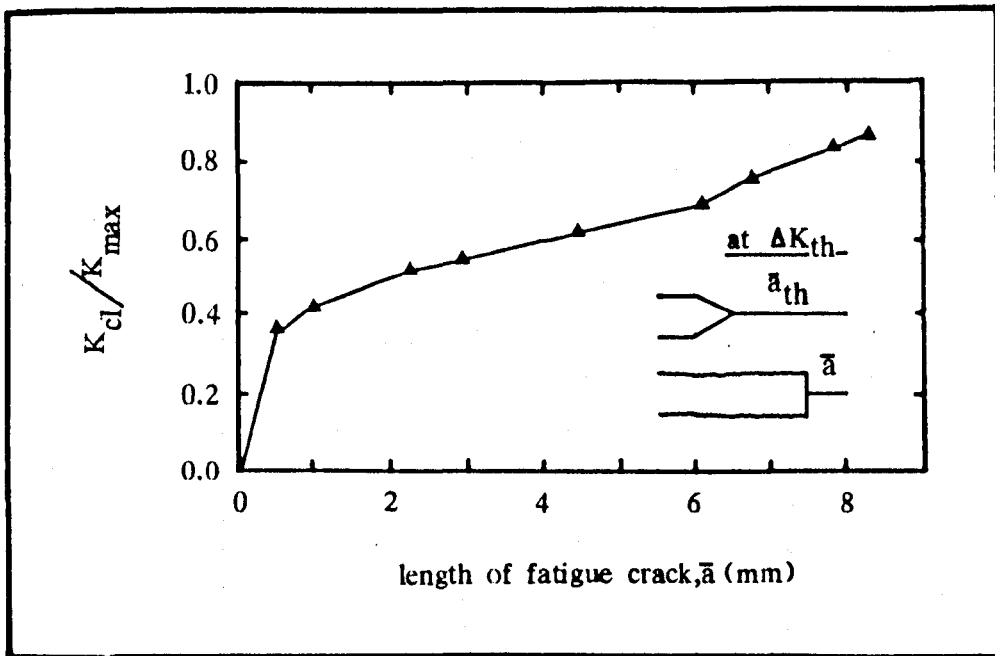
2.6 Comparison of fatigue crack propagation in air and vacuum at  $R = 0.35$  for a dual phase  $\alpha_p +$  transformed  $\beta$  microstructure in Ti-6Al-4V. (28)



2.7

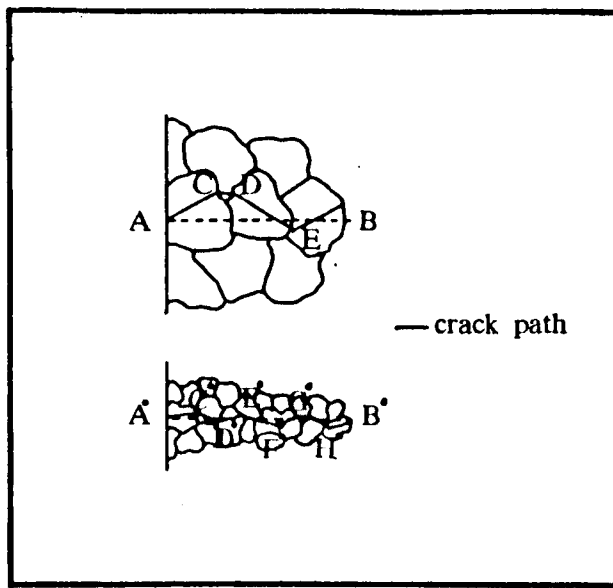
Schematic illustration of crack growth

(a) Mode I growth (b) Mode II & Mode I (42)

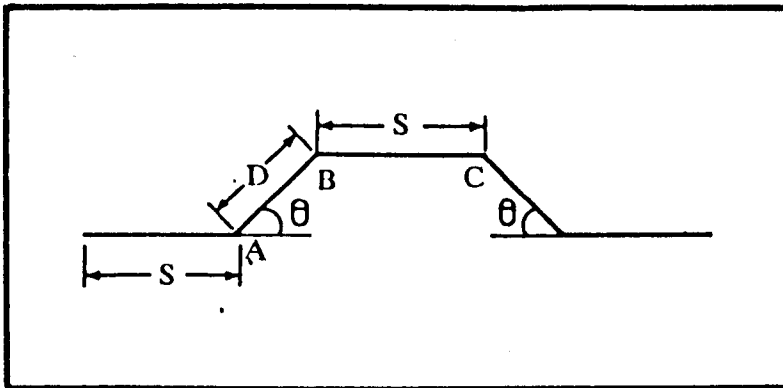


2.8

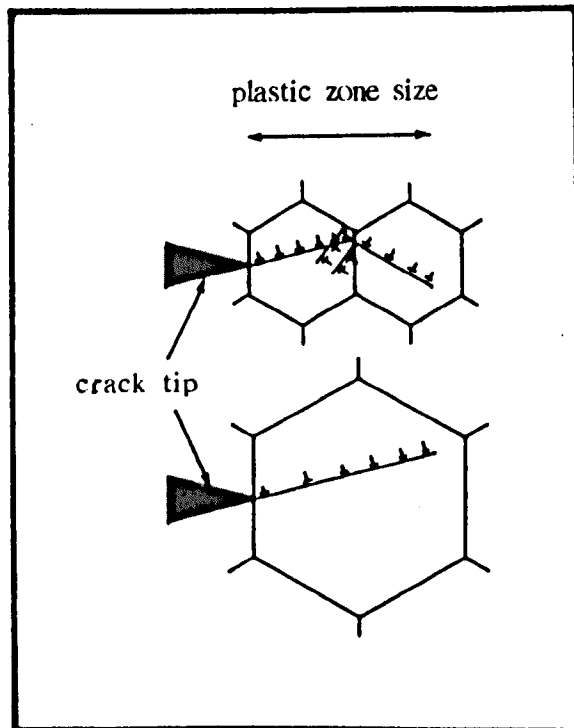
Variation in crack closure for 7150-T6 measured in terms of  $K_{cl}/K_{max}$ , for an arrested crack at  $K_{th}$  ( $R = 0.1$ ) as a function of remaining fatigue crack length,  $\bar{a}$ , during progressive machining away of material in the wake of the crack tip. (52)



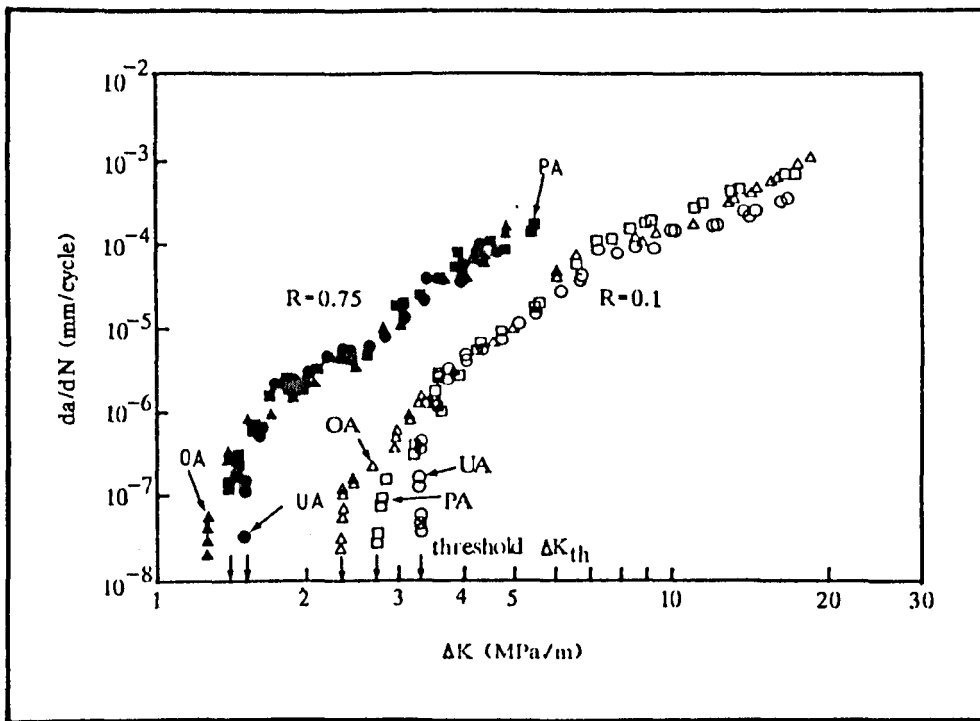
2.9 Fatigue crack path in (a) coarse grained microstructure and (b) fine grained microstructure (60, 61)



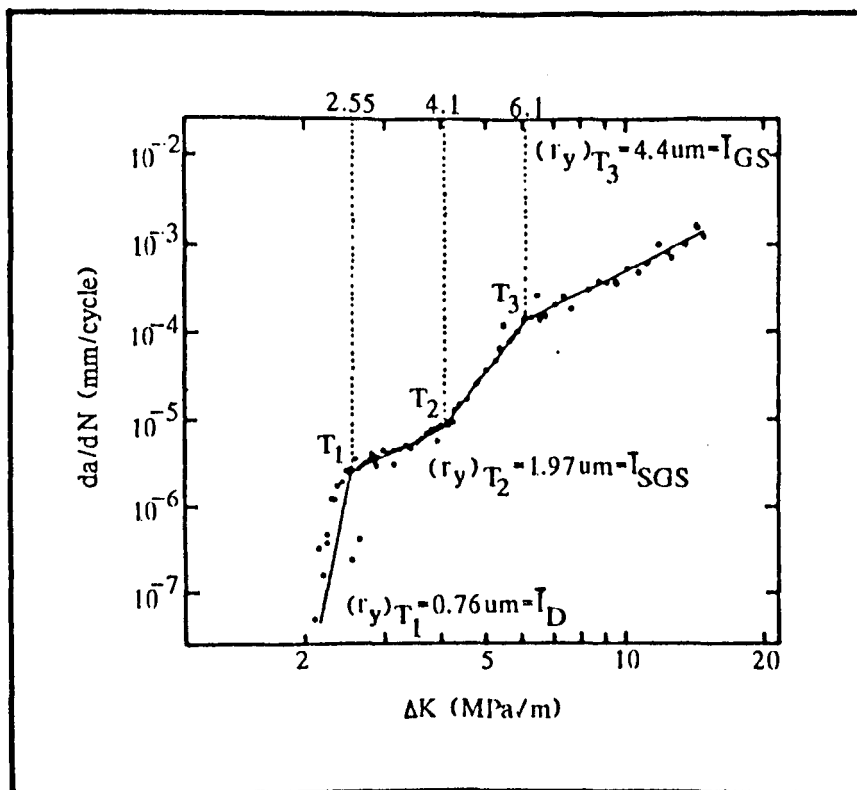
2.10 Idealization of a small segment of a crack with periodic tilts (73)



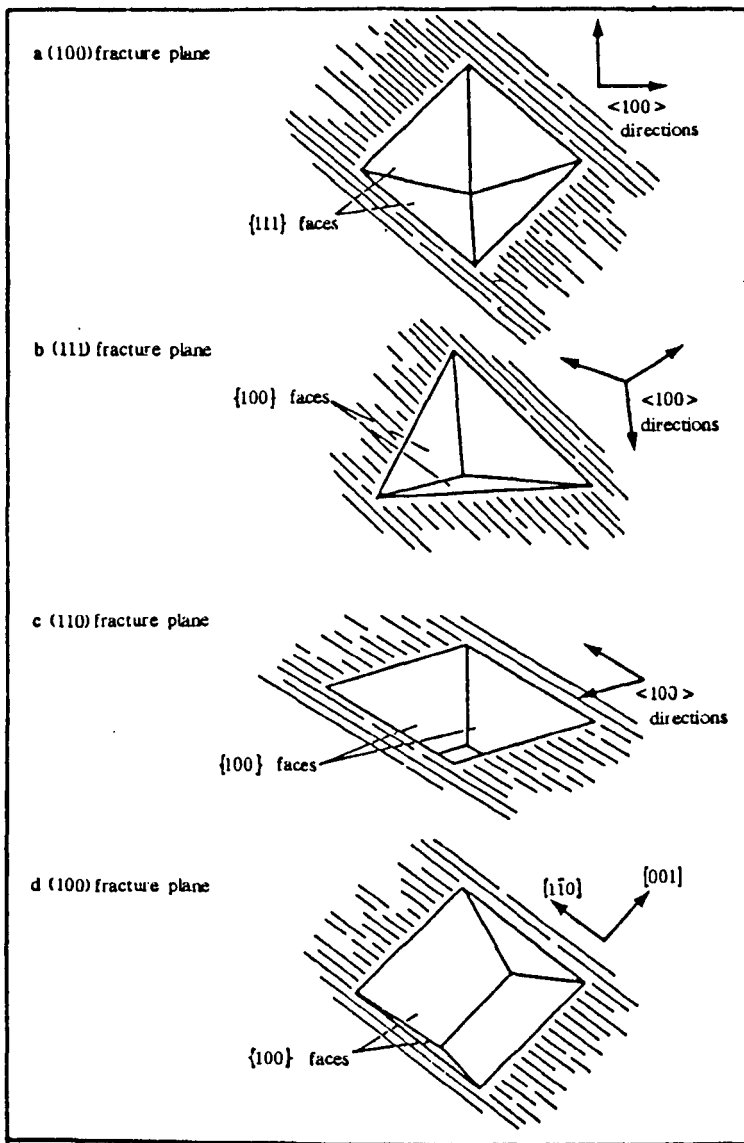
2.11 Schematic illustration of the effect of grain size on dislocation structure at the crack tip (a) small grain size (b) large grain size (71)



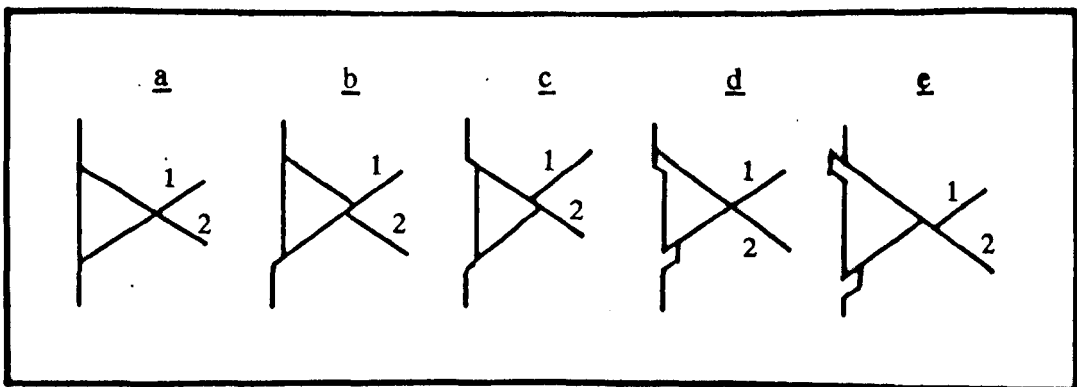
2.12 Variation in fatigue crack growth rate ( $da/dN$ ) as a function of  $\Delta K$  for 7150 tested at  $R = 0.1$  and  $R = 0.75$  in moist air. Data are shown for underaged, peakaged and overaged microstructures (90)



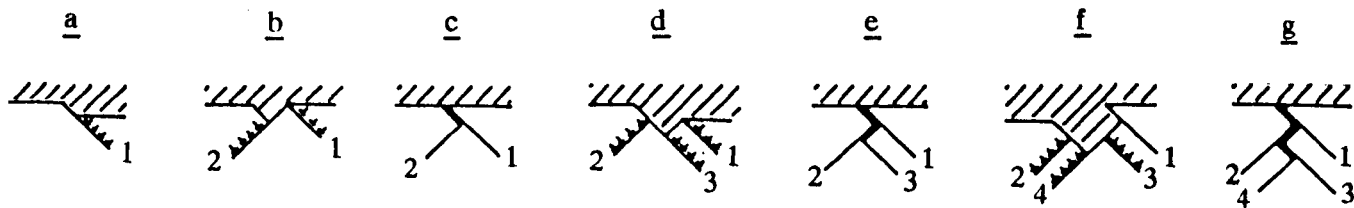
2.13 Fatigue crack growth rates in 7075-T6 alloy (107)



2.14 Crystallography of etch pits (a) (100) fracture plane, (b) (111) fracture plane (c) (110) fracture plane, (d) (100) fracture plane

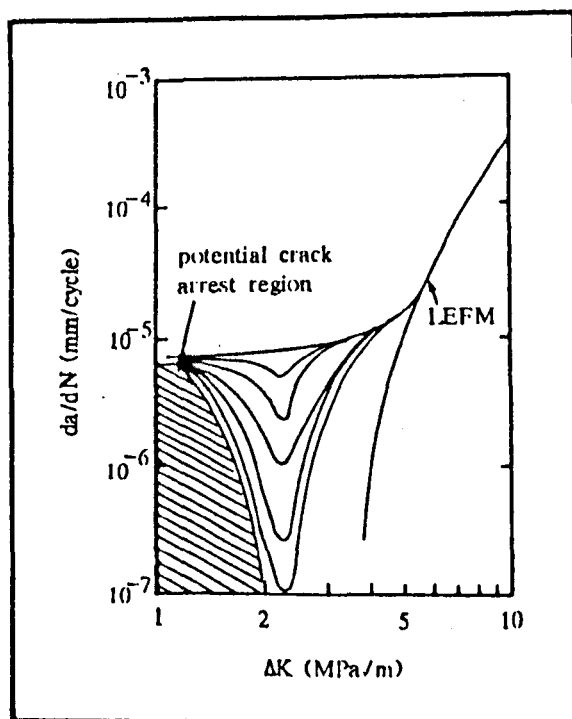
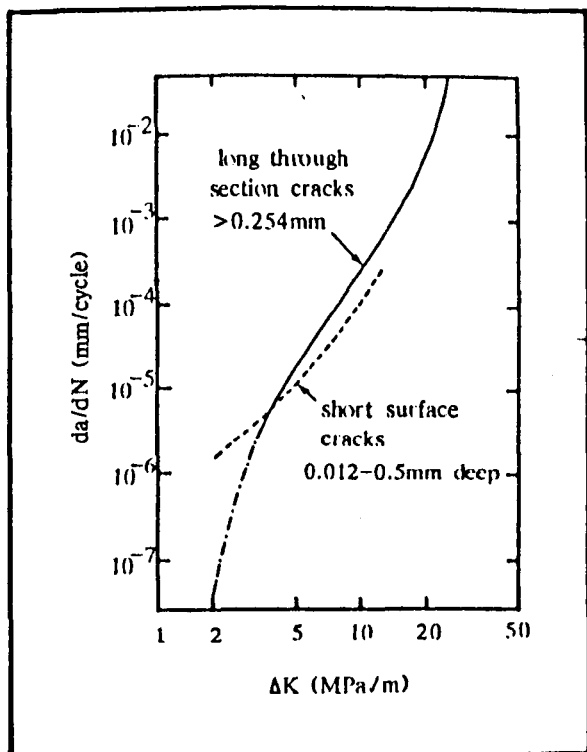


2.15 Cottrell-Hull model for formation of intrusions and extrusions. Operation of two intersecting slip bands is assumed to occur in the sequence show. (b) and (c) represent forward cycle, (d) and (e) the reverse cycle. (124)



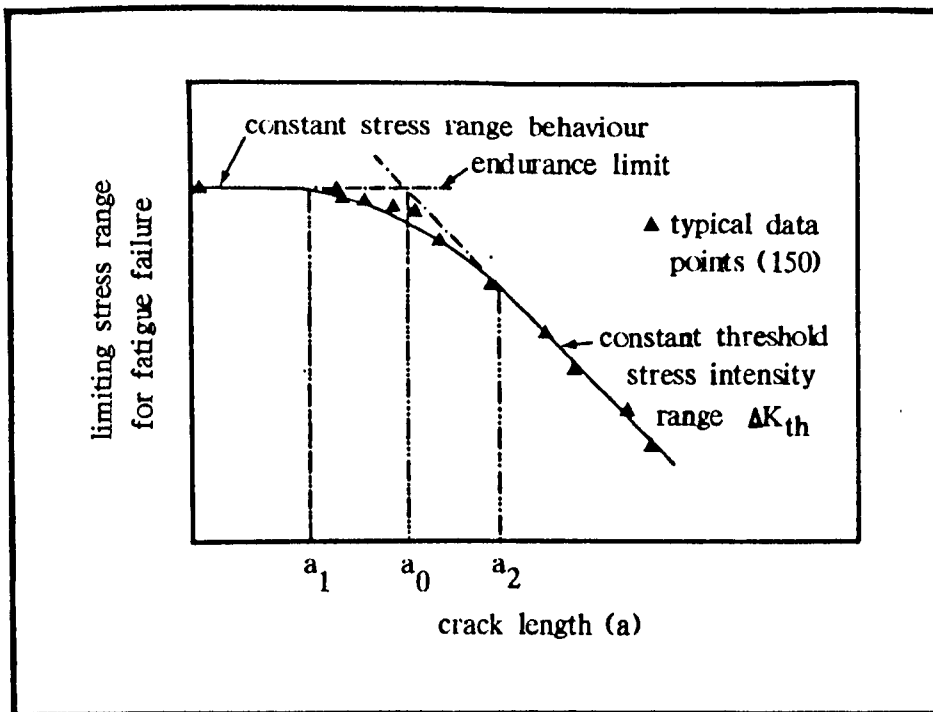
2.16 Neumann model for formation of a crack by coarse slip. Sequence of events is a, b, c, d, e, f, g. Figures c, e and g represent zero or compressive stress. As the dislocations indicated by  $\perp$  run out, a crack is created because motion along two planes occurs simultaneously (125)

2.17 Fatigue crack propagation curves for long and short cracks in 7075 (4)



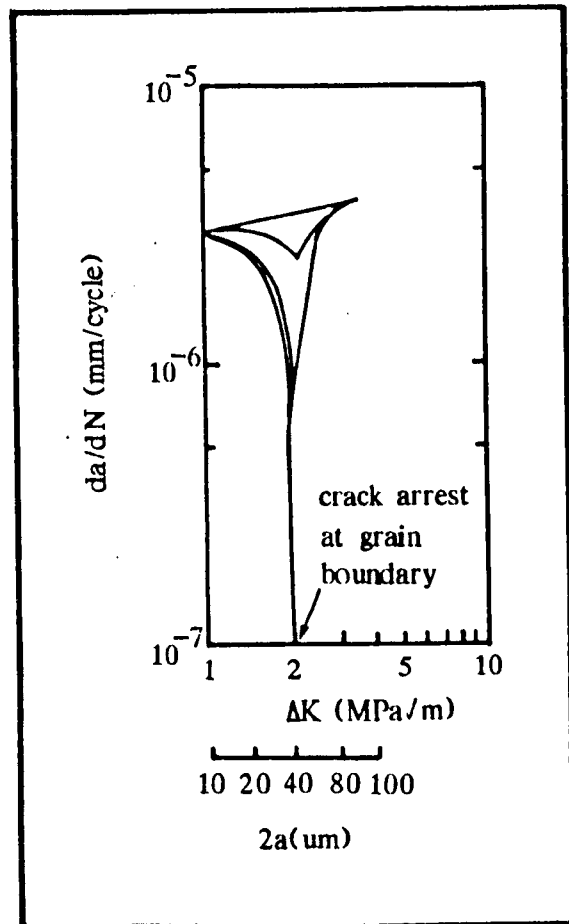
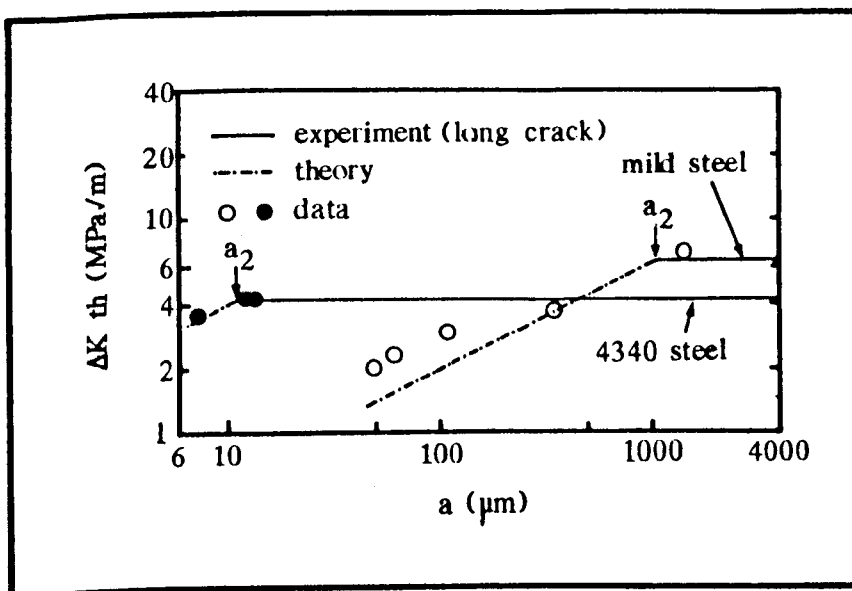
2.18

Schematic idealisation of the growth of long and short cracks (7075-T6) (148)

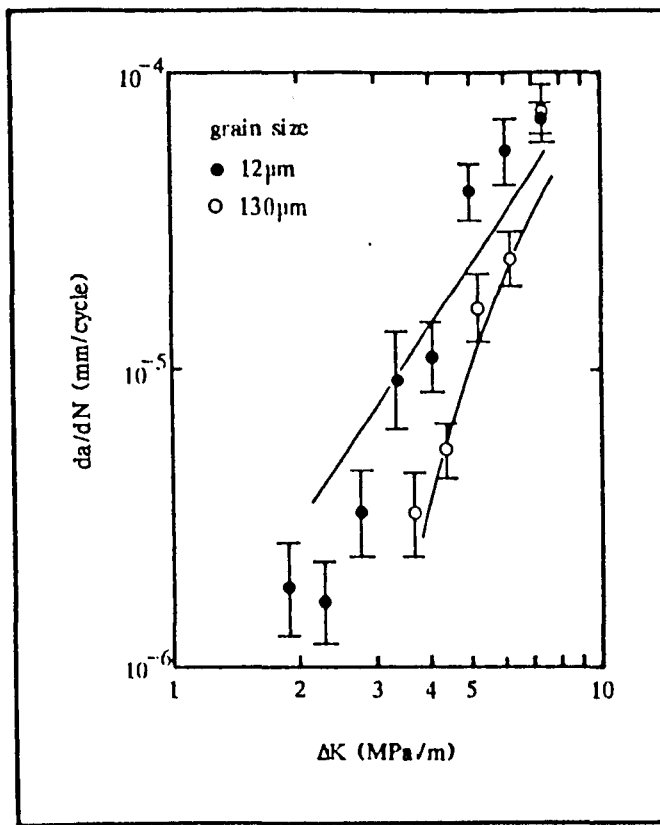


2.19 The limiting stress range for fatigue failure as a function of crack length, with typical data (151)

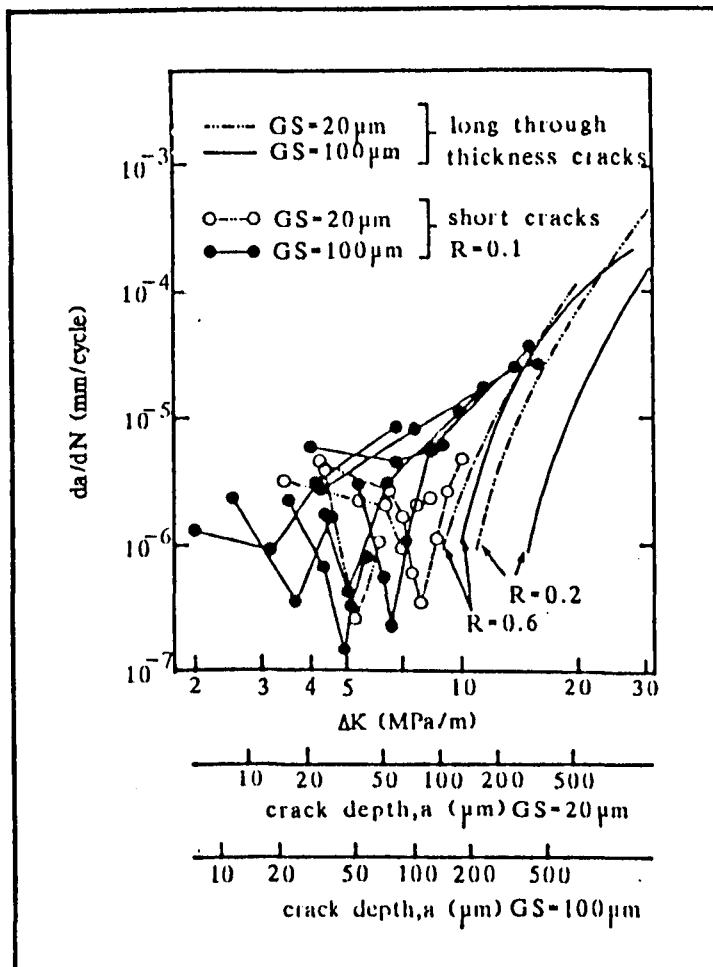
2.20 Threshold stress intensity factor range vs crack depth (a) for high strength and mild steel (154)



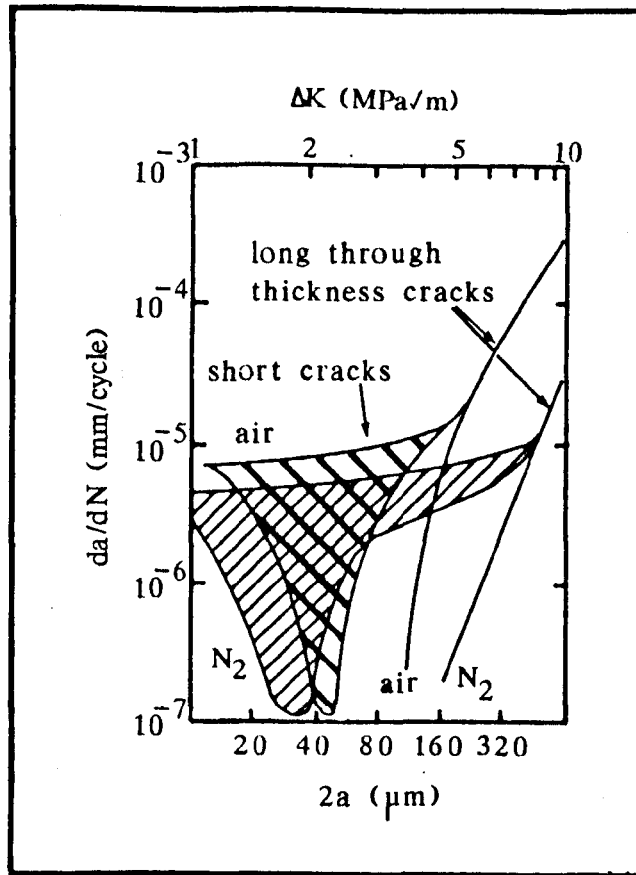
2.21 Crack growth rate vs  $\Delta K$  for 7075-T6 indicating that the crack tip strain model can simulate crack arrest at grain boundaries (159)



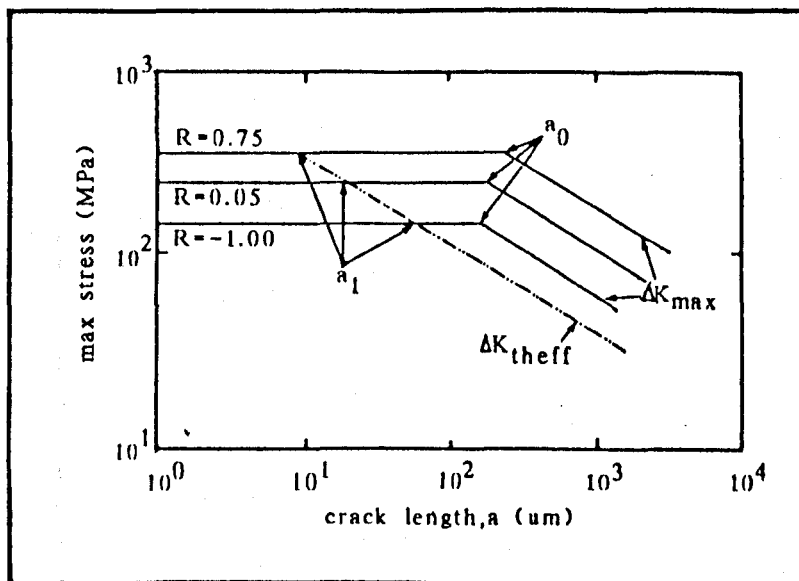
2,22 Comparison of predicted and measured crack growth rates for 12 μm and 130 μm grain size 7010-T6 alloy (163)



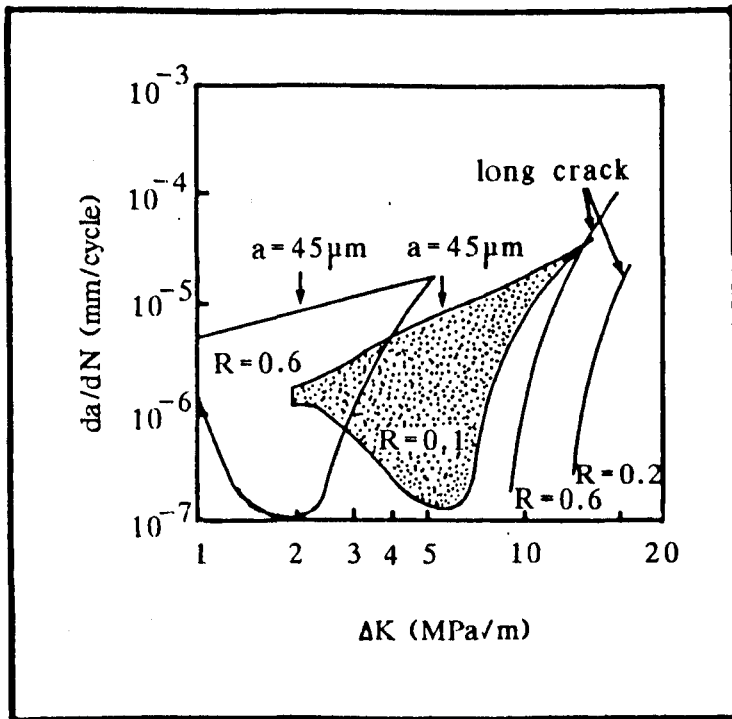
2.23 Vacuum fatigue crack propagation curves of long and short surface cracks in Ti-8.6Al with two different grain sizes. (166)



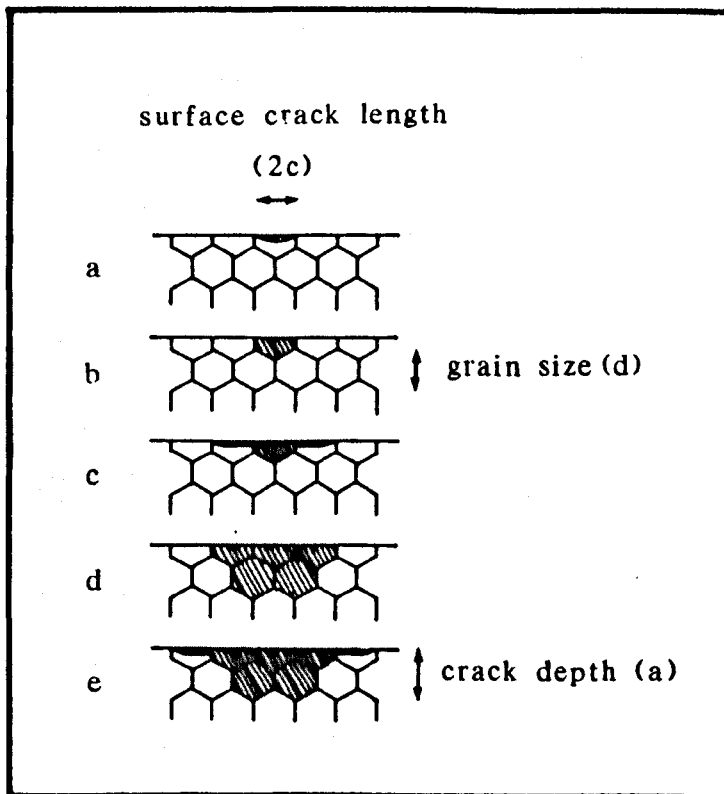
2.24 Summary of microcrack growth in moist air and dry nitrogen (149)



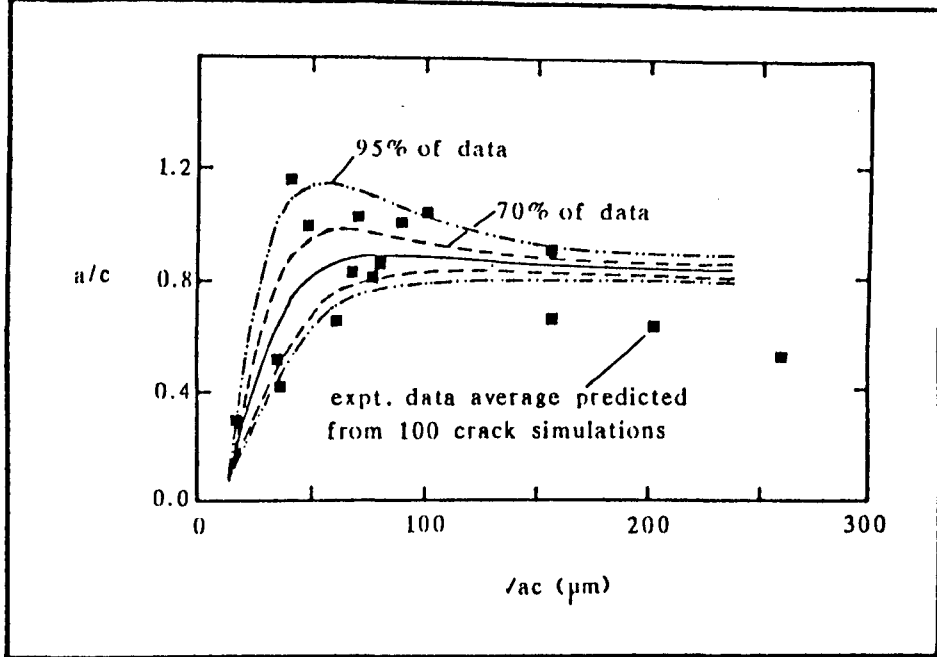
2.25 Semi-schematic modified Kitagawa diagram showing the effect of stress ratio on crack length for 7475-T6 (174)



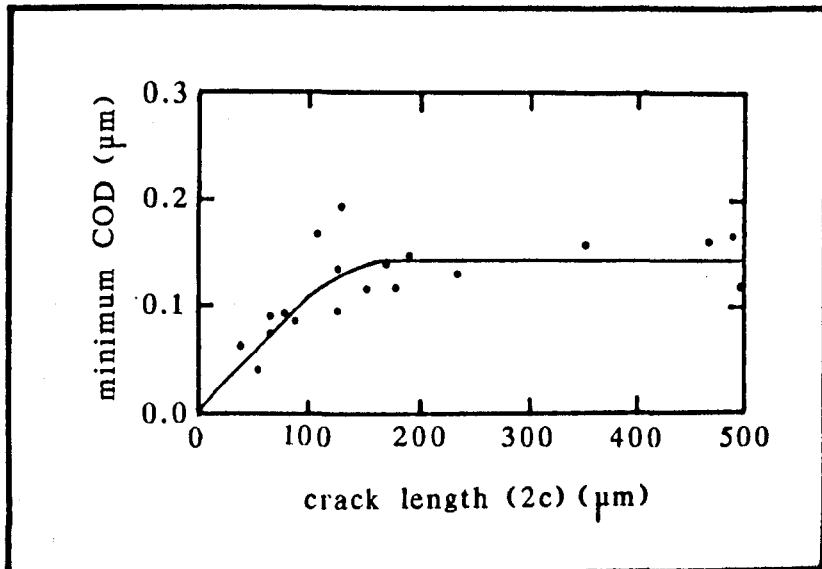
2.26 Crack growth rate vs  $\Delta K$  for long and short cracks in Ti-8.6Al at  $R = 0.1$  and  $R = 0.6$  (166)



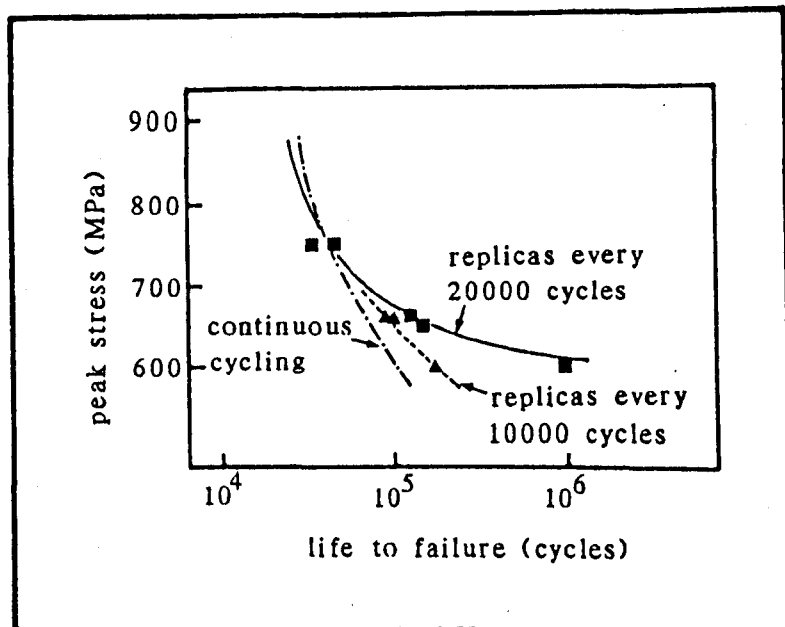
2.27 Schematic illustration showing the development of crack shape in Ti-8.6Al. a and b,  $2c = D$ ; c and d,  $2c = 3D$ ; e,  $2c = 5D$  (181)



2.28 Simulation of crack shape development with increasing crack depth for 7075-T6 (182)



2.29 Minimum crack opening displacement (COD) of surface cracks in Ti-6Al-2Sn-4Zr-6Mo as a function of crack length (188)



2.30 Peak stress vs fatigue life showing the effect of replication on fatigue crack growth in Ti-6Al-4V (190)

## CHAPTER 3

### EXPERIMENTAL TECHNIQUES

#### 3.1 INTRODUCTION

The object of this study was to analyse the short fatigue crack behaviour of selected commercial aluminium and titanium alloys. An evaluation was also made of the long, through thickness fatigue crack behaviour for the purpose of comparison with that of the short cracks. This chapter describes the experimental techniques used in the fatigue testing programme and in addition, associated aspects such as material mechanical property data accumulation and optical and electron microscopy analysis of fatigue cracks. Microstructural evaluation of the materials involved and a description of the heat treatments used are presented in subsequent chapters (Chapters 4 & 7 for the aluminium and titanium alloys respectively).

#### 3.2 TENSILE TESTING

Tensile tests were performed on the 7010 and 2014A aluminium alloys and on the titanium alloy, IMI 318. It was done initially to obtain basic mechanical property data, however, in addition, for the aluminium alloys data was used to evaluate ageing curves to facilitate a choice of ageing times for subsequent fatigue testing. For all the alloys studied, this data was supplemented with Vickers hardness or microhardness testing.

The 7010 and 2014 alloys were evaluated on a Hounsfield testometer using standard 20mm diameter, round Hounsfield tensile specimens, the dimensions of which are shown in figure 3.1a.

All testing was carried out at room temperature. For the titanium alloy IMI 318, a more detailed study was made using the specimens shown in figure 3.1b, tested on a 100KN capacity, screw driven, mechanical Mayes machine operating at an initial strain rate of  $10^{-4} \text{ sec}^{-1}$ . An extensometer was used to measure the change in length of each specimen to help determine the 0.2% proof stress. Elongation to failure was measured using marks scribed on the gauge length of each specimen. Ultimate tensile strength and reduction in area were measured using standard techniques.

Hardness measurements were made on a conventional Vickers hardness indenter for both the aluminium and titanium alloys. For the two titanium alloys, IMI 318 and IMI 550 a further study was conducted on a Vickers Microhardness indenter using a 50g load, which allowed microhardness measurements to be made, where possible, on both the primary  $\alpha$  and transformed  $\beta$  phases.

### 3.3 LONG, THROUGH THICKNESS FATIGUE CRACK TESTING

Although long, through thickness fatigue crack behaviour of the alloys under consideration here, and other similar alloys, have been studied in detail elsewhere, e.g. (20, 23, 52, 107, 196), a testing programme was formulated to obtain comparison data for the subsequent short crack testing using the same alloys in identical heat treatment conditions.

Conventional single edge notch bend (SENB) specimens were used, loaded in 4-point bend on a Mayes, closed loop, servo-hydraulic testing machine equipped with either a 25KN or 50KN load cell.

4-point bend specimens were also to be used for the short crack testing. For all the alloys tested the SENB specimens were machined from plate material so that their top surfaces were parallel to the rolling direction of the plate. Specimen dimensions are shown in figure 3.2. In all but one case,  $B = W = 20$  mm,  $L = 100$  mm, and  $a = 5$  mm. The central notch (depth  $a$ ) was machined with an included angle of  $45^\circ$  nominal. Screw holes (OBA) were machined in each end of the specimen at points where the current for the p.d. crack length monitoring system was to be connected. The exception to these specimen dimensions was for a  $\beta$ -annealed IMI 318 microstructure (specified 318D). Whereas, for the other microstructures examined in this part of the study, heat treatments, where necessary, were performed after specimens had been cut to shape, this was not possible for 318D. Due to the affinity of titanium for oxygen, heat treatment was performed in a vacuum furnace operating at better than  $10^{-4}$  torr. As a further precaution against oxygen contamination, 2.25 mm of material was machined ground from both sides of the specimen, reducing  $W$  to 15.5 mm. The central notch was also added at this stage.

Top roller spacing on the 4-point bend rig was kept constant at 80 mm, the roller being positioned in the small notches on the top surface of each specimen (figure 3.2). The bottom rollers were spaced equi-distant either side of the specimen's mid-point giving a bending moment arm of 20 mm (figure 3.2). All fatigue cycling was carried out at 50 Hz in laboratory air between 15 and  $20^\circ\text{C}$ .

The increase in crack depth at the bottom of the notch during fatigue testing was monitored using a d.c. potential drop technique. A constant d.c. current supply was applied through the length of the specimen via bolts screwed into the specimen ends. Two thin wires (0.25mm diameter) of similar composition and electrical conductivity to the specimen, had previously been spot welded and secured with epoxy resin as close as possible to the notch, across it on diagonally opposite sides. Al-1Mg-0.6 Si and pure titanium wires were used for the aluminium and titanium alloys respectively. The voltage across the notch was monitored through the thin wires and was recorded, after amplification, on a chart recorder. The current through the specimen was allowed to stabilize, usually overnight, at a convenient value to produce a voltage across the notch after <sup>if</sup> application of either 0.2V (aluminium alloy) or 2.0V (titanium alloy). The lower value for the aluminium alloy was due to its lower resistivity. The use of higher currents resulted in excessive specimen heating. During fatigue testing an increase in crack depth at the bottom of the notch resulted in an increase in the voltage measured across it, which could be related to crack depth through a calibration curve.

Near threshold crack growth rates were approached using a load turndown technique similar to that described by Ritchie (197). Initially fairly high loads were applied to the specimen in order to produce a propagating, sharp crack across the whole specimen thickness. Once it had propagated through the notch tip plastic zone, the loads were reduced in steps of approximately 10%. At each new load range the crack was allowed to grow at least four times the size of the plastic zone generated at the

previous, higher load level. This minimised any retardation effects due to plasticity ahead of the crack tip. The maximum plastic zone size ( $r_{mpz}$ ) at the crack tip in the centre of a specimen ~~which is~~ subjected to plane strain conditions was calculated from the equation:

$$r_{mpz} = \frac{1}{6\pi} \left( \frac{K_{max}}{\sigma_y} \right)^2 \dots\dots\dots 3.1$$

where  $K_{max}$  is the maximum stress intensity factor and  $\sigma_y$ , the yield stress of the material.

As near threshold growth rates were approached, the reductions in load range were decreased to <2%. This procedure was repeated until no detectable growth was recorded in  $10^6$  cycles. Once certain that this condition had been satisfied, the loads were slightly increased and the crack allowed to propagate until the crack depth: specimen thickness (a/W) ratio of ~0.6 was reached. As the servohydraulic testing machine could not reliably maintain loads above this ratio, cycling was then stopped. Through this procedure, near threshold propagation rates could be monitored under decreasing and increasing stress intensity factor conditions.

For all the microstructures examined here (7010 OA1, 7010 UA, 318A and 318D) threshold tests were performed at an R - ratio ( $K_{min}/K_{max}$ ) = 0.1. The maximum and minimum loads were reduced by a constant ratio to each other throughout the test until threshold was reached. This is shown schematically in figure 3.3(a) in terms of stress intensity factor (K) vs number of cycles (N). As can be seen, during this procedure the value of minimum stress intensity factor ( $K_{min}$ ) stays below the stress intensity factor below which the crack can be assumed

to be closed ( $K_{c1}$ ) and the threshold values reached are, therefore, influenced by the crack closure phenomenon. Further tests were performed on 7010 OA1 and 7010 UA specimens using a method developed by Lewis ( 198 ) to obtain closure free threshold stress intensity, factor ranges. Initially cycling was operated at  $R = 0.1$  as before, however, near-threshold behaviour was approached by increasing the minimum load and keeping the maximum load constant. This is shown schematically in figure 3.3(b). By choosing appropriate loads at which the minimum load was first increased, it was possible to obtain propagation in the near-threshold regime at  $R$  - ratio  $\geq 0.8$ . Here growth is assumed to be closure free and the values of threshold can be taken as intrinsic material parameters.

A computer programme ( 199 ) was used to process the data for presentation in terms of crack growth rate ( $da/dN$ ) vs stress intensity factor range ( $\Delta K$ ).

Fracture surfaces were examined in detail on a JEOL 35C scanning electron microscope operating at 25KV. Additionally, some fracture surfaces of the 7010 OA1 and UA microstructures, that had been etched in Pelloux's Reagent, were examined in the electron microscope. By etching in Pelloux's Reagent ( 25 ) (2% HF, 24% HCl, 37% HNO<sub>3</sub>, 37% H<sub>2</sub>O) for 5+10 seconds, a number of etch pits were produced, the shape and orientation of which could be related to the crystallographic orientation of regions of the fracture surfaces.

### 3.4 SHORT FATIGUE CRACK TESTING

#### 3.4.1 General Testing Technique

The initiation and subsequent propagation behaviour of short fatigue cracks from smooth stress free surfaces was monitored using an interrupted cycling, replication technique. Periodically through the fatigue life of a specimen, cycling was suspended and a plastic replica of the specimen surface taken for later examination. The method encompassed simplicity and excellent resolution and has previously been used to a wide extent. (e.g. 138, 148, 149, 166, 168, 47).

Smooth bar specimens, machined with their long axis parallel to the rolling direction of the plate material, were fatigued in 4-point bend. The exact dimensions of the specimens changed slightly from alloy to alloy depending on the quantity of material available, but in all cases initiation occurred within an area approximately 100mm<sup>2</sup> on the top surface of each specimen between the bottom rollers. Figure 3.4 schematically describes the specimen shape and roller positions of the 4-point bend test rig. The specimen dimensions for each alloy studied are indicated in table 3.1. Top and bottom roller spacings of 50mm and 10mm were used throughout the study, giving a moment arm of 20mm. This type of loading arrangement produced an area on the top surface, above the bottom rollers, subjected to a uniform stress field and hence a large, representative area for initiation and growth.

After any necessary heat treatment and prior to fatigue testing, the top surface of each specimen was prepared to a high quality, stress free finish in the following manner.

First between 30 and 50  $\mu\text{m}$  of material was hand ground from the surface of 240 grit emery paper. Further grinding down to 1200 grit paper was followed by 8  $\mu\text{m}$  and 1  $\mu\text{m}$  diamond paste polishing. Electropolishing further improved the surface finish by eliminating any scratches or marks left by the grinding and polishing procedure. It was also assumed that any residual stresses produced from the machining and heat treatment stages would be removed. To ensure that only the top surface and tops of the specimen sides would be electropolished the remainder of each specimen was protected by "lacomite". For both the aluminium and titanium alloys a glacial acetic acid/perchloric acid solution was used. The concentrations of each constituent are shown in table 3.2, together with the polishing conditions. The electropolishing produced a slight surface etch which was further accentuated by chemical etching in either Keller's reagent (1% HF, 1.5% HCl, 2.5% HNO<sub>3</sub>, 95% H<sub>2</sub>O) or Kroll's reagent (2% HF, 10% HNO<sub>3</sub>, 88% H<sub>2</sub>O) for the aluminium and titanium alloys respectively.

Fatigue testing was again carried out on a closed loop, servohydraulic, Mayes testing machine in laboratory air between 15 and 20°C. The cyclic frequency was reduced from 50 Hz <sup>to 10Hz</sup> for the aluminium alloys and 20 Hz for the titanium alloys. This was because the relatively high loads required to initiate short cracks from a smooth surface could not be accurately maintained at the higher frequency.

Minimum ( $\sigma_{\min}$ ) and maximum ( $\sigma_{\max}$ ) applied stresses were calculated using the standard bending beam formula for a tensile stress on the surface of an elastically bent beam (200). Hence for the maximum stress ( $\sigma_{\max}$ )

$$\sigma_{\max} = \frac{3P_{\max} d}{th^2} \dots\dots\dots 3.2$$

where  $P_{\max}$  is the maximum applied load, d is the bending arm and t and h the specimen thickness and height. Initially all testing was carried out at an R ratio of 0.1.

Relatively high stresses were required to initiate cracks from the un-notched surface. For each alloy maximum stress levels of approximately 0.9 x 0.2% proof stress were chosen. Table 3.3 shows the 0.2% proof stress of each alloy and the corresponding maximum stresses used for short crack fatigue testing. The 0.2% proof stresses shown for the titanium alloys are for the alloys in their as received condition. Although subsequent heat treatments to produce alternative microstructures changed the tensile properties, the value of  $\sigma_{\max}$  shown in table 3.3 remained unaltered.

In addition to changes in the microstructure, which will be described in chapters 4 & 7, variations in mechanical testing procedure were also studied. These were confined to the 7010 OAl microstructure and included examining the effects of maximum stress and R - ratio. To assess the effects of maximum stress on short fatigue crack behaviour, testing was carried out with  $\sigma_{\max}$  equal to 500 MPa and 225 MPa to accompany the base line testing of 440 MPa.

At the lower of these stress levels initiation was found not to occur within a reasonable number of cycles and a slight change in testing procedure was adopted. Initiation was monitored at a maximum stress of 440 MPa and the load was then decreased in small steps (<10%) until a crack was growing at  $\sigma_{\max} = 225$  MPa. Care was taken to ensure that as each new load range the crack grew a distance greater than 4 x plastic zone size generated at the previous higher load, as with the long, through thickness, threshold testing. However, this method did not yield any data for cracks less than about 100  $\mu\text{m}$  in surface crack length. To evaluate the effects of R - ratio on short fatigue crack behaviour, testing was initially carried out with an R - ratio of 0.5 ( $\sigma_{\max} = 440$  MPa). However, once again initiation was found not to occur within a reasonable number of cycles, possibly due to the stress range being too small. Testing was found to be successful at an R - ratio = 0.25 ( $\sigma_{\max} = 440$  MPa) and it was hoped that this modest increase in R - ratio would indicate any effects of stress range on short crack behaviour.

The replication technique used to monitor crack growth involved stopping the cycling periodically throughout the test. The interval between replicas depended on the expected life and the growth characteristics of the microstructure and was typically between 500+5000 cycles. Specimens were held at mean load to keep crack faces apart and to allow replicating material to penetrate the crack. Cellulose acetate sheets, 30mm x 15mm in area and 0.034mm thick, were softened briefly in acetone (<1 second) and delicately placed on the fatigued, specimen surface, taking care to avoid trapping any air bubbles.

Once the acetone had evaporated, the stiffened sheets could be peeled off the specimen and transferred to a glass microscope slide, on which they were held face up with double sided tape. The near perfect, negative impression of the specimen's surface could be examined directly by optical microscopy. However, the image was further improved by coating with a thin layer of gold which increased the reflectivity. This was performed in an EMSCOPE 500 gold sputter coater operating at 15 mA for 30 seconds. Magnifications up to 1000X could be easily achieved using a Nikon Photomicroscope.

#### 3.4.2 Determination of Crack Shape

To apply any kind of fracture mechanics analysis to microstructurally short cracks measured using a surface monitoring technique, the relationship between surface crack length ( $2c$ ) and depth ( $a$ ) must be established. With this in mind a series of tests were carried out to examine the change in crack shape with increasing crack depth.

For the 7010 in its OAl condition two different testing procedures were followed. Firstly, a number of specimens were fatigued until cracks between approximately 40  $\mu\text{m}$  and 4.0mm were present. Specimens were then broken open and measurements of  $2c$  and  $a$  were made either using a calibrated, travelling optical microscope or from electron microscopy examination. In addition, in order to follow any change in crack shape for a particular crack as it grew, an overload technique was developed to produce "beach marks" on the crack faces. Initially cycling was performed with a maximum tensile stress ( $\sigma_{\text{max}}$ ) = 440 MPa and

at R = 0.1. Once a crack had been detected overloads of 500 cycles at  $\sigma_{\max} = 550$  MPa and at R = 0.1 were added after every 5000 cycles. Any "beach marks" produced by such a method were examined in the SEM.

For the two titanium alloys a technique similar to the first method described above was used. Specimens containing cracks with depths between 150  $\mu\text{m}$  and 5.0 mm were broken open and the crack shape determined. However, as the fatigue fracture often appeared to be similar to the final, fast fracture some difficulty in determining crack shape was encountered. This was overcome by exposing the cracked specimen in a furnace at 600°C for one hour prior to breaking the specimen open. The fatigue fracture surfaces were oxidised to a blue/gold colour enabling crack length and crack depth measurements to be made more easily on the optical microscope.

### 3.4.3 Stress Intensity Solution

A number of stress intensity solutions were examined in detail with the view of using an appropriate one through out the study. The solutions under consideration included those developed by Shah and Kobayshi (201 - 203), Pickard (204) and Trantina et al (205). After careful assessment a solution evaluated by Shah and Kobayshi (presented in 206) was chosen. It predicted the stress intensity at the deepest point of a crack (depth a) emulating from the top surface of a large slab (thickness h) subjected to a uniform bending moment/unit thickness (M). The solution took the form:

$$K_o = \frac{6M\sqrt{\pi a}}{h^2} \dots\dots\dots 3.3$$

Where  $K_0$  was related to the maximum stress intensity factor ( $K_{max}$ ) for various a/c ratios by the curves depicted in figure 3.5. For all the cracks under study here, a/h ratios were <0.25 and for all crack shapes (a/c ratios between 0.1 and 1.0) evaluated by Shah and Kobayshi the relationships between  $K_{max}/K_0$  and a/h were linear.

It was found that data for long 'short cracks' (i.e. crack depth  $\gg$  grain size and usually deeper than 1mm) fitted the long, through thickness crack data better using this solution than any of the others. This will be considered in detail in chapter 6 which discusses the aluminium results and can be seen clearly in figure 6.1.

ALLOY	h (mm)	t (mm)	l (mm)
7010	12.5	12.5	100.0
2014 A	12.5	12.5	100.0
(	10.0	10.0	100.0
IMI318 (	10.0	12.5	100.0
(			
IMI550	8.0	10.0	100.0

TABLE 3.1 SHORT CRACK SPECIMEN DIMENSIONS

ALLOY SYSTEM	SOLUTION CONCENTRATION	VOLTAGE (V)	TEMP (°C)	ANODE : CATHODE SEPARATION (MM)	CATHODE TYPE	TIME (SECS)
	ACETIC ACID : PERCHLORIC ACID					
ALUMINIUM	90 : 15	40	~12*	10+20	STAINLESS STEEL	240
TITANIUM	100 : 6	40	~14*	10+20	TITANIUM	6x30#

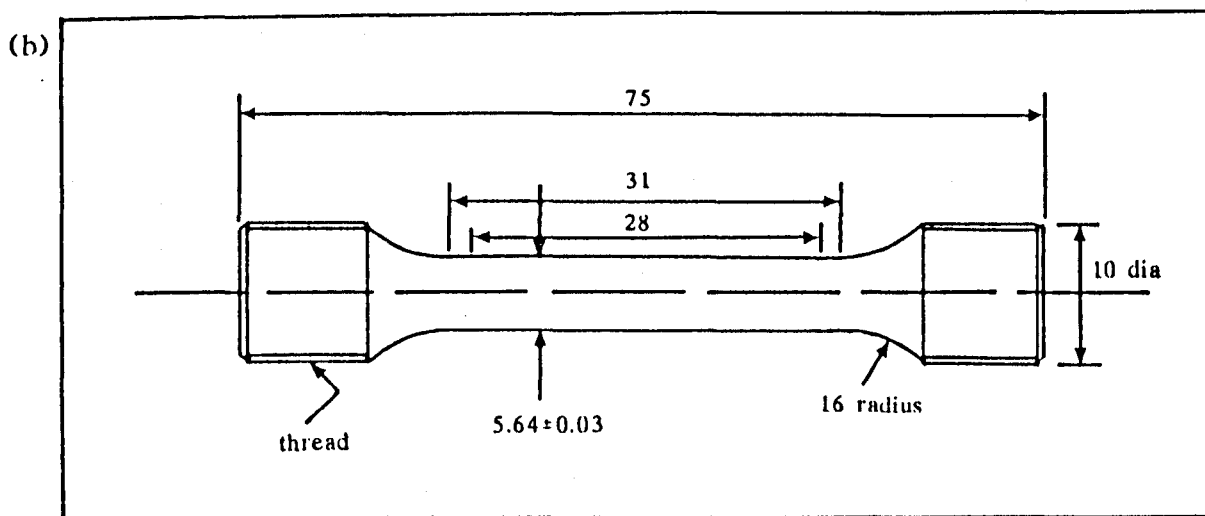
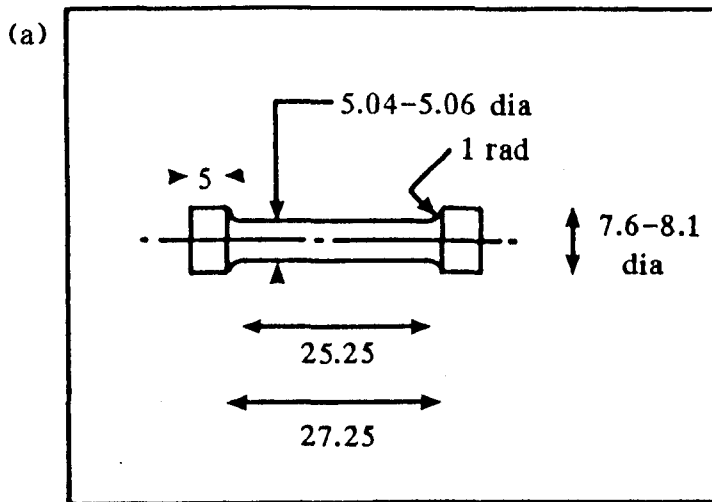
\* Temperature reduced to lowest possible without freezing solution  
# 6 x 30 second bursts required as thin film built up on surface which needed to be removed between bursts

TABLE 3.2 ELECTROPOLISHING CONDITIONS USED IN SPECIMEN PREPARATION PROCEDURE

ALLOY	0.2% PROOF STRESS (MPa)	MAX. TENSILE TESTING STRESS (MPa)
7010	495	440
2014 A	435	380/400*
IMI318	950	750
IMI550	990	850

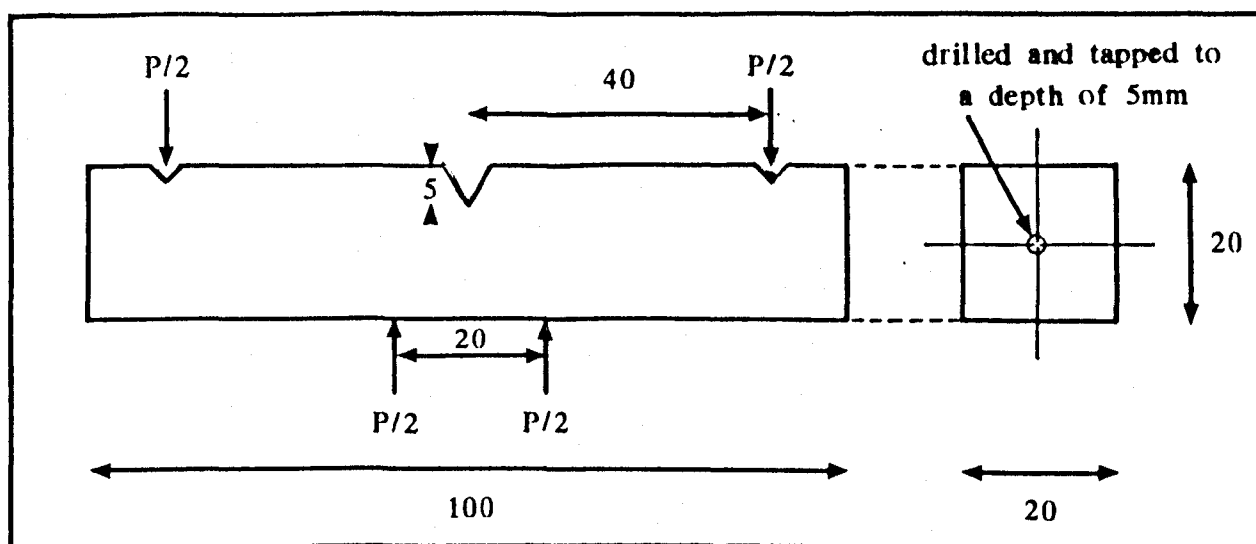
\* 380MPa used for OA material, 400MPa used for UA material

TABLE 3.3 0.2% PROOF STRESSES & MAXIMUM TENSILE STRESSES USED FOR SHORT CRACK TESTING FOR ALLOYS UNDER STUDY

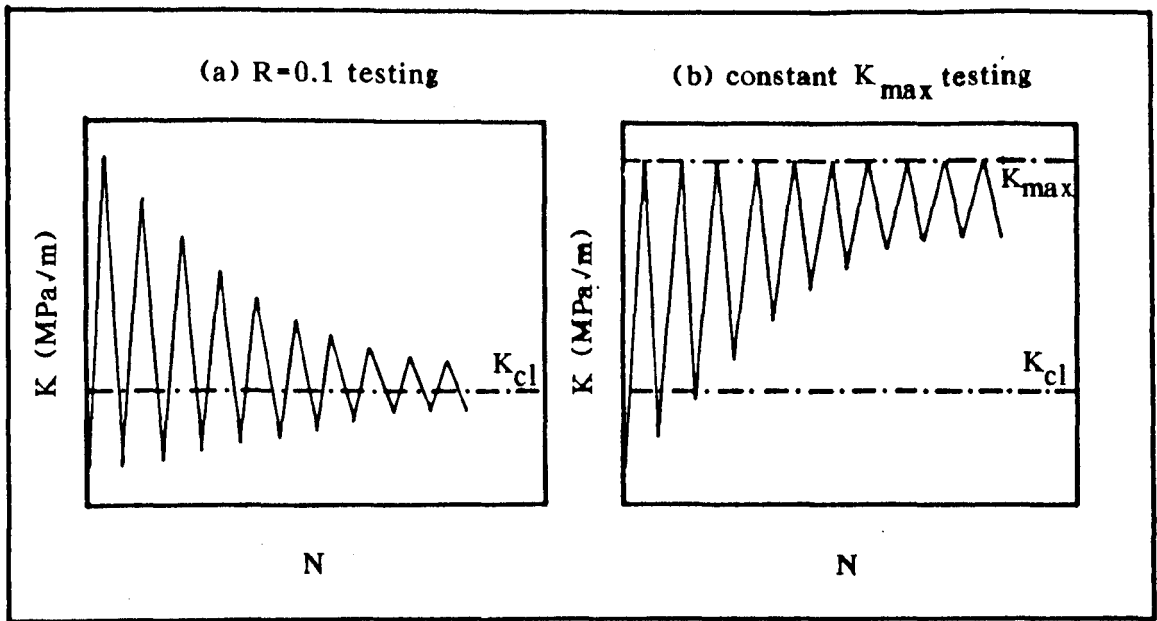


3.1 Dimensions of tensile test specimens (in mm)

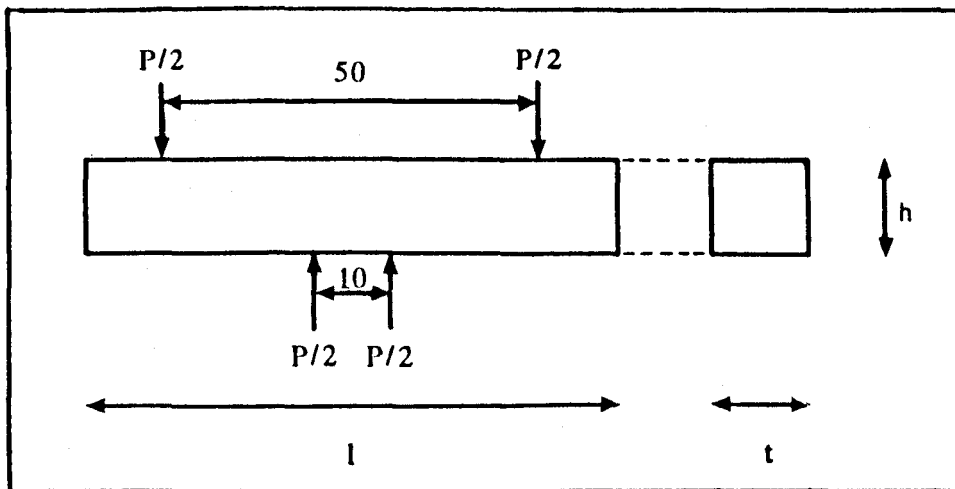
(a) Houndsfield, (b) Mayes.



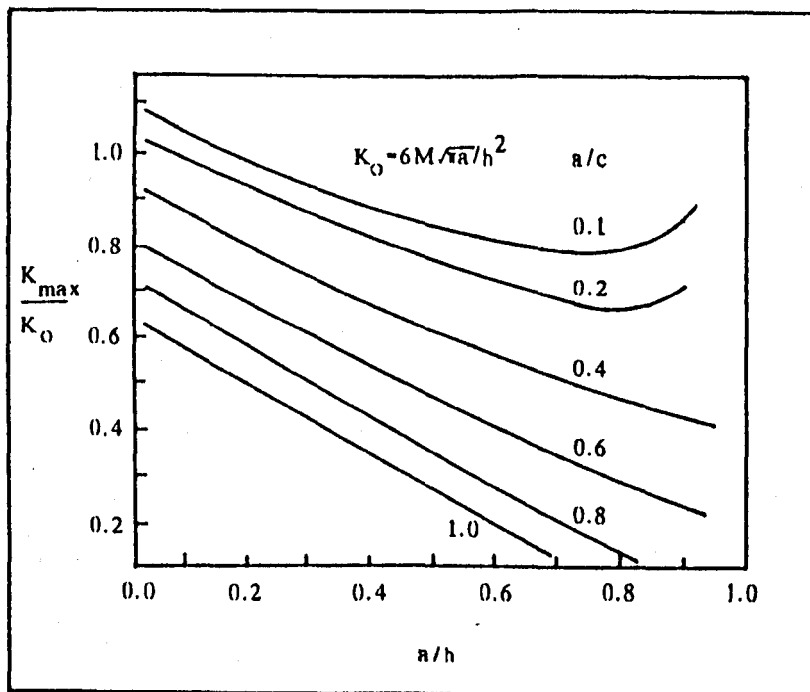
3.2 Dimensions of long, through thickness fatigue crack specimens (SENB) (in mm)



3.3 Schematic illustration of the variation in stress intensity with the number of cycles for (a)  $R = 0.1$  and (b) constant  $K_{max}$  testing



3.4 Dimensions of smooth, short crack specimens (in mm)



3.5 Variation in  $K_{max}$  with crack depth for the deepest point of a crack in a slab subjected to pure bending (201-203)

## CHAPTER 4

### ALUMINIUM ALLOYS - MATERIALS

#### 4.1 INTRODUCTION

The development of high strength aluminium alloys in the latter half of the twentieth century has mainly been due to the demand from the aerospace industry, where materials with high specific strength have been required. Furthermore, the good corrosion resistance and formability of these alloys have contributed to their extensive usage. This chapter briefly reviews the development and strengthening mechanisms of the alloys under examination in this study (7010 and 2014A). In addition, descriptions of the thermal processing routes analysed during the short fatigue crack testing programme, are presented.

#### 4.2 ALLOY DEVELOPMENT

The foundation for modern aluminium alloys was established in 1906 by the accidental development of age hardening by Wilm (208). In trying to produce strong aluminium alloys, to replace brass in the manufacture of cartridge cases, Wilm developed the alloy duralumin (Al-3.5Cu-0.5Mg-0.5Mn), which exhibited substantial improvements in mechanical properties over previous aluminium alloys. Commercial developments over the following thirty years were based on this Al-Cu-Mg system. For example the alloy 2014 (Al-4.5Cu-0.5Mg-0.8Mn-1.0Fe-0.9Si-0.25Zn-0.1Cr-0.15Ti) contained a small silicon addition, which made it more responsive to artificial ageing than duralumin and consequently higher strengths were attained.

Similarly 2024 (Al-4.4Cu-1.5Mg-0.6Mn-0.5Fe-0.5Si-0.25Zn-0.1Cr-0.15Ti) was developed as a high strength, naturally aged alternative to duralumin. The increase in magnesium content and the reduction in silicon content to the lowest level possible, resulted in the formation of an Al,Cu,Mg phase which produced significant natural hardening. The more recent 2XXX series alloys (e.g. 2014A, 2124, 2224, 2048) attribute their beneficial mechanical properties mainly to the tight control of impurity content (through the use of high purity aluminium) and to a slight reduction in copper levels. Both these modifications tend to suppress the formation of large, brittle intermetallics, which adversely affect the ductility and fracture toughness.

Greater potential for age hardening existed however through the evolution of the Al-Zn-Mg-Cu system. Early alloys, such as those developed by Rosenhain et al (209) and Sander and Meisser (210) demonstrated the strength potential of this alloy system, but were very susceptible to stress corrosion cracking (SCC). During the early 1940's, two alloys became commercially available, 7076 and 7075 (Al-5.5Zn-2.5Mg-1.6Cu-0.3Mn-0.5Fe-0.4Si-0.23Cr-0.2Ti) (211). The former was employed, to a limited extent, as a forgeable alloy for propellers, however, it's low chromium level, which was found to quell problems associated with SCC, restricted use to sheet material. The 7075 alloy, and derivatives, have remained the most extensively used Al-Zn-Mg-Cu alloys to the present day. Higher strength alloys, such as 7001 and 7198, have been prone to fracture toughness problems and have not been as popular.

The modern derivatives of 7075, such as 7475, 7050 and 7010, have improved mechanical properties (especially fracture resistance) due to the reduction in impurity levels through the use of high purity aluminium. Furthermore, the replacement of chromium with zirconium in 7050 and 7010, has led to a reduction in quench sensitivity in larger sections, allowing slower cooling rates and a reduction in residual stresses.

#### 4.3 STRENGTHENING MECHANISMS

Aluminium alloys exhibit the basic requirement for strengthening by precipitation hardening, i.e. the rapid decrease in solid solubility of one or more elements with decreasing temperature. Heat treatment routes involve the following three stages. First solution treatment in a single phase region (e.g. the  $\alpha$  phase in the aluminium/copper system shown in figure 4.1). Secondly, quenching from this region sufficiently quickly to avoid any precipitation of the solute atoms, to form a supersaturated solid solution (SSSS). Finally, the controlled precipitation of fine particles from the SSSS by naturally ageing at room temperature or artificially ageing at an elevated temperature.

##### 4.3.1 2XXX series alloys

Precipitation hardening in 2XXX series aluminium alloys, from the decomposition of the SSSS to the formation of the equilibrium  $\theta$  precipitate ( $\text{CuAl}_2$ ), occurs in the sequence shown below:



At room temperature, hardening usually results from the formation of GP[1] zones by the localised clustering of copper atoms. These form as discs, only a few atoms thick and are orientated parallel to (001)<sub>α</sub> planes. Further ageing results in the number of GP[1] zones being increased, rather than their size which remain at 3 to 5 nm in diameter. Fully naturally aged material contains discs typically 100 nm apart.

At elevated temperatures (>100°C), GP[1] zones are replaced by GP[2] zones (θ'') which are usually about 15 nm in diameter and 0.8 nm thick. Although their tetragonal structure is coherent with the aluminium lattice, it is slightly smaller than the aluminium unit cell in one direction, which leads to elastic-coherency strains distorting the matrix planes in that direction (212). Further ageing causes transformation to the intermediate phase, θ', which has the same composition as the equilibrium phase θ (CuAl<sub>2</sub>) but is still semi-coherent with the aluminium matrix. The greatest strength is attained when the maximum number of GP[2] zones are present and this is usually augmented by some strengthening from the θ' precipitates. Additional ageing leads to the evolution of the non-coherent equilibrium phase (θ) from the θ' and is accompanied by a loss in strength.

#### 4.3.2 7XXX series alloys

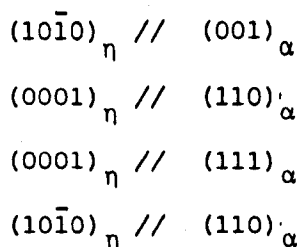
In a similar manner to 2XXX alloys, 7XXX series alloys develop their strength, through ageing, by the formation of GP zones and the evolution of intermediate and equilibrium precipitates. The sequence of structural changes for these alloys is shown below;



The GP zones are approximately spherically shaped segregations of zinc and magnesium atoms, which increase in size with ageing time. There are some indications that they start as zinc clusters and magnesium atoms diffuse to them at a slower rate. The solute concentration in the zones can be as much as 50% and leads to strengthening predominantly by chemical hardening, where the increased resistance to dislocation movement arises from the stronger atomic bonds existing in the zones.

The intermediate phase  $\eta'$  ( $MgZn_2$ ) can form at these GP zones, however, it is uncertain whether the zones are just preferred nucleation sites or if the larger and more favourably orientated zones transform directly to  $\eta'$ .  $\eta'$  forms as platelets, partly coherent on  $(111)_\alpha$  planes, densely populated throughout the  $\alpha$  matrix.

Increased ageing leads to the formation of the hexagonal, equilibrium phase  $\eta$ , which forms at or from the  $\eta'$ .  $\eta$  can take one of nine orientation relationships with fcc aluminium, the four most common of which are shown below:



The small misfit between  $\eta'$  and  $\eta$  and the matrix means that large precipitates can grow before coherency is lost. This can result in a well dispersed strain throughout the structure and substantial strengthening. Peak ageing conditions result in a microstructure with few GP zones and predominantly  $\eta'$  precipitates.

At the same time as the homogeneous nucleation of GP zones in the matrix, heterogeneous nucleation of both  $\eta'$  and  $\eta$  can occur at "irregularities" in the structure, such as grain and sub-grain boundaries and lattice dislocations. This has an effect to reduce the attainable strength as the amount of solute available for homogeneous nucleation is reduced, especially close to the grain boundaries (212). The tendency to form large precipitate free zones (pfz) around the grain boundaries, either due to heterogeneous nucleation or by the grain boundary acting as a vacancy sink, also leads to a degradation in stress corrosion cracking resistance. Compositional changes and alterations in heat treatment practice resulting in a narrower pfzs benefit SCC resistance. These factors include increasing the alloy content, the addition of precipitation nucleating reagents, the raising of quenching temperatures and rates from the solution treatment temperature and the lowering of the ageing temperature. Modern ageing treatments involve either a 2 stage age or an isothermal age with slow heating rates up to the ageing temperature. Both techniques have been designed to produce microstructures with narrow pfzs.

The duplex ageing technique (213) involves a pre-age at a temperature below the GP zone solvus temperature allowing the nucleation of a large number of GP zones, many of which grow to reach a critical size. During ageing at the second higher temperature, these GP zones can transform to  $\eta'$  and  $\eta$ , producing a fine dispersed structure of precipitates in the matrix. Additionally, the GP zones that have attained the critical size close to grain boundaries are not dissolved at the higher temperature leading to a narrower pfz.

7XXX series alloys also contain elements such as chromium and zirconium, which raise the recrystallisation temperature in solid solution and favour the formation of fine grains and sub grains (214 - 216). As a consequence of this, the volume of the precipitate free zone is increased, however, the thickness is actually reduced due to greater number of grain and sub grain boundaries. The 7010 alloy contains zirconium, rather than chromium, which forms as fine intermetallic dispersoids with a structure approximating to  $ZrAl_3$ . This has a lattice parameter close to aluminium and is crystallographically orientated to the matrix through the following relationship:

$$(001)_{\alpha} // (001)_{ZrAl_3}$$

$$[100]_{\alpha} // [100]_{ZrAl_3}$$

The advantage of using zirconium over chromium, is that it forms dispersoids that are more coherent with the matrix and therefore do not act as vacancy sinks. This makes the alloy slightly less quench sensitive.

#### 4.4                    MICROSTRUCTURAL EVALUATION

For the two commercial aluminium alloys chosen for this study 7010 and 2014A, the effects on short crack propagation behaviour of precipitate type, size and distribution were examined. This section describes the microstructures produced by the processing route and the various heat treatments evaluated.

##### 4.4.1                    7010

The composition of the 25mm thick plate of 7010 alloy produced by Alcan is shown in table 4.1. The as-received grain structure, which was maintained through all subsequent solution treatment and ageing, is shown in figure 4.2. The figure illustrates the pancake shaped grain structure characteristic of the manufacturing process. Typical grain size ranges in the three sections were:

- L : 100  $\mu\text{m}$   $\rightarrow$  1  $\mu\text{m}$
- LT: 60  $\mu\text{m}$   $\rightarrow$  200  $\mu\text{m}$
- ST: 10  $\mu\text{m}$   $\rightarrow$  40  $\mu\text{m}$  (Average = 20  $\mu\text{m}$ )

Three distinct microstructural variations were produced for long and short crack fatigue testing. Primarily, underaged (UA) and overaged (OA1) material with very similar 0.2% proof stresses were prepared to compare the effects of type and size of precipitate. Furthermore, a commercial temper (OA2) in the T7451 condition was examined. The heat treatment routes involved for these three tempers are shown in table 4.2. The final ageing times at 170°C, for the OA1 and UA conditions, were determined from ageing curves evaluated in terms of 0.2% proof stress and hardness vs ageing time. These are shown in figure 4.3.

Times of 1 hour and 20 hours were chosen for the UA and OA1 conditions respectively. This resulted, for both cases, in a microstructure with a 0.2% proof stress of approximately 495 MPa and a Vickers hardness of about 170 VHN. The 0.2% proof stress of OA2 was taken to be 425 MPa (217).

A detailed examination of the three microstructures was carried out using a Philips EM301 transmission electron microscope. 3mm diameter thin foil specimens were prepared in a Struers twinjet electropolisher, using a solution of 10% nitric acid in methanol. With the solution at a temperature of  $-30^{\circ}\text{C}$ , a current of approximately 200 mA was required to polish the specimens satisfactorily. Electron micrographs of the three heat treated conditions are shown in figure 4.4.

Figure 4.4a reveals the precipitate size and distribution in the UA microstructure. It shows that a fine, uniform precipitate, probably  $\eta'$ , is present throughout the matrix. Coarser  $\text{MgZn}_2$  precipitates exist at the grain boundary, which is bordered by a small precipitate free zone, less than  $0.2\ \mu\text{m}$  in diameter. In comparison, the OA1 microstructure, figure 4.4b, exhibits fewer, coarser precipitates in the matrix. As the microstructure is slightly overaged, it is thought that a number of these may be the equilibrium precipitate,  $\eta$ , the remainder being  $\eta'$ . As for UA, coarse  $\text{MgZn}_2$  precipitates populate the grain boundaries. A further difference between UA and OA1 however, is the width of the pfz. For the latter microstructure, pfz up to  $0.5\ \mu\text{m}$  in diameter were observed (figure 4.4b).

The commercial temper (OA2), figure 4.4c, shows considerably coarser  $\eta$  and  $\eta'$  precipitates in the matrix to either OA1 or UA, although the  $MgZn_2$  precipitates at the grain boundaries appear to be of comparable size. The uniformity and relative coarseness of the  $\eta$  and  $\eta'$  precipitates is not only a consequence of the long ageing time, but also due to the pre-stretch of 3% between the solution treatment and ageing. This has the effect of encouraging heterogeneous nucleation in the matrix on dislocations produced during the stretch. This process may also stimulate precipitate formation close to grain boundaries, which would help explain why the pfzs around these boundaries are relatively narrow compared to OA1.

#### 4.4.2            2014A

The 2014A material was also produced by Alcan in 25mm thick plate form. The composition of the alloy is shown in table 4.1. Typical grain structures in the L and ST directions, (shown in figure 4.5) again reveal a pancake shaped microstructure, with the long, flat grains elongated in the L direction (rolling direction). Grain sizes in the three sections did not alter noticeably during thermal processing and are shown below;

L :    100  $\mu$ m + 300  $\mu$ m

LT:    50  $\mu$ m + 200  $\mu$ m

ST:    10  $\mu$ m + 60  $\mu$ m (Average = 25  $\mu$ m)

For this alloy only 2 heat treatment conditions were studied. Underaged (UA) and overaged (OA) microstructures with similar 0.2% proof stresses were produced for fatigue testing.

The heat treatment routes, displayed in table 4.2, show that UA and OA only differ in final ageing times. These ageing times were chosen from ageing curves produced in terms of 0.2% proof stress and hardness (figure 4.6). Three ageing temperatures were examined in terms of Vickers hardness (170, 185 and 195°C), before an ageing temperature of 185°C was chosen for tensile and, ultimately, fatigue testing. Ageing times of 3 and 20 hours at this temperature produced material with 0.2% proof stresses of approximately 425 MPa.

Thin foil specimens, for electron microscope examination, were prepared in an identical manner to that described previously in 7010. Figure 4.7 reveals the differences in precipitate distribution and size for UA and OA. The UA condition material (figure 4.7a) contains an even distribution of very fine, matrix precipitates probably  $\theta''$ , with coarser precipitates at the grain boundaries. In addition, coarse spheres (or possibly discs), are present in the matrix, approximately 0.1  $\mu\text{m}$  in diameter. These spheres are also present in the overaged condition, OA (figure 4.7b & 4.7c). The fact that they have not become any larger or more abundant after longer ageing, suggests that these constituents existed in the microstructure prior to ageing. The major difference between UA and OA can be seen to be in the type of matrix precipitate. In the overaged condition, the  $\theta'$  and  $\theta$  precipitates are in the form of rods, up to 0.1  $\mu\text{m}$  in length and aligned parallel to the (100) planes in the matrix. Furthermore, in both UA and OA precipitate free zones, approximately 0.1  $\mu\text{m}$  across exist at the grain and sub-grain boundaries.

ALLOY	Zn	Mg	Cu	Zr	Fe	Si	Ti	Mn	Cr	Al
7010	6.2	2.35	1.7	0.13	0.15	0.12	0.06	0.10	0.05	REM
2014A	0.25	0.5	4.5	-	0.7	0.9	0.15	0.8	0.1	REM

TABLE 4.1 Nominal compositions of 7010 and 2014A

CONDITION	SOLUTION TREATMENT* + WATER QUENCH	ARTIFICIAL STRETCH	PRE-AGE+ & AIR COOL	FINAL AGE# & AIR COOL	0.2% PROOF STRESS (MPa)
7010 UA	470 ± 5°C, 1 hour	-	90°C, 8 hours	170 ± 2°C, 1 hour	495
7010 OA1	470 ± 5°C, 1 hour	-	90°C, 8 hours	170 ± 2°C, 20 hours	495
7010 OA2	465 ± 10°C,	1.5+3.0%		172 ± 3°C, 10+24 hours <sup>x</sup>	425
2014 UA	505 ± 5°C, 1 hour	-		185 ± 2°C, 3 hours	425
2014 OA	505 ± 5°C, 1 hour	-		185 ± 2°C, 20 hours	425

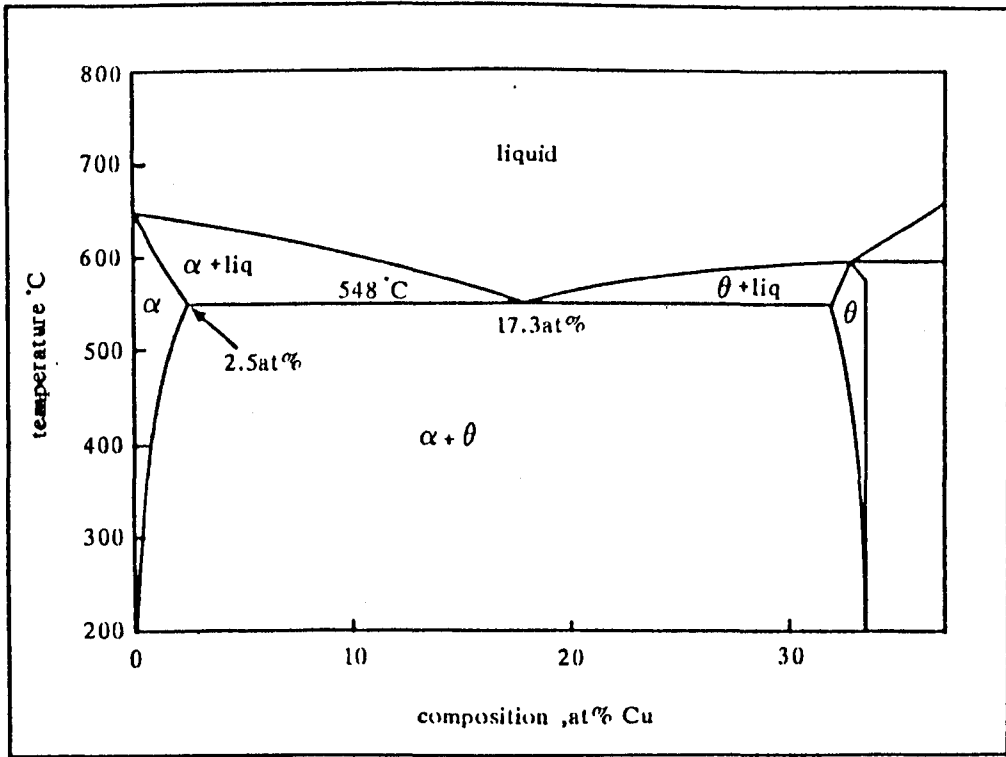
\* Solution treatment in an air circulating furnace and followed by quenching into water at 20°C.

+ Pre-age in air circulating furnace.

# Final age in thermostatically controlled oil bath.

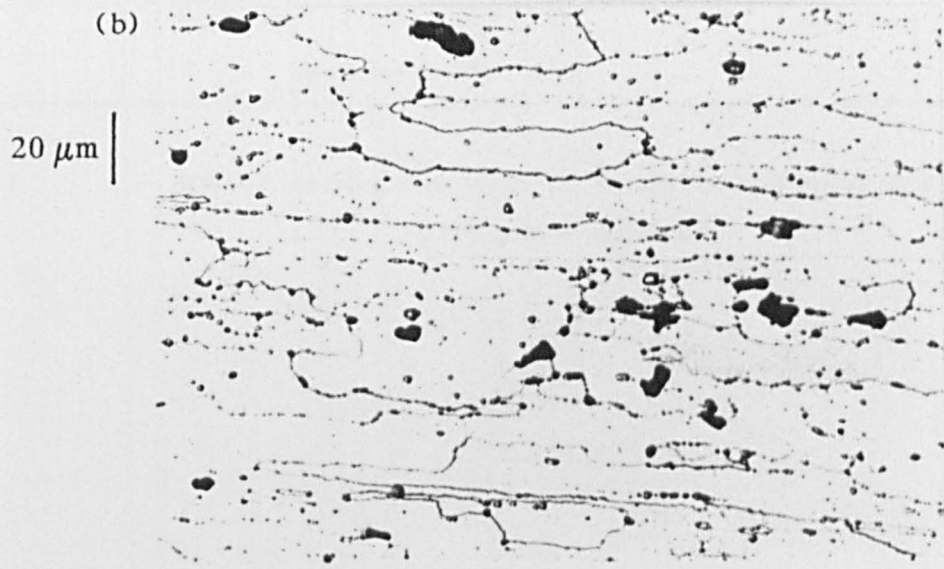
x Material placed in cold furnace and heated to temperature at a rate not exceeding 20°C per hour

TABLE 4.2 Thermal processing routes used for 7010 and 2014A



4.1

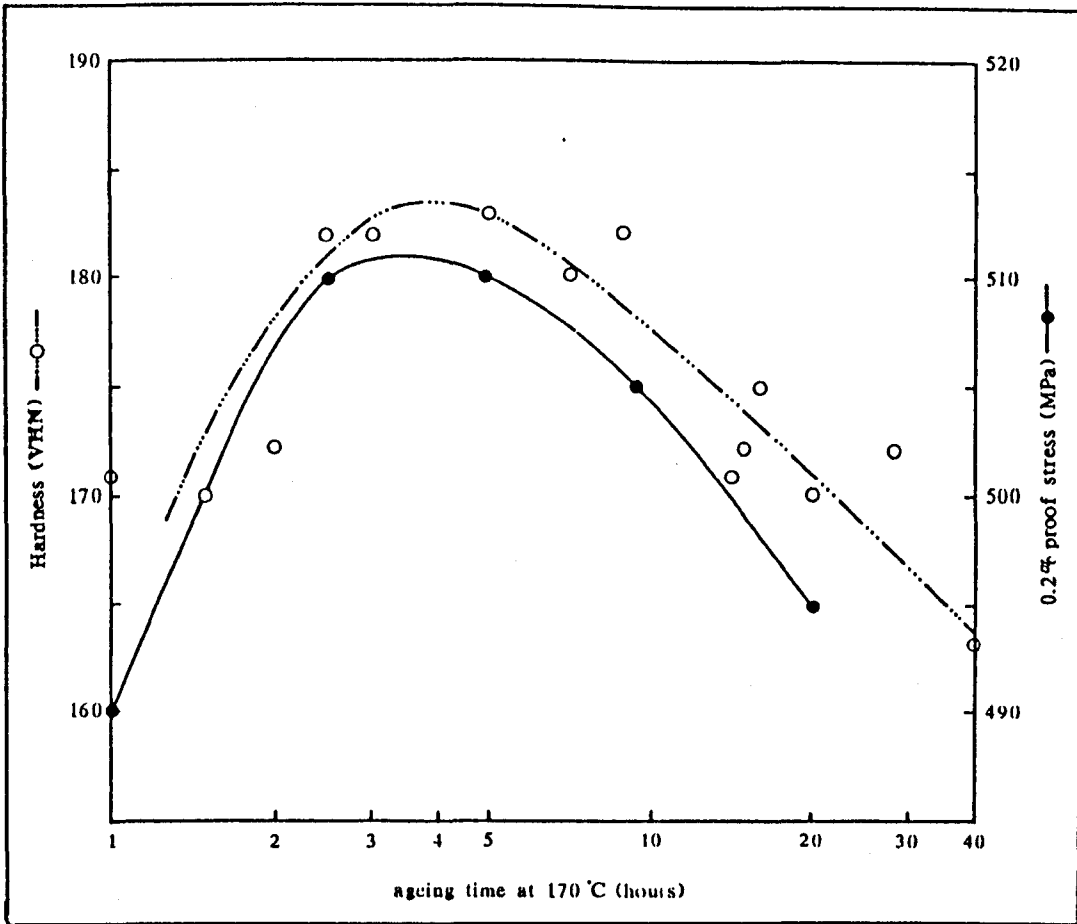
Aluminium rich end of Al-Cu phase diagram



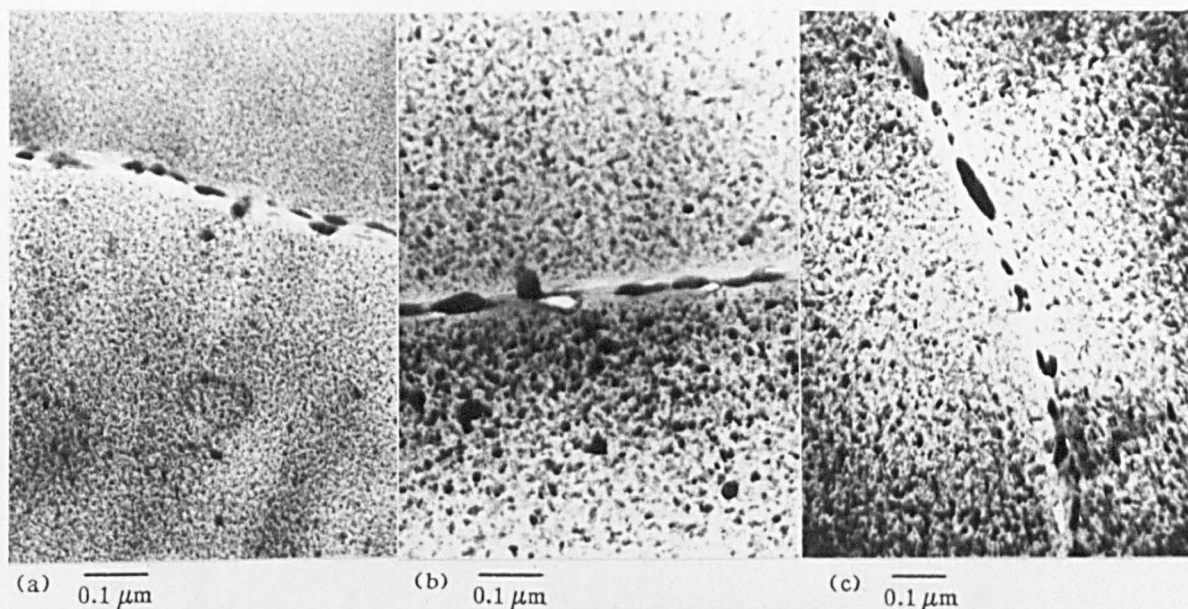
4.2

Optical micrographs of as-received 7010 alloy

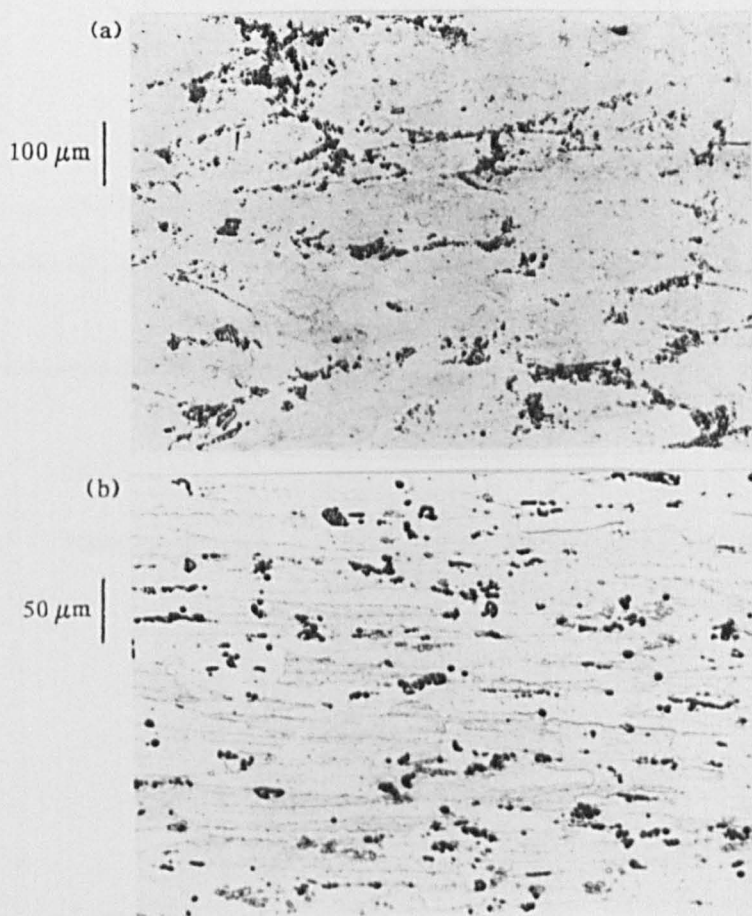
(a) top surface (b) short-transverse (ST) section



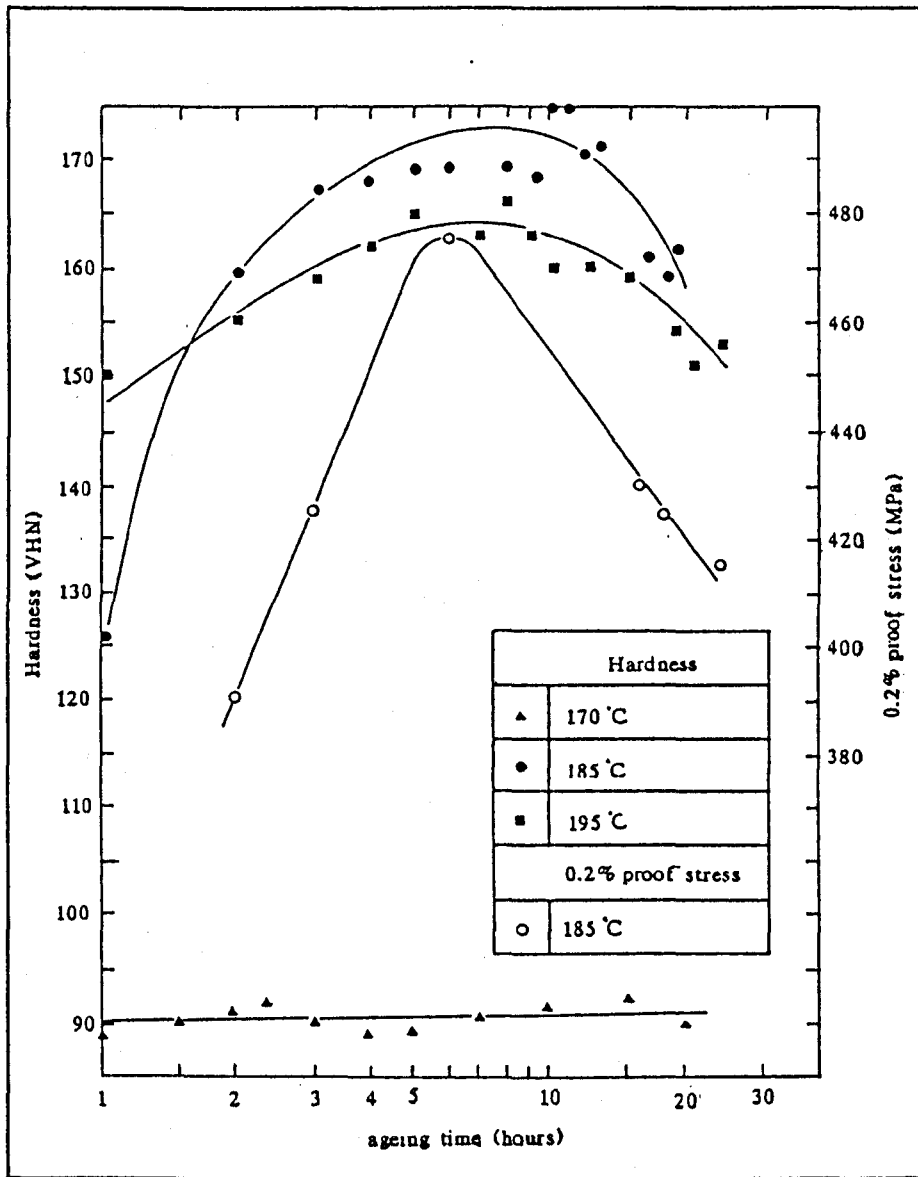
4.3 Ageing curves for 7010 in terms of hardness and 0.2% proof stress



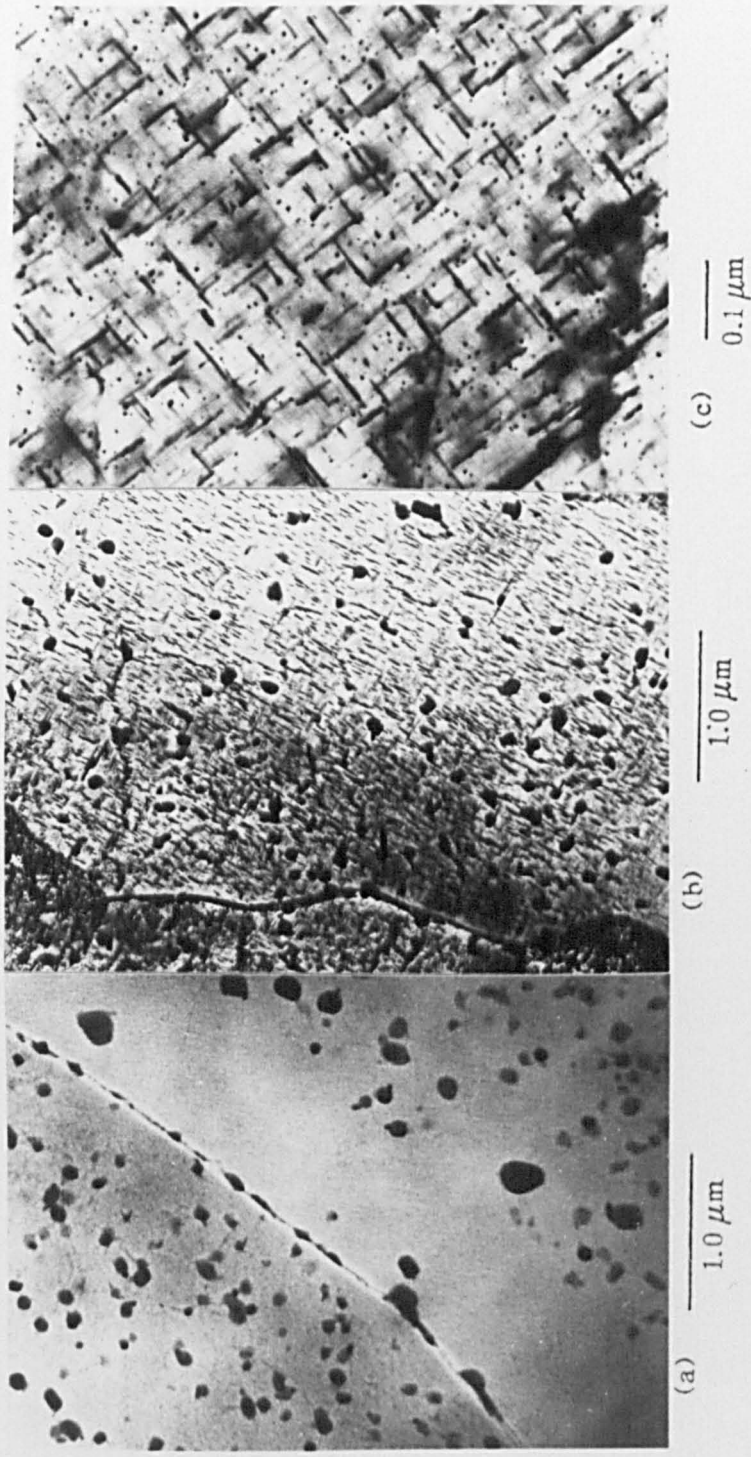
4.4 Transmission electron micrographs of 7010 alloy  
 (a) UA (b) OA1 (c) OA2



4.5 Optical micrographs of as-received 2014A  
 (a) top surface (b) short-transverse (ST) section



4.6 Ageing curves for 2014A in terms of hardness and 0.2% proof stress



4.7 Transmission electron micrographs of 2014A alloy  
(a) UA (b)(c)OA

## CHAPTER 5

### ALUMINIUM ALLOYS - RESULTS

#### 5.1 LONG, THROUGH THICKNESS FATIGUE CRACK BEHAVIOUR IN 7010

Results from the long, through thickness crack testing programme are shown in figure 5.1 in terms of a  $da/dN$  vs  $\Delta K$  plot. The figure contains data for the two microstructures, OAl and UA, tested under constant load ratio ( $R = 0.1$ ) and constant maximum stress intensity ( $R > 0.1$ ) conditions.

For the  $R = 0.1$  tests, comparable growth characteristics for OAl and UA were observed in the Paris regime, at  $\Delta K$  values greater than approximately  $6.0 \text{ MPa}\sqrt{\text{m}}$ . At lower stress intensity factor ranges however, UA was considerably more propagation resistant, displaying a higher threshold stress intensity factor range ( $\Delta K_{th}$ ). Values of  $\Delta K_{th}$  for OAl and UA of  $2.7 \text{ MPa}\sqrt{\text{m}}$  and  $3.9 \text{ MPa}\sqrt{\text{m}}$  respectively were obtained. The near-threshold fracture surfaces of OAl and UA are shown in figure 5.2a and b. In both cases crack propagation was of a faceted, crystallographic, transgranular nature. In many places, ridges were apparent, running parallel to the crack growth direction. Furthermore, slight changes in the orientation of the crack front were observed where the crack tip had been deflected by microstructural interactions. The distance between successive deflections was typically  $20+50 \mu\text{m}$ . At higher growth rates only the ridges running parallel to the crack growth direction were visible, however, fine fatigue striations were also observed (figure 5.2c).

Figure 5.3 shows examples of the near-threshold fracture surfaces of UA etched in Pelloux's reagent. In certain areas etch pits of a specific shape were produced. These were generally of one of two shapes, either square based or triangular based. The square based pits, shown in figure 5.3a and at the top of figure 5.3b, were orientated so that the edge of the base or the diagonal of the base was parallel to the crack growth direction. It was not clear however, what the shape going into the material bulk was. It is equally possible that they may have been square based pyramidal or cubic pits. In the bottom half of figure 5.3b, equilateral triangular based pits can be discerned. Here, the crack propagation direction appears to be close to the height of the base triangle. Similar shaped etch pits were observed on fracture surfaces of OAl material.

Also shown in figure 5.1 are data corresponding to the constant maximum stress intensity testing. At high values of  $\Delta K$ , the lines coincide with the  $R = 0.1$  data for both OAl and UA. As the propagation rates are reduced however, and the load ratio starts to increase, the constant  $\Delta K_{\max}$  lines are transposed to lower values of  $\Delta K$  than the constant R-ratio tests. The point of divergence depended upon the crack length and the stress conditions operative, but for both OAl and UA it corresponded to an R-ratio of between 0.2 and 0.3. Threshold stress intensity factor ranges were reached by steadily increasing the load ratio, so that eventually closure free  $\Delta K_{\text{th}}$  values are attained at an R-ratio greater than 0.8.

$\Delta K_{th}$  values for OAl and UA obtained by this method were determined to be approximately  $1.4 \text{ MPa}\sqrt{\text{m}}$  and  $2.0 \text{ MPa}\sqrt{\text{m}}$  respectively. Figure 5.2d and e show the near-threshold fracture surfaces for OAl and UA. The crack paths were very similar to those from the  $R = 0.1$  tests (figures 5.2a and b).

## 5.2 ASPECTS OF SHORT CRACK GROWTH

In this section data are presented for short crack growth in 7010 OAl to demonstrate the characteristics of propagation behaviour. Figure 5.4a shows the data on a  $da/dN$  vs  $\Delta K$  diagram. In addition to the stress intensity factor range axis, a further abscissa equates to the crack depth. All the data contained in figure 5.4a have been derived from one crack subjected to a maximum tensile stress on the top surface of the specimen of 440 MPa and a load ratio (R) of 0.1. The dotted line and triangular data points have been calculated using the whole surface crack length (2c) measured perpendicular to the stress axis and assuming a semi-circular crack shape (crack depth (a) to half surface crack length (c) ratio of 1.0). At low growth rates corresponding to very short crack depths ( $a < 100 \mu\text{m}$ ), propagation has occurred in a discontinuous manner. At higher propagation rates the degree of scatter has diminished and growth is almost homogeneous.

The two unbroken lines and their corresponding data points in figure 5.4a were derived from the same test data but from considering growth in both directions from the initiation site separately. Hence two lines can be drawn each representing the growth of one crack tip. Although very similar to the line describing the whole crack length ( $2c$ ), distinctions can be observed regarding the extent of the deceleration dips at short crack depths. There are points at which the crack tip was held up for many cycles at some type of obstacle, thus producing growth rates too low to be plotted within the axes of this figure. These large deceleration dips tended to be disguised when the whole crack length ( $2c$ ) was considered, as it is unlikely that both crack tips would be arrested simultaneously. By monitoring the growth of surface crack tips individually, a better representation of the conditions of the crack tip at the bottom of the crack in the material bulk can be made. The deceleration 'wells' occur at crack depths between 7 and 20  $\mu\text{m}$  (approximately 1.2 to 2.1  $\text{MPa}\sqrt{\text{m}}$ ) for this particular crack. Furthermore, less pronounced dips persist to crack depths of about 50  $\mu\text{m}$ , above which more continuous growth takes over.

Although data presented in the form shown in figure 5.4a can describe the growth characteristics of one crack, it would become increasingly complicated if additional data from other cracks were included. A more appealing method of data presentation to solve this problem is shown in figure 5.4b. Here an envelope has been drawn around all the non-zero growth rate data points in this case from six cracks in the OAl microstructure.

Such a method not only shows the degree of scatter associated with short cracks from test to test, but also allows a means of comparison, between different microstructures and stress conditions to be based on data from a number of cracks.

Optical micrographs of the surface crack, described by figure 5.4a, are shown in figure 5.5 at stages through the fatigue life. Although initially the crack tips are slightly deflected away from the perpendicular to the stress axis, figure 5.5c shows that once the crack length is in excess of approximately 100  $\mu\text{m}$  the crack is virtually undeviated. The figures also show that initiation appears to occur at or close to the dark feature in the centre of the micrographs. A similar, though larger, initiation site is shown in figure 5.6a at higher magnification through observation in the SEM. Fracture surfaces of OAl are also shown in figure 5.6. Figure 5.6b, taken close to the initiation site, reveals a similar crystallographic, transgranular fracture to that of the near-threshold fracture surfaces of long, through thickness cracks (figure 5.2a). Distinct changes in crack tip orientation occur approximately every 25  $\mu\text{m}$ . In higher propagation rate regions, about 500  $\mu\text{m}$  from the initiation site, the fracture surface takes a flatter, but still transgranular, appearance (figure 5.6c). Broad, evenly spaced fatigue striations can also be seen by this stage in the life.

5.3                    EFFECT OF AGEING CONDITION ON SHORT CRACK  
PROPAGATION BEHAVIOUR

The effect of changing the type and size of precipitate on the short crack growth behaviour of 7010 was examined by comparing the behaviour of the three ageing conditions, OA1, OA2 and UA at  $R = 0.1$ . Figure 5.7 displays data in terms of  $da/dN$  vs  $\Delta K$  and  $a$  for the three microstructures. In figure 5.7a, characteristic behaviour, taken from data for one crack tip growing in each ageing condition, is plotted for direct comparison of variation in precipitate. Figure 5.7b considers the degree of scatter associated with the data. As in figure 5.4b, envelopes containing all the results from a number of tests for each condition have been drawn. In total the data comes from 6 cracks for OA1, 5 for OA2 and 2 for UA. For the sake of clarity, individual data points have not been included.

The collation of the individual data in figure 5.7, reveals that discrepancies exist between OA1, OA2 and UA over a wide range of growth rates. Generally, an increase in the degree of ageing leads to a degradation in crack propagation resistance. Two crack depth scales are shown at bottom of this plot, one corresponding to OA1 and UA, the second to OA2. As the latter condition exhibited a lower 0.2% proof stress than either OA1 or UA (section 4.4.1) and short crack testing was still carried out at  $0.9 \times 0.2\%$  proof stress, a lower maximum tensile stress was used. Hence, the crack depth scale is slightly displaced to the left with respect to the scale for OA1 and UA. Figure 5.7a shows that irregular short crack propagation occurs in each ageing condition.

For all the examples cited in the figure, only one minimum was observed in each case, corresponding to complete, temporary crack arrest. Other cracks studied however, had a number of arrests, whilst some grew to failure without any complete arrest being detected.

Fractographic studies close to initiation sites revealed similar crack paths for all three ageing conditions. (figures 5.6b, 5.8a, b). Indeed, the facted, transgranular appearance of the OA1 material described previously (figure 5.6b) was very similar to that of UA and OA2 (figure 5.8a, b).

#### 5.4 EFFECT OF GRAIN ORIENTATION ON SHORT CRACK PROPAGATION BEHAVIOUR

The elongated grain structure of the rolled 7010 aluminium plate allowed the comparison to be made between two different grain configurations. This was achieved by simply rotating the specimen through  $90^\circ$  about the long axis. Through this procedure, it was possible to induce cracking in the LT direction of the plate, rather than the LS direction. The two grain configurations are shown schematically in figure 5.9. The influence this has on short crack propagation behaviour is shown in figure 5.10 in terms of  $da/dN$  vs  $\Delta K$  and  $a$ , for cracks in 7010 OA1. The specimens were subjected to a maximum tensile stress of 440 MPa and a load ratio = 0.1. Cracks were assumed to be semi-circular in shape (i.e.  $a/c$  ratio = 1.0). The data for the LS direction crack is that shown previously in figure 5.4a for one surface crack tip.

The data for the LT direction crack in figure 5.10a is from one crack with the two surface crack tips considered separately, and is typical of the behaviour of the 5 cracks studied growing under these conditions. The data for all 5 cracks are shown in figure 5.10b, where an envelope has been drawn around the non-zero growth rate data points.

Examination of fracture surfaces close to the initiation site (figures 5.6b and 5.11) indicates a similar transgranular mode for both crack orientations. Differences occur however, in the changes in crack path orientation with respect to the propagation direction. Whereas for the LS direction crack (figure 5.6b) these occur perpendicular to the crack propagation direction into the bulk of the specimen, they occur in the LT direction cracks perpendicular to the specimen surface.

#### 5.5 EFFECT OF TESTING CONDITIONS ON SHORT CRACK PROPAGATION BEHAVIOUR

The effect of changing the mean and maximum stresses on short crack propagation behaviour was studied for the OA1 microstructure. The  $da/dN$  vs  $\Delta K$  curves in figure 5.12 indicate the effect of R - ratio. The base line data at R = 0.1 (solid line) are those previously shown in figure 5.4a. The additional data have been collected at a R - ratio of 0.25 and represent measurements of the two surface crack tips of one crack growing under these conditions. Both cracks studied growing at R = 0.25 and  $\sigma_{max} = 440\text{MPa}$  showed similar behaviour with growth consistently faster than the R = 0.1 cracks over the whole range of crack depths followed.

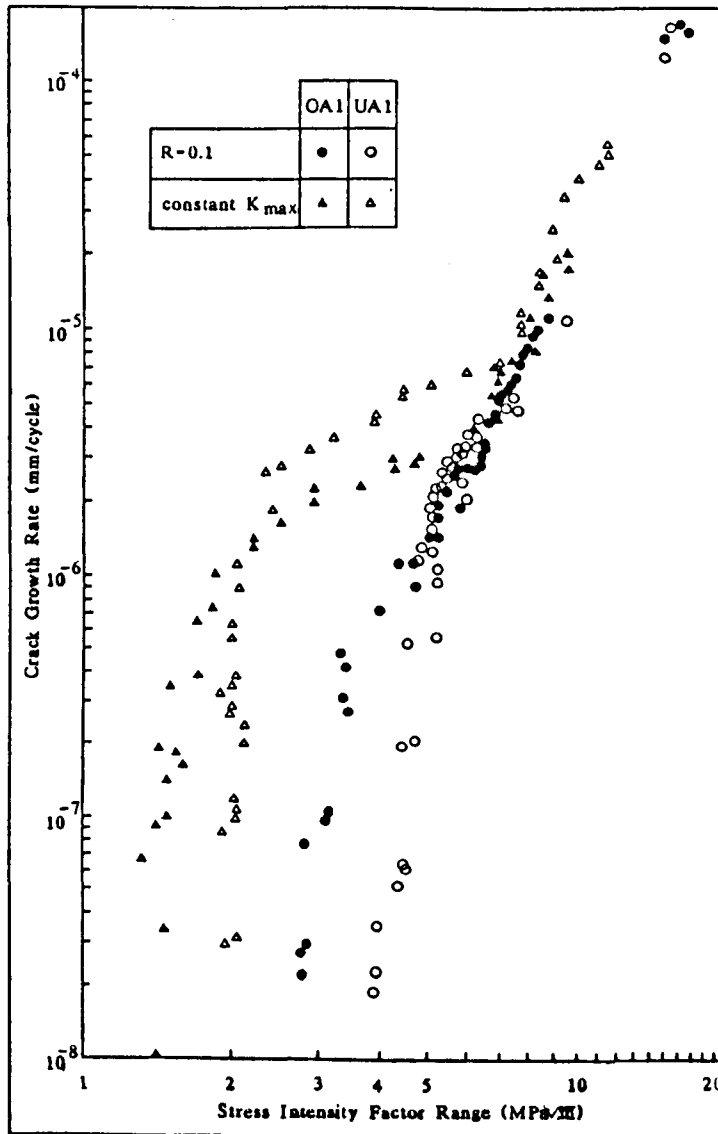
Attempts to obtain data for cracks growing at higher mean loads proved unsuccessful, possibly because the stress range was too small to cause initiation on the specimen surface within a reasonable number of cycles.

Figure 5.13 shows the outcome of varying the maximum tensile stress on the specimen surface, keeping the R - ratio = 0.1, again for the OA1 material. The  $da/dN$  vs  $\Delta K$  plot shows no data points, only envelopes containing all the data collected at the different maximum stresses. The data for  $\sigma_{max} = 440$  MPa is that already described in figure 5.4b. Additional data has been collected from short crack testing at  $\sigma_{max} = 500$  MPa and 225 MPa. Testing at the lower stress was accomplished by a load turn down technique, as described in section 3.4.1 and consequently the shortest crack from which data could be used was of the order of 100  $\mu m$  deep. Hence only a limited number of data were obtained. In total 7 cracks were studied for  $\sigma_{max} = 500$  MPa, 6 for  $\sigma_{max} = 440$  MPa and 2 for  $\sigma_{max} = 225$  MPa.

## 5.6 BEHAVIOUR OF SHORT CRACKS IN 2014A

To complement the data for 7010, short crack testing of OA and UA 2014A was carried out. The results are shown in figure 5.14a on a  $da/dN$  vs  $\Delta K$  plot with envelopes containing all the non-zero growth rate data for the 4 cracks followed in OA and 7 in UA. The most notable difference between the two envelopes is the better overall fatigue crack growth resistance of the UA material over the whole of the stress intensity factor range studied.

In figure 5.14b the behaviour of short cracks in the UA and OA material is shown in detail. The  $da/dN$  vs  $\Delta K$  plot contains data for one crack tip from each microstructure considered independently from the initiation site ( $\sigma_{max} = 380$  MPa (UA) and 400 MPa (OA),  $R = 0.1$ ). The data shows a continued occurrence of growth rate minima up to approximately 100  $\mu\text{m}$  in crack depth for UA. This was distinct from the OA condition where propagation was almost continuous at crack depths greater than around 50  $\mu\text{m}$ . Figure 5.15 shows the near-initiation site fracture surface of UA material, which was typical of both ageing conditions. The crystallographic, transgranular appearance was similar to those of the 7010 alloy shown in figures 5.6b and 5.8a. Surface micrographs of a UA crack through the fatigue life (figure 5.16), reveal that initiation occurred from or close to a constituent particle at a grain boundary, and initial growth was along slip bands. Figure 5.16d showing the crack approximately 800  $\mu\text{m}$  in total surface length, indicates that a fairly undeviating path is initially taken, with more pronounced crack tip deflection only occurring at slightly larger crack lengths, hence, significant crack propagation rate minima are more apparent at higher values of  $\Delta K$ .



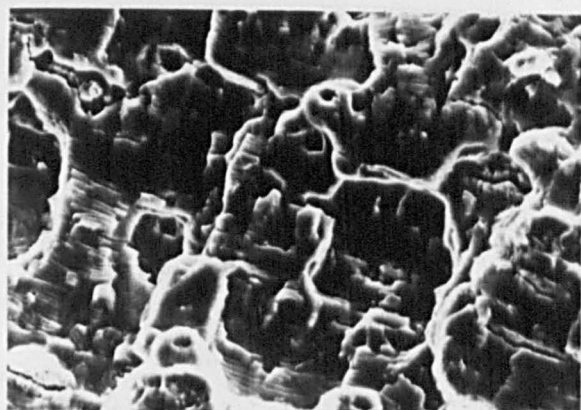
5.1  $da/dN$  vs  $\Delta K$  for long, through thickness cracks for  
 $R = 0.1$  and constant  $K_{max}$  testing of OA1 and UA 7010



(a)  $10\ \mu\text{m}$

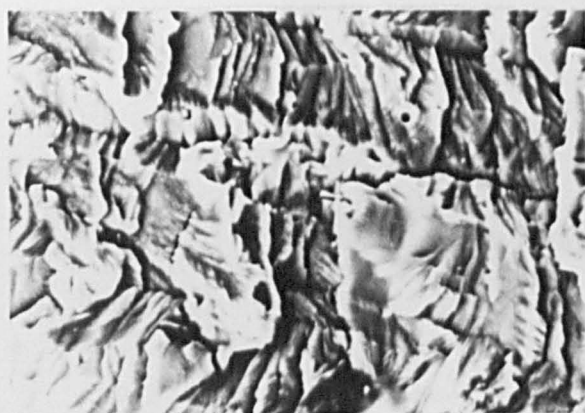


(b)  $10\ \mu\text{m}$



(c)  $10\ \mu\text{m}$

crack growth  
direction



(d)  $10\ \mu\text{m}$



(e)  $10\ \mu\text{m}$

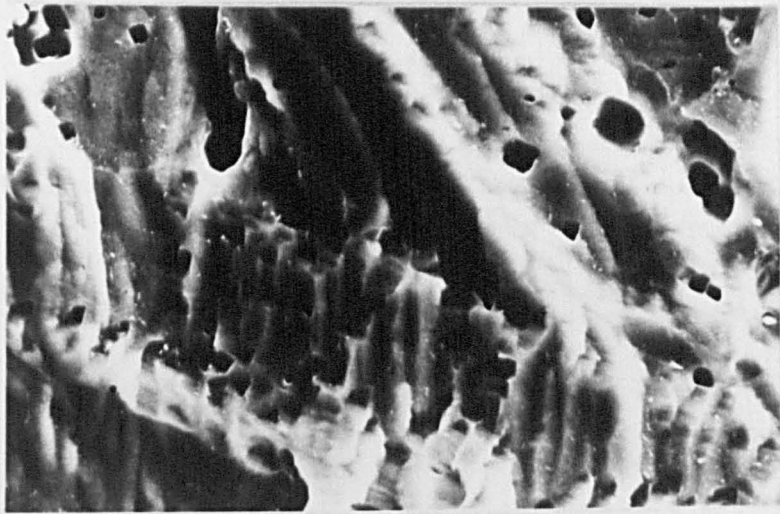
5.2

Long, through thickness crack fracture surfaces

- (a)  $R = 0.1$  OA1 near-threshold growth
- (b)  $R = 0.1$  UA near-threshold growth
- (c)  $R = 0.1$  UA  $da/dN = 6.8\text{MPa}\sqrt{\text{m}}$
- (d)  $R = 0.8$  OA1 near-threshold growth
- (e)  $R = 0.8$  UA near-threshold growth



(a)  $10\ \mu\text{m}$



(b)  $10\ \mu\text{m}$

5.3 (a) & (b) Etched near-threshold fracture surfaces - 7010 UA

## IMAGING SERVICES NORTH

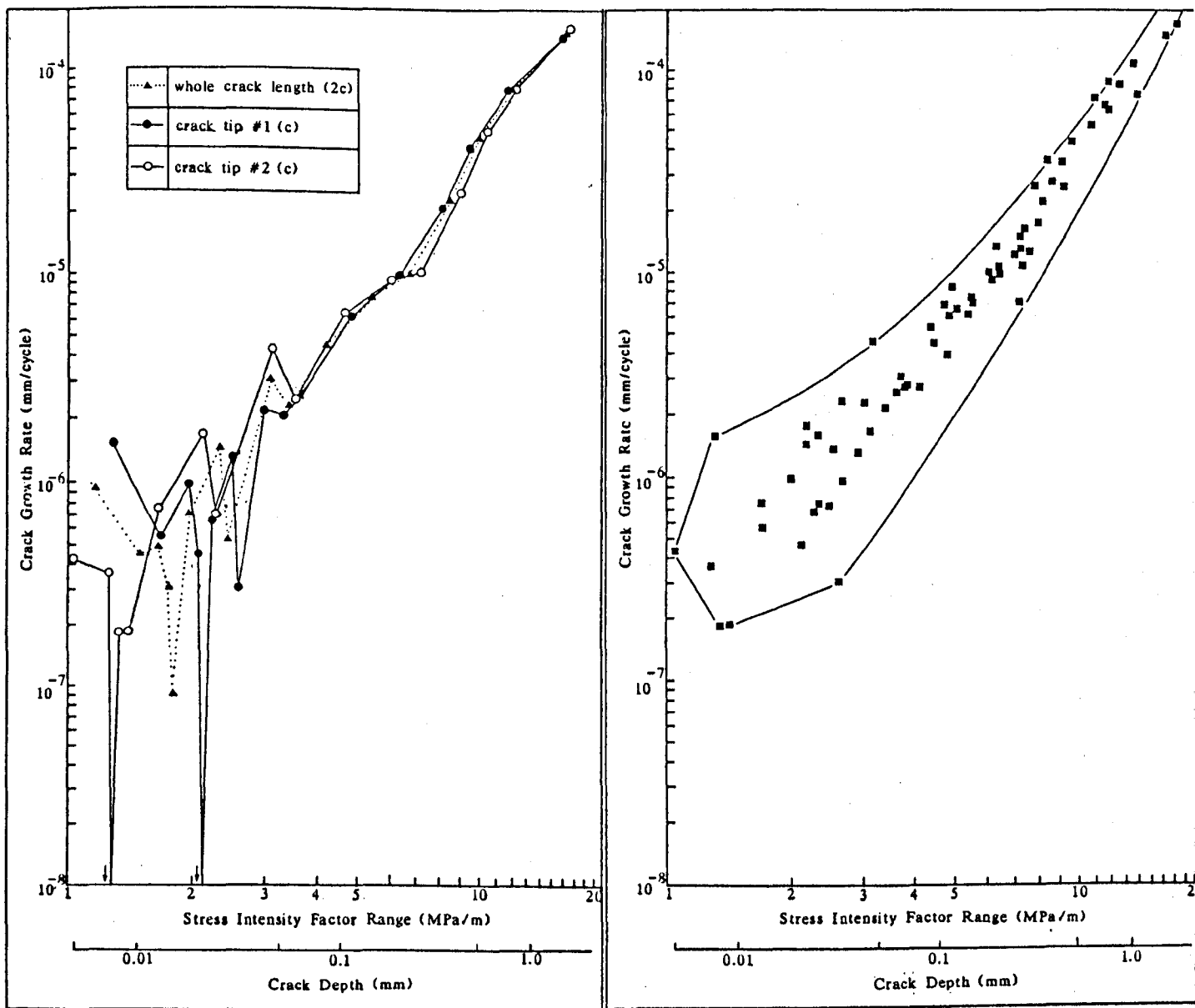
Boston Spa, Wetherby

West Yorkshire, LS23 7BQ

[www.bl.uk](http://www.bl.uk)

TEXT CUT OFF IN THE  
ORIGINAL

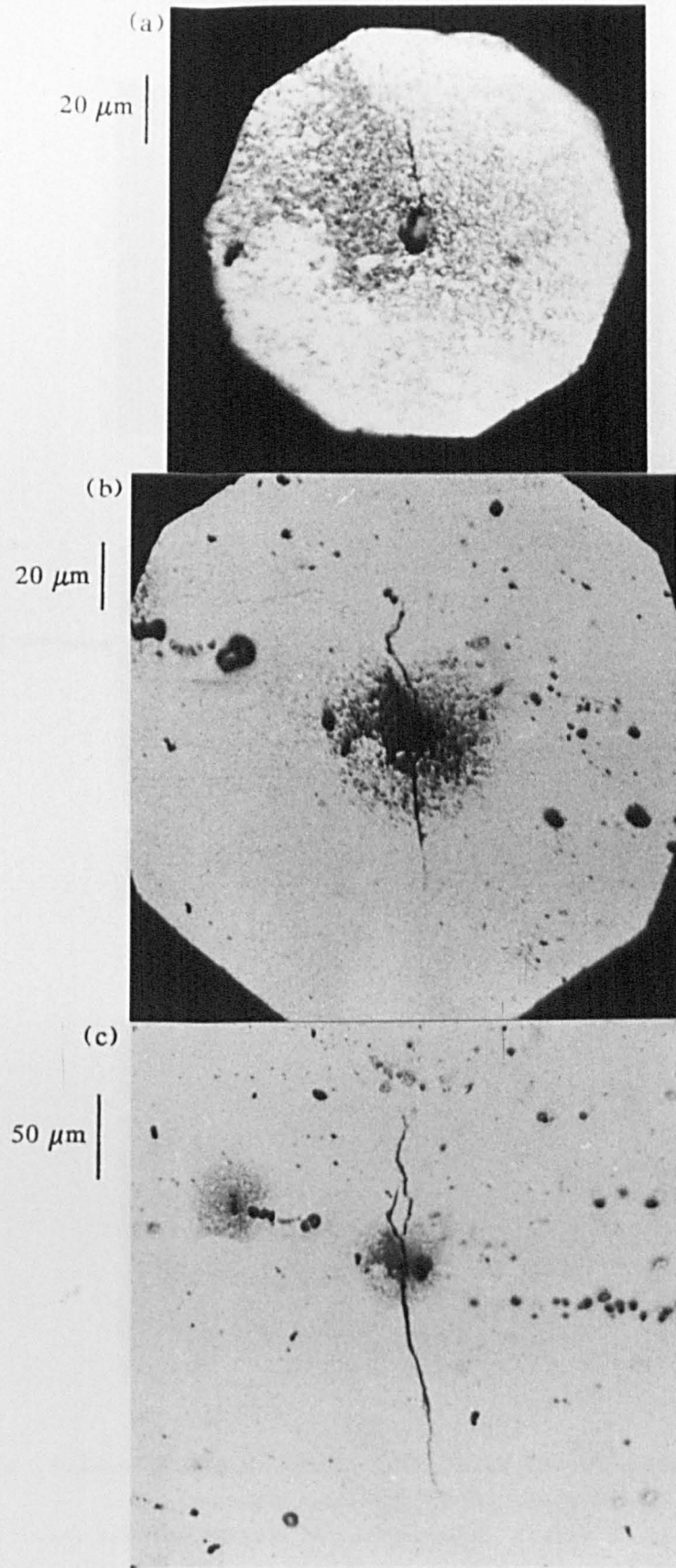




(a)

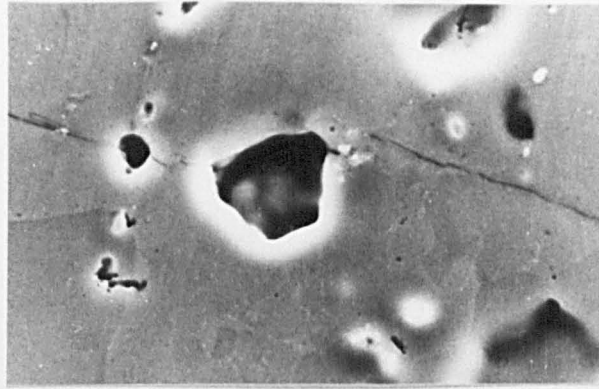
(b)

- 5.4  $da/dN$  vs  $\Delta K$  and  $a$  for short crack growth in 7010 OAl
- (a) specific data from one crack showing variation in  $a$  behaviour when both crack tips are considered independently.
- (b) envelope containing all non-zero growth rate data from 5 cracks

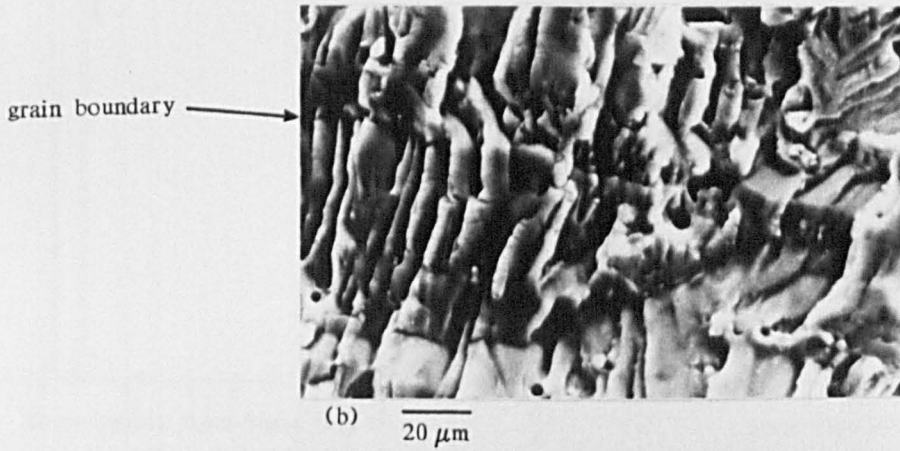


5.5

Optical micrographs showing the development of a short crack in 7010 OAl



(a)  $\overline{10 \mu\text{m}}$

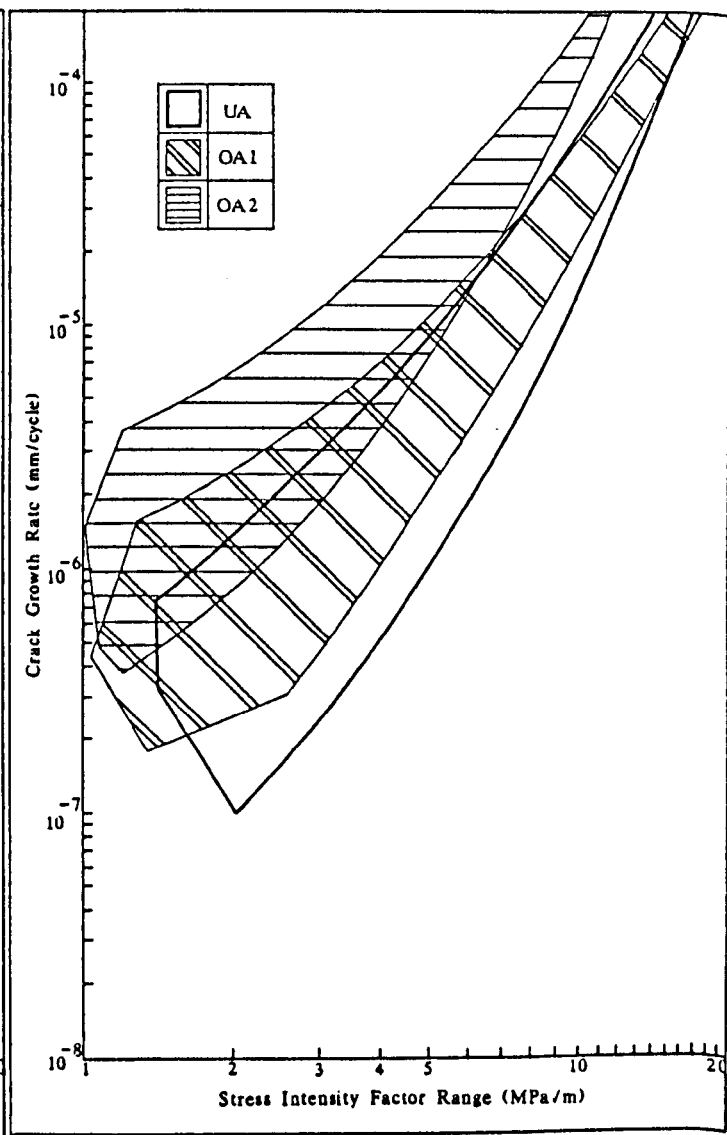
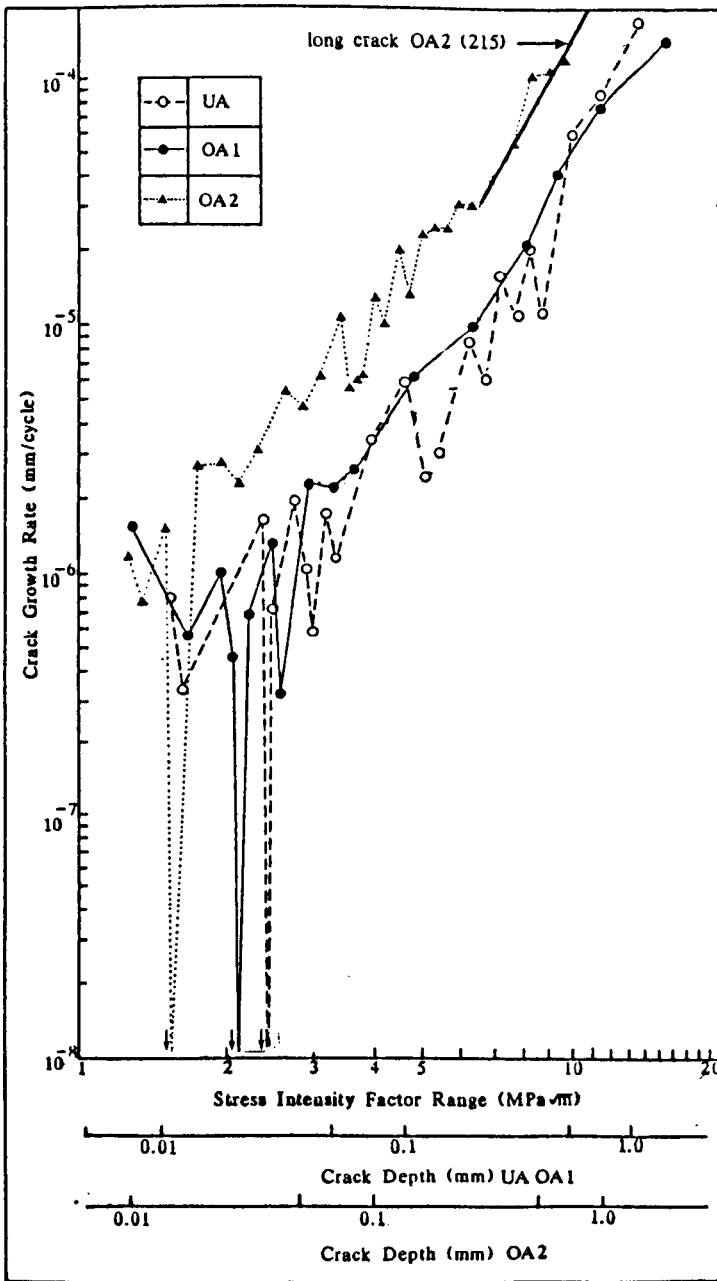


(b)  $\overline{20 \mu\text{m}}$



(c)  $\overline{20 \mu\text{m}}$

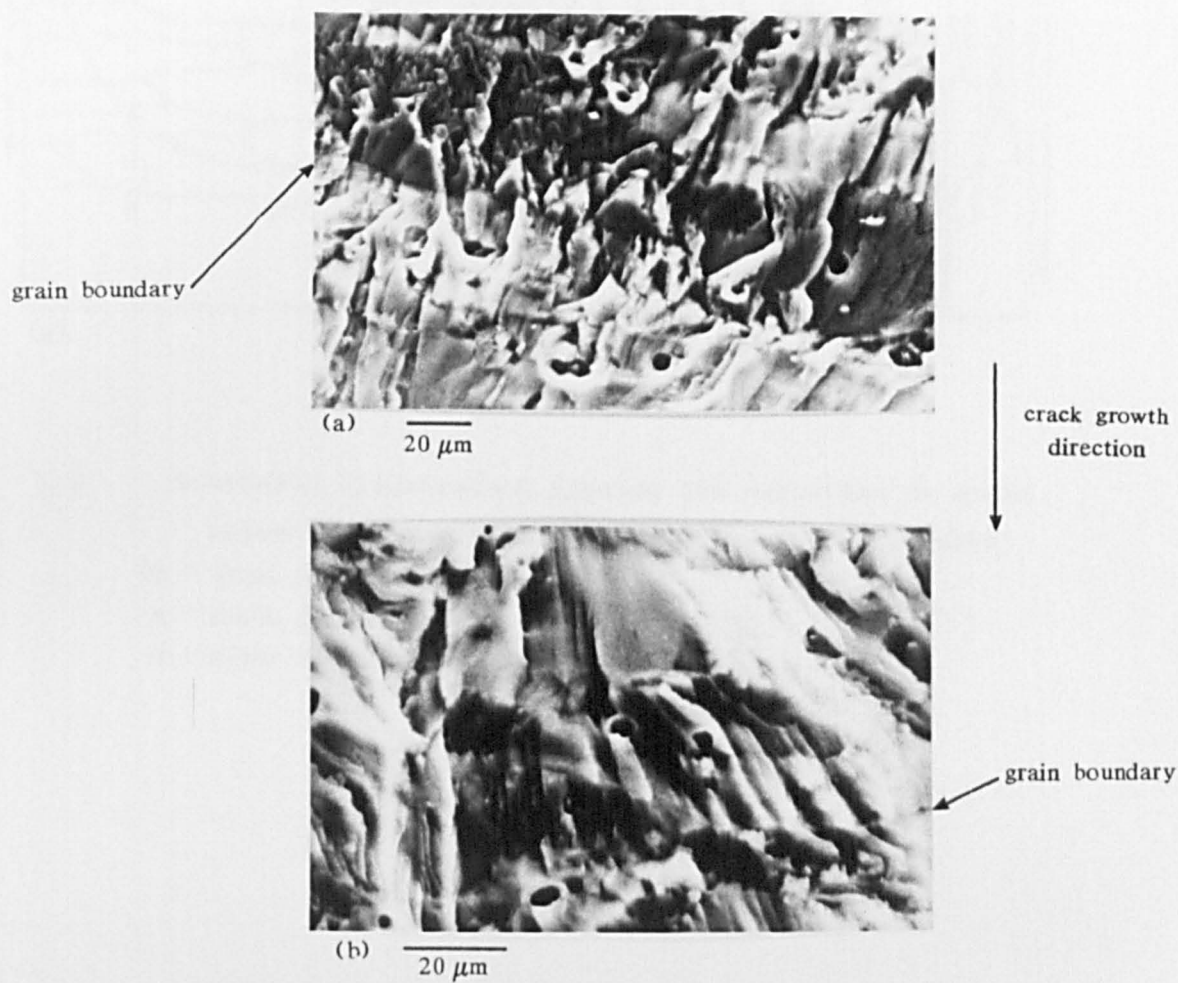
5.6 Fracture surfaces of short crack in OAl (a) initiation site,  
(b) fracture surface close to initiation site,  
(c) fracture surface approximately 500  $\mu\text{m}$  from initiation site



(b)

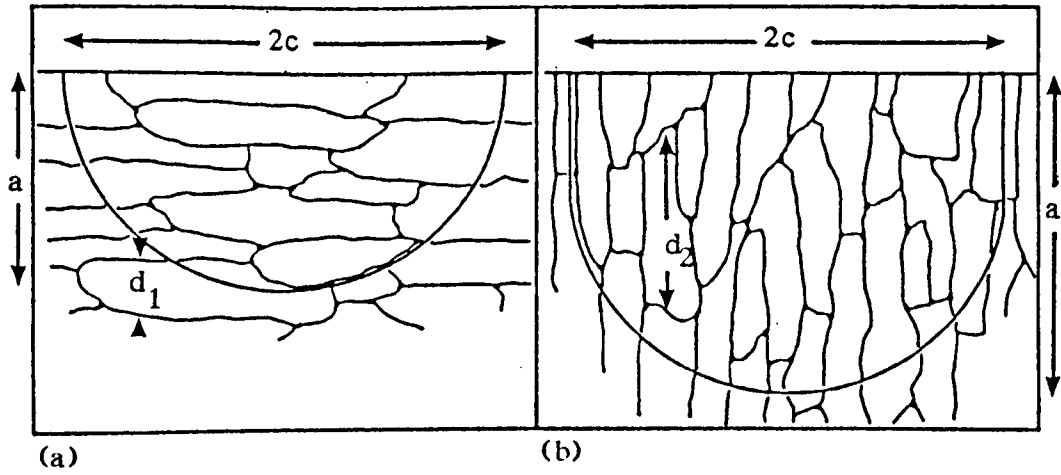
(a)

5.7  $da/dN$  vs  $\Delta K$  and  $a$  for short crack growth in 7010 OA1, UA & OA2  
 (a) specific data for one crack tip from each microstructure  
 (b) envelope containing all non-zero crack growth rate data from a number of cracks in each case.



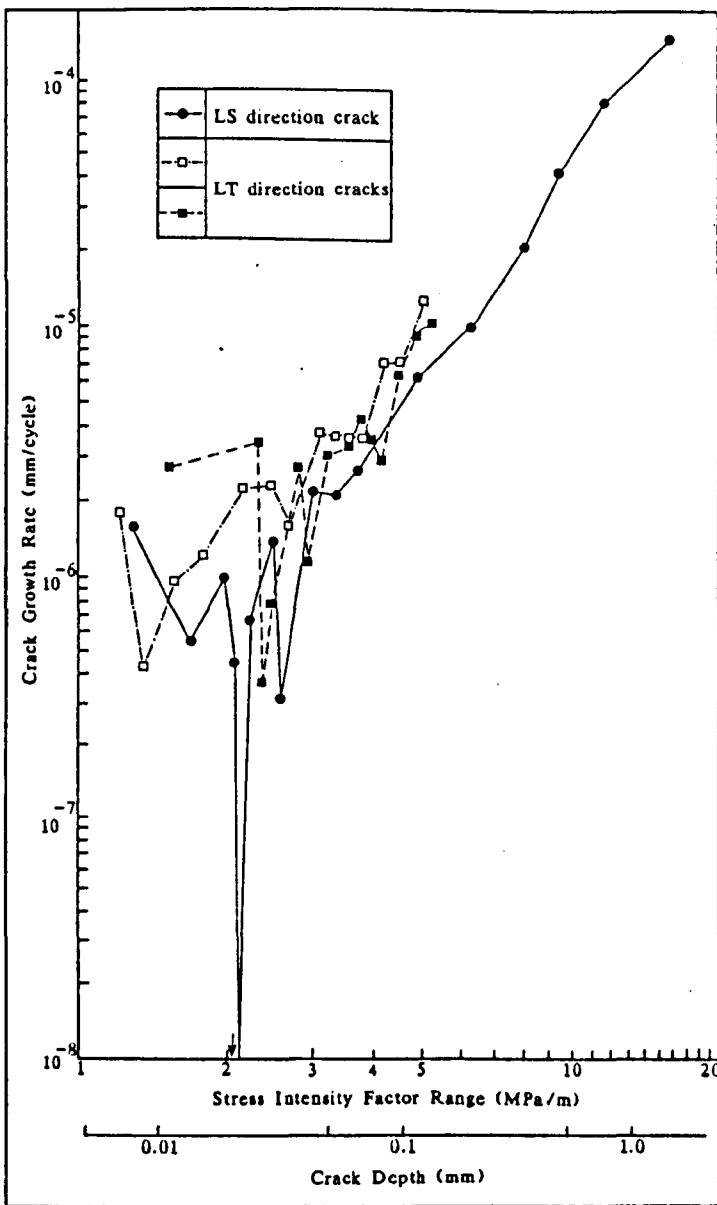
5.8 Fracture surfaces of short cracks close to initiation site

(a) UA, (b) OA2

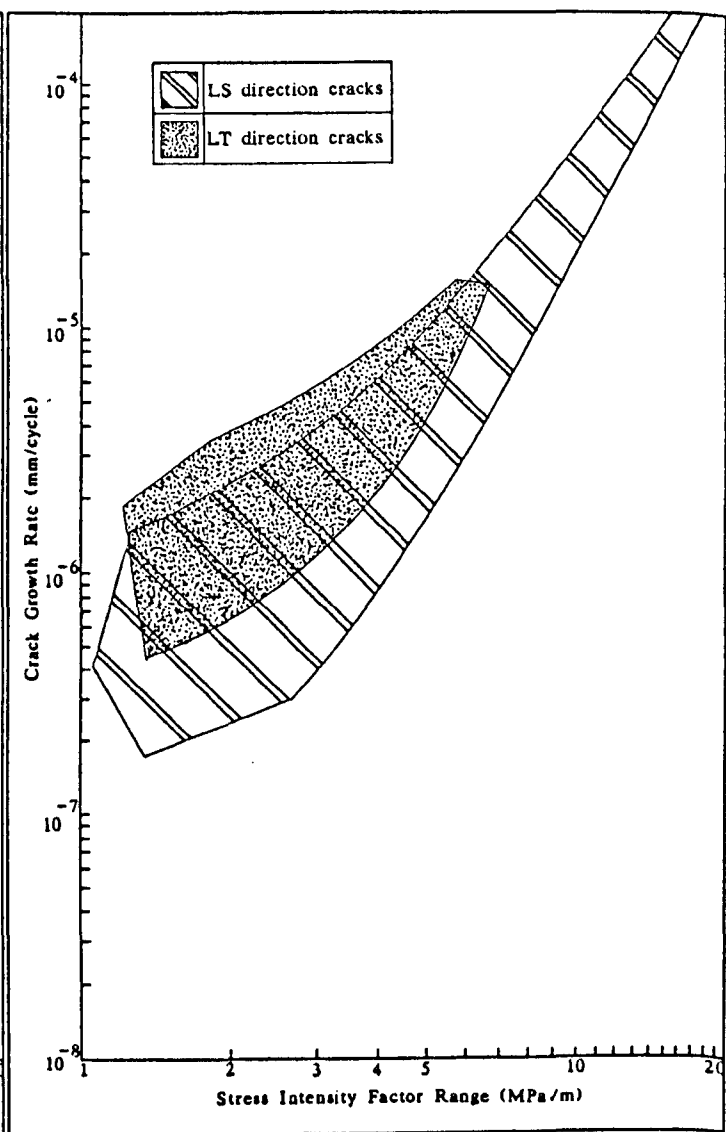


5.9 Schematic illustration showing the variation in grain orientation for (a) LS cracks and (b) LT cracks

$2c$  - total surface crack length  
 $a$  - crack depth  
 $d$  - grain size in crack direction



(a)



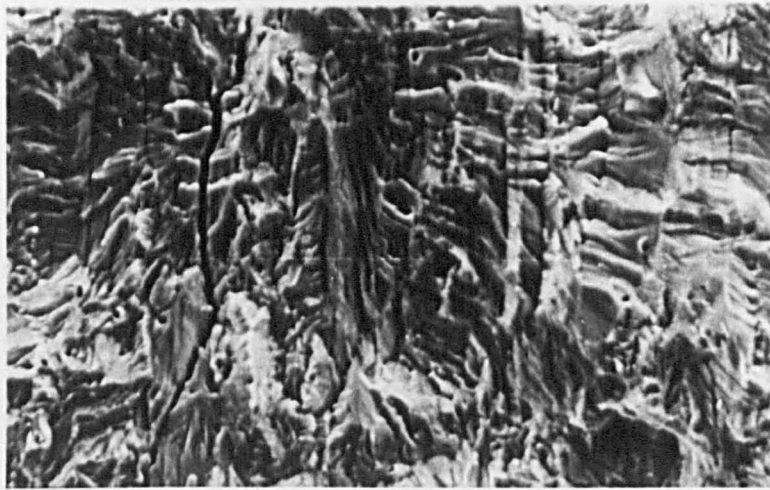
(b)

5.10  $da/dN$  vs  $\Delta K$  and  $a$  for LS & LT short cracks. (7010 OA1).

(a) specific data for one crack in each case,

(b) envelope containing all non-zero crack growth rate data

for both microstructures from a number of cracks.

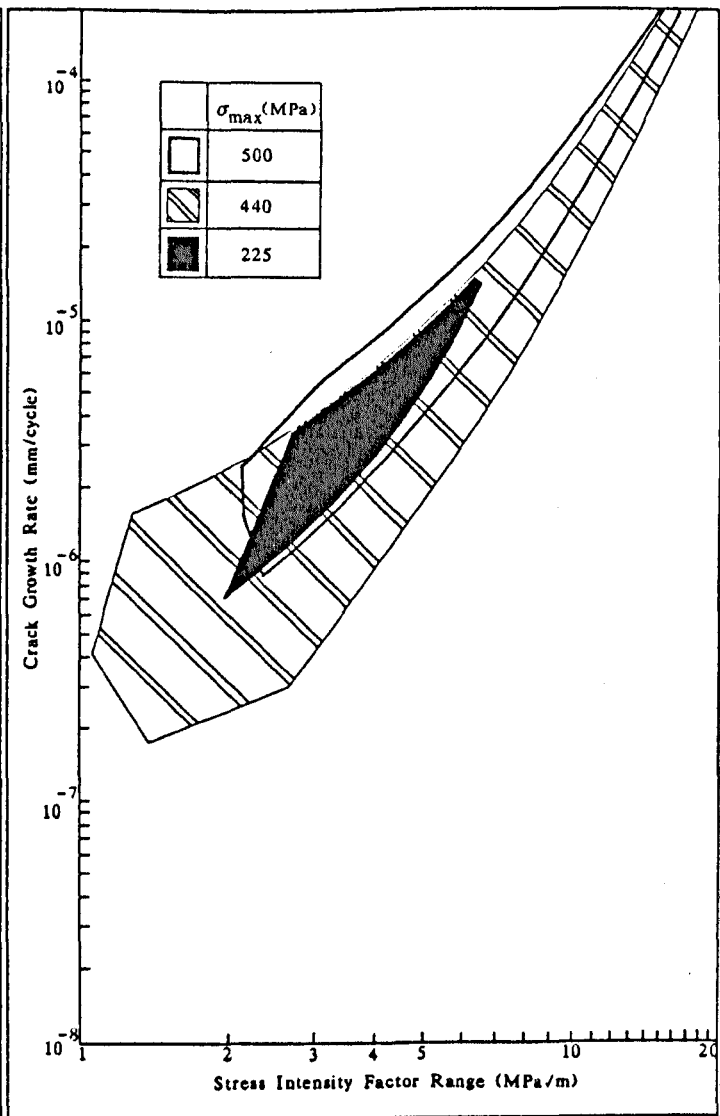
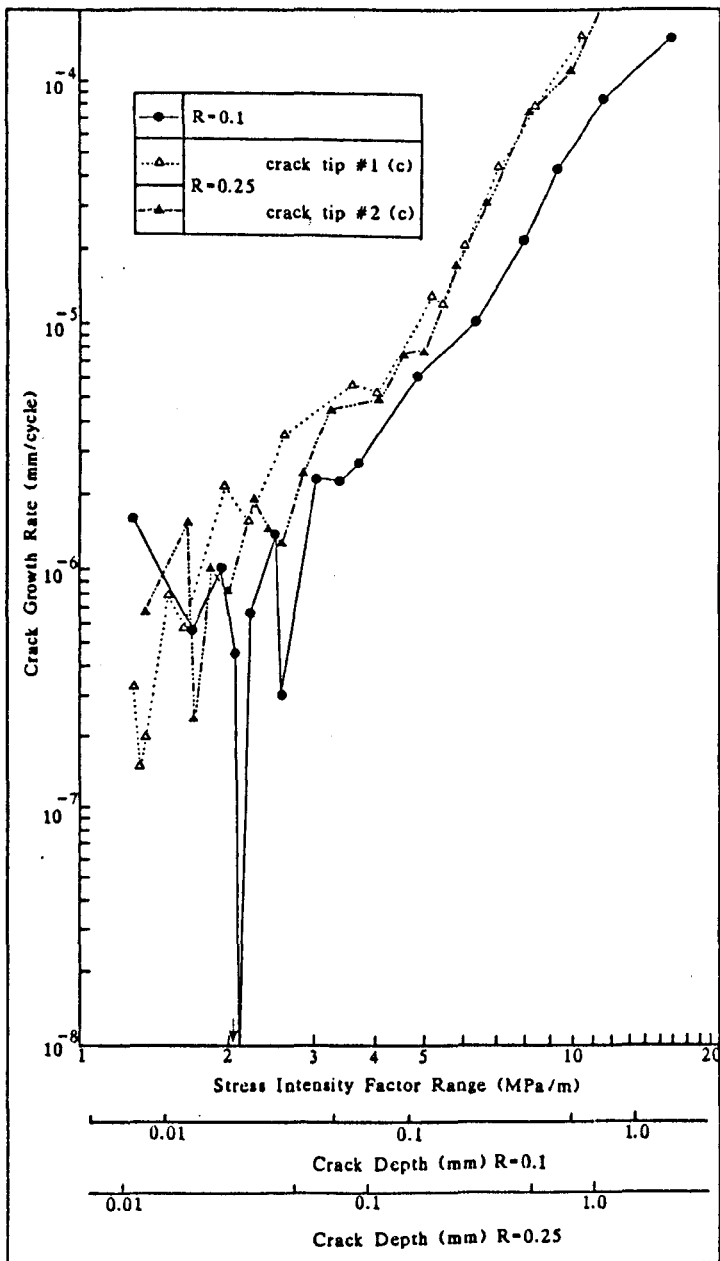


crack growth  
direction  
↓

50  $\mu\text{m}$

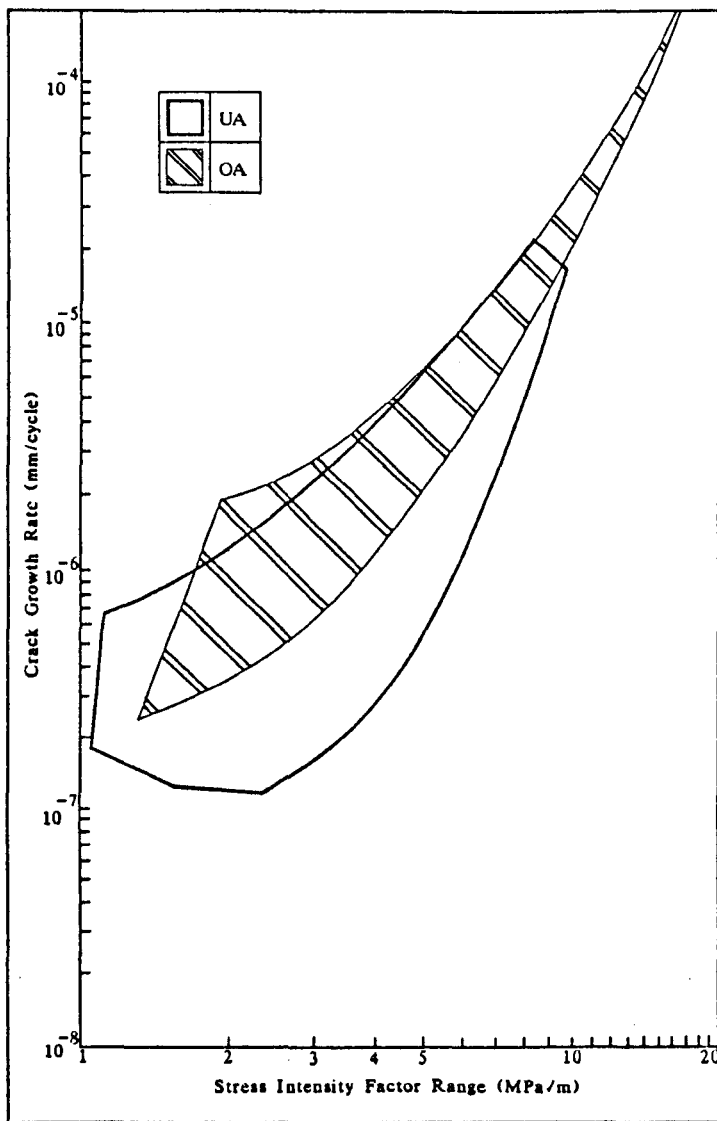
grain boundary

5.11 Fracture surface of short fatigue crack near initiation site for LT orientated crack.

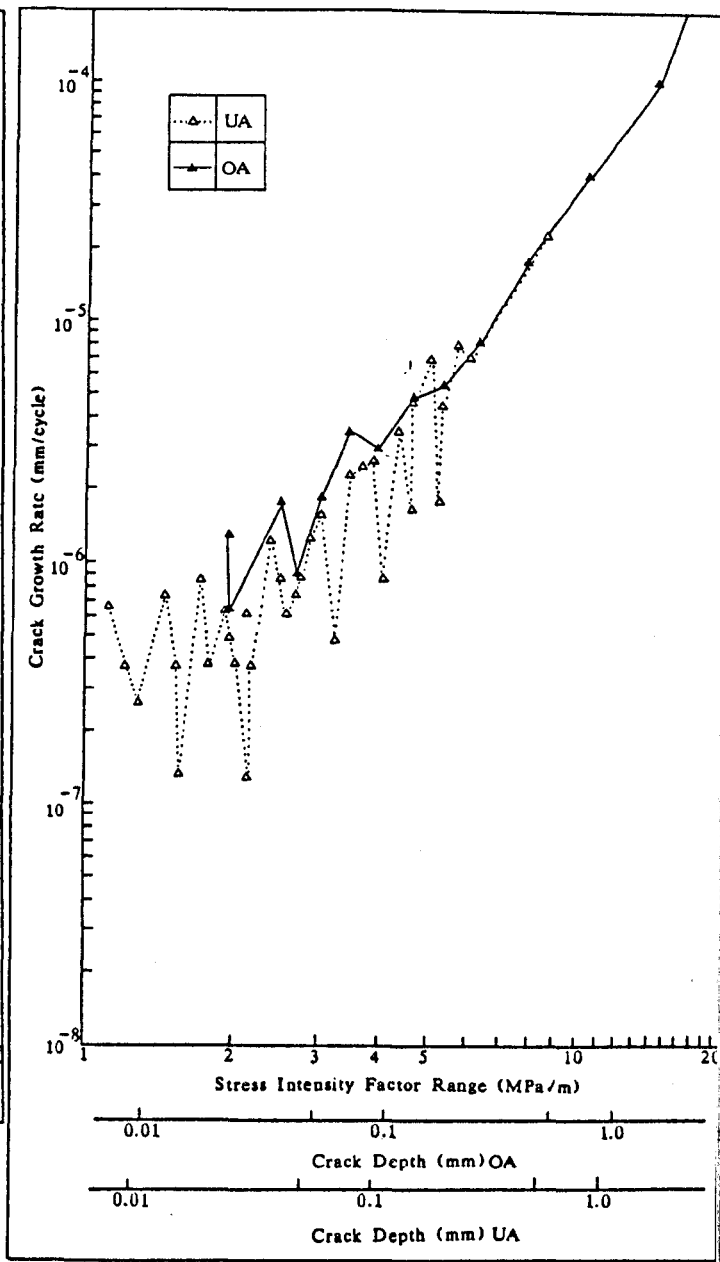


5.12  $da/dN$  vs  $\Delta K$  and  $a$  for short cracks in 7010 OAl growing at  $R = 0.1$  and  $R = 0.25$

5.13  $da/dN$  vs  $\Delta K$  for short cracks in 7010 OAl growing at under  $\sigma_{max} = 225, 440$  and  $500$  MPa - envelope contains all non-zero growth rate data for a number of cracks in each case.



(a)



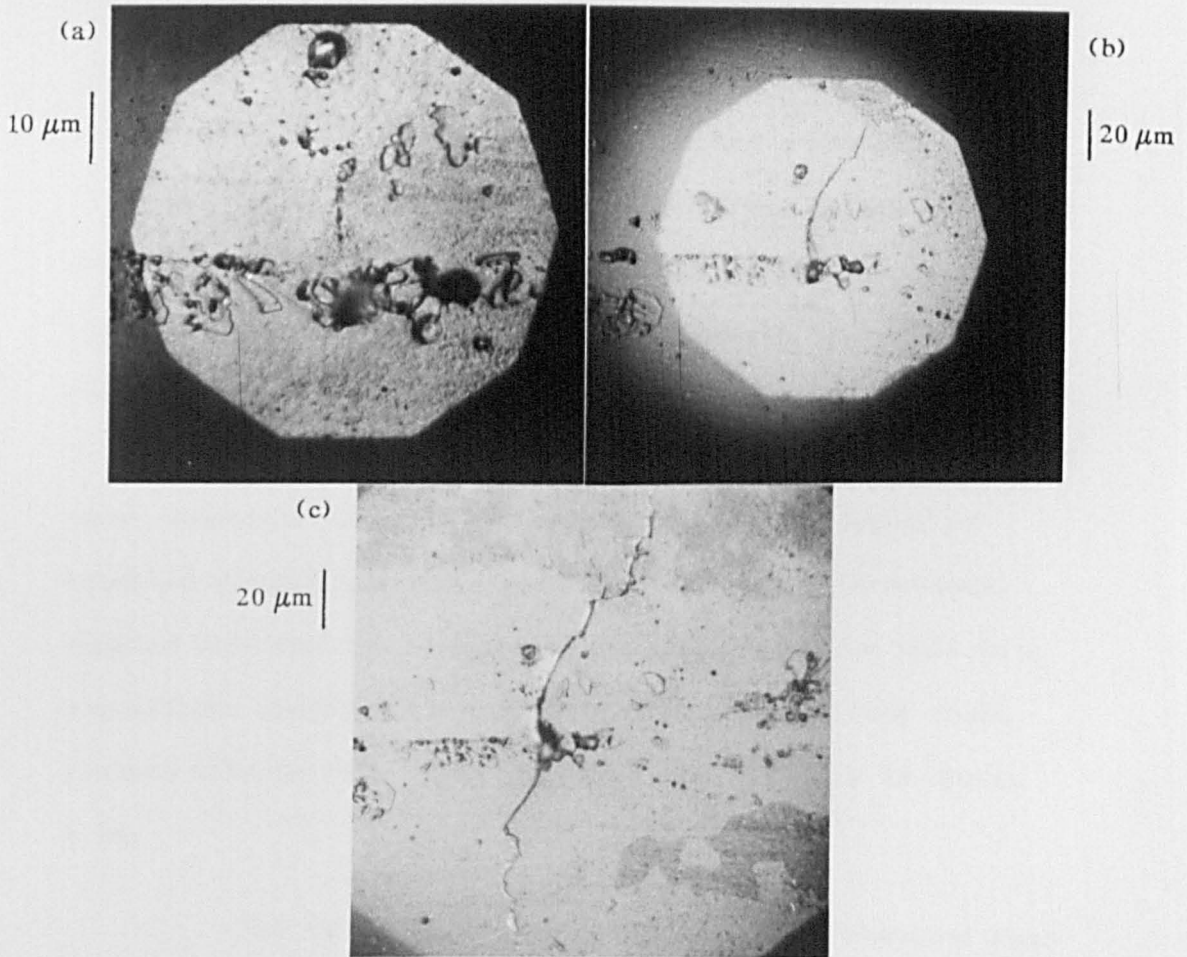
(b)

5.14  $da/dN$  vs  $\Delta K$  and  $a$  for short cracks in 2014A at  $R = 0.1$  for UA and OA. (a) envelopes containing all non-zero growth rate data for a number of cracks in each case, (b) specific data for one crack from each microstructure.



20  $\mu\text{m}$

5.15 Near-initiation site fracture surface for short crack in 2014A UA



5.16 Optical micrographs showing advancement of short crack throughout fatigue life for short crack in 2014A UA

## CHAPTER 6

### ALUMINIUM ALLOYS - DISCUSSION

#### 6.1 BEHAVIOUR OF LONG, THROUGH THICKNESS CRACKS

At a load ratio of 0.1 the long crack fatigue behaviour shows the commonly reported trend of higher threshold stress intensity factor ranges at lower near-threshold crack propagation rates in UA material than in OAl material (figure 5.1). The threshold values obtained,  $2.7 \text{ MPa}\sqrt{\text{m}}$  (OAl) and  $3.9 \text{ MPa}\sqrt{\text{m}}$  (UA) are in good agreement with those quoted in the literature. For the similar high strength, 7XXX series alloy, 7075, Lankford (145) reported a threshold of  $3.8 \text{ MPa}\sqrt{\text{m}}$  for an underaged microstructure and Suresh et al (21) recorded values of  $3.7 \text{ MPa}\sqrt{\text{m}}$  and  $2.6 \text{ MPa}\sqrt{\text{m}}$  for underaged and overaged material respectively. The faceted nature of the near-threshold fracture surfaces of both OAl and UA (figure 5.2a, b) suggests that there will be a significant asymmetrical shear component in crack tip deformation. The degree of mismatch between opposing crack faces that this introduces, coupled with the low load ratio, implies that there will be a significant contribution to the threshold values from crack closure effects (3). This is shown schematically in figure 6.1a.

The threshold stress intensity values obtained from constant  $K_{\text{max}}$  testing will be free from roughness and oxide induced crack closure effects due to the larger crack openings involved.

During the approach to threshold, as the propagation rates are slowly reduced through the testing procedure, the minimum stress intensity ( $K_{min}$ ) is gradually increased to a point where the crack faces are kept apart over the whole loading cycle, so removing any effect of these closure modes (figure 6.1b). Since the fracture surfaces indicate that the mechanism of crack propagation is the same as at  $R = 0.1$ , the  $R > 0.8$  threshold values can be taken as intrinsic material thresholds and will thus be equal to the effective crack tip stress intensity ranges ( $\Delta K_{eff}$ ) at threshold in the  $R = 0.1$  tests. The measured values of  $1.4 \text{ MPa}\sqrt{\text{m}}$  (OA1) and  $2.0 \text{ MPa}\sqrt{\text{m}}$  (UA) are again in good agreement with those quoted in the literature. Suresh et al (21) reported closure free thresholds in overaged and underaged 7075 of  $1.2 \text{ MPa}\sqrt{\text{m}}$  and  $1.7 \text{ MPa}\sqrt{\text{m}}$  respectively.

The fact that superior near-threshold crack propagation resistance persists for the UA material at  $R > 0.8$ , suggests that the difference between threshold stress intensity factors ranges of UA and OA1 at  $R = 0.1$  is partly due to the UA material's inherent resistance to propagation as well as to any mechanical effects, such as crack closure. Greater roughness and oxide induced crack closure is normally associated with underaged microstructures due to a more intense slip distribution, which promotes more angular and rougher fatigue fracture surfaces (20, 21, 23, 70, 90, 91, 94). The near-threshold fracture surfaces reported for UA and OA1, shown in figure 5.2, however, are very similar. This may be a consequence of the ageing times chosen for OA1 and UA, both being quite close to that for the peak aged condition (figure 4.3).

A more definite difference in fracture surface appearance and in propagation behaviour might have resulted from considering microstructures which were more markedly underaged and more heavily overaged, but with the same 0.2% proof stresses.

A material's intrinsic resistance to fatigue crack propagation, such as proposed by Hornbogen and Zum Gahr (92), is based on the relative number of dislocations able to reverse, during unloading, on the same slip bands as they moved away from the crack tip on loading. In underaged microstructures, where deformation occurs heterogeneously, few dislocations are removed from their original slip bands through cross slip and little overall crack tip damage results. As such a mechanism would still be expected to operate at high load ratios, it may be a useful tool in explaining the difference in near-threshold crack propagation behaviour of UA and OA1. The mode of deformation however, also determines the fracture path and as the fracture surfaces of OA1 and UA are very similar (figure 5.2), this type of model may not account for all the observed differences between the ageing conditions.

A further mechanism (89) proposed that the dispersoid mean free path can control the near-threshold fatigue behaviour of aluminium alloys, through the refinement of the slip length. This suggestion was based on the observation of fatigue characteristics of two aluminium alloys, one produced by conventional ingot metallurgy and the other by a powder technique.

Although the alloys had significantly different grain sizes their fatigue behaviours were comparable and this was attributed to their similar mean free paths between dispersoids. In the present study, the spacing between  $ZrAl_3$  dispersoids would not be expected to change appreciably through the ageing process. Hence any effect on fatigue crack propagation properties through this process would be absent.

At high propagation rates away from the near-threshold region, growth becomes more continuous and the effect of microstructure plays a less significant role. It has been suggested (3, 92, 107) that the transition, from microstructurally sensitive to microstructurally insensitive growth, occurs when the plastic zone size ahead of the crack tip becomes equal in size to the controlling microstructural dimension of the material. This would be consistent with the slip reversibility model proposed by Hornbogen and Zum Gahr, as once the plastic zone size encompasses many grains slip becomes more homogeneous, due to the effect of the grain boundaries, and microstructural influences are less pronounced.

Yoder et al (103-107) have suggested that these transitions will be sharp on the  $da/dN$  vs  $\Delta K$  plot. Furthermore, they suggest that not only will they appear when the plastic zone size equals the grain size, but also, for 7XXX series aluminium alloys (107), when it reaches the subgrain size and the mean free path between dispersoids (figure 2.13).

Yoder et al used the following equation to calculate the size of the plane strain reverse plastic zone size ahead of the crack tip ( $r_{rpz}$ ) (218)

$$r_{rpz} = \alpha \left[ \frac{\Delta K}{2\sigma_y} \right]^2 \dots\dots\dots 6.1$$

where  $\sigma_y$  = monotonic yield strength of the material and  $\alpha = 0.132$ . The expression was based on Rice's derivation (109) from the monotonic plastic zone size ( $r_{max}$ ) (219).

$$r_{max} = \frac{1}{6\pi} \left[ \frac{K_{max}}{\sigma_y} \right]^2 \dots\dots\dots 6.2$$

with the maximum stress intensity ( $K_{max}$ ) being replaced by  $\Delta K$  and the yield strength ( $\sigma_y$ ) replaced by  $2\sigma_y$  to account for yielding within the plastic zone in both tension and compression. Hence, Rice's equation for the plane strain reverse plastic zone size could be defined as:

$$r_{rpz} = \frac{1}{6\pi} \left[ \frac{\Delta K}{2\sigma_y} \right]^2 \dots\dots\dots 6.3$$

The constant at the front of Yoder's expression (equation 6.1) was devised experimentally by Hahn et al (218) and, as such, differs to that predicted by theoretical calculations (equations 6.2 and 6.3).

Equation 6.1 can be used to establish where transitions should be seen for the  $R = 0.1$  data for 7010 OAl and UA (figure 5.1) according to Yoder et al. If an average grain size of  $20 \mu\text{m}$  is taken for both microstructures and  $\sigma_y = 495 \text{ MPa}$ , the transition when the reversed plastic zone size equals the grain size should occur at a  $\Delta K$  of  $12.2 \text{ MPa}\sqrt{\text{m}}$ . Similarly, if the average dispersoid spacing is assumed to be similar to that determined for 7075 by Bucci et al (110) (i.e.  $\sim 0.7 \mu\text{m}$ ), the transition when the reverse plastic zone size equals the mean free path between dispersoids should occur at a  $\Delta K$  of  $2.3 \text{ MPa}\sqrt{\text{m}}$ . Clearly, no transition is possible at the latter  $\Delta K$  as it is below  $\Delta K_{th}$  for both OAl and UA at  $R = 0.1$ . Insufficient data in the region between  $\Delta K = 10 \text{ MPa}\sqrt{\text{m}} + 16 \text{ MPa}\sqrt{\text{m}}$  means that the former transition point can not be verified. However, the smooth nature of the curves in figure 5.1 suggests that the positioning of any transition would be speculative. Furthermore, the accurate interpretation of any transitions would be difficult because of the large number of varying plastic zone size equations quoted in the literature (e.g. 109, 180, 218, 219). Due to variations in grain size in the ST direction ( $10 \times 40 \mu\text{m}$ ) of the 7010 alloy and to the fact that at any one time the crack front will be at grain boundaries in some grains at within grains of other points, means that the transition from structure sensitive to insensitive growth would be expected to occur over a range of  $\Delta K$ .

The determination of crack path in the near-threshold region from the shape of etch pits (figure 5.3), reveals that fracture occurred on either {100} planes (square based cubic or pyramidal pits) or on {111} planes (triangular base pyramidal pits). The presence of areas containing irregular, undistinguishable etch pits however, indicates that the fracture path was not always close to a low index plane. In general, the direction of propagation was difficult to determine accurately, though it appeared to be between  $\langle 100 \rangle$  and  $\langle 110 \rangle$ . Both the fracture plane and the direction changed from grain to grain due to the crystallographic misorientation about grain boundaries.

Previous research (25, 111-114), 116) has highlighted a variety of possible failure mechanisms in 7XXX series alloys and other aluminium based alloys, including fatigue on {100}, {111} and {110} planes. In some studies (e.g. 114) it was concluded that growth was not confined to a single crystallographic path, but fluctuated from grain to grain as is the case in this study. The majority of evidence indicates that restricted slip mechanisms are responsible for failure along {100} or {111} planes, generally in  $\langle 110 \rangle$  directions (25, 93, 111, 112, 113). Other workers, however, have reported fracture on {110} planes (114, 116), though the results produced by Nix and Flower (116) were influenced by the strong texture of their 7010 alloy, which produced higher tensile stresses in {110} planes than on {100} planes.

Garrett and Knott (112) have demonstrated using a simple dislocation model, that crack advance would be more energetically favourable on {100} planes rather than on {110} planes in fcc metals, and that the resulting fracture surface would be consistent with the 'cleavage like' fracture commonly observed. The authors did emphasize however, that in commercial alloys the effect may be inhibited leading to fracture on both {100} and {110} planes.

## 6.2 ASPECTS OF SHORT CRACK GROWTH

The irregular growth of short fatigue cracks, similar to that presented in figure 5.4a for OA1, has also been reported for other 7XXX series alloys (148, 149, 161-164, 174, 176, 207) and in a 2XXX series alloy (174). In all cases the discontinuous growth characteristics have been associated with microstructural effects and especially the interaction between the crack tip and grain boundaries, or rather the relative crystallographic orientations of adjoining grains. The dips or crack growth rate minima shown in figure 5.4a occur between crack depths of 7  $\mu\text{m}$  and 50  $\mu\text{m}$ . As the grain size in the direction of crack growth at the bottom of the crack (i.e. ST direction) is in the range between 10 and 40  $\mu\text{m}$  and averages about 20  $\mu\text{m}$ , it is possible that the crack tip may be held up at the first or second of these microstructural barriers. This view is supported by the appearance of the fracture surface close to the initiation site (figure 5.6b) which shows the crack tip changing direction around grain boundaries.

It has been reported in the literature (148, 149) that the interaction of the crack tip, or the plastic zone ahead of the crack tip, with the grain boundary causes these decelerations in propagation rate, as slip across the interface is impeded. Growth into the adjoining grain is difficult until a mature plastic zone has been generated in it. The ease with which this occurs will depend in part, on the relative orientation of the neighbouring grains. Hence, the incubation time at the grain boundary will be longer, when the crystallographic orientations of two touching grains are very different and when the plastic zone size is small. In addition, Morris and co-workers (161-164) have considered that crack closure stresses are important. These they calculated would be at their largest value when the distance between the crack tip and the next grain boundary was the greatest. As this condition is satisfied when a crack just enters a new grain, retardation close to a grain boundary would also be observed.

The effect of microstructure on longer cracks (greater than 100  $\mu\text{m}$  for example) seems to be less pronounced and almost continuous growth results. By this depth, the crack tip samples between 5 and 25 grains around the crack perimeter and hence overall measured growth rates become more homogeneous, as any crack tip: grain boundary interactions, which temporarily reduced local propagation rates, are averaged out around the crack periphery.

This suggestion assumes that the measured surface crack growth rates are influenced not just by the local microstructure at or just beneath the surface, but also by the microstructure around the crack front. Support for this is shown in figure 5.16 which shows a crack in 2014 UA at various stages through the fatigue life. Both crack tips show crack deflection before the first grain boundary is reached. These deflections were accompanied by deviations in crack propagation rate and could be associated with crack tip : grain boundary interactions at points around the crack front.

In the region of continuous growth rates when the crack depth  $>100 \mu\text{m}$ , the maximum plastic zone size is larger than the grain size of the material. The condition for compatible deformation, of slip on five independent slip systems, is satisfied and as growth is no longer confined to individual  $\{111\}$  planes, an easier path for propagation from grain to grain is achieved.

### 6.3 EFFECT OF AGEING CONDITION ON SHORT CRACK PROPAGATION BEHAVIOUR

The  $da/dN$  vs  $\Delta K$  plots showing short crack behaviour in 7010 (figure 4.7a and b) and 2014A (figure 5.14b) reveal that the effect of ageing is similar to that reported for long cracks in section 6.1. A deterioration in short crack propagation resistance accompanies an increase in ageing time. This effect is further emphasized by the data for OA2 (figure 4.7a and b) which shows that the more heavily overaged, commercial temper exhibits worse propagation resistance than OA1.

The fact that this trend for OA2 continues up to crack depths in excess of 500  $\mu\text{m}$ , is an indication of the inferior crack propagation resistance of this material even for long cracks in the Paris region. Further evidence to support this is also shown in figure 5.7a by the available long crack data quoted in the literature (215). These data are for crack propagation in 100  $\mu\text{m}$  thick plate at an R-ratio = 0.1.

These observations, plus the similarities between the fracture surfaces of the three ageing conditions for 7010 (figure 5.6a, 5.8a and b) and the two for 2014A (figure 5.15), suggest that extrinsic effects, such as crack closure, will only account for a portion of the variation in propagation behaviour. It appears that phenomena specific to a particular microstructure are also important. For instance, the degree of slip reversibility in the plastic zone ahead of the crack tip, as has been discussed in section 6.1. The fact that for relatively long cracks ( $>500 \mu\text{m}$ ) growth is almost continuous and the propagation behaviour of each of the microstructures is more comparable, is also consistent with Hornbogen and Zum Gahr's model (92). Slip becomes more homogeneously distributed through the microstructure when the plastic zone size ( $r$ ) ahead of the crack tip is larger than the grain size ( $d$ ). Hence a change in propagation behaviour, marking the end of microstructurally short crack growth, should occur when  $r \sim d$ . A similar transition is seen for long cracks from microstructurally sensitive to insensitive crack growth at this point, as has been discussed in section 6.1.

The transition however should be more apparent for short cracks as the number of grains being sampled by the crack tip is considerably smaller.

Calculations to determine plastic zone sizes have been evolved through theoretical arguments (200, 219) and subsequently modified through experimental evidence. (159, 180, 218). In addition some authors claim that the important dimension is the maximum plastic zone size (180) while others consider that the reverse plastic zone size is a more appropriate correlator (103-107). In plane strain, equations 6.2 and 6.3, can be used as approximations for the maximum plastic zone size ( $r_{max}$ ), based on Irwin's original calculations, and the reverse plastic zone size ( $r_{rpz}$ ), subsequently determined by Rice (109). Equation 6.1 was experimentally derived by Hahn (218) who found that a value of  $\alpha = 0.132$  fitted his data more closely than  $1/6\pi$ . More recently, Davidson and Lankford (220) have shown, through electron channeling measurements, that  $\alpha = 0.7$  for long and short cracks in a 7075-T651 aluminium alloy. These equations are represented in table 6.1 (equations 6.1 - 6.6) together with calculations of  $\Delta K$  when  $r=d$  for the various microstructures of 7010 and 2014. Also included are the values of  $\Delta K$  where continuous, uninterrupted growth is first observed for 7010 UA, OA1 and OA2 (figure 5.7a) and 2014 UA and OA (figure 5.14b). The table suggests that the stress intensity factor ranges at the transitions appear to lie between the  $\Delta K$ s predicted by equations 6.2 and 6.4, which are both based upon the maximum plastic zone size.

Irwin's equation (equation 6.2) consistently overestimates the observed transition, while the equation used by Yoder et al (equation 6.4) often leads to underestimations. Although the position of the transitions shown in figure 5.7a and 5.14b may be subject to movement due to the experimental scatter associated with short crack behaviour, their correlation with the equations based on the maximum plastic zone size is significant, for it may mark the end of the microstructurally short crack regime. Deeper cracks grow more homogeneously and, the affects of the local microstructure of the crack tip are diminished. Any difference between the growth behaviour of these cracks and long, through thickness cracks should be in the closure contribution, which will increase with crack depth.

The data contained in table 6.1 also indicate that the observed behaviour corresponds to some extent with Davidson and Lankford's analysis for the size of the reverse plastic zone, which was based on experimental evidence of cracks growing in a 7075-T6 alloy. Their equation (equation 6.6) differs dramatically to the majority of other analyses based on experimental obserations (e.g. equation 6.1 (103-107,218)) and to those based on theoretical arguments (e.g. equation 6.3 (109)). The sizeable dissimilarity between these studies suggests that further verification of Davidson and Lankford's model is required before it can be broadly accepted.

Differences in propagation behaviour between 7010 and 2014A are difficult to assess due to the relatively large degree of scatter associated with short crack propagation data. Both show similar short crack growth characteristics, with the OA material exhibiting worse propagation resistance and the establishment of continuous, uninterrupted growth at short crack depths. Initiation in both alloys was seen to occur from or near constituent particles, however the presence of larger particles in the 2014A alloy meant that initiation resistance was generally poorer in this alloy. Overall propagation rates for both alloys were seen to be similar (figures 5.7b and 5.14a), which may be a result of a number of contributing factors. For instance, grain size, precipitate size, type and distribution and texture.

#### 6.4 COMPARISON OF LONG AND SHORT CRACK BEHAVIOUR

##### 6.4.1 The anomalously rapid growth of short cracks

A comparison of the long and short crack propagation behaviour can be made from figure 6.2, which contains the long and short crack data for 7010 OA1 and UA. It is apparent that below crack depths of approximately 400  $\mu\text{m}$  short surface cracks grow at faster rates than corresponding long cracks under similar nominal stress intensity conditions. Although the irregular nature of growth has been generally interpreted in microstructural terms, the causes of accelerated growth, below long crack threshold values, are less well defined. The results of this study suggest that differences in closure contributions are at least in part responsible.

Similar conclusions have been made by others (47, 148, 159, 187) who consider that due to a smaller closure contribution for short cracks, enhanced propagation rates are observed under similar applied driving forces.

The initial work by Chan and Lankford (148, 159) showed that crack tip opening displacements (CTODS) were larger for short cracks than for long cracks in a 7075-T6 alloy. They suggested that a change in stress state, from one of plane strain for long cracks to one of plane stress for short cracks, was responsible for the broad plastic strain range ahead of the crack tip which caused the larger CTODS and resulted in faster propagation rates. If the size of the maximum plane stress plastic zone at the tip of a short crack growing on the surface of a slab is assumed to extend into the material by the same distance before plain strain conditions prevail, an approximation of the extent of the plane stress region can be made. According to Irwin the maximum plane stress plastic zone size ( $r_{max}$ ) can be calculated for a surface crack from the yield strength ( $\sigma_y$ ) and  $K_{max}$  ( $\sim 1.12 \sigma_{max} \sqrt{\pi a}$  where  $\sigma_{max}$  = max stress and  $a$  = crack depth) by:

$$r_{max} = \frac{1}{2\pi} \left[ \frac{K_{max}}{\sigma_y} \right]^2 \dots\dots\dots 6.7$$

In the present study  $\sigma_{max} = 0.9 \sigma_y$  and hence  $\frac{r_{max}}{a} \sim 0.5$ .

Dugdale (221) however, proposed that for high applied stress situations the maximum plastic zone size could be better described by:

$$r_{\max} = a \left[ \sec \left[ \frac{\pi \sigma_{\max}}{2 \sigma_y} \right] \right] - 1 \quad \dots\dots\dots 6.8$$

and thus if  $\sigma_{\max}/\sigma_y = 0.9$ ,  $\frac{r_{\max}}{a} \sim 5.4$ . In these circumstances short cracks would grow under plane stress conditions even at the deepest point of the crack. Brown, King and Hicks (47) have recently considered that this large maximum plastic zone size coupled with a small reverse plastic zone size, caused by a lack of gross reverse yielding on unloading, would simulate testing at a high load ratio. Hence growth would appear to be closure free and higher propagation rates would be observed. For their Ni-base superalloy it was calculated that short crack growth at  $R = 0.1$  corresponded to long, through thickness crack growth at  $R \sim 0.65$ . The results shown on figure 6.2 appear to support Brown et al's theory, with very short crack data ( $a < 20 \mu\text{m}$ ) lying close to high R - ratio, closure free, long crack lines.

A further consideration concerns the generation of irregular fracture surfaces which promote both roughness-induced and oxide-induced crack closure. For a crack only one or two grains deep, it is likely that minimal mode II displacements, coupled with the relatively planar fracture surfaces, would produce little or no closure and the crack would effectively grow at a high R - ratio (187). As the crack advances however, an increasing closure contribution by these means would result, thereby effectively reducing the load ratio. Eventually the long and short crack data should meet when the effective load ratio for the short cracks is reduced to a level which allows the same range of  $\Delta K$  to be experienced at both the long and short crack tips.

The fact that little short crack data have been collected below the long crack  $R = 0.8$  lines is not significant in terms of non-closure arguments. The high stress levels required for initiation in the smooth bar, short crack specimens, coupled with the observation that initiation commonly occurred for these high strength aluminium alloys from inclusions up to 15  $\mu\text{m}$  deep, meant that it was not possible to collect data corresponding to very low  $\Delta K$ s.

So far correlations between long and short cracks have been made in terms of linear elastic fracture mechanics (LEFM). As a number of studies (e.g. 5, 127, 180) have highlighted however, LEFM is, in theory, not applicable to the short crack situation due to the violation of the concept of similitude. LEFM is generally only appropriate if the maximum plastic zone size ahead of the crack tip ( $r_{\text{max}}$ ) is small (typically  $< 0.07a$  (5)). According to Dugdale (221) for high stress situations  $r_{\text{max}} \sim 5.4a$ , considerably greater than  $0.07a$ . Even if plane strain conditions are assumed to operate at the tip of a crack subjected to high maximum stresses (equation 6.2)  $r_{\text{max}} \sim 0.5a$ . To overcome this problem, some authors have attempted to use elastic-plastic fracture mechanics (EPFM) (e.g. 127, 183, 184). Although long and short crack data has shown more correlation, difficulties are still apparent, especially when the non-continuum nature of short cracks is considered.

The  $\Delta K$  scales used in this work to describe short crack growth, are intended mainly for comparative purposes for use with long crack data. For very short cracks this scale will be inappropriate, however, the good correlation between the long and short crack lines in figure 6.2 above the points of convergence, indicates that the use of LEFM is justified in this region.

Even though similitude concepts are violated, some authors (172, 174) have demonstrated that LEFM can describe cracks down to very small crack depths, if the effective stress intensity factor ( $\Delta K_{eff}$ ) is used. Tokaji and al (172) consider the minimum crack depth to which LEFM can be used simply to be 3x grain diameter. Above this depth it was thought that  $\Delta K_{eff}$  can adequately describe short crack growth while the crack closure contribution associated with such cracks increases. Similarly Blom and al (174) predict, using a modified Kitagawa diagram (figure 2.25), that the critical crack depth ( $a_2$ ), representing the border between true short crack and long crack behaviour, can be calculated from the following equation:

$$a_2 = \frac{1}{\pi} \left[ \frac{\Delta K_{eff,th}}{\Delta \sigma_0} \right]^2 \dots\dots\dots 6.9$$

where  $\Delta K_{eff,th}$  = effective threshold  $\Delta K$  and  $\Delta \sigma_0$  = endurance limit. For 7010 OAl  $\Delta K_{eff,th}$  can be assumed to equal  $\Delta K_{th}$  from the constant  $K_{max}$  tests (i.e. 1.7 MPa $\sqrt{m}$ ). If  $\Delta \sigma_0 \sim 200$  MPa (215), then  $a_2 \sim 23 \mu m$  which approximates to the grain size in the crack direction.

At these crack depths, propagation behaviour is still heavily dependent on local microstructural features at the crack tip and the use of LEFM, even with closure contributions taken into account, still causes problems due to the discontinuous crack tip deformation behaviour. Further work is still required to model short crack propagation accurately.

Changes in testing frequency have also been suggested to be a cause for differences in propagation behaviour in high strength aluminum alloys (26). In the work of Vasudévan & Bretz (26), an order of magnitude increase in frequency reduced long crack propagation rates. This was attributed to a build up of a thicker oxide layer on the fracture surfaces, therefore increasing crack closure contributions. The smaller increase in frequency between the short and long crack work reported here (10+50 Hz), coupled with the relatively un-reactive testing environment, was not thought to influence propagation behaviour significantly, especially in view of the good equivalence of the short and long crack lines in figure 6.2 above the point of convergence.

#### 6.4.2 The transition from short to long crack growth

The point of convergence of the short and long crack lines in figure 6.2 is of particular importance to the engineer, as it indicates the stress intensity factor range above which it can be considered 'safe' to use conventional LEFM characterisations in design. However in using this data one may have to assume that cracks longer than the crack depth at the point of convergence are already present in the material.

Such a design philosophy is undesirable for critical aerospace applications where strict weight restrictions are imposed. Unfortunately, it is in this type of high stress application where problems associated with short cracks may arise.

In figure 6.2 the point of convergence for both 7010 OAl and UA occurs by a  $\Delta K \sim 9.0 \text{ MPa}\sqrt{\text{m}}$ , corresponding to a crack depth of approximately 400  $\mu\text{m}$  for the short cracks. For cracks greater than this length almost continuous growth is observed. Both de Lange (147) and Taylor and Knott (151) have indicated, for a variety of materials with different grain sizes, that uninterrupted growth occurred after cracks reached approximately 10 X grain size (d). If the average grain size in the ST direction of 7010 is assumed to be approximately 20  $\mu\text{m}$ , reasonable agreement with these studies is seen. These observations however, are based purely on microstructural findings and therefore do not consider the micromechanical aspects of short crack growth.

Other characterisations of the short : long crack transition are based on the size of the plastic zone size ahead of the crack tip. Lankford (180) for example has predicted that the transition should occur when the maximum plastic zone size ( $r_{\text{max}}$ ) equals the microstructural dimension. If plane strain conditions are experienced at the crack tip of the deepest point of a crack, the  $\Delta K$  of which the short and long, through thickness crack lines should merge can be obtained from table 6.1.

Comparison of the various equations describing the maximum plastic zone size (equations 6.2, 6.4 and 6.5) indicates that the observed point of merger for 7010 OA1 and UA is best described by Irwin's calculations (equation 6.2), i.e.  $8.7 \text{ MPa}\sqrt{\text{m}}$ .

The equivalence of the long and short crack data above the point where they should theoretically merge is not exact. The choice of K solution, the effect of crack shape and specimen thickness considerations can all influence the relative positioning of the data and thus make comparisons more difficult.

#### 6.5 EFFECT OF GRAIN ORIENTATION ON SHORT CRACK BEHAVIOUR

The consistently faster propagation rates reported for semi-circular cracks up to approximately 100  $\mu\text{m}$  deep growing in the LT direction compared to those growing in the LS direction (figure 5.11a and b) can be partially explained by considering arguments based on grain size effects. If the effective grain size is regarded as the grain size in the direction of growth at the deepest point of the crack (i.e. a, figure 5.10), the LT cracks would be expected to exhibit inferior short crack propagation behaviour due to their larger effective grain size. The anisotropic microstructure (figure 4.2b and schematically figure 5.9) results in an effective grain size in the LT direction approximately twice that in the LS direction.

Studies of the effect of grain size on short crack behaviour (166-169, 172, 47) argue that the detrimental effect of increasing the grain size is a result of less frequent crack tip interactions with grain boundaries.

The whole issue of grain size effects is further complicated for 7010, as here surface crack behaviour is being observed and assumed to describe conditions at the deepest point of the crack. This premise may be justified for equiaxed microstructures, however, the anisotropic nature of the 7010 microstructure may make such an assumption invalid. As had been discussed previously however, surface observations have revealed that deceleration and crack tip deflection can occur away from grain boundaries, suggesting that surface crack behaviour is affected by subsurface crack tip : microstructural interactions. Similar observations have been made by others (148, 149, 172), though the fact remains that in attempting to relate surface crack measurements to the behaviour at the deepest point of the crack, actual crack tip effects are somewhat obscured.

For microstructurally short cracks, grain configuration will be important in determining crack shape. The grain shape encountered by cracks growing in the LT direction may encourage growth into the specimen interior while inhibiting a propagation at the surface, due to the greater density of grain boundaries. Such a hypothesis would lead away from a semi-circular crack shape to one with a higher a/c ratio and may cause further disparity between the data for LS and LT cracks in figure 5.11. This effect of crack shape is discussed in detail in Chapter 10.

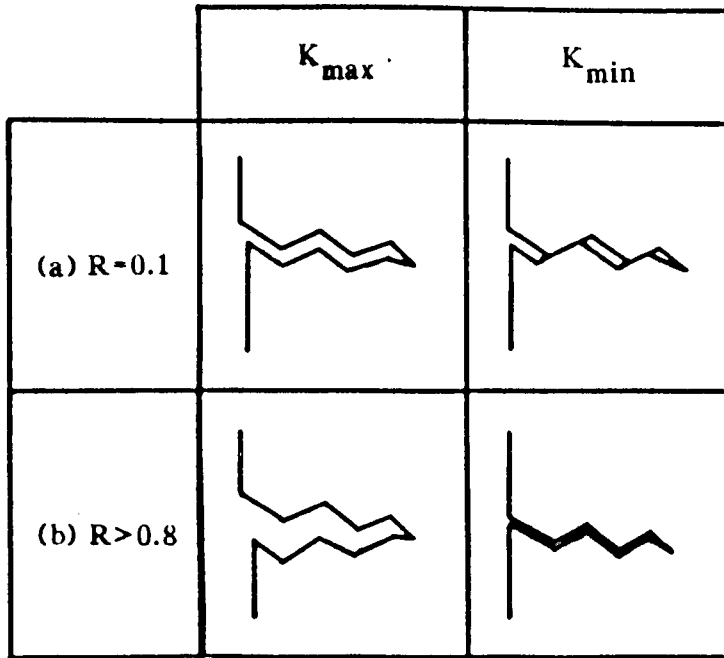
The implications from the two different R - ratio short crack tests (figure 5.12) are that, in a similar way to long, through thickness cracks, an increase in R - ratio increases fatigue crack propagation rates of short cracks. This observation may be expected for 'long' short cracks, greater than approximately 200  $\mu\text{m}$  deep, where propagation is more uniform and the effects of microstructure are less pronounced. For microstructurally short cracks,  $<200 \mu\text{m}$  deep, however, this behaviour is slightly more surprising if it is assumed that these cracks are effectively growing under closure free conditions. as has been suggested by Brown et al (47). Similar behaviour has been reported by Gerdes et al (166) who studied high and low R - ratio short crack behaviour in a binary  $\alpha$  titanium alloy (Ti-8.6Al). Their results were used later (180) to show that closure effects were still important for microstructurally short cracks. It is interesting to note that, as with Gerdes et al's results (166), a better correlation between the two R - ratios is obtained when compared in terms of  $K_{\text{max}}$  instead of  $\Delta K$ . (figure 6.3). More data at a higher R - ratio is required to substantiate this correlation, however, such data is difficult to obtain for this alloy under these testing conditions. To achieve initiation on a smooth specimen surface necessitates a large stress range which may require cycling with  $\sigma_{\text{max}}$  greater than the yield stress of the material for high R - ratio tests.

The effect of varying the maximum tensile stress whilst keeping the R - ratio constant at 0.1 is shown in figure 5.13 for 7010 OAl. The figure indicates that little difference in propagation behaviour is apparent considering the degree of scatter associated with this type of testing over the range of  $\Delta K$  studied. This implies that LEFM can be applied to obtain base data for an engineering application, if a suitable K solution is employed, even though in theory the conditions for use are violated. As a consequence of the experimental scatter associated with short crack data, however, the worst possible situation must be considered from a design standpoint. Furthermore, data for the cracks subject to  $\sigma_{\max} = 225 \text{ MPa}$  were not collected below crack depths of approximately  $50 \mu\text{m}$ . It is in this region that microstructural effects will be most apparent and where changes in  $\sigma_{\max}$  may have the greatest effect on short crack propagation behaviour.

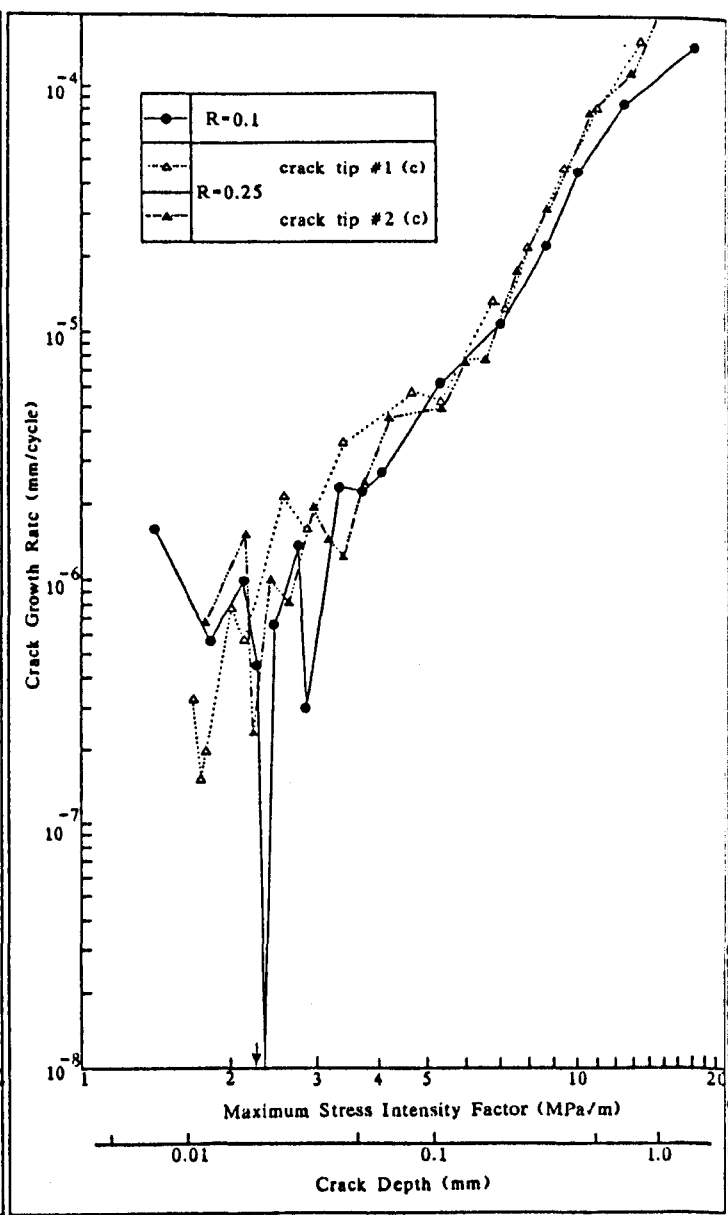
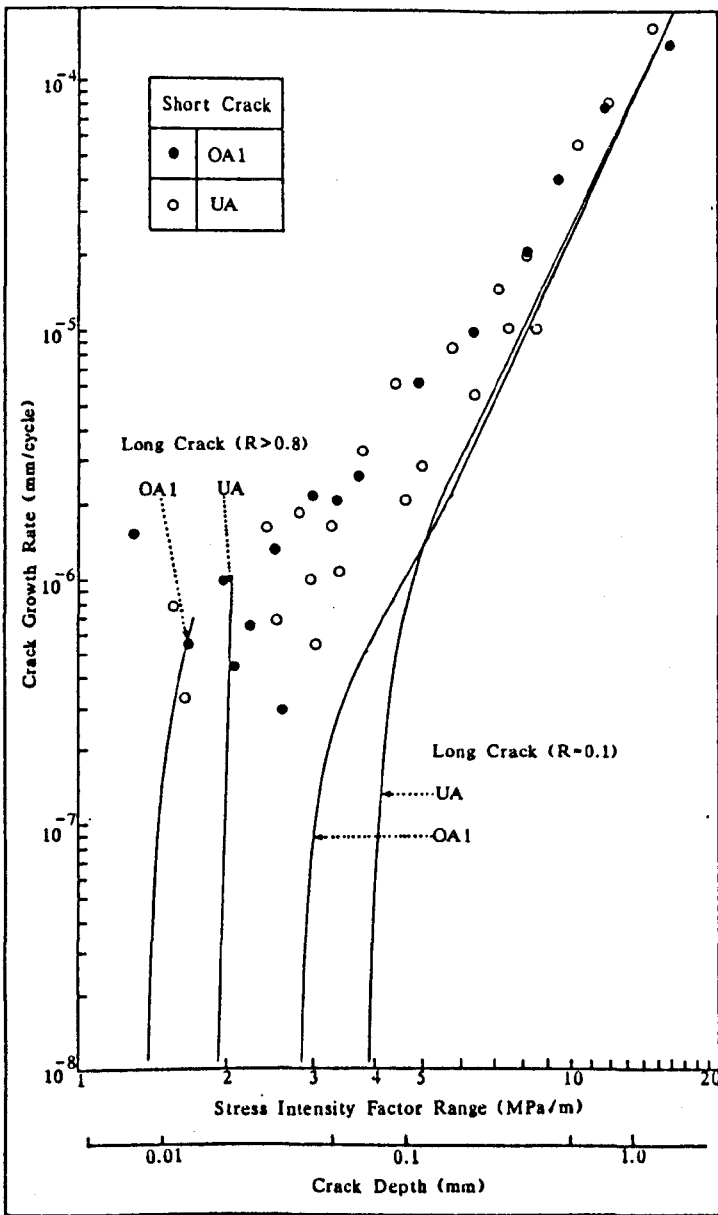
Microstructure	Average grain size ( $\mu\text{m}$ )	0.2% proof stress ( $\sigma_Y$ ) (MPa)	$\Delta K_T$ observed (MPa $\sqrt{\text{m}}$ )	$\Delta K$ calculated (MPa $\sqrt{\text{m}}$ )					
				$\Delta K_{T1}$	$\Delta K_{T2}$	$\Delta K_{T3}$	$\Delta K_{T4}$	$\Delta K_{T5}$	$\Delta K_{T6}$
7010 UA	20	495	7.8	8.7	19.2	5.5	12.2	2.5	5.3
7010 OA1	20	495	4.5	8.7	19.2	5.5	12.2	2.4	5.3
7010 OA2	20	425	5.8	7.4	16.3	4.7	10.3	2.0	4.4
2014 UA	25	425	6.4	8.4	18.5	5.3	11.7	2.3	5.1
2014 OA	25	425	4.4	8.4	18.5	5.3	11.7	2.3	5.1

TABLE 6.1 Calculations for  $\Delta K$  at the transition from intermittent to continuous, uninterrupted short crack growth ( $\Delta K_T$ ) based on the size of the plastic zone ahead of the crack tip.

$\Delta K_{T1}$	(equation 6.2)	$r_{\text{max}} = 0.053 \left[ \frac{K_{\text{max}}}{\sigma_Y} \right]^2$	$\Delta K_{T2}$	(equation 6.3)	$r_{\text{rpz}} = 0.053 \left[ \frac{\Delta K}{2\sigma_Y} \right]^2$
$\Delta K_{T3}$	(equation 6.4)	$r_{\text{max}} = 0.132 \left[ \frac{K_{\text{max}}}{\sigma_Y} \right]^2$	$\Delta K_{T4}$	(equation 6.1)	$r_{\text{rpz}} = 0.132 \left[ \frac{\Delta K}{2\sigma_Y} \right]^2$
$\Delta K_{T5}$	(equation 6.5)	$r_{\text{max}} = 0.7 \left[ \frac{K_{\text{max}}}{\sigma_Y} \right]^2$	$\Delta K_{T6}$	(equation 6.6)	$r_{\text{rpz}} = 0.7 \left[ \frac{\Delta K}{2\sigma_Y} \right]^2$



6.1 Schematic illustration of crack faces for long, through thickness cracks at  $K_{max}$  and  $K_{min}$   
 (a)  $R = 0.1$ , (b) constant  $K_{max}$  testing.



6.2  $da/dN$  vs  $\Delta K$  and a diagram comparing long and short crack growth of 7010 OA1 and UA.

6.3  $da/dN$  vs  $K_{max}$  for short cracks in 7010 OA1 at  $R = 0.1$  and  $R = 0.25$

## CHAPTER 7

### TITANIUM ALLOYS - MATERIALS

#### 7.1 INTRODUCTION

The demand from the aerospace industry for materials with good specific strength has been the stimulus for titanium alloy development in recent years. Apart from this excellent strength : weight ratio (density =  $4.51 \text{ g/cm}^3$ ), these alloys possess a number of other attractive properties to the aerospace design engineer. These include good corrosion resistance and creep resistance up to about  $600^\circ\text{C}$  in certain alloys. A limiting factor however, is their high fabrication costs relative to alternative materials. These arise from the sophisticated melting and fabrication techniques required and because scrap produced during manufacture can not be readily recycled.

This chapter considers the metallurgy of titanium and it's alloys and includes a brief resumé of the development of the alloys involved in this study. Finally, a micro-structural analysis is presented for the alloys in their heat treatment conditions for fatigue testing.

Pure titanium exists as its hexagonal close packed,  $\alpha$  phase up to 882°C. At this temperature it undergoes an allotropic phase transformation to  $\beta$  (body centre cubic), which remains stable up to the melting point at  $1668 \pm 5^\circ\text{C}$ . Alloying elements are characterised by their ability to stabilize either the  $\alpha$  or  $\beta$  phases and to change the size and extent of the  $(\alpha+\beta)$ , phase regions. Commercial alloys are classified as either  $\alpha$ ,  $(\alpha+\beta)$ , near  $\alpha$ , or  $\beta$  alloys depending on the predominant phase present and ultimately on the alloying additions (222-224). The complicated phase diagrams that result are considerably simplified by referring to pseudo-binary equilibrium diagrams which show the effect of type of stabilizer on the stable phases. Figure 7.1 schematically shows the three types of pseudo-binary phase diagrams that exist.

Elements that dissolve preferentially in the  $\alpha$  phase and so raise the  $\alpha+\beta$  transformation temperature ( $\beta$  transus), are known as  $\alpha$  stabilizers. Al, O, N and C are the predominant elements in this group. Figure 7.1a shows the pseudo-binary phase diagram for this type of addition. The  $\alpha_2$  phase is  $\text{Ti}_3\text{Al}$ . Some elements, such as Sn, Zr and Si, also strengthen the  $\alpha$  phase, but are equally soluble in both  $\alpha$  and  $\beta$  phases and therefore do not appreciably alter the  $\beta$  transus temperature.

The most notable  $\beta$ -isomorphous additions are V, Mo and W. These elements have limited  $\alpha$  solubility and reduce the  $\beta$  transus temperature with increasing concentration, widening the  $(\alpha+\beta)$  field. (Figure 7.1b). Mo and W have the most marked effect, though due to its high density, tungsten is rarely used as it can lead to problems in alloy fabrication. Vanadium is also a popular addition, although it is less effective at high temperatures so making it a less attractive addition to modern, high temperature, creep resistant alloys.

The final group of elements, called  $\beta$ -eutectoid stabilizers, include Cr, Fe, Mn, Cu and H. These elements reduce the  $\beta$  transus temperature through encouraging the formation of a eutectoid (figure 7.1c). They also have very limited solubility in the  $\alpha$  phase. Eutectoid reactions are usually too slow for substantial strengthening to occur in commercial alloys, however in certain systems, usually those containing copper, the kinetics of  $\beta$  phase decomposition by the eutectoid are sufficiently fast to allow intermediate compound formation (e.g.  $\text{TiCu}_2$ ) and improved mechanical properties result.

It is the  $(\alpha+\beta)$  alloys, like IMI 318 (Ti-6Al-4V) and IMI 550 (Ti-4Al-4Mo-2Sn-0.5Si) and more recently the near  $\alpha$ , high temperature creep resistant alloys that are, at present, the most used in the aerospace industry. Commonly used heat treatments to further improved mechanical properties of IMI 318 and IMI 550 are mill annealing and  $\beta$ -annealing techniques.

Mill annealing provides stress relief and results in the formation of an equiaxed primary  $\alpha$  and transformed  $\beta$  microstructure. The primary  $\alpha$  ( $\alpha_p$ ) content in the final structure is dictated to the Lever rule of mixtures. Often a second (duplex) anneal is given, causing further partitioning of alloying additions between the  $\alpha$  and  $\beta$  phases, enriching the  $\beta$  phase to give increased alloy stability during high temperature operations.

In  $\beta$ -annealing, slow cooling from above the  $\beta$  transus temperature causes the transformation from  $\beta$  to  $\alpha$ , which form as Widmanstätten laths. The final structure is comprised of Widmanstätten laths, delineated by retained  $\beta$ . The latter phase is rich in  $\beta$ -stabilizing elements as a result of the rapid diffusion of these elements in front of the migrating interface. The thickness and continuity of this phase around the  $\alpha$  laths is dependent on the  $\beta$ -stabilizer concentration and the cooling rate. Typically it is a continuous layer, 0.2  $\mu\text{m}$  thick. The cooling rate also dictates the size, shape and relative orientations of the  $\alpha$  laths. Slow cooling, particularly in alloys with high  $\beta$ -transus temperatures, causes the Widmanstätten  $\alpha$  to form as large colonies or packets of parallel sided platelets. Each colony appears to nucleate at  $\alpha$  at the prior  $\beta$  grain boundary. In contrast, faster cooling rates result in microstructures consisting of small colonies or packets, with individual, Widmanstätten laths misorientated with respect to each other. These are referred to as 'basketweave' structures. Nucleation of the transformed  $\beta$  is independent of the  $\alpha$  at prior  $\beta$  grain boundaries in this case.

### 7.3            TEXTURE

Hexagonal close packed metals, including  $\alpha$  titanium, exhibit some degree of anisotropy due to their crystallographic morphologies. The control of preferred crystallographic orientations in titanium alloys can lead to improved mechanical properties (138, 141, 225). In the  $\alpha$  titanium unit cell (figure 7.2), three planes are available for slip, the basal plane (0001), the prism plane (10 $\bar{1}$ 0) and the pyramidal plane (10 $\bar{1}$ 1). There is only one major slip direction,  $\langle 11\bar{2}0 \rangle$ , however and hence if deformation is to occur along the c-axis slip must take place along a different direction, usually  $\langle 11\bar{2}3 \rangle$ , which is more difficult. Bowen (141) for example, found that variations in texture in Ti-6Al-4V bar material, caused by temperature gradients or inhomogeneous working, tended to orientate the basal planes normal to the rolling direction. Bowen (141) showed that mechanical properties in this direction, the LT direction, were significantly better than in either the ST or L directions. There was however, a reduction the fatigue life in the LT direction, which was attributed to the lower Poisson's ratio in this direction, thus resulting in higher strains normal to the stress axis.

In a later study, Bowen (226), monitoring the changes in texture with heat treatment temperature, reported that some of the original texture was maintained virtually up to the  $\beta$  transus temperature. At higher temperatures a complete loss in the original texture and grain growth was observed.

If the subsequent cooling from the heat treatment temperature was slow enough however, the  $\beta \rightarrow \alpha$  transformation that occurred could be identical to the  $\alpha \rightarrow \beta$  transformation on heating and a similar texture to the pre-heat treated material resulted. At faster cooling rates this 'memory' effect disappeared and new crystallographic orientation variations appeared.

#### 7.4 ALLOY DEVELOPMENT

The emergence of commercial ( $\alpha+\beta$ ) alloys in the mid 1950's came from previous development of both  $\alpha$  and  $\beta$  alloys. Ogden et al (227) had shown that the addition of  $\alpha$  stabilizers (e.g. Al) to titanium produced solid solution strengthening. The further increase in  $\alpha$ -stabilizer concentration however, led to fabrication difficulties and embrittlement. The latter was caused by ordering and  $\alpha_2$ (Ti<sub>3</sub>Al) formation (228, 229). Furthermore, other elements apart from aluminium were found to promote embrittlement when present in large enough quantities. Rosenberg (230) developed an empirical formula which predicted the maximum, combined alloying addition, in weight percent, to avoid ordering;

$$\text{Al} + \frac{1}{3} \text{Sn} + \frac{1}{6} \text{Zr} + 10(\text{O} + \text{C} + \text{N}) \leq 9.$$

Concurrent research into  $\beta$  alloys was centred around the premise that strengthening of the  $\beta$  phase could be obtained by additions of elements such as Cr, Mn, Fe and Cu. The formation of intermetallics, such as TiMn and TiCr<sub>2</sub>, and the  $\omega$  phase however, caused embrittlement and applications of these alloys were limited.

With the development of ( $\alpha + \beta$ ) alloys, a combination of the strengthening characteristics of both  $\alpha$  and  $\beta$  stabilisers resulted in alloys with both good strength and creep resistance at intermediate temperatures. The addition of  $\beta$  stabilizers also allowed substantial amounts of  $\beta$  to be retained on quenching from both the ( $\alpha + \beta$ ) and  $\beta$  phase fields. The introduction of Ti-2Al-2Mn (IMI 315) as a gas turbine compressor blade material in Rolls-Royce engines in 1953, heralded the introduction of commercial ( $\alpha + \beta$ ) alloys. The alloy Ti-6Al-4V (IMI 318) was being developed at the same time in the U.S.A. and has since become the most widely used, general purpose alloy in the aerospace industry. (231, 232).

The need for an alloy with higher temperature capabilities than Ti-6Al-4V (IMI 318) led to the development of Hylite 50 by Jessop-Saville Limited (233), which was later designated IMI 550 by IMI (234). The composition, Ti-4Al-4Mo-2Sn-0.5Si, comprised of aluminium and tin to strengthen the  $\alpha$  phase, with the tin also improving forgeability. Molybdenum was chosen as the  $\beta$ -stabilizer, allowing the retention of strength at higher temperatures than Ti-6Al-4V and improving the forgeability of heat treatment response. The silicon addition was found to improve high temperature creep resistance and this was initially attributed to the precipitation of fine silicides (233). More recent studies (229, 235, 236) however, have suggested that silicon stays in solid solution in  $\alpha$ , even though it's stability is low, and that the beneficial properties arise from a strain ageing effect from a silicon-interstitial atom interactions.

Further silicon additions were found to precipitate as silicides ( $Ti_5Si_3$ ) during ageing or high temperature operation, resulting in a reduction in creep resistance.

## 7.5 MICROSTRUCTURAL EVALUATION

For the two ( $\alpha + \beta$ ) alloys considered in this study, Ti-6Al-4V (IMI 318) and Ti-4Al-4Mo-2Sn-0.5Si (IMI 550), a total of seven microstructural variations were examined. The heat treatment routes used to produce these microstructures are described in table 7.1, along with detailed chemical compositions of the materials. Throughout this study the various microstructures will be referred to by the designations shown in table 7.2 (i.e. 318A+318E for Ti-6Al-4V and 550A and 550B for Ti-4Al-4Mo-2Sn-0.5Si). Excluding the as-received conditions, all heat treatments of specimens were carried out in encapsulated silica tubes. These were evacuated and back filled with argon, to atmospheric pressure, prior to sealing. This procedure prevented oxygen diffusion into specimen surfaces during heat treatment and hence ensured a homogeneous microstructure for mechanical testing.

Table 7.3 contains data, for all seven microstructures, on grain sizes, phase proportions and mechanical properties. The grain sizes were measured by the linear intercept method and the phase proportions using an image analyser technique. Mechanical property evaluation is described in Chapter 3.

Each microstructure is now described individually and reference to figure 7.3 should be made in each case.

(i) 318A (figure 7.3a). This was the as-received microstructure, which had previously been mill annealed (700°C + air cool). The microstructure consisted of a dual,  $\alpha_p$  and transformed  $\beta$  structure. Table 7.3 shows that the  $\alpha_p$  grain size was approximately 50% larger than that of the transformed product and a higher proportion of the former morphology was present. It was also apparent from studying this condition that a microstructural texture was present. Although this can not be seen in figure 7.3a, it can be clearly noted in figure 8.5d, which shows the path of a short crack through 318A.

(ii) 318B (figure 7.3b). Annealing high in the ( $\alpha + \beta$ ) field (950°C) followed by a very slow furnace cool (9 hours to cool from 950°C to 20°C), produce the microstructure shown in the figure. Primary  $\alpha$  grains were slightly enlarged compared to 318A and transformed  $\beta$  grains considerably smaller. The slow cooling rate allowed more of the  $\beta$  phase present at the annealing temperature, to transform to primary  $\alpha$ , leaving little transformed  $\beta$  in the final structure. The phase surrounding the  $\alpha_p$  grains is expected to be rich in  $\beta$  stabilizing elements.

(iii) 318C (figure 7.3c). A faster air cooling from 950°C resulted in a microstructure consisting of fairly equiaxed  $\alpha_p$  grains in a transformed  $\beta$  matrix. Primary  $\alpha$  grain sizes were of similar size to those in 318A, however the faster cooling rate preserved large areas of transformed  $\beta$ , on average 15.7  $\mu\text{m}$  in diameter.

(iv) 318D (figure 7.3e). Slow cooling from above the  $\beta$  transus temperature produced an aligned Widmanstätten microstructure. The fine transformed  $\beta$  laths, approximately 1  $\mu\text{m}$  across, form in aligned colonies and packets, about 65  $\mu\text{m}$  in size. These, in turn, are contained within prior  $\beta$  grains, about 350  $\mu\text{m}$  in diameter. A continuous layer of  $\alpha$ , typically 10  $\mu\text{m}$  thick exists at these prior  $\beta$  grain boundaries.

(v) 318E (figure 7.3f). In contrast to 318D, a faster cooling rate from in the  $\beta$  phase field, resulted in a microstructure consisting of the fine Widmanstätten  $\alpha$  laths, formed in a basketweave structure. Within each prior  $\beta$  grain, these laths were aligned in one of three orientations with respect to each other. Prior  $\beta$  grains were of identical size to 318E (~ 350  $\mu\text{m}$ ), however, no colony or packet boundaries were present.

(vi) 550A (figure 7.3d). The as-received Ti-4Al-4Mo-2Sn-0.5Si plate was supplied in a fully heat treated form (table 7.1). The  $\alpha_p$  and transformed  $\beta$  grain structure consisted of grains of approximately equal size, with a slightly higher proportion of the latter product present (table 7.2).

(vii) 550B (figure 7.3g). A similar heat treatment to that given to 318D produced a comparable microstructure. Widmanstätten  $\alpha$  laths formed colonies and packets of similarly aligned platelets. The average packet size of 161  $\mu\text{m}$  was considerably larger than for 318D, though prior  $\beta$  grain sizes were very similar.

ALLOY	Al	V	Mo	Sn	Si	Fe	C	O	N	H	Ti
IMI 318	6.43	4.02	-	-	-	0.19	0.01	0.205	0.0075	0.002	REM
IMI 550	4.13	-	3.98	2.0	0.54	0.03	0.03	0.22	0.0025	<0.006	REM

TABLE 7.1 Alloy compositions (WT%) of IMI 318 & IMI 550  
(Analysis carried out by IMI Titanium)

Microstructure Designation	Heat Treatment Temp. (°C)	Heat Treatment Time (Hours)	Cooling Medium
318A*	700		Air Cool
318B	950	1	Furnace Cool
318C	950	1	Air Cool
318D	1100	1	Furnace Cool
318E	1100	1	Air Cool
550A*	900		Air Cool #
550B	1100	1	Furnace Cool

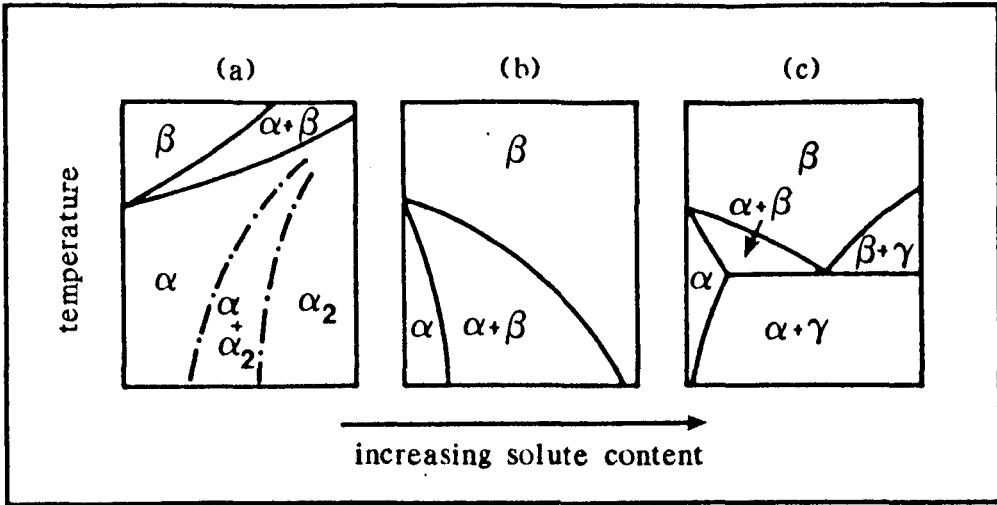
\* Material in as received condition  
# + 24 Hours at 500°C and air cool

TABLE 7.2 Material designation & heat treatments for  
IMI 318 and IMI 550

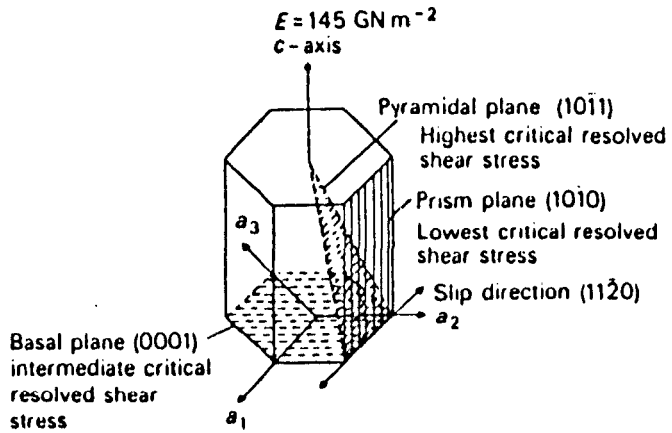
MICROSTRUCTURE	GRAIN SIZES						HARDNESS & MICRO HARDNESS					MECHANICAL PROPERTIES		
	PRIMARY $\alpha$		TRANSFORMED $\beta$		PRIOR $\beta$ GRAIN SIZE ( $\mu\text{m}$ )	AVERAGE COLONY SIZE ( $\mu\text{m}$ )	HARDNESS (30 Kg LOAD) (VHN)	MICROHARDNESS (50g load)(VHn)				0.2% PROOF STRESS (MPa)	UTS (MPa)	% ELONGATION
	GRAIN SIZE ( $\mu\text{m}$ )	%	GRAIN SIZE ( $\mu\text{m}$ )	%				PRIMARY $\alpha$	TRANSFORM $\beta$	$\alpha$ LATHS	GRAIN BOUNDARY $\alpha$			
318A	6.0	61	4.2	39			323	401	430			948	1011	14.6
318B	8.6	70	1.8	30			323	401				925	983	16.4
318C	5.9	30	15.7	70			319	350	394			900	1026	11.9
318D					350	65	318			429	521	976	1049	11.4
318E					350		325			403		887	1014	5.0
550A	5.9	45	7.0	55			357	439	387			989*	1130*	16.0*
550B					337	161	339			417				

\* IMI TITANIUM RELEASE DATA

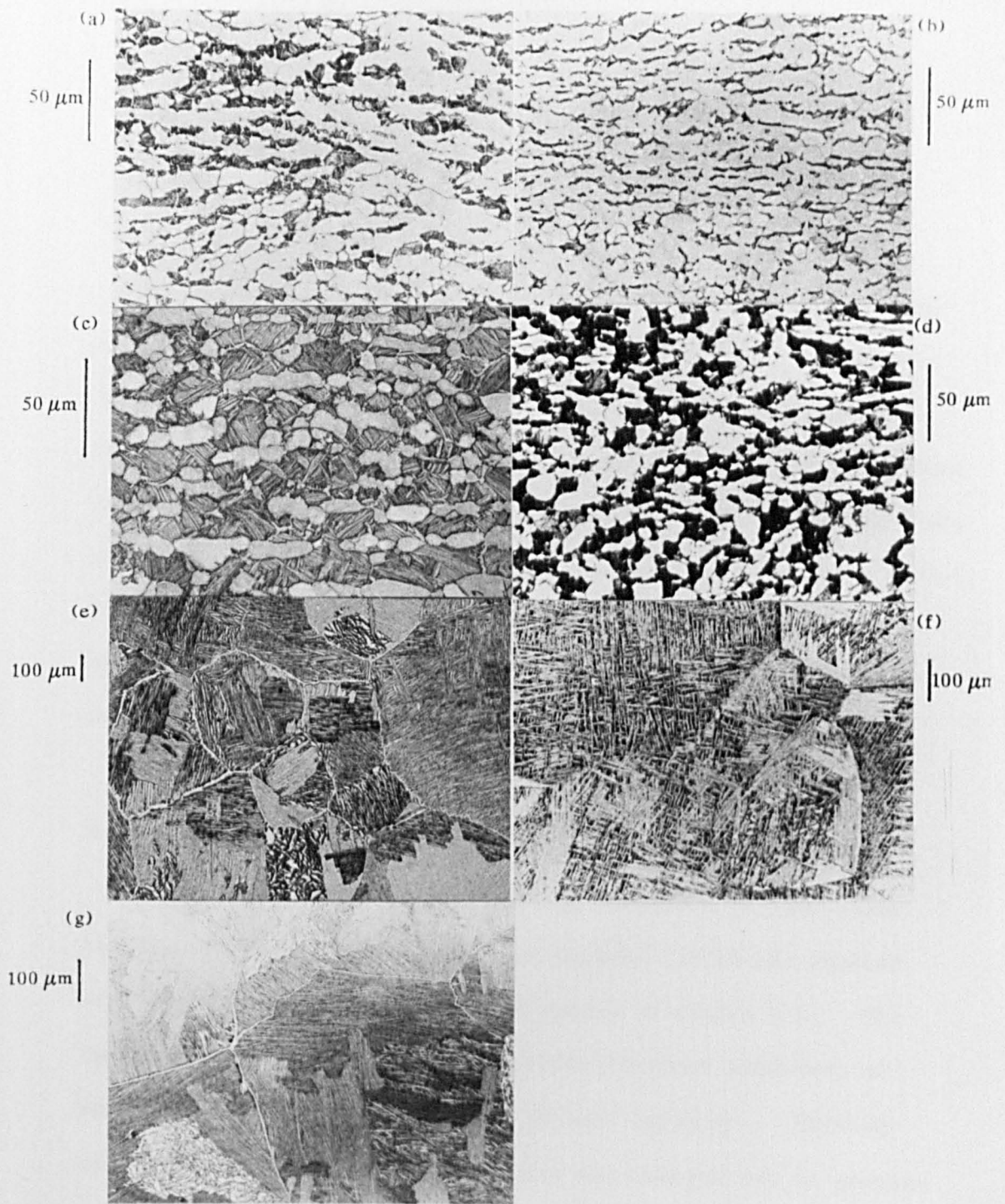
TABLE 7.3 GRAIN SIZES, PHASE PROPORTIONS & MECHANICAL PROPERTIES OF MATERIALS STUDIED



7.1 Pseudo-binary phase diagrams for titanium alloys.  
 (a)  $\alpha$ -stabilizers, (b)  $\beta$ -isomorphous type and  
 (c)  $\beta$ -eutectoid type



7.2  $\alpha$ -Titanium unit cell



7.3 Optical micrograph of heat treated titanium alloys.

(a) 318A, (b) 318B, (c) 318C, (d) 550A

(e) 318D, (f) 318E, (g) 550B.

## CHAPTER 8

### TITANIUM ALLOYS - RESULTS

#### 8.1 INTRODUCTION

The seven different ageing variants investigated for the two titanium alloys, IMI 318 and IMI 550, described in Chapter 7 can be broadly divided into two categories - those resulting from an  $\alpha + \beta$  heat treatment (318A, 318B, 318C, 550A) and those from a heat treatment above the  $\beta$  transus (318D, 318E, and 550B). For the purpose of much of this chapter it is useful to discuss the behaviour in terms of these two microstructural groups. For the long crack behaviour however, only one microstructure from each category was examined.

#### 8.2 LONG, THROUGH THICKNESS CRACK BEHAVIOUR

Results from long, through thickness fatigue crack testing of IMI 318 in the two heat treated conditions studied are shown in terms of  $da/dN$  vs  $\Delta K$  curves in figure 8.1. The two conditions were (i) 318A (recrystallisation annealed, as-received material) and (ii) 318D ( $\beta$ -heat treated). Testing of these two extreme microstructures was carried out to provide reference data for comparison with the short crack results. One specimen was tested for the  $\beta$ -annealed material (318D) and emphasis was placed on obtaining data in the near-threshold region. Consequently no data were collected above crack growth rates of  $2 \times 10^{-6}$  mm/cycle.

For 318A, data were recorded through a range of growth rates from  $10^{-8}$  to  $10^{-4}$  mm/cycle from a number of tests. The data from individual specimens showed good consistency and no distinction is made between them on figure 8.1.

Threshold stress intensity values for 318A and 318D were determined as  $4.5 \text{ MPa}\sqrt{\text{m}}$  and  $7.5 \text{ MPa}\sqrt{\text{m}}$  respectively. Crack growth rates were significantly lower at corresponding  $\Delta K$ s over the range of crack growth rates studied for the coarser  $\beta$  heat treated microstructure (318D). From the scanning electron micrographs taken in the near threshold region shown in figure 8.2, a marked difference in the fracture surfaces of 318A and 318D can be seen. For the  $\alpha_p +$  transformed  $\beta$  microstructure (318A) (figure 8.2a) fatigue fracture occurred on a fine scale and consisted mainly of slip band facets through the primary  $\alpha$  phase and mixed, occasionally, with a stepped fracture through the transformed  $\beta$  phase. Figure 8.2b shows that for 318D fracture occurred in an extremely coarse faceted manner through colonies and grains of the transformed  $\beta$  laths. In both cases at higher growth rates, the fracture surface became much flatter with respect to a plane perpendicular to the stress axis. An example for 318A is shown in figure 8.2c. Furthermore, the appearance of striations is evident in figure 8.2c.

### 8.3 SHORT FATIGUE CRACK BEHAVIOUR

#### 8.3.1 $\alpha + \beta$ heat treated microstructures

Figures 8.3a+d indicate the short crack behaviour of the four microstructures heat treated at temperatures below the  $\beta$  transus thereby resulting in two 'phase'  $\alpha_p$  and transformed  $\beta$  morphologies. Differences between the microstructures through changing the heat treatment temperature, include the primary  $\alpha$  volume fraction, the scale of the transformed  $\beta$  structure (plate width and colony size) and grain sizes. In addition 550A was of a different alloy composition.

The figures show short crack behaviour in terms of crack growth rate vs stress intensity factor range ( $\Delta K$ ) and crack depth ( $a$ ). In all cases an  $a/c$  ratio of 1.0 was assumed and the two crack tips of each crack were considered separately from the initiation site. As for the aluminium alloys (Chapter 5) it is thought that such an analysis highlights short crack behaviour. Further, data from only one crack for each microstructure is presented in order to maintain clarity in the figures. At least three cracks were examined for each condition and, while variations in the position and depth of the minima occurred, overall propagation characteristics were very similar in all cases. As with the results from the aluminium alloy fatigue testing (Chapter 5) individual data points have been connected to adjoining points. This has been done to try to clearly illustrate the data of each test, rather than to imply that crack growth was continuous and uninterrupted between the points.

Before studying the individual results in detail, the general short fatigue crack behaviour of all the  $\alpha + \beta$  processed morphologies will be considered. For all cracks studied initiation occurred along slip bands in primary  $\alpha$  grains or at  $\alpha_p/\alpha_p$  grain boundaries. Initial rapid propagation took place along these  $\alpha_p$  slip bands until a grain boundary was reached. Often this boundary was an  $\alpha_p$ /transformed  $\beta$  grain boundary and had the effect of rapidly decelerating growth. After a short period of incubation, growth continued in rapid manner once again until a further grain boundary, or lath boundary in some circumstances in transformed  $\beta$  grains, was encountered. Again a discontinuity in propagation rate occurred. Such behaviour was generally repeated until crack depths of between 100-200  $\mu\text{m}$  were attained. Subsequent growth was usually perpendicular to the stress axis and was no longer significantly affected by the grain structure. The crack path through each microstructure can be discerned from the fracture surfaces shown in figure 8.4. Each micrograph was taken close to the initiation site of the short crack. In each case, two modes of fracture can be identified, a faceted, transgranular fracture through the  $\alpha_p$  phase and a stepped fracture through transformed  $\beta$  laths or colonies.

#### 8.3.1.1 316A

For the as-received microstructure the short crack propagation behaviour is shown in figure 8.3a. In the subsequent results and discussion sections reference will be made to this data for comparison with other microstructures. To facilitate this, a transparency of figure 8.3a, with data from only one crack tip, can be found in Appendix 1 which can be laid on top of other figures.

Figure 8.3a reveals that up to crack depths of about 150  $\mu\text{m}$ , irregular growth persists, with the most discontinuous growth occurring at crack depths  $<50 \mu\text{m}$ . The two major interruptions in propagation (marked 1 & 2 in figure 8.3a) can be associated with microstructural features. This is shown clearly in figure 8.5, a set of micrographs following the development of this crack through its 'short crack' life. The numbers marked on figure 8.5c correspond to those on figure 8.3a and confirm that regions of transformed  $\beta$  are responsible for the temporary interruptions in propagation behaviour. The micrographs also give evidence of the path of crack propagation. Where possible the crack tips attempt to follow slip bands in the  $\alpha_p$  grains. Indeed, initiation is generally seen to occur along a developed slip band in a grain suitably orientated with respect to the stress axis. For this particular crack however, initiation has taken place preferentially along an  $\alpha_p/\alpha_p$  grain boundary. Growth continues in this manner of slip band cracking in  $\alpha_p$  grains and discontinuous growth across  $\alpha_p$ /transformed  $\beta$  grain boundaries up to crack depths in excess of 100  $\mu\text{m}$ . Figure 8.5d shows that even at these crack depths the crack path is not perpendicular to the stress axis, but appears to vary with the microstructural texture of the material.

Examination of the fracture surfaces near the initiation site (figure 8.4a) shows the type of fracture previously described, a crystallographic faceted fracture along slip bands in  $\alpha_p$  and a stepped, flat fracture through regions of transformed  $\beta$ .

At higher propagation rates and greater crack depths, a much smoother fracture surface results with fewer facets visible and fine striations present (figure 8.6).

#### 8.3.1.2 318B

Figure 8.3b shows a  $da/dN$  vs  $\Delta K$  and a plot for a short crack growing in 318B. Again two lines are illustrated depicting the growth of each surface crack tip away from the initiation site. Similar initiation and propagation behaviour was observed both in this microstructure and in 318A. In all three cracks studied, initiation occurred within an  $\alpha_p$  grain and growth was almost exclusively confined along slip bands within  $\alpha_p$  grains. Early growth was generally more regular than in 318A and by a crack depth of approximately 100  $\mu\text{m}$  the crack path was virtually perpendicular to the stress axis (figure 8.7). Fracture surfaces close to the initiation site (figure 8.4b) reinforce surface observations of a crack path mainly confined to the  $\alpha_p$  phase. The scanning electron micrograph reveals a fracture nearly completely faceted in nature.

#### 8.3.1.3 318C

The short crack growth behaviour of 318C is shown on a  $da/dN$   $\Delta K$  plot in figure 8.3c. Data from just one of the four cracks studied in this microstructure are shown. Again similar growth characteristics are exhibited to both 318A and 318B. A more detailed evaluation of this particular test can be made by referring to the crack history micrographs in figure 8.8.

For crack tip #1, figures 8.8a+c correspond to the position of the crack tip growing vertically upwards at each of the dips in propagation rate. The first dip, shown in figure 8.8a, occurred when the crack tip reached the end of the slip band in which the crack initiated. The slip bands ends at an  $\alpha_p$ /transformed  $\beta$  grain boundary. In the second figure (8.8b) the crack tip has again been halted, this time at the boundary between two individual laths in the transformed  $\beta$  grain. The third deceleration appears to be due to the crack tip being held up at the end of a slip band close to an  $\alpha_p$ /transformed  $\beta$  grain boundary in the next  $\alpha_p$  grain. Instead of reinitiating in the transformed  $\beta$  grain a number of cycles later however, the crack found an easier propagation path further back towards the initiation site and the original crack tip became dormant.

Figure 8.8 also shows that crack tip #2 initially found an easier path. It was able to run through 4  $\alpha_p$  grains before having to encounter a transformed  $\beta$  grain and hence the  $da/dN$  vs  $\Delta K$  curve (figure 8.3c) showed no major dips. The behaviour of both the top and bottom crack tips demonstrates that propagation through  $\alpha_p$  grains and regions of aligned transformed  $\beta$  laths occurred rapidly and only grain boundaries and certain lath and colony boundaries had the effect of interrupting growth.

The fracture surface near the initiation site (figure 8.4c) resembles those of 318A and 318B. The higher proportion of transformed  $\beta$  present in this microstructure can be seen by the increase in the amount of stepped fracture through colonies and laths.

#### 8.3.1.4     550A

Figure 8.3d shows a  $da/dN$   $\Delta K$  and a diagram for the two ends of a crack in the as-received IMI 550 microstructure (550A). In addition data reported in the literature for long, through thickness crack propagation in IMI 550 with the same heat treatment and testing conditions is shown for comparison (160). As for 318A, 318B and 318C minima are observed at short crack depths associated with the crack tips encountering regions of transformed  $\beta$ , however, these became less marked with increasing crack depth. It appears that the most effective barriers are those closest to the initiation site. An optical micrograph of the crack shown in figure 8.9a, reveals that after 230,400 cycles, when this replica was taken, the crack had a surface crack length of 345  $\mu\text{m}$ . The figures in the micrograph indicate the position of the crack tip at various stages in it's "short crack" life. Corresponding figures are shown on the  $da/dN$  vs  $\Delta K$  plot (figure 8.3d), indicating that the minima are associated with the crack tips encountering transformed  $\beta$  grain boundaries.

From figure 8.9b, it is also evident that initiation occurs from a suitably orientated slip band in a  $\alpha_p$  grain and that early growth follows the slip band to the edge of that grain. Once, through the first few transformed  $\beta$  grains, when the crack depth is only approximately 50  $\mu\text{m}$ , propagation is much more uniform and the crack path is only slightly influenced by the local microstructure.

### 8.3.2        $\beta$ heat treated microstructures

The  $da/dN$  vs  $\Delta K$  and  $a$  plots for the 3  $\beta$  heat treated microstructures (318D, 318E, 550B) are presented in figure 8.10. Heat treatments above the  $\beta$  transus produced a noticeable change in short crack behaviour, however initiation was generally still from slip bands in the  $\alpha$  phase, though this was now positioned along prior  $\beta$  grain boundaries. Crack propagation into adjoining colonies of transformed  $\beta$  laths was either very rapid or slow, depending on the relative crystallographic and microstructural orientations of the laths. Overall, propagation rates were approximately an order of magnitude higher than those for the  $\alpha + \beta$  heat treated microstructures at corresponding  $\Delta K$ s. Examination of fracture surfaces close to the initiation sites (figure 8.11) revealed striking differences when compared with those of the  $\alpha + \beta$  processed microstructures (figure 8.4). Fracture occurred on a very coarse scale with large, flat facets being formed on growth through colonies of  $\alpha$  laths.

#### 8.3.2.1        318D

The  $da/dN$  vs  $\Delta K$  and  $a$  plot for one crack tip of a short crack growing in the aligned, Widmanstätten 318D microstructure is shown in figure 8.10a. Due to the very erratic nature of propagation only one crack tip has been described in the figure so that a clearer view of the behaviour can be made. The propagation characteristics shown in figure 8.10a are typical of each crack tip of the eight cracks studied in this microstructure.

Two major differences to the  $\alpha + \beta$  heat treated microstructure can be identified. Firstly, average propagation rates are approximately an order of magnitude higher over the complete range of crack depths studied. Secondly, there is a continued occurrence of growth rate minima even at crack depths in excess of 1mm when an a/c ratio of 1.0 is considered.

Examination of replicas after the completion of testing revealed that, prior to crack initiation, deep slip bands of cracks formed across whole packets of  $\alpha$  laths within the first 5% of life. Examples of such slip band cracks are shown in figure 8.12. It appeared that the ends of these slip band cracks were pinned at colony or packet boundaries and no further growth occurred during the remaining 95% of the fatigue life.

Initiation of cracks which lead to failure occurred late in the lives of the specimens (> 90%). In all cases, cracks appeared in slip bands within the  $\alpha$  phase at prior  $\beta$  grain (PBG) boundaries (figure 8.13a). Subsequent growth into the Widmanstätten  $\alpha$  appeared to be either very fast where favourable slip band orientations were encountered, or slow or negligible in less favourably orientated microstructure. The resulting crack paths (figure 8.13b-e) were comprised of angled steps produced by cracking along slip bands. Generally the crack growth rate minima on the  $da/dN$  vs  $\Delta K$  and a plot (figure 8.10a) corresponded to the crack tip being positioned at the end of a slip band.

A period of incubation then occurred while the crack tip tried to reinitiation itself in a slip band in the adjoining colony or packet.

Later crack growth minima, at crack depths  $>100 \mu\text{m}$ , often arose in a slightly different manner. After the crack tip appeared to have stopped it re-emerged on the surface, a number of cycles later, away from the original crack tip and once again proceeded to propagate at a fast rate. The point marked "1" on figure 8.13e indicates a position where this happened. The material between the original, dormant crack tip and the reinitiated, growing crack tip was subsequently cracked. In other cases, crack branching occurred behind a stationary crack tip, as shown by position "2" in figure 8.13e. In this particular figure, the dominant crack tip is that growing towards the top right of the micrograph. The smaller crack growing vertically upwards was the sole crack before it branched, however, it had been stopped at some microstructural barrier for several thousand cycles.

Figure 8.13f shows the initiation facet produced by growth through the initial slip band in the grain boundary  $\alpha$ .

#### 8.3.2.2 318E

The short crack growth behaviour of one of the four cracks studied in the basketweave Widmanstätten microstructure (318E) is depicted in figure 8.10b. Again, as with 318D, relatively high propagation rates were recorded across the range of crack depths studied, though fewer growth rate minima were observed.

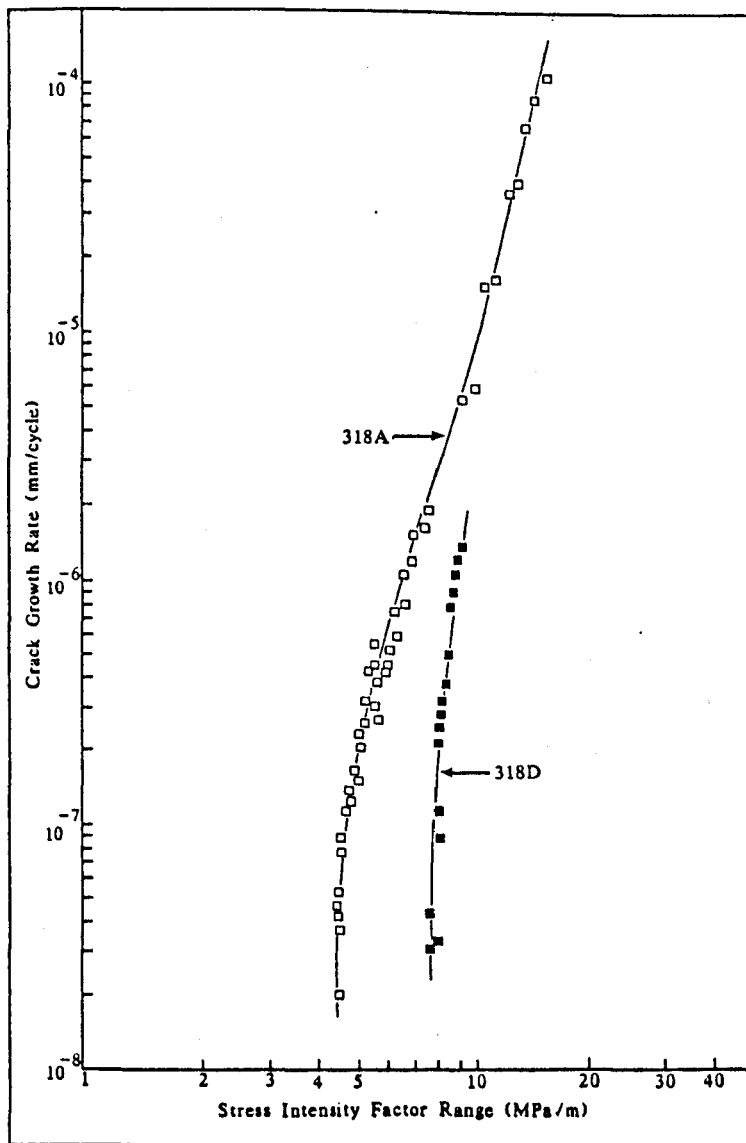
Major decelerations occurred for one crack tip between crack depths of about 50-100  $\mu\text{m}$ , the reasons for which can be seen with reference to figure 8.14 showing the crack in question at stages through its life. Figure 8.14b reveals that the top crack tip has branched in a similar way to that described for 318D. The repetition of this procedure three or four times resulted in the minima on figure 8.10b between 50-100  $\mu\text{m}$ . Figure 8.14a shows the crack at a fairly late stage in its life and indicates the growth perpendicular to the stress axis, which resulted in the regular growth characteristics shown for cracks greater than about 100  $\mu\text{m}$ .

For this microstructure, instead of initiation occurring in the  $\alpha$  phase at PBG boundaries, as for 318D, cracks were initiated within  $\alpha$  lath colonies. Figure 8.14c shows a relatively short crack (total surface length = 89  $\mu\text{m}$ ) where initiation seemed to have occurred close to the point marked "1" in the figure, within a single transformed  $\beta$  lath. As for 318D, initiation occurred late in the fatigue life (>90%). Furthermore, fine slip bands developed in the first 10% of life, reached across prior  $\beta$  grains where some alignment of the Widmanstätten laths occurred. Examples are shown in figure 8.14d. In all cases, one end of the slip bands were pinned at PBG boundaries and the other end within the basketweave, lath structure.

The appearance of short crack fracture surfaces (figure 8.11b) closely resembled those of 318D with large, flat facets produced by growth through Widmanstätten colonies. Also included in figure 8.10b are data for long, through thickness cracks taken from the literature for a similar microstructure ( $\beta$  quenched). (78).

#### 8.3.2.3    550B

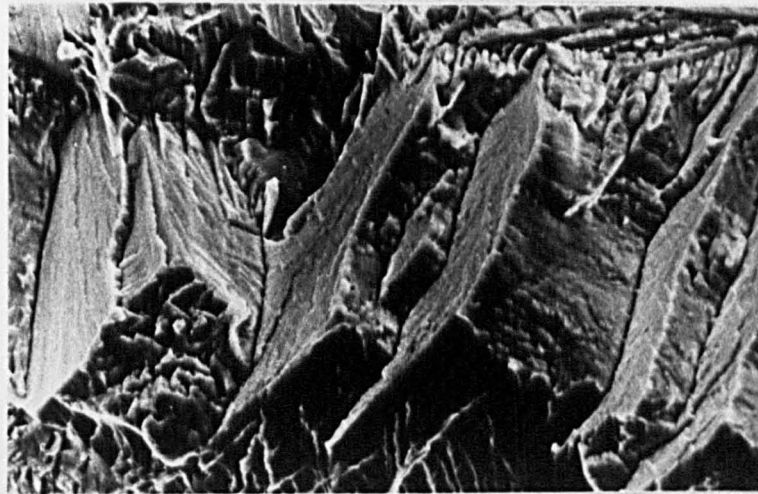
Figure 8.10c shows the short crack behaviour of one of the three cracks studied for the  $\beta$  heat treated IMI 550 microstructure in a  $da/dN$   $\Delta K$  and a plot. As for IMI 318, the effect of heat treatment above the  $\beta$  transus was to produce a significant deterioration in short crack propagation resistance. Initiation and propagation behaviour closely resembled that of 318D. Again slip band cracking occurred within the first 5% of fatigue life and quickly stretched across packets of  $\alpha$  laths until being pinned at packet boundaries (figure 8.15a). Initiation of the crack which lead to failure occurred in all cases late in life in the  $\alpha$  phase at PBG boundaries (figure 8.15b). Initial growth into the aligned Widmanstätten microstructure was rapid where favourably orientated laths were encountered. A noticeable difference to 318D however, was in the propagation characteristics of cracks  $> 50 \mu\text{m}$  in depth. For 550B, the cracks seemed to have less difficulty in passing through the local microstructure, leading to a slightly more uniform propagation behaviour.



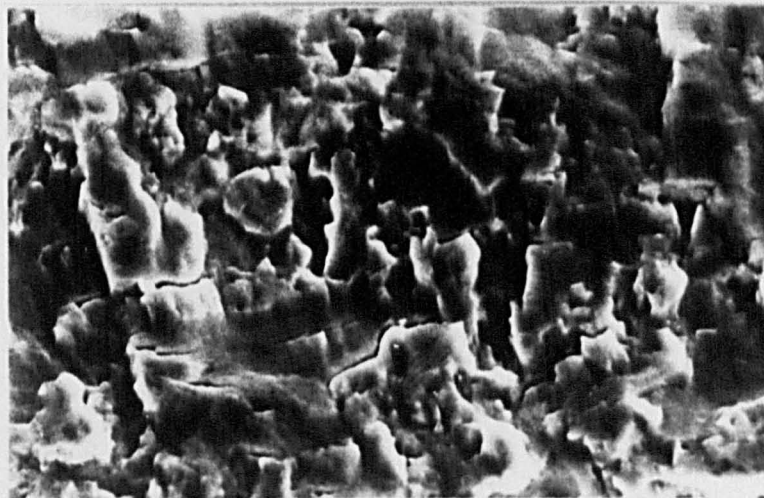
8.1  $da/dN$  vs  $\Delta K$  for long, through thickness cracks at  
 $R = 0.1$  for 318A and 318D



(a)  $10\ \mu\text{m}$



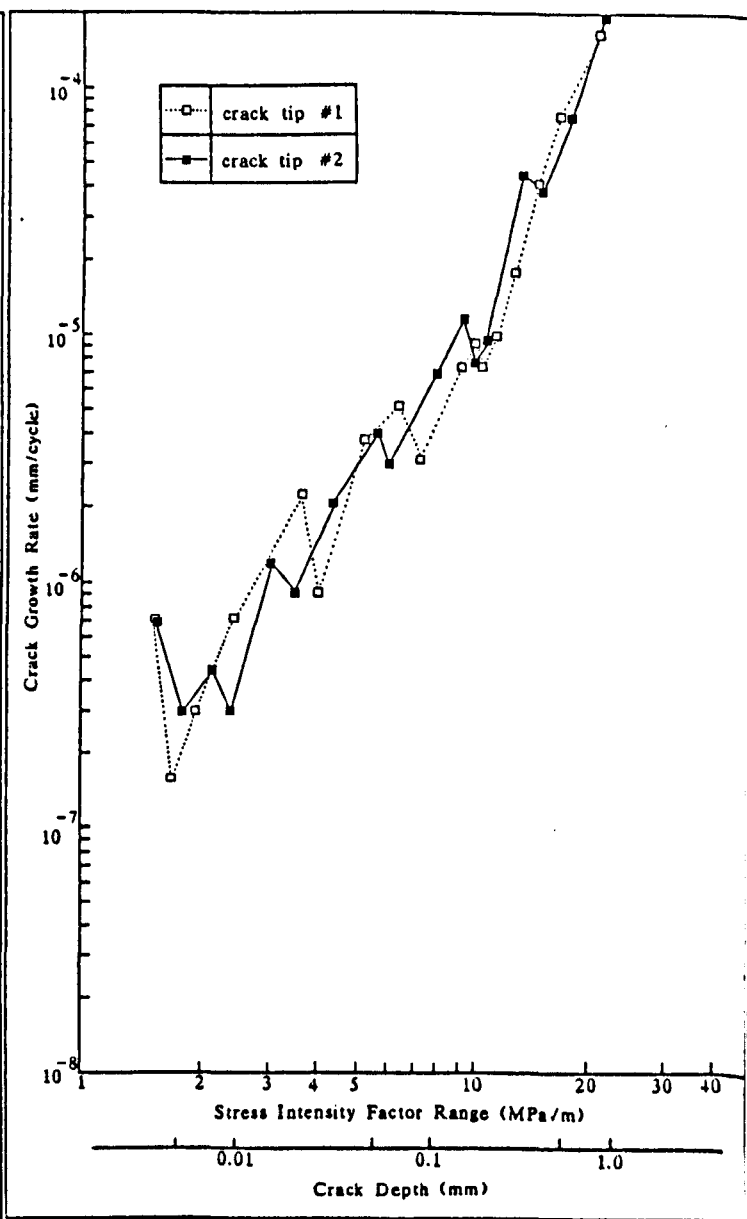
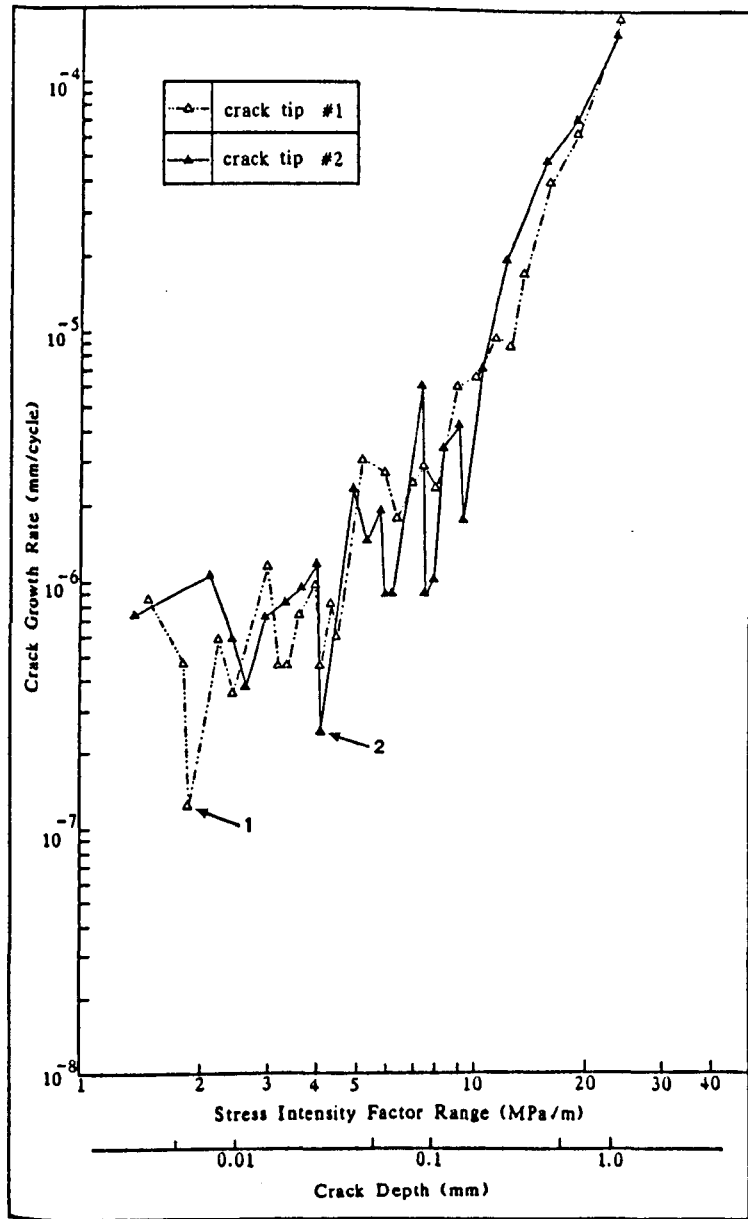
(b)  $50\ \mu\text{m}$



(c)  $10\ \mu\text{m}$

crack growth  
direction

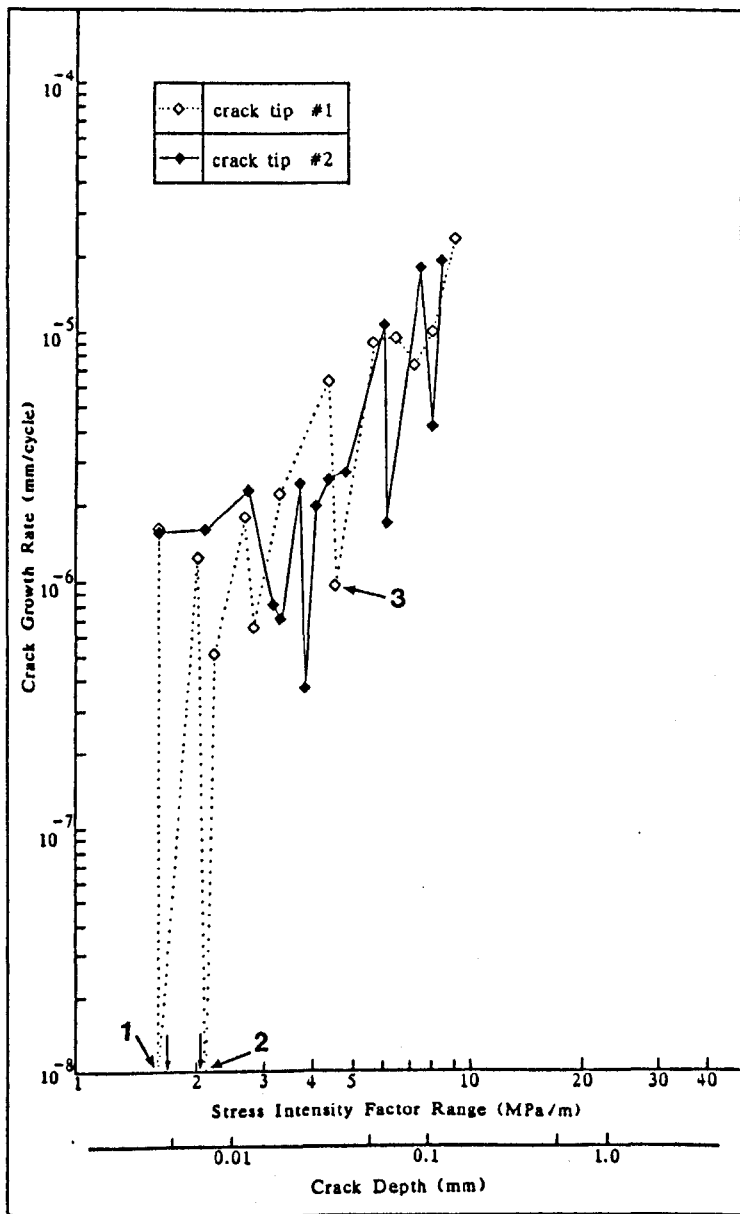
- 8.2 Fracture surfaces of long, through thickness cracks  
(a) 318A near-threshold growth, (b) 318D near-threshold growth,  
(c) 318A fast fatigue fracture ( $\Delta K = 11.0\text{MPa}\sqrt{\text{m}}$ )



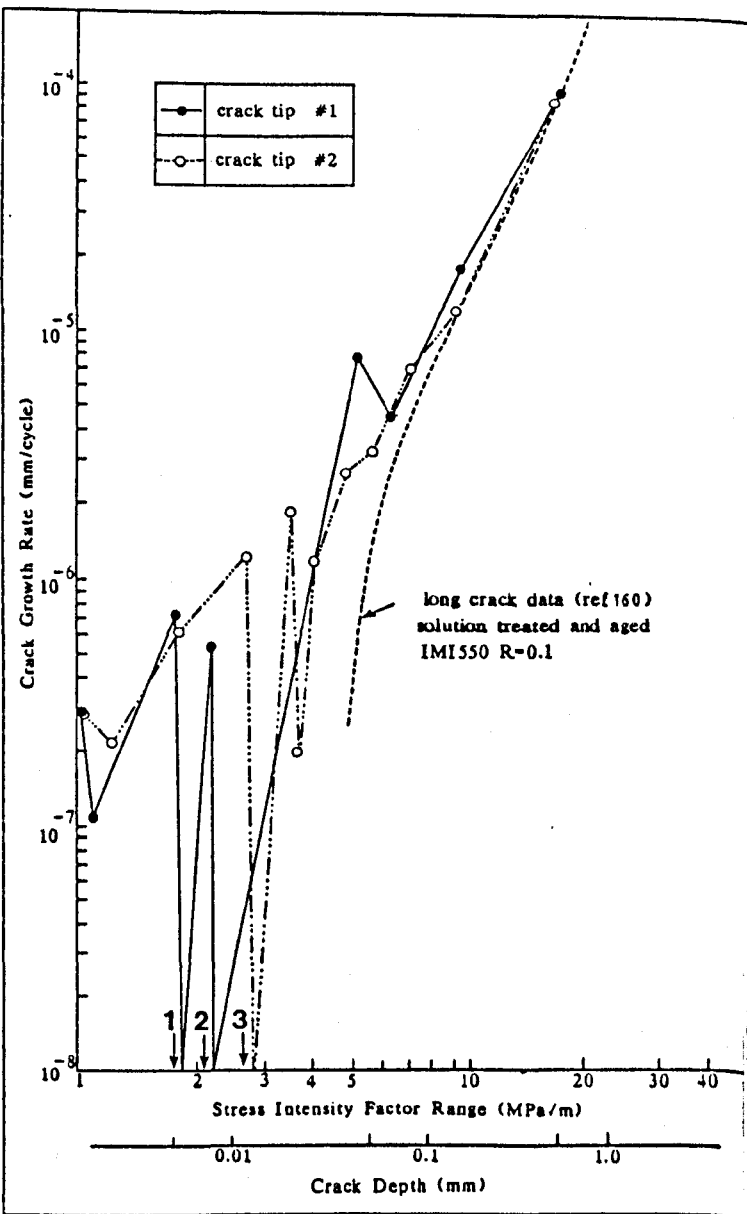
(a)

(b)

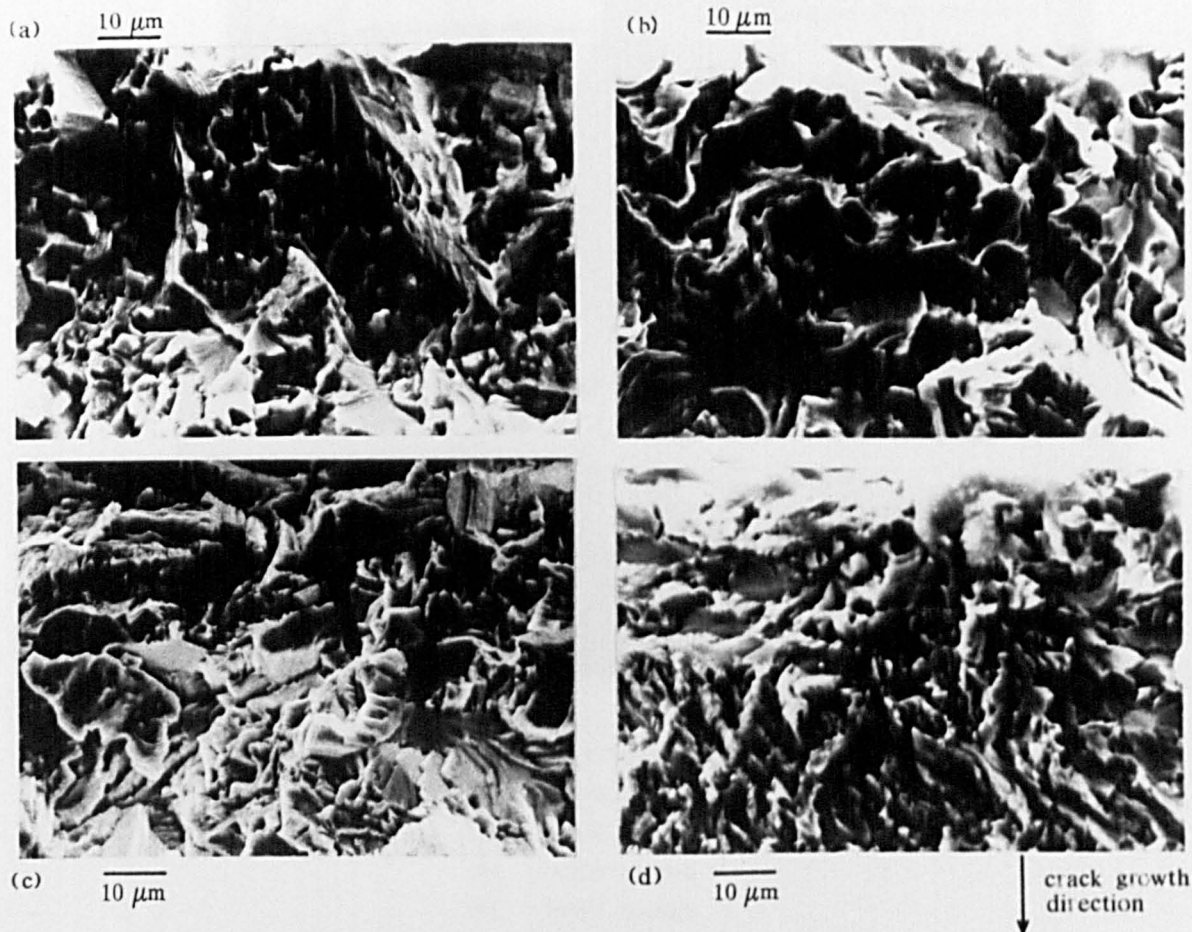
8.3  $da/dN$  vs  $\Delta K$  and  $a$  for short cracks in  $\alpha+\beta$  heat treated microstructures. (a) 318A, (b) 318B, (c) 318C, (d) 550A containing long crack data taken from the literature (160)



(c)

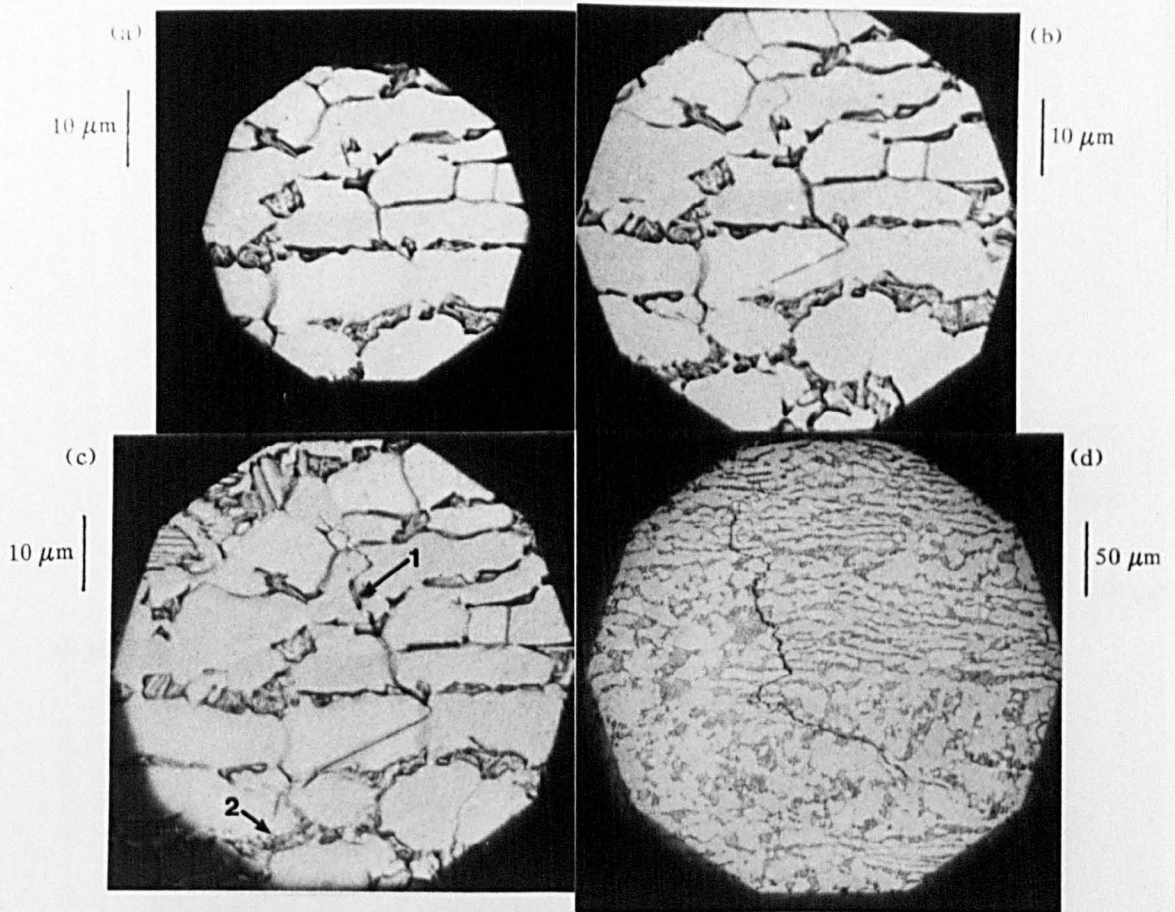


(d)



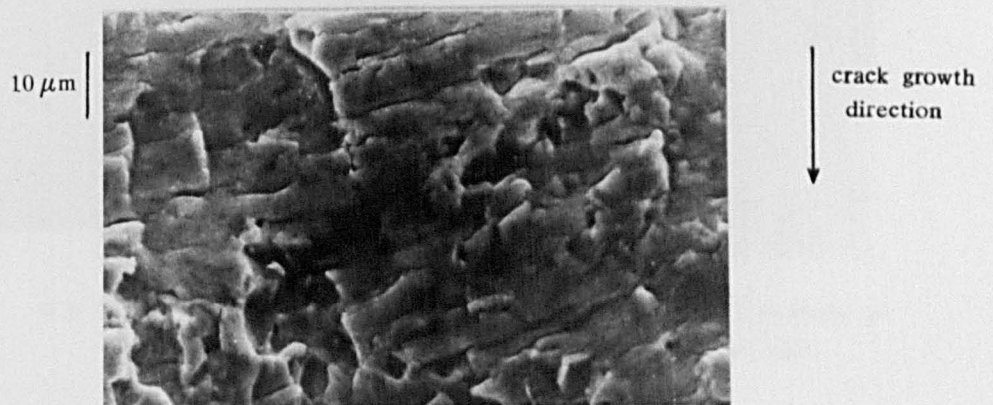
8.4 Near-initiation site fracture surfaces of short fatigue cracks in  $\alpha+\beta$  heat treated microstructures.

(a) 318A, (b) 318B, (c) 318C, (d) 550A.



8.5 Optical micrographs illustrating surface crack history of the short fatigue crack described in figure 8.3a, for 318A.

- (a) 16000 cycles
- (b) 24000 cycles
- (c) 36000 cycles
- (d) 80000 cycles



8.6 Electron micrograph showing fast fatigue fracture 2.7mm from initiation site in 318A.



## IMAGING SERVICES NORTH

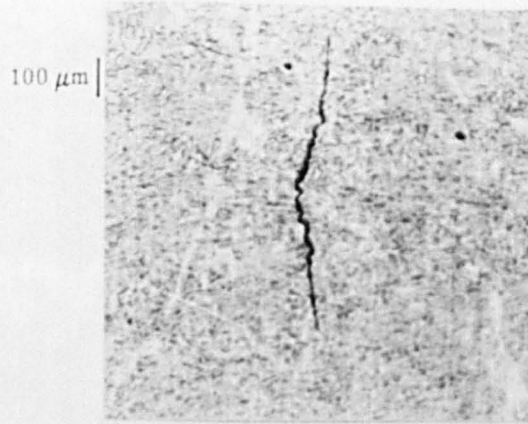
Boston Spa, Wetherby

West Yorkshire, LS23 7BQ

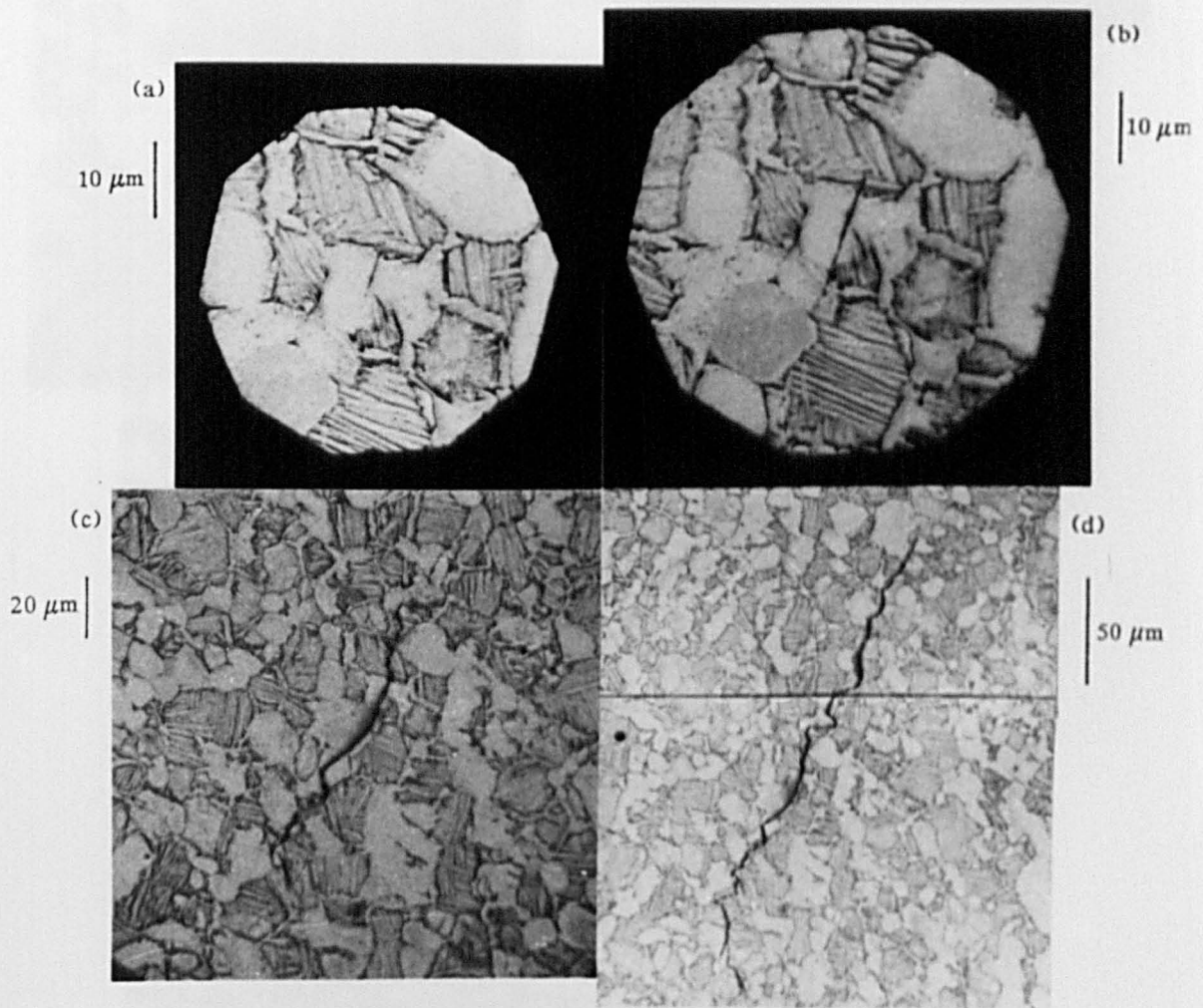
[www.bl.uk](http://www.bl.uk)

**BEST COPY AVAILABLE.**

**VARIABLE PRINT QUALITY**

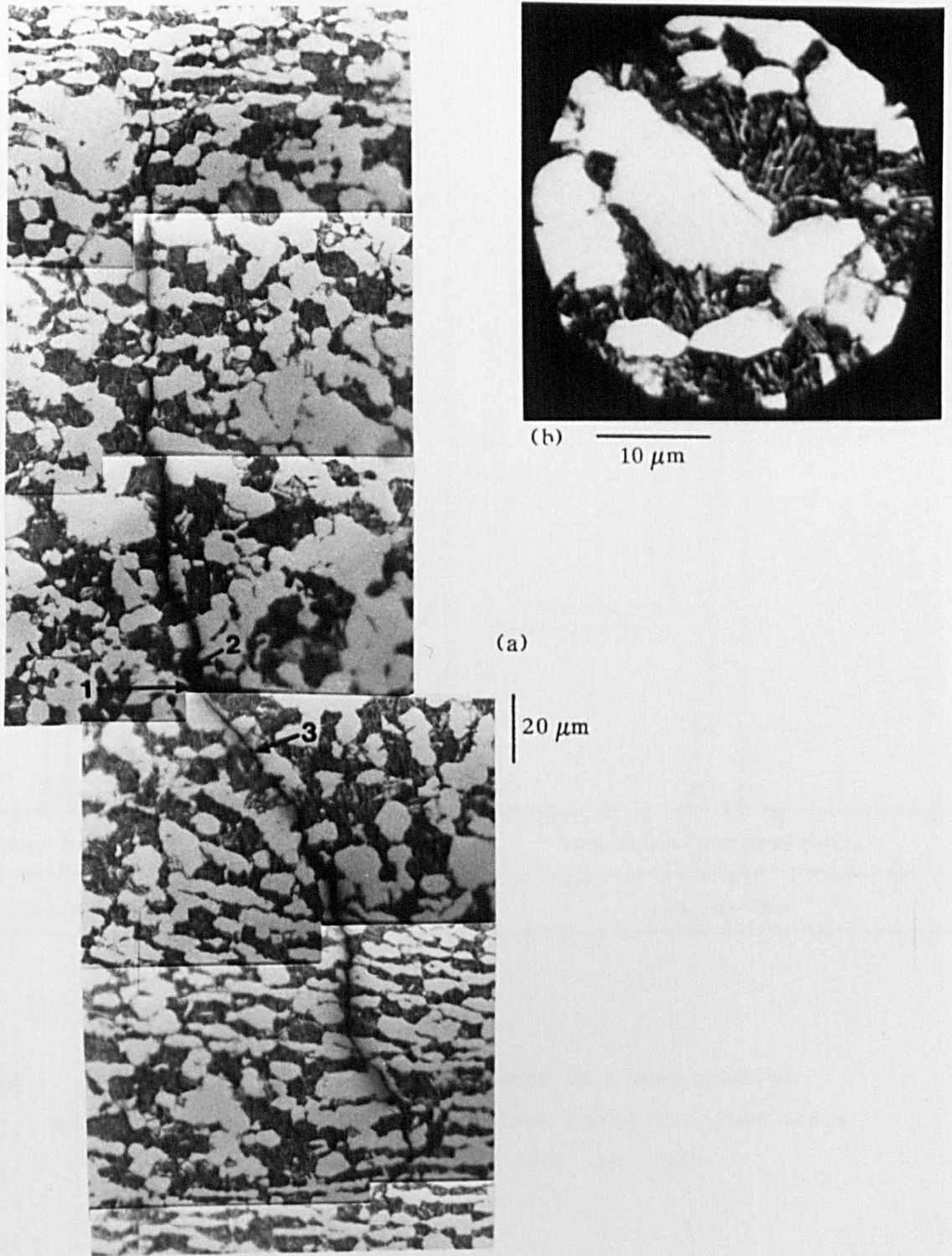


8.7 Optical micrograph showing surface crack in 318B

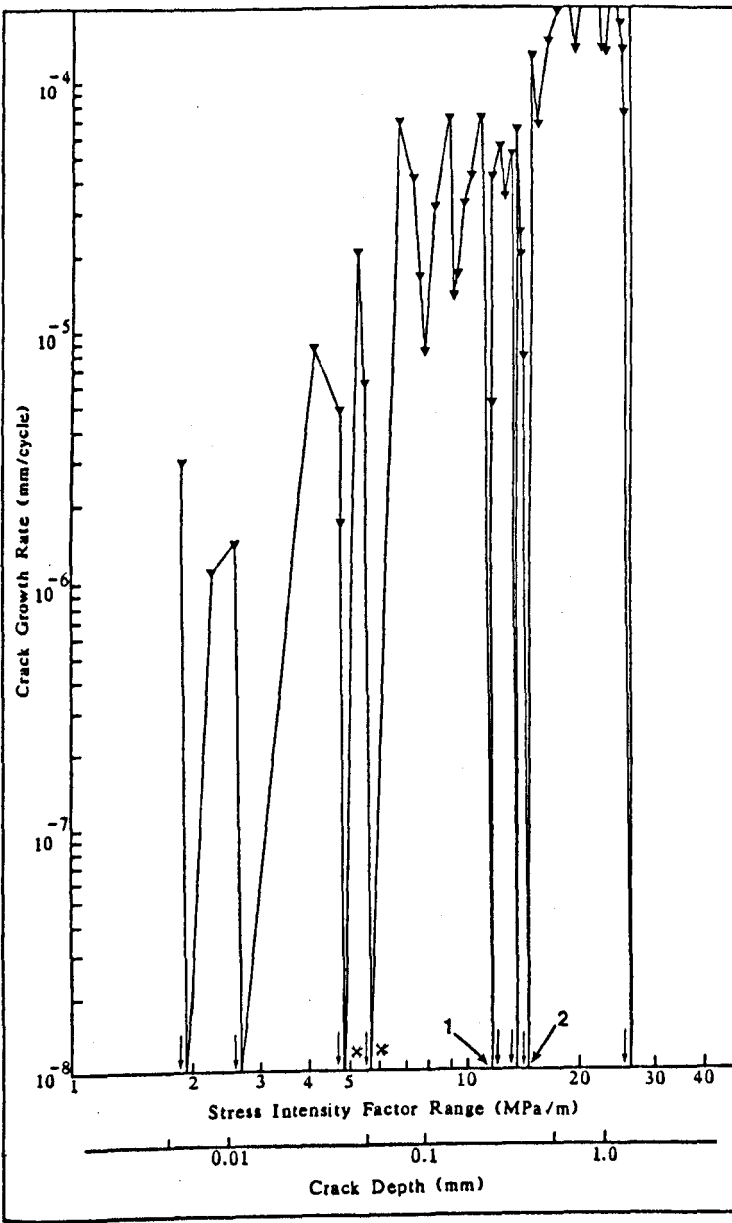


8.8 Optical micrographs illustrating surface crack history of short crack described in figure 8.3c for 318C.

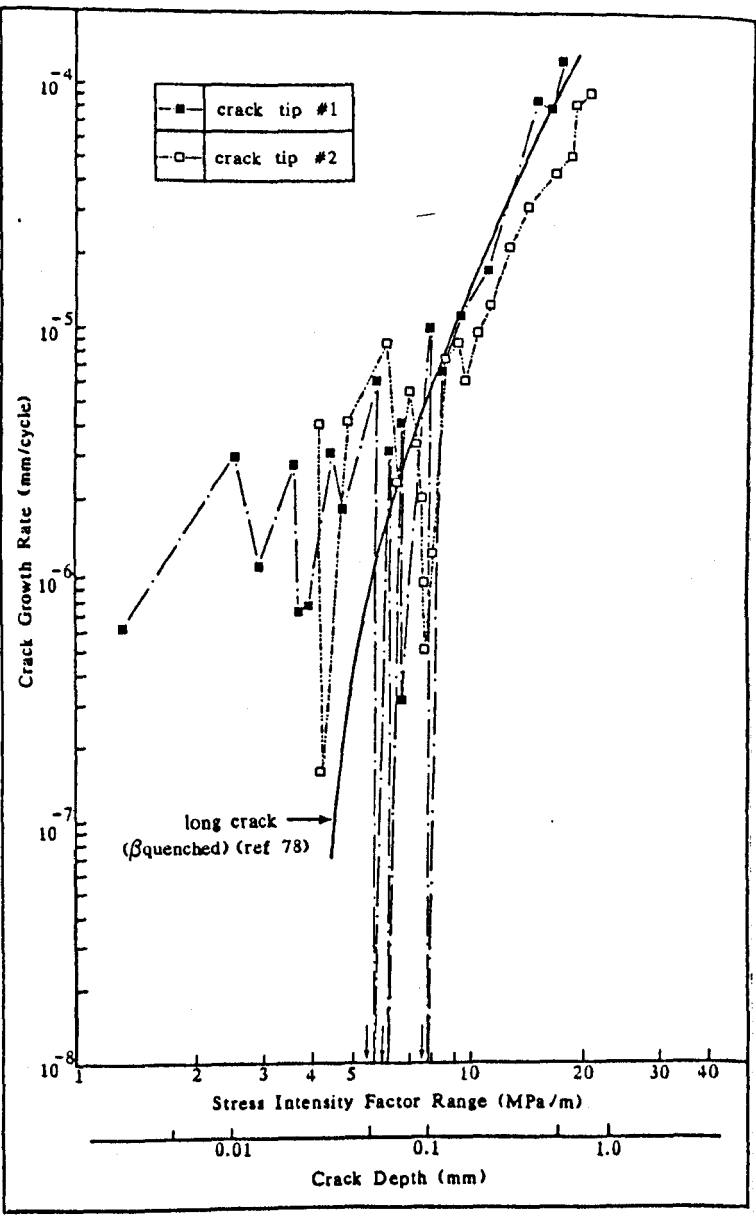
- (a) 20000 cycles
- (b) 26000 cycles
- (c) 40000 cycles
- (d) 52000 cycles



8.9 (a) detail of surface crack described in figure 8.3d for 550A.  
 (b) same crack showing initiation in  $\alpha_p$  grain.  
 (a) 230400 cycles  
 (b) 175000 cycles

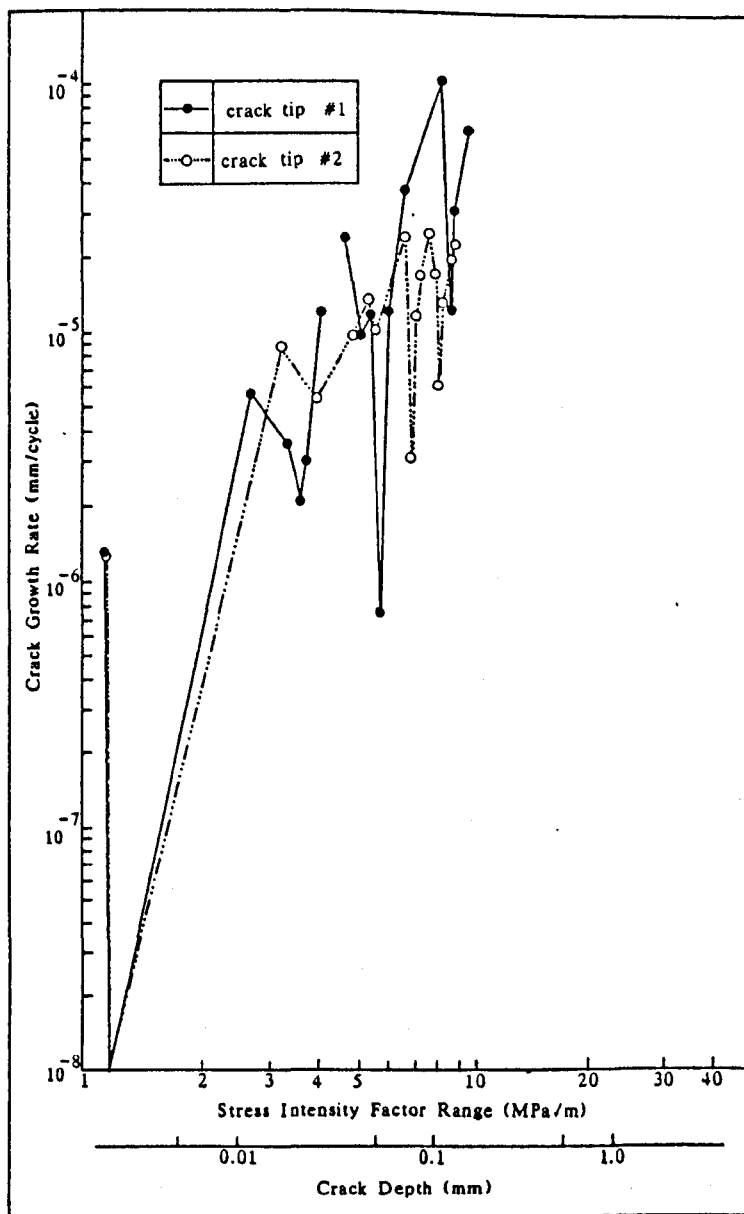


(a)



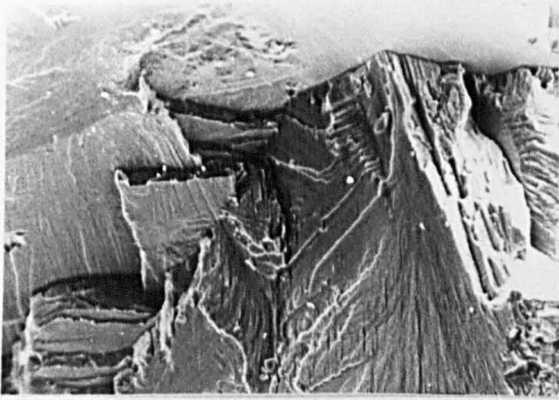
(b)

8.10  $da/dN$  vs  $\Delta K$  and  $a$  for short cracks in  $\beta$  heat treated microstructures. (a) 318D, (b) 318E containing long crack data from the literature (78) (c) 550B.

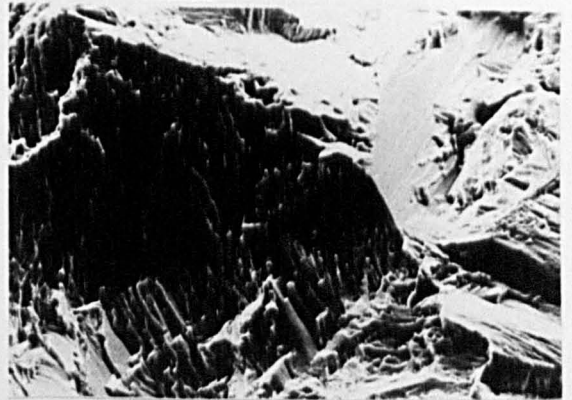


(c)

(a) 100  $\mu\text{m}$

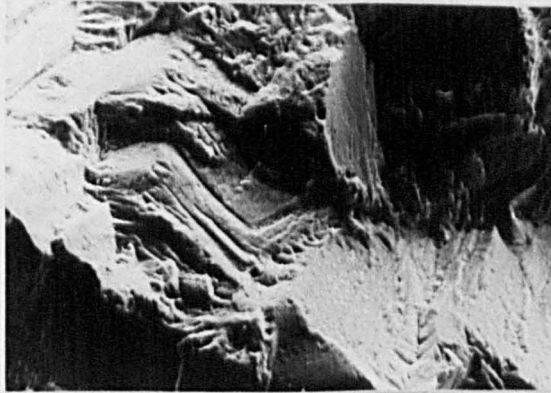


(b) 100  $\mu\text{m}$



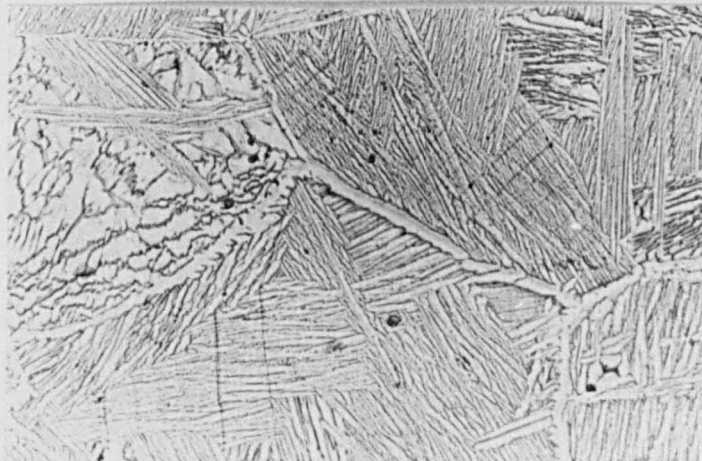
(c)

100  $\mu\text{m}$

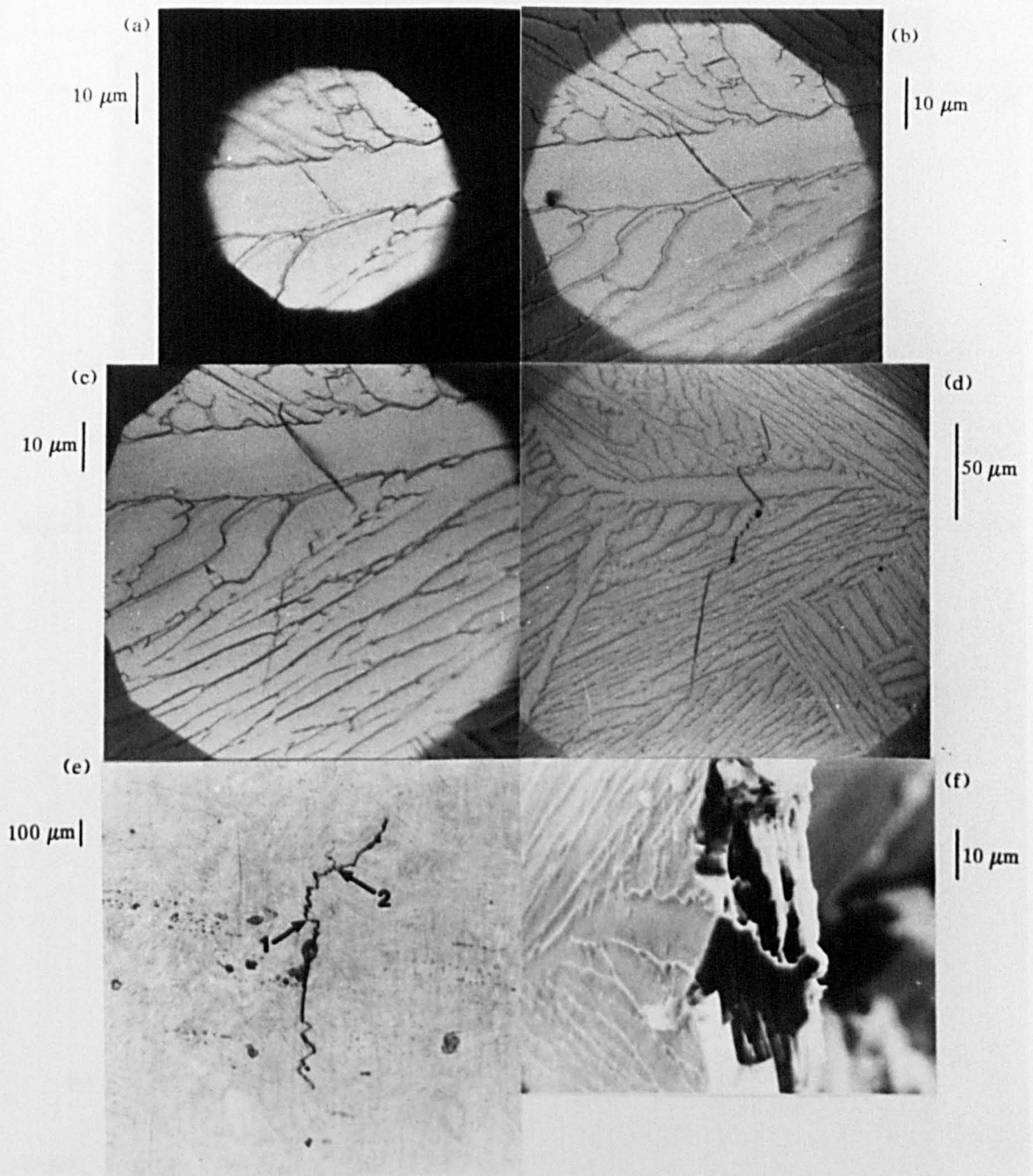


8.11 Near-initiation site fracture surfaces of short cracks in  $\beta$  heat treated microstructures. (a) 318D, (b) 318E, (c) 550B.

50  $\mu\text{m}$

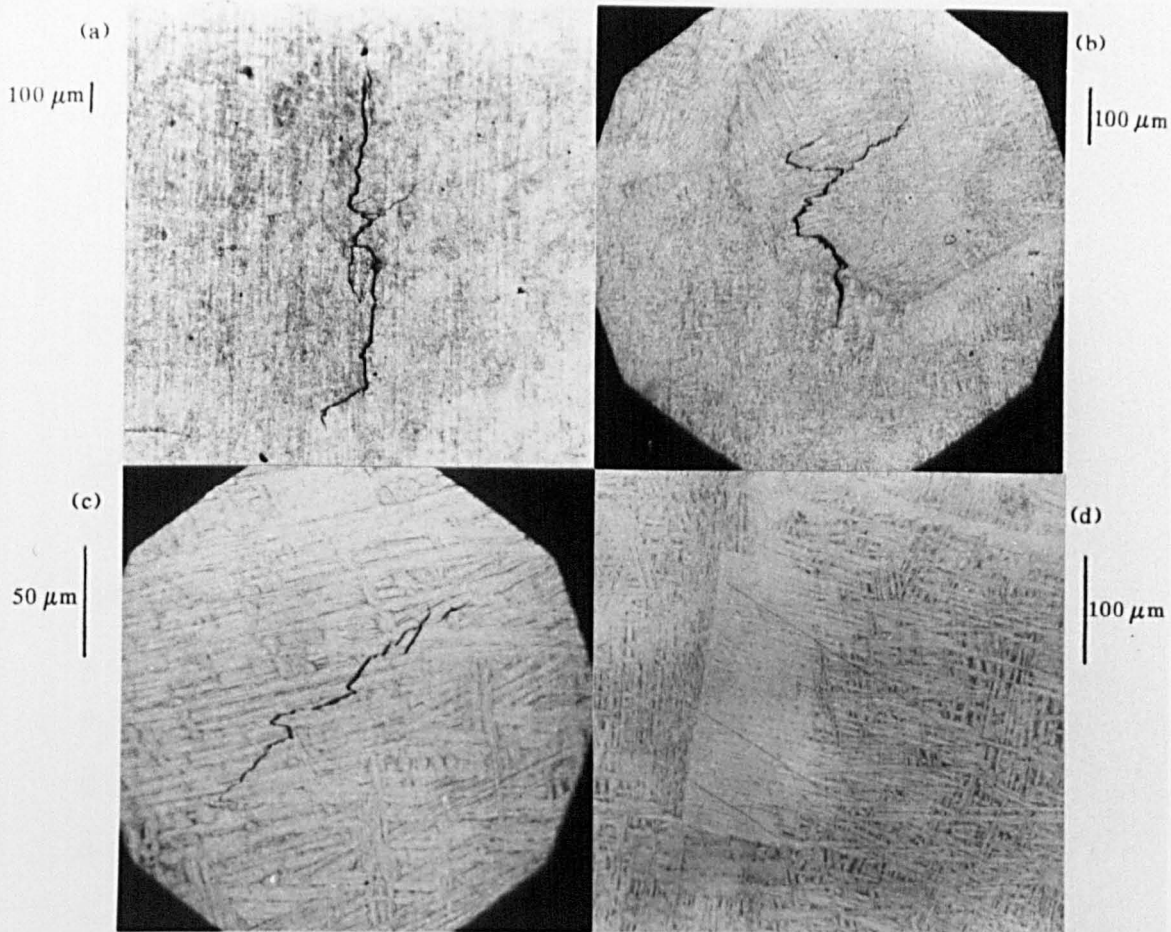


8.12 Optical micrograph showing slip band cracking in 318D.



8.13 (a) - (e) Optical micrographs illustrating surface crack history of short crack described in figure 8.10a for 318D. (f) Electron micrograph showing initiation facet in 318D.

- (a) 236000 cycles
- (b) 240000 cycles
- (c) 244000 cycles
- (d) 250400 cycles
- (e) 263200 cycles



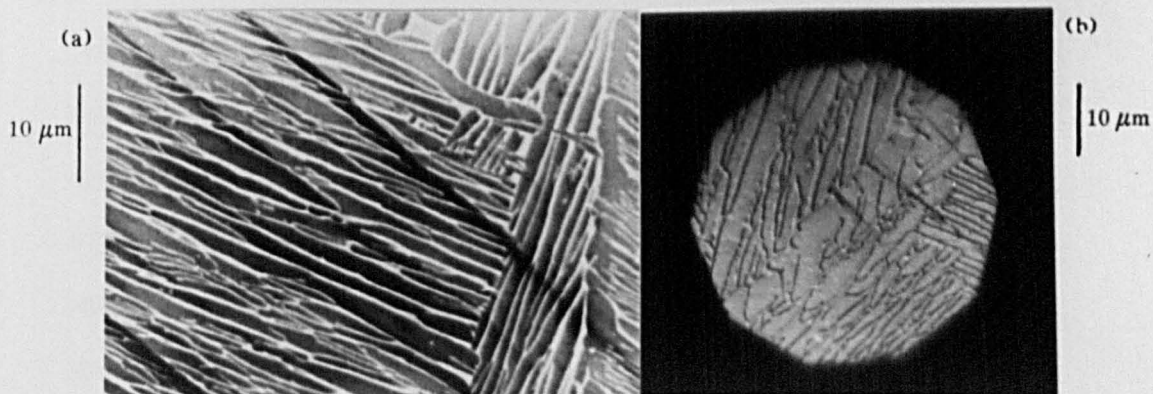
8.14 (a) - (c) Optical micrographs showing surface crack history of short crack described in figure 8.10b for 318E.

(d) Optical micrograph showing slip band cracking in 318E.

(a) 580000 cycles

(b) 570000 cycles

(c) 430250 cycles



8.15 (a) Electron micrograph of slip band cracking in 550B.

(b) Optical micrograph showing initiation of short fatigue crack at a prior grain boundary in 550B.

## CHAPTER 9

### TITANIUM ALLOYS - DISCUSSION

#### 9.1 LONG, THROUGH THICKNESS FATIGUE CRACK BEHAVIOUR

The long crack propagation behaviour of 318A and 318D, shown in figure 8.1, is similar to that commonly reported in the literature (32, 38, 63-67), with the  $\beta$  heat treated microstructure exhibiting consistently superior propagation resistance over the  $\alpha + \beta$  heat treated morphology throughout the range of  $\Delta K$ s studied. Furthermore, measured thresholds, 4.5 MPa $\sqrt{m}$  for 318A and 7.5 MPa $\sqrt{m}$  for 318D, are similar to those reported by other workers. Brown and Taylor (170) determined a value of 3.9 MPa $\sqrt{m}$  for mill annealed IMI 318 (similar to 318A) ( $R = 0.2$ ), Gray and Lütjering (34) reported  $\Delta K_{th}$  values of about 4.9 MPa $\sqrt{m}$  and 7.0 MPa $\sqrt{m}$  for a fine grained equiaxed  $\alpha + \beta$  microstructure and a coarse lamellar microstructure respectively and Chesnutt (78) obtained values of 5.9 MPa $\sqrt{m}$  and 6.2 MPa $\sqrt{m}$  for recrystallisation annealed and  $\beta$ -annealed microstructures at an  $R$  - ratio of 0.3. Additional substantance to the present results comes from figure 9.1, which compares the crack growth data of 318A with reported data in the literature for the same alloy in a similar,  $\alpha + \beta$  heat treated condition. Some difference between data collected by various workers is expected, through dissimilarities in heat treatment and testing conditions and procedures, though the correlation is remarkably good.

An explanation for the contrasting propagation characteristics of 318A and 318D has previously been presented in terms of crack closure arguments and in particular, roughness induced crack closure (34, 65, 66, 78). This is supported by the present results and can be further illustrated by the appearance of the near-threshold fracture surfaces (figure 8.2). As the effective grain size of the  $\beta$  heat treated microstructure (318D), either the colony size or the prior  $\beta$  grain size, is about an order of magnitude larger than that of 318A, the relative scale of the fatigue facets produced are similarly enlarged. Therefore, it is expected that an increase in closure contributions from this rougher, larger scale fracture surface would result. Although no data have been collected in this study at higher stress ratios, other studies have shown that differences in near-threshold behaviour between  $\alpha + \beta$  and  $\beta$  heat treated microstructures diminish as the R - ratio increases (34, 63).

Besides enhancing the effects of crack closure, a rougher, more irregular fracture surface can also promote crack propagation resistance through greater crack tip deflection and, subsequently, by producing a longer overall fracture path. As described in Chapter 2, the former has the effect of reducing crack tip driving forces and the latter tends to disguise true crack propagation rates, as the crack is forced to go along a path which can be significantly longer than one perpendicular to the stress axis. A study by Peters et al (79) attempted to quantify the consequences of these processes on the fatigue behaviour of  $\alpha + \beta$  heat treated and  $\beta$  heat treated Ti-6Al-4V microstructures.

From crack profile measurements they showed that the  $\beta$  processed microstructure had an effective crack length 17% longer than that measured macroscopically across the specimen, perpendicular to the stress axis, while for the  $\alpha + \beta$  heat treated morphology, this figure was only 2% greater. Furthermore, when the authors considered the effect over the whole of the fracture surface area, the effective area for the coarse microstructure was 37% greater than the planar surface area. An approximation was also made to assess the effectiveness of crack tip deflection using measurements of the angle of deviation from the perpendicular to the stress axis. A reduction in the effective stress intensity factor range ( $\Delta K_{eff}$ ) to approximately 68% of the measured  $\Delta K$  for the  $\beta$  annealed microstructure was calculated. When these two effects were taken into account, Peters et al demonstrated that the crack resistance of the  $\beta$ -annealed microstructure worsened to an extent that in a  $da/dN$  vs  $\Delta K$  plot, data for both microstructures overlapped. Although only simple calculations were performed and no account was taken of the effects of other factors, such as slip reversibility and crack branching, the study did highlight the magnitude of crack deflection processes.

A number of relationships appear in the literature which attempt to correlate  $\Delta K_{th}$  and grain size ( $d$ ). Beevers et al (46) in their crack closure model predict that the stress intensity above which the crack can be assumed to be fully opened ( $K_{op}$ ) is proportional to both the asperity height ( $L$ ) and one over the square root of the distance of the asperity from the crack tip.

For a predominantly transgranular failure Beevers et al (46) argue that both will be proportional to the grain size ( $d$ ) and hence  $K_{op} \propto d^{\frac{1}{2}}$ . As  $\Delta K_{th} \propto K_{op}$ , then  $\Delta K_{th} \propto d^{\frac{1}{2}}$ . Masounave and Bailon (60), through their expression analogous to the Hall-Petch equation, also predict that  $\Delta K_{th} \propto d^{\frac{1}{2}}$ . The measured  $\Delta K_{th}$  values of  $4.5 \text{ MPa}\sqrt{\text{m}}$  and  $7.5 \text{ MPa}\sqrt{\text{m}}$  for 318A and 318D in this study, coupled with the average grain size of about  $5 \mu\text{m}$  for 318A and average colony size of  $65 \mu\text{m}$  for 318D, does imply that  $\Delta K_{th}$  and  $d$  are in some way proportional to each other. They do not seem to be related through the expression  $\Delta K_{th} \propto d^{\frac{1}{2}}$  however, as this would predict that an order of magnitude increase in grain size, as there is between 318A and 318D, would result in a much larger rise in  $\Delta K_{th}$  than is observed. Masounave and Bailon (60) also widened their model to incorporate the Hall-Petch equation and postulated that there was an inverse relationship between  $\Delta K_{th}$  and yield strength ( $\sigma_{0.2\%}$ ). The tensile data presented in Chapter 7 however, shows that  $\sigma_{0.2\%}$  for 318A and 318D are very similar ( $946 \text{ MPa}$  and  $976 \text{ MPa}$  respectively), suggesting that such a relationship is invalid for this material.

At higher propagation rates the curves in figure 8.1 are tending to converge, though comparison is limited by the small range of data for 318D. The fracture surfaces at these propagation rates are much flatter than those produced in the near-threshold regime and crack growth is by a striation forming mechanism. Any microstructural effects that influence growth at lower propagation rates are less apparent in this region and overall fatigue behaviour is similar.

It has even been reported by Chesnutt et al (65, 78) that at these higher growth rates, the  $da/dN$  vs  $\Delta K$  curves for  $\alpha + \beta$  and  $\beta$  heat treated microstructures cross over and the  $\beta$  annealed microstructures exhibit worse propagation resistance thereafter, though verification of such an observation is not possible from the present results.

## 9.2 ASPECTS OF SHORT CRACK GROWTH - $\alpha + \beta$ HEAT TREATED MICROSTRUCTURES

For all the cracks studied from the  $4 \alpha + \beta$  heat treated microstructures (318A, 318B, 318C, and 550A) initial growth, after crack initiation, occurred in a very rapid manner through the first  $\alpha_p$  grain along a well developed slip band. As Miller (127, 128) has commented, this observation may not be unexpected when compared to long, through thickness cracks, as growth would be unconstrained, along a favourably orientated slip plane which offers little resistance to propagation. A longer crack, where the crack tip encounters many grains along its periphery, is forced to propagate via some unfavourably orientated slip system as well, so reducing overall growth rates. The length of the slip band in the initiating primary  $\alpha$  grain determines the extent of this rapid propagation. This in turn is dependent on the  $\alpha_p$  grain size, as an increase in the microstructural unit size will allow the rapid growth to continue to greater crack depths.

The first minimum on the  $da/dN$  vs  $\Delta K$  curves (figure 8.3a-d) should therefore occur at a crack depth approximately equal to half the  $\alpha_p$  grain size, or about 5  $\mu m$ , which can be seen to be the case in the majority of the examples presented.

From the optical micrographs of short cracks (e.g. figures 8.5, 8.8, 8.9) it is evident that subsequent minima on the  $da/dN$  vs  $\Delta K$  plots are due to the repeated interactions of the crack tip with primary  $\alpha$ /transformed  $\beta$  grain boundaries. This type of behaviour has previously been reported by Brown (138) and Hicks and Brown (167) in a similar titanium alloy and is analogous to the behaviour seen by others working with dual phase microstructures in steels (128, 177, 178). In the latter cases, cracks were seen to initiate along slip bands in the soft ferrite phase and were subsequently decelerated or halted by regions of hard martensite (177) or fine structured pearlite (128, 178). According to microhardness indentation measurements the transformed  $\beta$  phase in the microstructure under study here is not appreciably harder than the  $\alpha_p$  phase, though the fine nature of the transformed  $\beta$  product may have an effect on short crack growth behaviour.

For steels, it was concluded (128, 178) that the pearlite, due to the fine banding of ferrite and cementite, reduced the slip length considerably which consequently reduced crack propagation rates. However, even though the transformed  $\beta$  product in  $\alpha + \beta$  processed titanium alloys is much finer than the  $\alpha_p$  phase, it has been reported (82) that slip bands can form across whole packets of colonies of laths whether they are aligned or in a basketweave morphology.

This will be considered in more detail in section 9.3. Crack propagation rates across colonies in a  $\beta$  processed Ti-11 alloy (Ti-6Al-2Sn-1.5Zr-1Mo-0.4Bi) were found to be no slower than through  $\alpha + \beta$  processed microstructures, which indicates that unlike ferrite/pearlite steels, it is not just the fine nature of the microstructure which controls short crack propagation behaviour in this case. This is further supported by the present work on 318C, the microstructure containing the highest proportion of transformed  $\beta$  out of the four  $\alpha + \beta$  processed morphologies studied. Figure 9.2 compares the overall crack propagation rates of 318A, 318B, 318C and 550A on a  $da/dN$  vs  $\Delta K$  diagram with envelopes containing data collected from all the cracks studied for each microstructure. The diagram shows that the average short crack propagation rate is higher for 318C than for 318A and 318B over the whole range of  $\Delta K$  studied. This is despite the fact that in 318C the crack tip encounters considerably more transformed  $\beta$  than in either 318A or 318B. Through monitoring crack growth rates in this microstructure it was noticeable that propagation through the fine transformed  $\beta$  laths was at a comparable rate to that through the larger, equiaxed primary  $\alpha$  grains.

If, as was stated earlier, the propagation of short cracks is slowed down as the crack tip approaches  $\alpha_p$ /transformed  $\beta$  grain boundaries, it is plausible that the number of such interactions will affect overall growth characteristics.

For the three IMI 318 microstructures considered in figure 9.2, the average number of  $\alpha_p$ /transformed  $\beta$  grain boundaries per 100  $\mu\text{m}$  on the specimen surface, measured perpendicular to the stress axis in the direction of crack propagation, is 11.8, 6.7 and 4.6 for 318A, 318B and 318C respectively. Thus, over twice as many crack tip/grain boundary interactions are encountered for 318A compared with 318C, even though their  $\alpha_p$  grain sizes are equal. If it is the process of reinitiation and reorientation of the crack tip from an  $\alpha_p$  grain into a transformed  $\beta$  grain that is the cycle consuming step, then the microstructure with the greater density of such boundaries will exhibit the most beneficial short crack propagation resistance.

Both grain size and volume fraction of the phases will affect the number of  $\alpha_p$ /transformed  $\beta$  grain boundaries. To maximise the resistance to growth the grain size of each phase should be small and the phases equally divided throughout the microstructure. Hence for 318B, where the structure is largely primary  $\alpha$ , the crack is able to take a path predominantly through this phase, so minimising the number of  $\alpha_p$ /transformed  $\beta$  grain boundaries encountered. The crack path through the  $\alpha_p$  can be seen clearly on the scanning electron micrograph of the fatigue fracture (figure 8.4b). This is translated onto a  $da/dN$  vs  $\Delta K$  plot as a 'curve' with less pronounced minima and therefore less scatter in propagation rates (figures 8.3b) and inferior overall propagation resistance compared to 318A (figure 9.2).

Additionally the effect of grain size has to be considered. There is strong evidence that for short cracks the effect of increasing grain size is in direct contrast to that for long, through thickness cracks (5, 73, 148, 149, 159, 166-169) with an increase in the microstructural unit size leading to a degradation in short crack propagation resistance. However, it seems likely that the range of grain sizes in the four  $\alpha + \beta$  heat treated microstructures studied is not large enough for any differences in propagation behaviour to be discernable. This is in agreement with the view of Brown and King (171) who, in reviewing earlier work by Brown and Taylor (170), concluded that the difference in grain size between the two  $\alpha + \beta$  heat treated microstructure studied (4.7  $\mu\text{m}$  and 11.7  $\mu\text{m}$ ) was not large enough to affect significantly short crack propagation behaviour, especially when the large degree of scatter associated with such data was considered.

Crystallographic texture has also been observed to affect the short crack growth behaviour of titanium alloys (138, 170). When basal planes in the  $\alpha$  phase were aligned in the direction of crack propagation an easier path to crack growth was noted. In another study (226) it was observed that upon heat treatment in the  $\alpha + \beta$  phase field, the texture of a Ti-6Al-4V alloy was partially maintained up to temperatures close to the  $\beta$  transus. Consequently for the three microstructures examined in this alloy (318A, 318B, 318C) any influence of texture may be expected to be apparent in each case.

A reason for the superior short crack propagation resistance of 318A particularly above crack depths of approximately 50  $\mu\text{m}$  however, might be associated with microstructural texture. It was apparent that in 318A banding sometimes occurred on a macrostructural scale as a result of the plate manufacture. Such microstructural fibring is evident in figure 8.5d. Subsequent heat treatment of the plate in the  $\alpha + \beta$  phase field to produce 318B and 318C resulted in more homogeneous, equiaxed microstructures. This change in grain size, shape and distribution caused extensive crack tip deviation in 318A which could promote propagation resistance by increasing the actual crack length, through a more tortuous crack path, and by reducing the crack tip driving forces, through crack tip deflection.

Differences in crystallographic texture between the two alloys studied may be useful in explaining the relative short crack propagation resistance of 318A and 550A. Texture measurements made on the IMI 318 and IMI 550 as-received plate (175) revealed that both have textures which could be described as  $(11\bar{2}0) [10\bar{1}0]$ . Hence the basal planes are aligned perpendicular to the rolling plane and the plane containing the propagation direction. The IMI 550 (550A) plate however, showed a stronger texture than 318A. Alignment of the basal planes in such a manner has been seen to assist propagation resistance (138, 170) and as the stronger texture is indicative of more planes lying in this arrangement, it may be expected that 550A would show a greater propagation resistance through these means.

Comparing the relative short crack propagation behaviour of 318A and 550A (figure 9.2) reveals however, that 550A exhibits worse short crack propagation resistance. It is possible that other factors may combine to produce the observed behaviour, for example the absence of microstructural texture in 550A and the higher maximum stress used in the short fatigue crack testing of this alloy. The latter factor however has not been seen to significantly influence the short crack propagation behaviour of the 7010 aluminium alloy (section 6.6). Finally the data shown in figure 9.2 may be a reflection of worse inherent fatigue crack propagation resistance of the IMI 550 alloy.

### 9.3 ASPECTS OF SHORT CRACK GROWTH - $\beta$ ANNEALED MICROSTRUCTURES

As with the  $\alpha + \beta$  heat treated microstructures, crack tip microstructural interactions caused major discontinuities in short crack propagation rates in the  $\beta$  annealed microstructures (318D, 318E, and 550B). In all cases a controlling aspect was the relative orientation of the crack tip to the local transformed  $\beta$  lath structure, which, in turn changed from microstructure to microstructure through the cooling rate from the  $\beta$  annealing temperature. The faster, air cool (318E) producing a basket-weave, Widmanstätten lath structure, for which no packet size could be defined, contrasted starkly with the slower, furnace cooled microstructures (318D, 550B) containing large areas of aligned, Widmanstätten, transformed  $\beta$  colonies.

Thus the heat treatments resulted in three microstructures of almost equal prior  $\beta$  grain sizes, but with varying packet sizes, 40, 65 and 161  $\mu\text{m}$  for 318E, 318D and 550B respectively. (table 7.3).

In the aligned Widmanstätten microstructures (318D and 550B) propagation rates were seen to be very high in regions where the crack tip grew across colonies along intense slip bands. These slip bands, formed across whole colonies of similarly orientated laths ahead of the crack tip, produced fracture via a shear mechanism and the resulting fracture surfaces had planar facets (figure 8.11a and c). Comparable observations have been made by other workers (82, 85, 167-169, 173). In other areas of the microstructure however, where less favourably orientated laths were encountered, a more tortuous crack path was taken and growth rates were seen to be less uniform. This type of behaviour is apparent in figure 8.13b just above the initiation site. This may be due to a restriction in slip length or because the predominant slip planes are lying unfavourably with respect to the tensile axis.

Additional crack propagation retardation occurs when the crack tip reaches colony or prior  $\beta$  grain (PBG) boundaries. As slip bands can not cross the boundaries, the crack tip has to reorientate and reinitiate itself along another slip band in the adjoining grain. Such a process is usually cycle consuming and leads to major reductions in propagation rates.

The first crack tip/grain boundary encounters observed in 318D and 550B occurred soon after initiation, as the crack tips emerged from the PBG boundary  $\alpha$  phase (figure 8.13a) and resulted in the minima at crack depth  $<10 \mu\text{m}$  in figures 8.10a and c. Subsequent minima usually occurred when the crack tips were close to colony boundaries. For example in figure 8.10a the two minima marked with asterisks around a crack depth of  $50 \mu\text{m}$  are associated with the crack tip close to the first colony boundary (as is shown by the position of the top crack tip in figure 8.13d). These and further major growth rate minima were often accompanied by the emergence of a second propagating crack tip away from a stationary crack tip. It is evident therefore that even though the original surface crack tip had stopped, subsurface growth was continuing.

The retardation effects of colony boundaries in Widmanstätten microstructures has been recorded by other workers, noticeably by Eylon (32, 85) who concluded that in order to reduce the overall fcg rate of this type of microstructure, the colony size should be reduced to obtain maximum benefit from this reinitiation effect. This hypothesis may help to explain the differences in the short crack propagation behaviour of 318D and 550B. Figure 9.3 shows a  $da/dN$  vs  $\Delta K$  diagram with envelopes containing data collected for all the cracks studied in 318D, 318E and 550B. As the purpose of the figure is to compare the average propagation behaviour of the microstructures, only non-zero growth rate data has been included. It can be seen that across the range of  $\Delta K$  examined 550B shows slightly high growth rates than 318D.

Apart from the differences in colony sizes other factors may influence the growth behaviour in these two microstructures. For example the 550B short crack fatigue testing was carried out at a higher maximum tensile stress on the specimen top surface (850 MPa for 550B, 750 MPa for 318D). However, for the 7010 aluminium alloy, the influence of  $\sigma_{\max}$  was found not be significant in short crack propagation behaviour. It is quite plausible that the differences in average propagation rates may be a result of inherent material resistance to fatigue and, as such, would be expected.

Further dissimilarities in propagation behaviour between 318D and 550B occur at greater crack depths, with the absence of effective crack retarding features in the latter microstructure (compare figures 8.10a and c). Lath and colony boundaries were much more effective in retarding crack growth in 318D, which may have been a consequence of more crystallographic misorientation between neighbouring colonies in this microstructure. Interestingly a similar observation was made for 550A when compared to 318A, which suggests that it may be due to inherent characteristics of the particular alloys.

Examination of the short fatigue crack behaviour of the basketweave microstructure (318E) highlights a number of contrasting aspects to those of the aligned Widmanstätten morphologies (318D and 550B).

The first difference, which can be seen by comparing the relevant  $da/dN$  vs  $\Delta K$  diagrams (figures 8.10a, b, c), is the lack of any major discontinuity in growth rate at crack depths below  $\sim 10 \mu\text{m}$ . This can be explained by considering the initiation process and early propagation in each microstructure.

Initiation in the aligned Widmanstätten structures occurred in the  $\alpha$  phase at prior  $\beta$  grain boundaries, however, as such features were absent in 318E less favourable initiation sites were found within the transformed  $\beta$  laths. Hence the crack growth retardation effects associated with the boundaries of the thin  $\alpha$  phase separating the prior  $\beta$  grains were absent.

A further difference in behaviour between the aligned and basketweave microstructures, which can be seen in figure 9.3, is the better overall propagation resistance of the basketweave transformed  $\beta$  microstructure. This is also supported by the work of Hicks et al (68). In comparison to 318D this is most noticeable between crack depths of  $50-500 \mu\text{m}$ . Such an effect has recently been reported for a near  $\alpha$  titanium alloy in similar microstructural conditions by Hastings et al (173). It is proposed that the improved short crack fatigue behaviour shown by 318E is due to the microstructural unit size. The effective colony size of 318E is one lath width which becomes the controlling microstructural dimension. Hence slip length is severely restricted and an irregular non-crystallographic crack path is initially favoured.

Up to  $\sim 100 \mu\text{m}$  crack depth, the lath morphology promoted a crack path well away from a plane perpendicular to the stress axis, assisting propagation resistance by increasing the ratio of actual/measured crack depth. However, it is at crack depths of greater than approximately  $50 \mu\text{m}$  that substantially better average propagation resistance is obtained. Figure 8.10b indicates that at these longer crack depths, growth in 318E is almost continuous and unaffected by the local microstructure. Examination of the path of such cracks (figure 8.14e) reveals that after an initially tortuous rate, a path almost perpendicular to the stress axis is maintained up to the end of the test when the crack was greater than 2mm. This transition occurs at a crack depth of approximately  $100 \mu\text{m}$ . It is likely that it marks the end of short crack behaviour and the beginning of the long crack regime. Indeed long crack data for beta quenched Ti-6Al-4V (78) also shown in figure 8.10b confirm that long and short crack data merge close to this point and exhibit excellent correlation at higher  $\Delta K$ s.

#### 9.4 COMPARISON OF LONG & SHORT CRACK BEHAVIOUR

In order to compare the contrasting long and short crack propagation behaviours of the  $\alpha + \beta$  and  $\beta$  processed microstructures, the relevant information has been plotted in figure 9.4. The figure shows both the long, through thickness propagation data and the short crack data for 318A and 318D, with the short crack results being represented by envelopes containing all non-zero growth rate data for all cracks studied in each microstructure.

Clearly, as opposed to the aluminium alloys, microstructural variables that promote long crack propagation resistance tend to have an opposite effect on the behaviour of microstructurally short cracks, even though the fracture surface appearance of both regimes are comparable (see figures 8.2a, b, 8.4a and 8.11a). The propagation resistance of long cracks at  $\Delta K$ s close to the  $\Delta K_{th}$  has previously been seen to depend on grain size for these types of microstructures (34, 65, 66, 78, 103, 104, 106). In particular, an increase in crack closure contribution, through a combination of greater crack tip deviation and crack bifurcation, accompanied a change from a fine, equiaxed grained  $\alpha + \beta$  microstructure to a coarse  $\beta$  annealed morphology, (where the colony or packet size is effectively the microstructural unit size). This study has shown that similar features in crack path are apparent in both long and short cracks and that while for long cracks they contribute to crack closure mechanisms, they do not for microstructurally or physically short cracks. It is concluded that the relationships between grain size, plastic zone size and crack depth are important, as well as the fact that if a crack is short with respect to the size of the local microstructure (i.e. there is a limited wake behind the crack tip), any closure contribution to propagation resistance will be diminished.

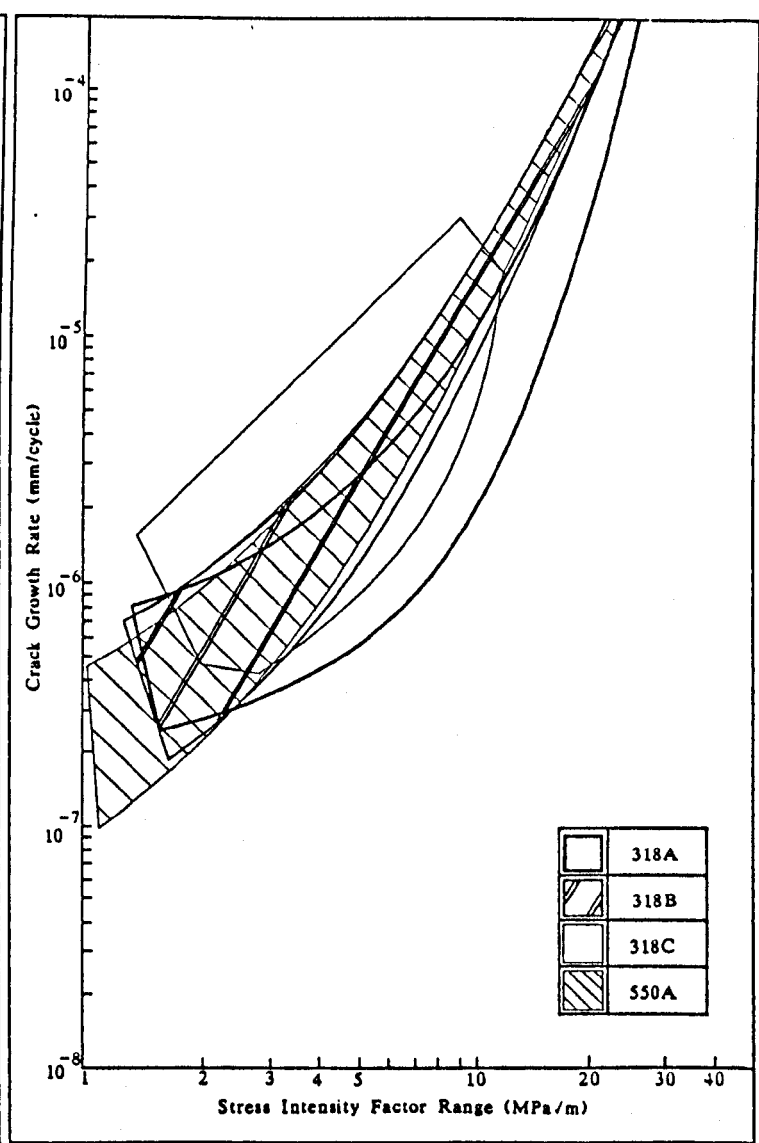
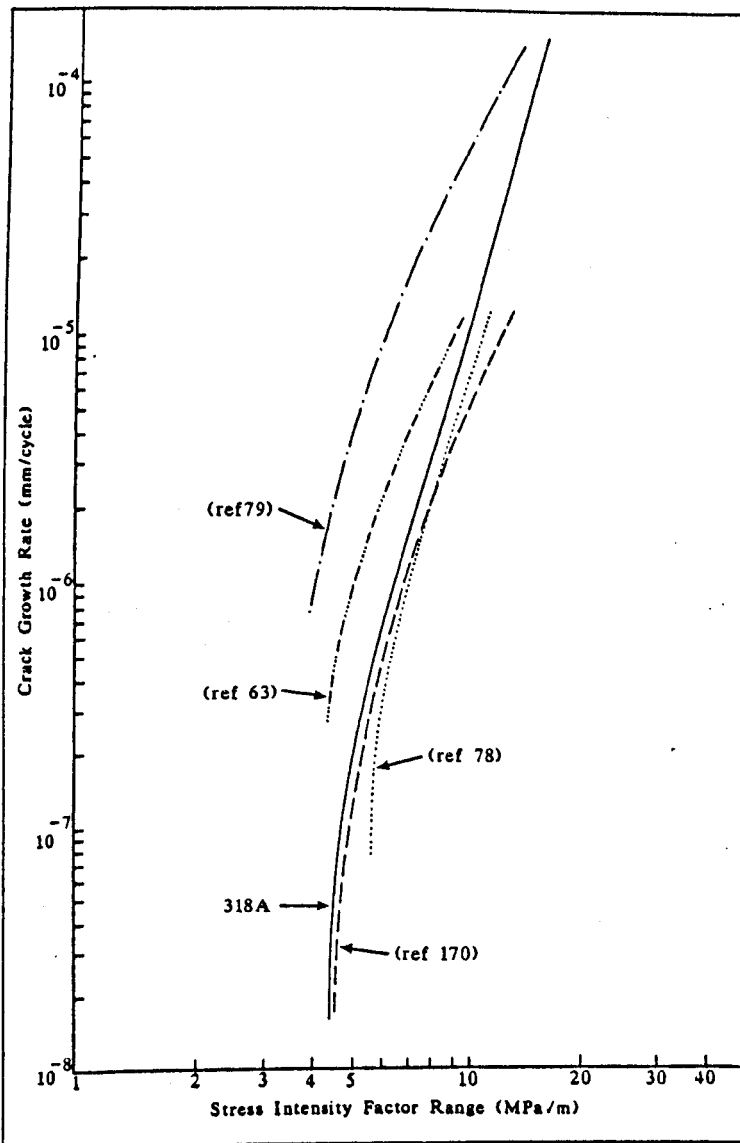
Although it is implied in figure 9.4 that the long and short crack lines for 318D will merge at a  $\Delta K > 15 \text{ MPa}\sqrt{\text{m}}$ , it is unclear why no such correlation is not observed for the  $\alpha + \beta$  processed microstructure, 318A.

Here, the data indicate that at  $\Delta Ks > 10 \text{ MPa}\sqrt{\text{m}}$  short cracks will exhibit greater propagation resistance than long cracks. This is in spite of the fact that at these  $\Delta Ks$ , where the short crack depth is much greater than the grain size, crack tip/micro-structural interactions are relatively ineffective in amending propagation and the cracks can be regarded as no longer micro-structurally short.

If, as for the aluminium alloy 7010, the transition from short to long cracks occur when the maximum plane strain plastic zone size ( $r_p$ ) equals the grain size, the transitions for 318A and 318D should occur at  $\Delta Ks$  of approximately  $8.8 \text{ MPa}\sqrt{\text{m}}$  and  $31 \text{ MPa}\sqrt{\text{m}}$  respectively, if Irwin's calculation is used (equation 6.2). Although it is possible that the long and short crack lines will merge for 318D at  $\sim 31 \text{ MPa}\sqrt{\text{m}}$ , such a transition is not observed for 318A. The reasons for this cannot be discerned from the present data. It is possible that variations in environmental interactions between long and short cracks for this heat treatment may be responsible or it could be a consequence of the short crack testing procedure.

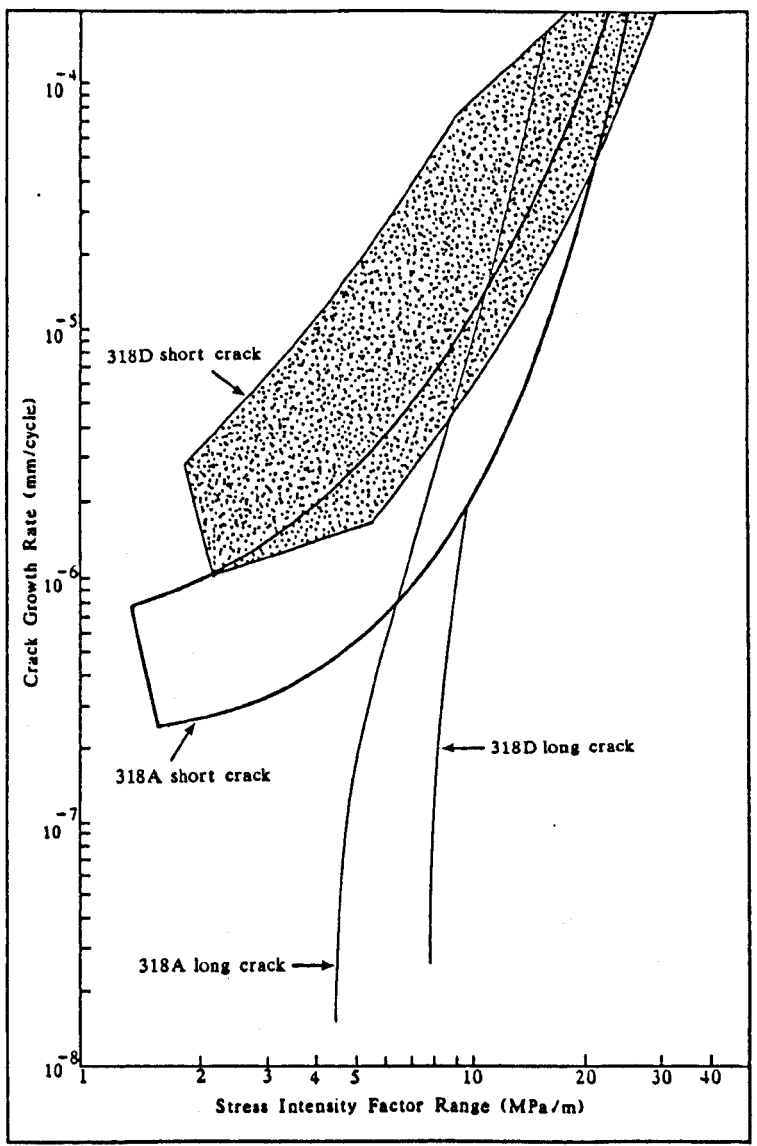
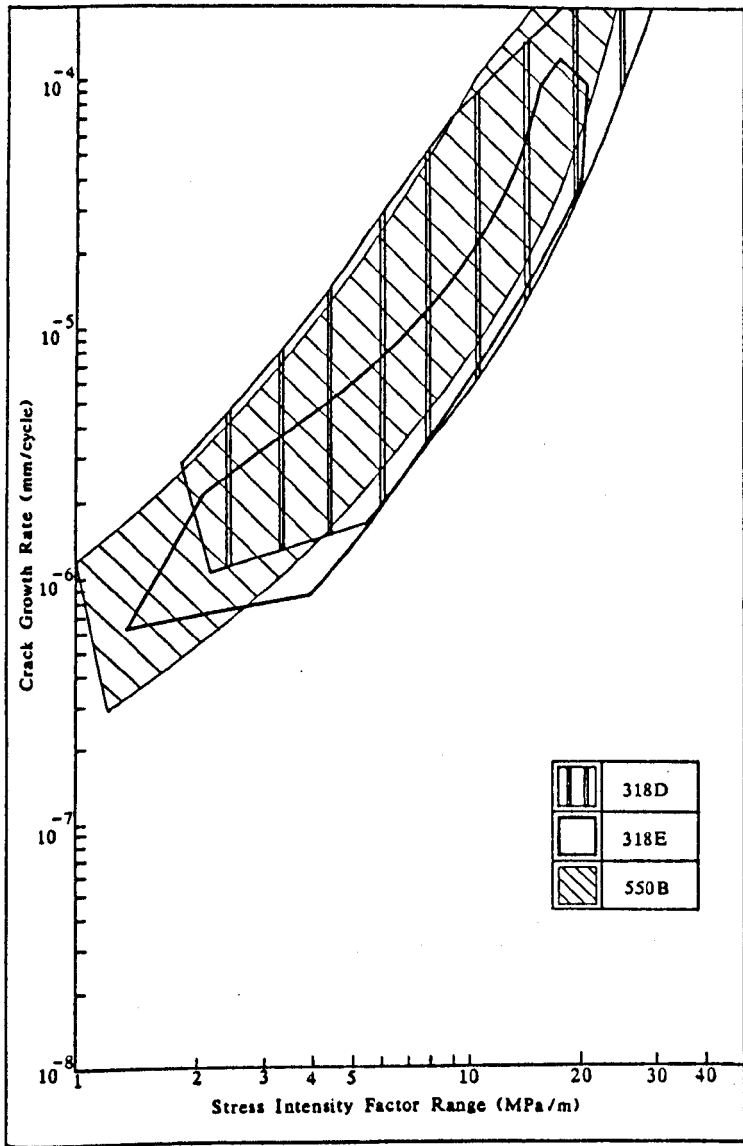
It is interesting to note from figure 8.10b that the long and short crack lines merge at about  $10 \text{ MPa}\sqrt{\text{m}}$  for the basketweave Widmanstätten microstructure, 318E. If the  $\alpha$  lath width is the controlling microstructural dimension for short crack growth, the short to long crack transition should occur at a  $\Delta K$  of approximately  $3.5 \text{ MPa}\sqrt{\text{m}}$ , according to the arguments based on the maximum plastic zone size, presented above.

Clearly this is not the case. If the proposal of Taylor (237) is considered however, whereby short crack behaviour persists up to crack depths of approximately 10 x grain size or 10 x plastic zone size, whichever is the larger, a closer comparison can be made. In this case the maximum plastic zone size ( $r_{\max}$ ) at the transition according to Irwin (equation 6.2) is 8.2  $\mu\text{m}$ . Hence  $10 \times r_{\max} = 82 \mu\text{m}$  which correlates more closely with the crack depth at the transition of approximately 100  $\mu\text{m}$ . Taylor (237) however gives no micromechanical explanation of his proposal.



9.1  $da/dN$  vs  $\Delta K$  for long, through thickness cracks in Ti-6Al-4V, comparing 318A to other studies quoted in the literature. Ref 63 Mill annealed  $R = 0.12$ ; ref 79 fine equiaxed  $\alpha + \beta$ ,  $R = 0.05$ ; ref 78 recrystallisation annealed  $R = 0.3$ ; ref 170 mill annealed,  $R = 0.2$ .

9.2  $da/dN$  vs  $\Delta K$  for all  $\alpha + \beta$  heat treated microstructures with envelopes containing all non-zero growth rate data for a number of cracks in each case.



9.3  $da/dN$  vs  $\Delta K$  for all  $\beta$  heat treated microstructures with envelopes containing all non-zero growth rate data for a number of cracks in each case.

9.4  $da/dN$  vs  $\Delta K$  comparing long, through thickness and short cracks in 318A and 318D.

## CHAPTER 10

### CRACK SHAPE

#### 10.1 THE EFFECT OF GRAIN SHAPE ON CRACK SHAPE

The pancake shaped grain structure in the aluminium alloy 7010 allowed an evaluation of the effect of grain shape on crack shape to be carried out on nominally identical specimens. By turning the square cross-sectioned specimens through 90° about their long axis an appreciably different grain structure could be analysed. The crack direction was transformed from the LS direction (figure 10.1a, c) to the LT direction (figure 10.1b, d) by such a rotation.

The series of experiments carried out on 7010 OA1, as described in section 3.4.2, produced data which can best be analysed in terms of the plots of aspect ratio ( $a/c$ ) vs crack depth ( $a$ ) in figures 10.2 and 10.3. For the LS direction cracks (figure 10.1c) the plot in figure 10.2 highlights the gradual trend of decreasing  $a/c$  ratio as the crack depth increases. Cracks initially take a semi-elliptical shape with an  $a/c$  ratio between 1.0 and 1.2. At greater crack depths (~2mm) a semi-circular form is apparent and finally (as indicated in the insert in figure 10.2) there is a tendency for semi-elliptical cracks, with  $a/c \sim 0.9$ , to develop at even greater crack depths. The use of regular bursts of overload cycles during testing produced direct evidence of this behaviour.

Figure 10.1e, the fracture surface of such a test, shows two 'beach marks' and indicates a drop in aspect ratio from 1.28 to 1.05 with an increase in crack depth from 25  $\mu\text{m}$  to 327  $\mu\text{m}$ . The larger 'beach mark' also highlights the irregularities of the crack front. Microstructural interactions with the crack tip cause local misorientations at the periphery of the crack even at this crack depth.

If grain boundaries are effective in interrupting the growth of microstructurally short cracks, the fact that the cracks are initially semi-elliptical with  $a/c > 1.0$  may appear somewhat surprising. From the pancake grain structure (figure 10.1a) it might be expected that growth into the bulk of the specimen would be disrupted to a greater extent than growth at the specimen surface, where the distance between grain boundaries is considerably larger. These high  $a/c$  ratios may be caused by the shapes of the initiating inclusion defects or the surface plane stress conditions, the effects of which could be still apparent at crack depths of a few hundred  $\mu\text{m}$ .

The tendency for the aspect ratio to fall to below 1.0 at crack depths greater than approximately 2 mm cannot be attributed to the effects of microstructure, rather it is a consequence of the crack depth relative to the size of the specimen. Similar behaviour has been reported by Smith (238) for a 2219-T87 aluminium alloy, who showed a decrease in aspect ratio as the crack depth tended towards the specimen thickness.

This effect can also be predicted if it is assumed that the crack growth is controlled by the stress intensity factor. Figure 10.4 compares the relationships between  $\Delta K$  and crack dimension for two stress intensity solutions, one for the deepest point of the crack (Shah and Kobayashi, 201-203) and the other for a crack at the specimen surface (Pickard 239). At short crack depths ( $<0.5 \mu\text{m}$ ) the solutions predict that the  $K$ 's driving crack growth at the surface and midpoint are almost the same, however, as the crack depth increases the solution for the deepest point of a crack (201-203) reaches a maximum of  $\sim 18\text{MPa}\sqrt{\text{m}}$ , and then falls off, due to the fact that the loading is inbending, while Pickard's surface crack solution (239) increases in a near linear fashion for the surface regions. Hence, for cracks greater than about  $0.5 \mu\text{m}$  faster growth would be predicted at the specimen surface and a semi-elliptical crack shape with  $a/c < 1.0$  would result.

The data presented in figure 10.2 bears some resemblance to the statistical simulations recently reported by Cox and Morris (182) as shown in figure 2.28. For their 7075-T6 alloy, which had a similar grain size to 7010 OAl, they predicted  $a/c$  ratios slightly above 1.0 for some cracks between  $50-100 \mu\text{m}$  and thereafter a fairly constant semi-elliptical crack shape ( $a/c \sim 0.8$ ). A major difference between this model and the data for 7010 OAl is apparent for cracks with a depth  $\leq 50 \mu\text{m}$ . This can be explained by the mode of initiation.

For 7010 OAl initiation was generally seen to occur at defects or inclusions, while for the simulations of Cox and Morris, initiation was modelled to occur from persistent slip bands forming long, thin microcracks with  $a/c < 0.05$ .

When the specimen orientation is rotated through  $90^\circ$  so that cracks now grow in the LT direction, a change in the crack shape is also observed. Figure 10.3 shows data for the LT direction cracks. In comparison to figure 10.2 for the LS direction cracks, little difference in  $a/c$  ratios is apparent for cracks deeper than about  $0.5 \mu\text{m}$ . For shorter cracks however, significantly higher aspect ratios are observed. An example of such a crack is shown in figure 10.1f ( $a/c$  ratio = 1.50). These observations are consistent with arguments based on the retarding effects of grain boundaries, hence the development of short crack shapes which reflect the grain morphology. The higher frequency of grain boundary interactions at the specimen surface compared to the direction into the specimen will restrict growth on the surface. This effect should continue to be apparent, if the driving forces at the surface and into the material bulk are the same, until the local microstructure no longer influences propagation. Thereafter, the shape of LS and LT direction cracks will become more similar once the effect of the initially higher  $a/c$  ratio of the LT direction cracks has disappeared.

The effect of specimen orientation on surface crack growth rates has already been analysed in Section 6.5 (figure 5.10). It was shown that if a semi-circular crack shape is assumed (i.e.  $a/c = 1.0$ ) crack growth rates in the LT orientated specimens (figure 10.1d) were consistently faster than in the LS orientation (figure 10.1c) for the range of crack depths studied. Unless the surface crack growth rate is significantly influenced by the propagation characteristics at the bottom of the crack, these observations seem slightly confusing at first sight. If grain boundaries are effective in retarding short crack propagation, better crack growth resistance would be expected for the LT direction cracks at the specimen surface, due to the higher density of boundaries. In considering only surface crack observations however, the effect of crack shape is ignored. Short cracks in LS and LT orientated specimens with identical surface crack lengths may have significantly different crack depths and a simple comparison in terms of surface crack growth rates may be unrealistic. A more appropriate parameter than crack depth may be crack area, thereby including the effects of crack shape. Figure 10.5 shows a plot of the rate of increase in crack area vs crack area for both the LS and LT orientated cracks depicted in figure 5.10. As can be seen, the curves are shifted so that they now almost lie on top of each other. This suggests that crack area may be a better parameter than surface crack length, if data from different shaped cracks needs to be correlated.

## 10.2 THE EFFECT OF GRAIN SIZE ON CRACK SHAPE

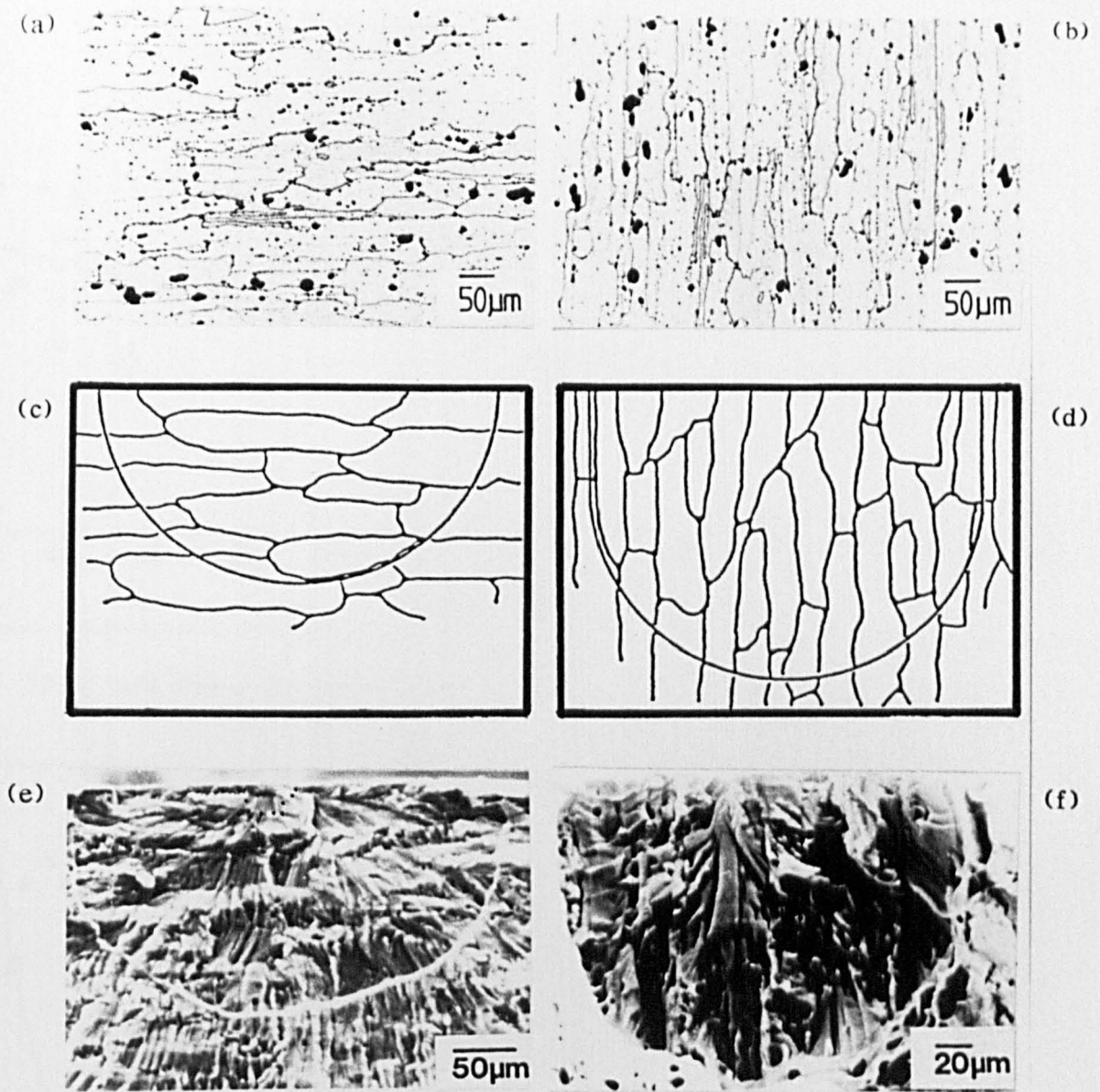
Figure 10.6 shows the a/c vs crack depth (a) relationships for the range of microstructures examined in the IMI 318 and IMI 550 titanium alloys. By dividing the microstructures into two groups, that is the  $\alpha + \beta$  heat treated (318A, 318B, 318C, 550A) and  $\beta$  heat treated (318D, 318E, 550B) microstructures, the effect of grain size on crack shape can be assessed. Although there are differences in grain size within each group, these are relatively small in comparison to the order of magnitude difference in microstructural unit size between the groups. The grain size of individual microstructures is shown in Table 7.3

For the dual phase,  $\alpha$ /transformed  $\beta$  microstructures (318A, 318B, 318C, 550A) a/c ratios generally fall between 0.8 and 1.0 over the range of crack depths studied (~0.1mm to ~3.2mm). Similar observations were made for the Widmanstätten microstructures (318D, 318E, 550B) at crack depths greater than approximately 0.75mm. Below this crack depth however, aspect ratios were seen to vary by a greater extent, with values of a/c ratio scattered between 0.75 and 2.50. Figure 10.7 shows the fracture surface of a crack in 550B which is 570  $\mu\text{m}$  deep and has a aspect ratio of 2.5. From the initiation site marked at the top of the figure, growth can be seen to have occurred along a single slip plane almost through an entire grain.

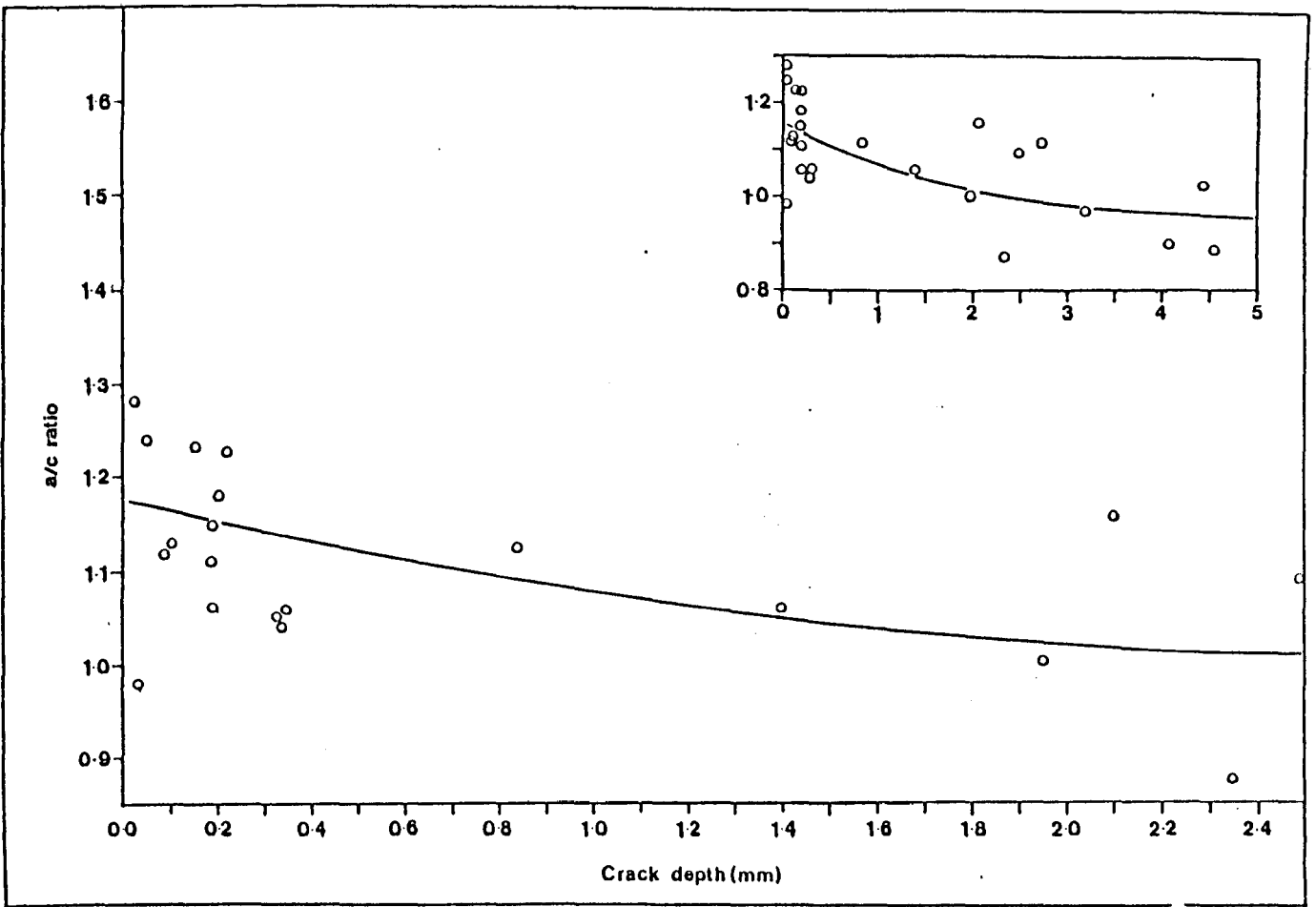
It is thought that one reason why the differences in crack shape are apparent between the two sets of microstructure, is the size of the crack relative to the grain size. For the crack depicted in figure 10.7 the crack depth is only approximately 4x Widmanstätten colony size and 2x the prior  $\beta$  grain size and hence can still be considered microstructurally short. For the  $\alpha + \beta$  heat treated morphologies a corresponding short crack, 4x size of the controlling microstructure, would only be about 40  $\mu\text{m}$  deep which is below the minimum crack depth examined in this study. It is expected that cracks of this depth would show a larger range in aspect ratio, as microstructural observations suggest that growth is confined to slip bands within the  $\alpha$  and transformed  $\beta$  phases, in a similar mode to that in the Widmanstätten morphologies. (Chapter 9).

Support for the conclusions of this study come from the work of Tokaji et al (172) who carried out similar testing on a steel with two different prior austenite grain sizes. Conversely, the work of Wagner et al (181) on a Ti-8.6 Al alloy which exhibited planar slip, suggested that grain size had less effect on crack shape and that aspect ratios were consistently less than 1.0 for both fine and coarse grained material. Their observations were dominated by the faster propagation along the specimen surface compared to the rate into the bulk, which they attributed to free surface effects. No such behaviour is reported in the present study, however a more detailed examination of crack of depth less than approximately 4x grain size would be useful in establishing a more comprehensive understanding of crack shape effects.

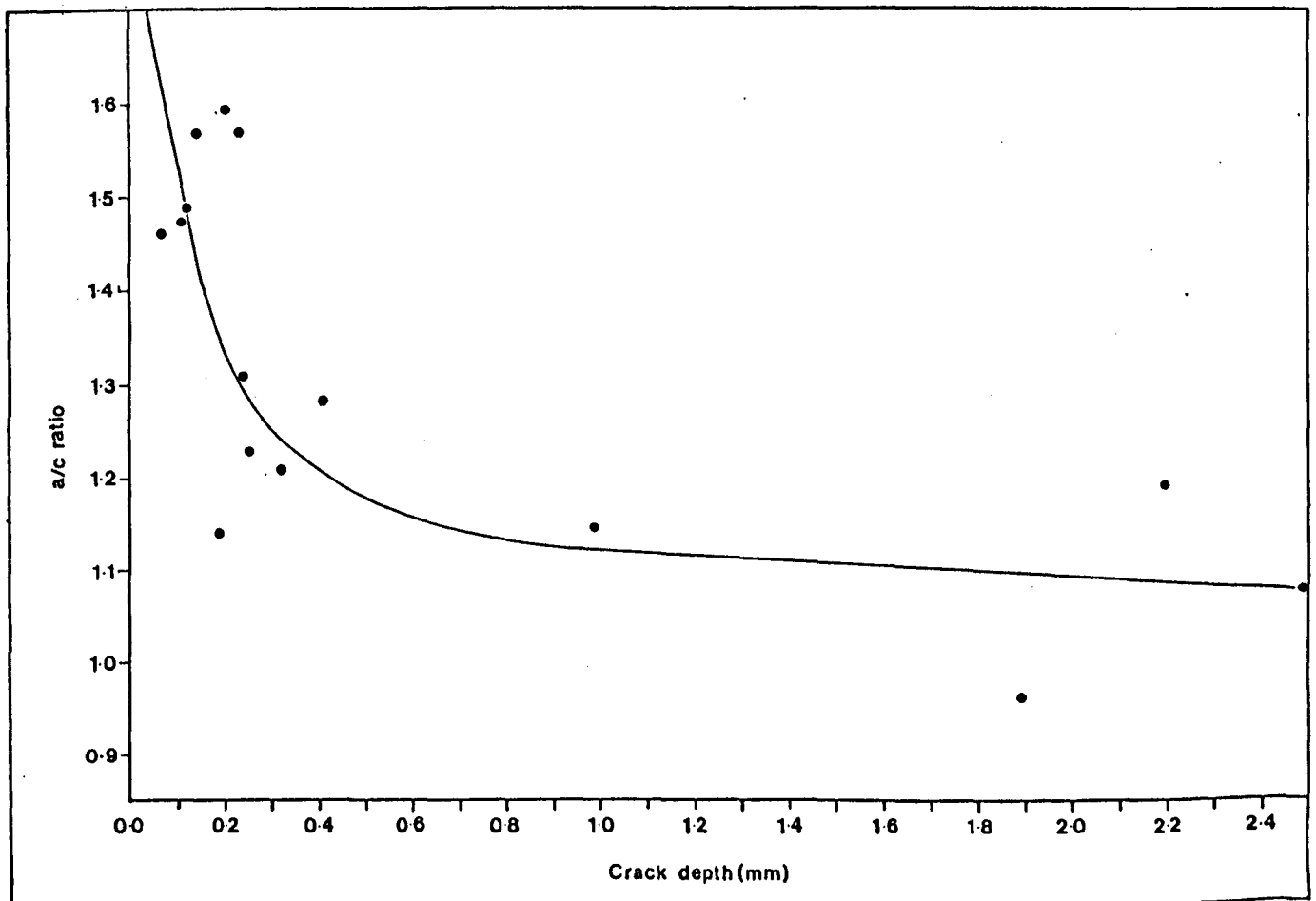
It is clear that for microstructurally short cracks an analysis based on surface crack observations may lead to errors in crack growth rate calculations. This effect will be particularly significant in cases where the controlling microstructural unit size is large. It is therefore important that crack shape determinations are carried out for individual microstructures and testing conditions before data is used in any comparative manner.



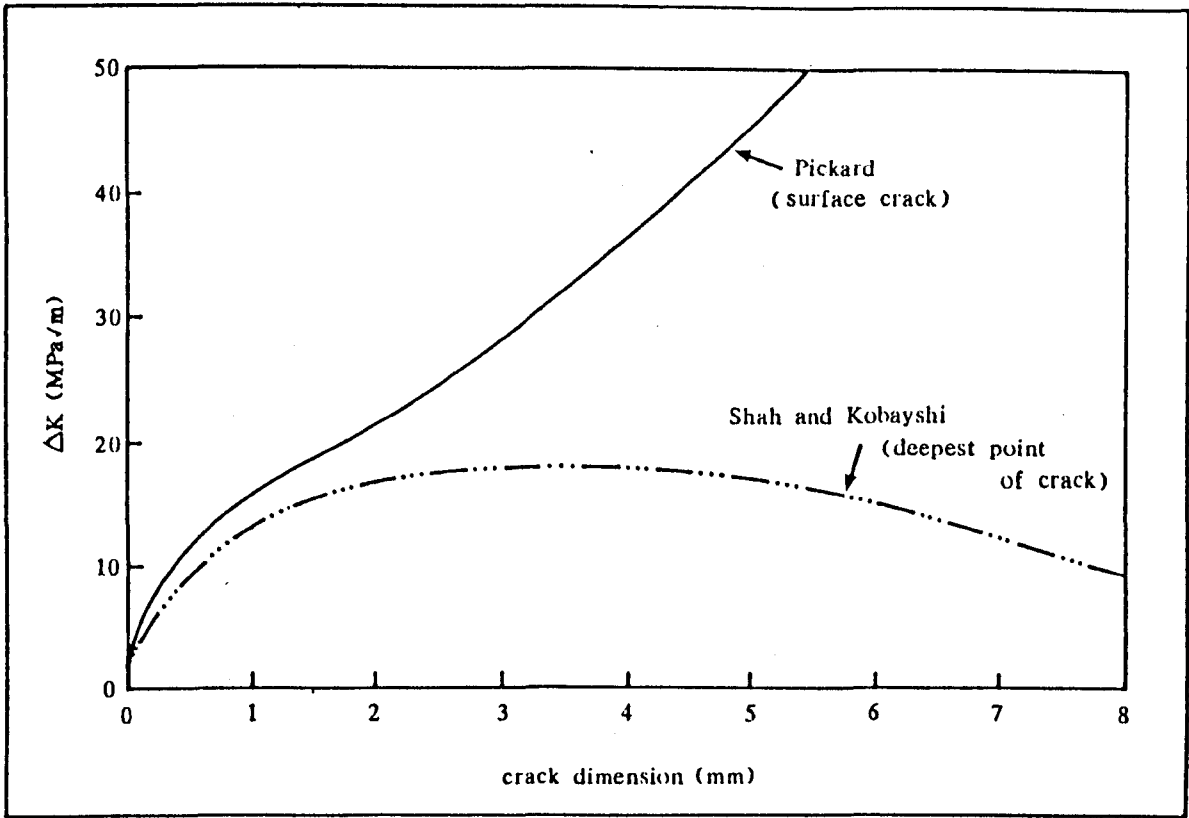
10.1 (a) (b) Optical micrographs of microstructure experienced by crack front in 7010 OAl, LS and LT direction cracks. (c) (d) schematic illustration of crack shape in LS and LT direction cracks, (e) (f) optical micrographs of crack shape in LS and LT direction cracks. (a) (c) and (e) represent LS direction cracks, (b) (d) and (f) represent LT direction cracks.



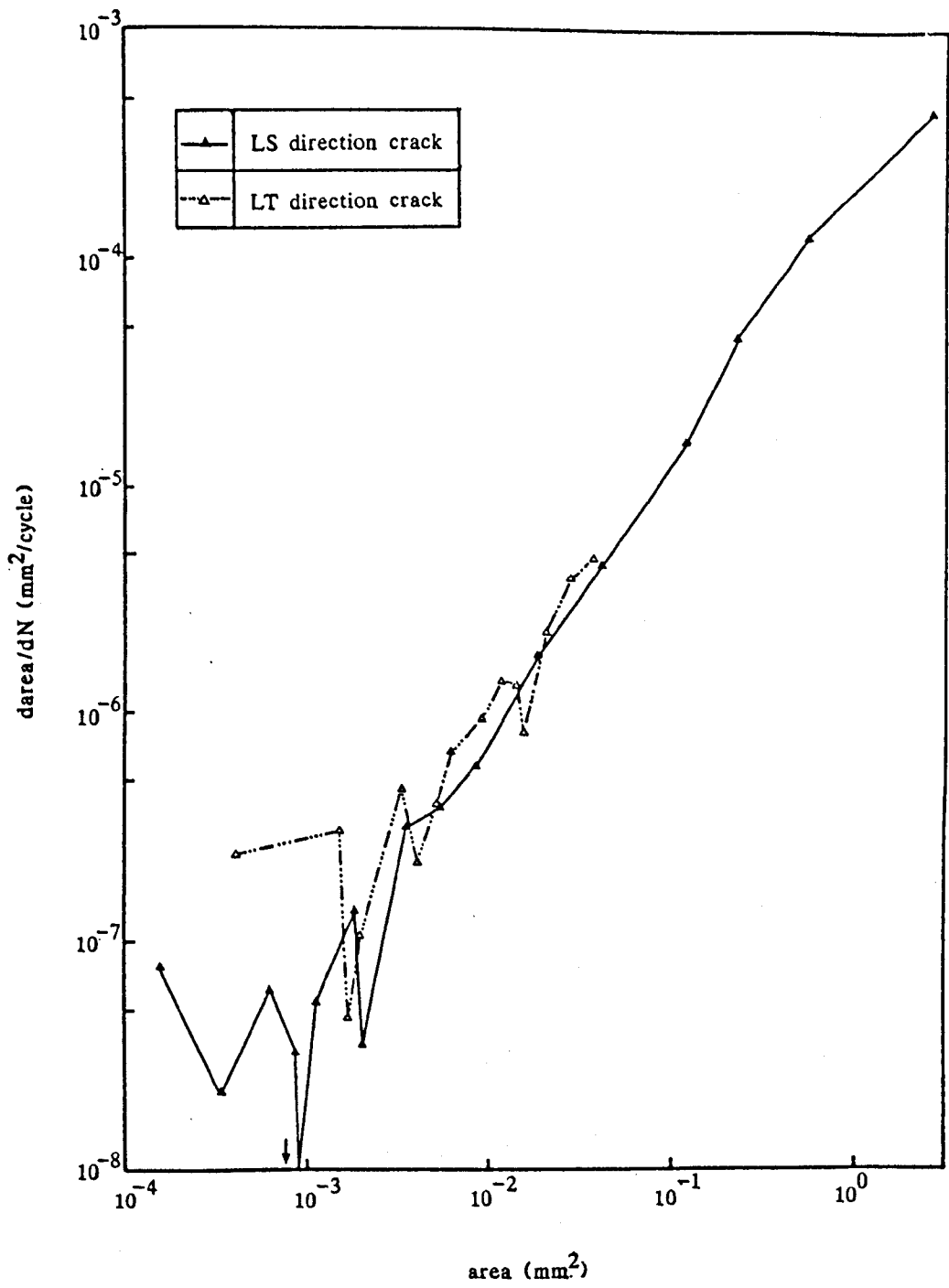
10.2 a/c ratio vs crack depth for LS direction cracks as 7010 OAl



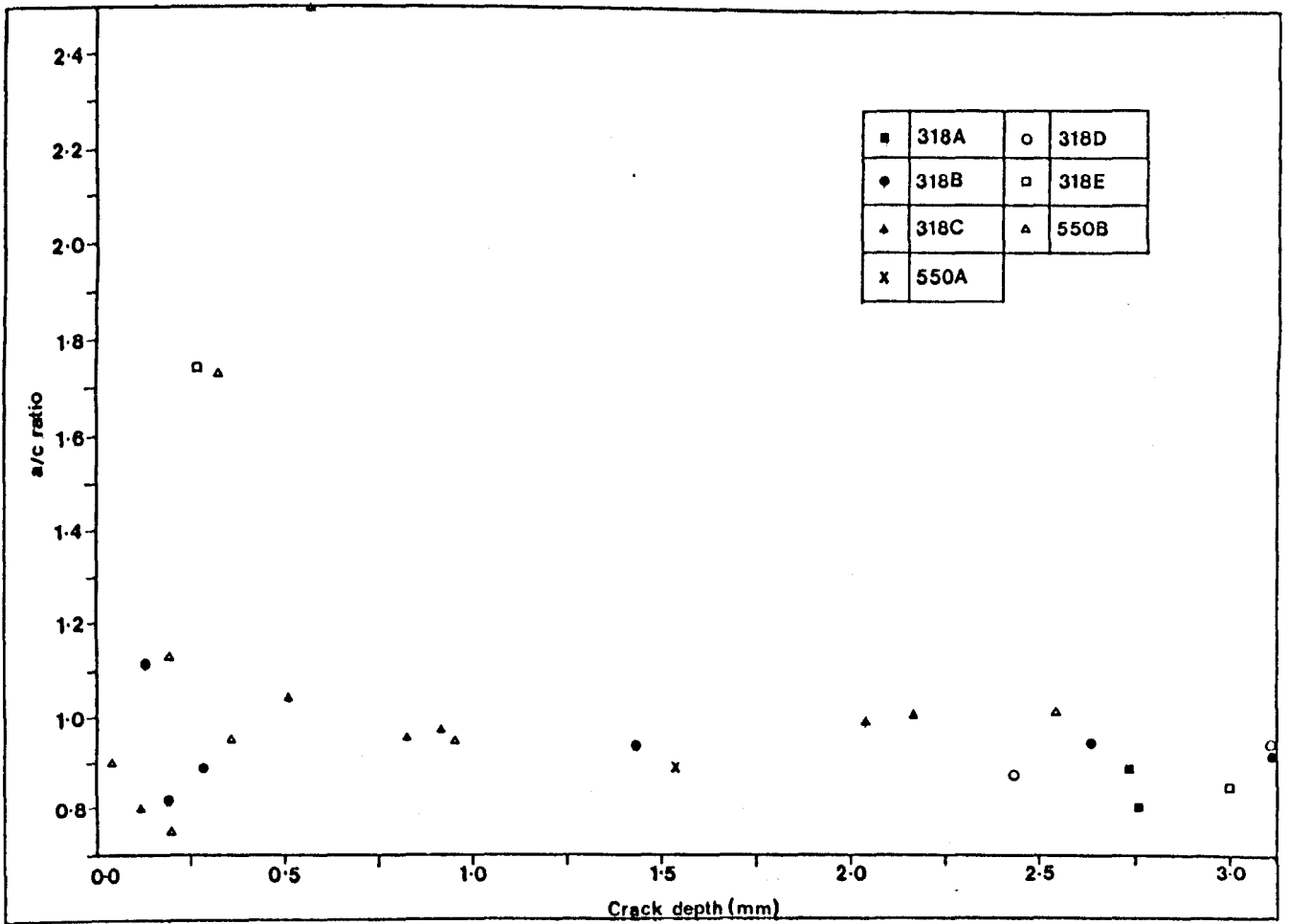
10.3 a/c ratio vs crack depth for LT direction cracks in 7010 OAl



10.4 Variation in  $\Delta K$  with crack dimensions for surface crack (239) and deepest point of crack. (201-203).

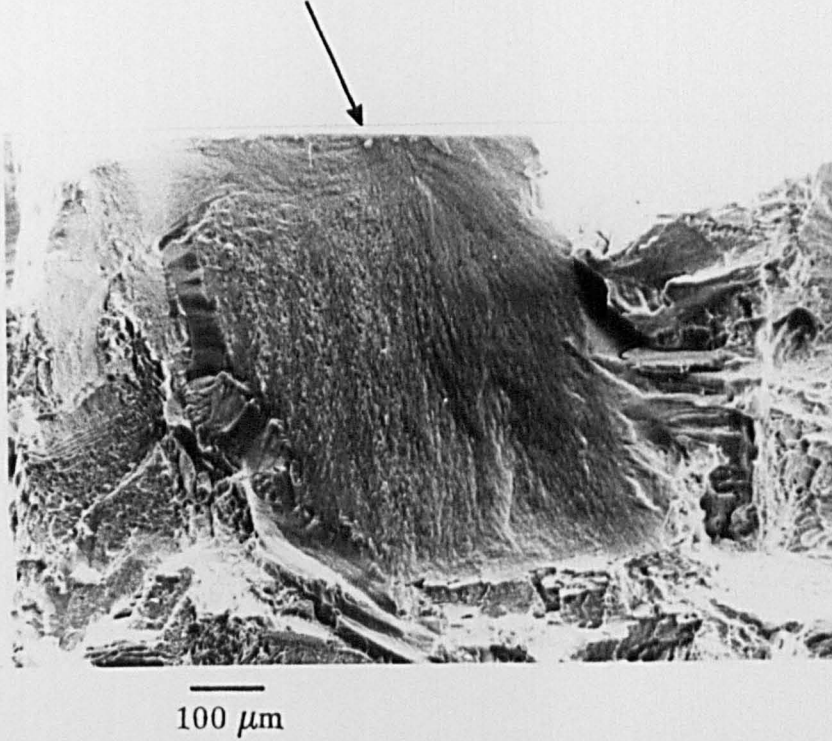


10.5 Increase in crack area per cycle vs crack area for LS & LT direction cracks in 7010 OAl.



10.6 a/c ratio vs crack depth for IMI 318 and IMI 550

initiation site



10.7      Electron micrograph of fracture surface of short crack  
            in 550B showing high aspect ratio.

## CONCLUSIONS

1. Microstructurally short fatigue cracks (cracks shorter than approximately ten times the size of the controlling microstructure) grow at substantially faster rates than long, through thickness cracks at the same apparent applied  $\Delta K$  and  $R = 0.1$ .
2. The non-continuum growth characteristics of these cracks when their depths are of the same magnitude as the material grain size, can be attributed to crack tip: local microstructure interactions. In particular, grain boundaries are seen to be effective in halting or decelerating growth.
3. The end of the microstructurally short fatigue crack regime can often be correlated with the maximum plastic zone size ahead of the crack tip reaching the size of the controlling microstructural dimensions.
4. Differences in propagation behaviour between long and short cracks at higher  $\Delta K$ s can be attributed to variations in closure contributions, ('physically short cracks') to the suitability of the stress intensity solutions used in the study and to the effects of specimen thickness. However, even though the conditions for the use of LEFM are violated, in describing short crack growth, it remains a useful parameter in modelling average growth behaviour of such cracks down to very short crack depths.

5. For the two high strength aluminium alloys studied, an increase in the degree of ageing leads to a degradation in short fatigue crack resistance. Similar behaviour is commonly observed for long, through thickness cracks in these alloys. For the 7010 alloy, short crack growth rates at  $R = 0.1$  are bounded by the long crack data measured at high  $R$  - ratio, over the range of crack length and  $\Delta K$  it has been possible to obtain in these tests, but lie above the long crack growth rates at  $R = 0.1$ . Furthermore, long and short cracks at low  $\Delta K$  for both underaged and overaged microstructures produce similar faceted fracture surfaces, indicating that the same crack propagation mechanism is operative despite the differences in propagation rate.
6. The limited data collected for microstructurally short cracks subjected to different maximum stress levels suggest that they have little influence on short crack propagation behaviour when analysed in terms of  $\Delta K$ . For such cracks growing at different load ratios however, an increase in  $R$  - ratio lead to an enhancement in propagation rates suggesting that crack closure may still be important for these cracks.

7. Data collected for the titanium alloys studied shows that, in contrast to conventional, long through thickness crack behaviour, an increase in grain size leads to a degradation in short fatigue crack resistance. These observations indicate that the influence of closure mechanisms are diminished when the crack depth is of the same order of magnitude as the microstructural unit size.
8. For the "dual phase"  $\alpha + \beta$  heat treated microstructures, short crack growth resistance is enhanced with the increased density of primary  $\alpha$ : transformed  $\beta$  grain boundaries which have the effect of disrupting uniform growth and deflecting the crack tip. A short fatigue crack resistant alloy would, therefore, require a fine grain size containing equal proportions of primary  $\alpha$  and transformed  $\beta$  phases. An equiaxed and distinct primary  $\alpha$  grain structure would also benefit initiation resistance.
9. The propagation resistance of  $\beta$  heat treated microstructures is dependent on the Widmanstätten packet and colony size, which appears to control slip length.

10. As grain boundaries can reduce local crack propagation rates they can also affect crack shape. The extent of this effect depends on both grain size and shape, however, as the replication technique used to monitor crack advance can only detect surface crack growth, crack shape development needs to be established by additional testing.
  
11. When comparing crack growth data for microstructures with different morphologies a better measure may be crack area rather than surface crack length, hence the influence of crack shape on driving forces can be accommodated. For longer cracks, which can no longer be described as microstructurally short, crack shapes tend towards the semi-elliptical shape ( $a/c = 0.8 \rightarrow 1.0$ ) predicted by stress intensity solutions for bars in bending.

#### FURTHER WORK

1. As assessment of the fatigue crack propagation resistance of more heavily overaged and less aged aluminium alloy microstructures, with identical 0.2% proof stresses, will exaggerate the ageing effects discussed in this study. This, coupled with an extensive transmission electron microscope evaluation of material close to the crack tip would provide details of the deformation mechanisms operating.
2. As differences in closure contributions at low growth rates have been proposed as being one of the major reasons why short cracks grow at faster rates than predicted by LEFM, operation of short crack testing at high R - ratios (up to 0.8) would be useful. Such testing would be difficult to achieve from naturally initiating cracks on a smooth specimen surface and alternative techniques would need to be developed. For example, a crack could be initiated at low R - ratio and the specimen re-heat treated, to relieve residual stresses, prior to continuation of cycling at a higher R - ratio.

3. A more comprehensive assessment of the effects of grain size on short crack propagation resistance of  $\beta$ - heat treated, Widmanstätten titanium microstructures could be made. By increasing the heat treatment time or temperature to promote  $\beta$  grain growth, microstructures with grain sizes ranging from a few hundred micrometres to several millimeters could be produced.
4. Controlled experiments need to be carried out to examine the effects of crystallographic texture on short crack propagation.
5. The collection of further crack shape data, specifically for cracks with depths approximating to the material grain size, will allow statistically based crack shape models to be verified.

#### ACKNOWLEDGEMENTS

I am deeply indebted to Dr. J. E. King for her supervision and guidance through this work. I would like to thank Mr. K. Dinsdale for his continued advice and assistance with the technical aspects of the project and this appreciation is also extended to the technical staff of the Department of Metallurgy and Materials Science. Thanks are due to the Royal Aircraft Establishment, Farnborough for financial support and in particular to Dr. R. N. Wilson for many helpful discussions. Gratitude is also expressed to Professor J. S. L. Leach for provision of laboratory facilities within the department and to Mrs. M. A. Dicker for typing the manuscript.

Finally, many thanks are due to friends for their continued encouragement during the long period of this study and in particular to Karen, John and Lorna.

## REFERENCES

1. PARIS P.C., GOMEZ M. & ANDERSON W.E., *Trend in Eng.*, 13, (1961), 9.
2. JOHNSTON R., BRETHERTON I, TOMKINS B., SCOTT P.M. & SILVESTER D.R.V., *European Offshore Research Sem., The Welding Inst.*, (1980), 387.
3. RITCHIE R.O. & SURESH S., *Met. Trans. A*, 13A, (1982), 937.
4. PEARSON S., *Eng. Fract. Mech.*, 7, (1975), 235.
5. SURESH S. & RITCHIE R.O., *Int. Met. Rev.*, 29, (1984), 445.
6. ENDO K., KOMAI K. & MATSUDA Y., *Memo. Fac. Eng., Kyoto Uni.*, 31, (1969), 25.
7. ELBER W., *Eng. Fract. Mech.*, 2, (1970), 37.
8. ELBER W., *ASTM STP 486*, (1971), 280.
9. HUDSON C.M., *NASA TN D-5390, Nat. Aero & Space Admin.*, (1969).
10. LINDLEY T.C. & RICHARDS C.E., *Mat. Sci. & Eng.*, 14, (1974), 281.
11. NEWMAN J.C., *AGARD Conf. Proc. 328, France*, (1983).
12. SURESH S. & RITCHIE R.O., *Fat. Crack Growth Thres. Concepts*, eds; DAVIDSON D. & SURESH S., Philadelphia, USA, (1984), 227.
13. SURESH S., ZAMISKI G.F. & RITCHIE R.O., *Met. Trans. A*, 12A, (1981), 1435
14. STEWART A.T., *Eng. Fract. Mech.*, 13, (1980), 463.
15. RITCHIE R.O., SURESH S. & MOSS C.M., *J. Eng. Mat. Tech., Trans ASME Series H*, 102, (1980), 293.
16. COOKE R.J., IRVING P.E., BOOTH G.S. & BEEVERS C.J., *Eng. Fract. Mech.* 7, (1975), 69.
17. TOPLOSKY J. & RITCHIE R.O., *Scripta Met.*, 15, (1981), 905.
18. RITCHIE R.O., SURESH S. & LIAW P.K., *Ultrasonic Fat.*, eds WELLS J.M., BUCK. O., ROTH L.D. & TIEN J.K., TMS-AIME, Warrendale, PA, (1982) 443.
19. AUSTEN I.M. & McINTYRE P., *Met. Sci.*, 13, (1979), 420.
20. VASUDÉVAN A.K. & SURESH S., *Met. Trans. A*, 13A, (1982), 2271.
21. SURESH S., VASUDÉVAN A.K. & BRETZ P.E., *Met. Trans. A*, 15A, (1984), 369.
22. DUQUETTE D.J., *Corr. Fat.*, *AGARD Conf. Proc. 316, Turkey*, (1981).
23. CARTER R.D., LEE E.W., STARKE Jr. E.A. & BEEVERS C.J., *Met. Trans. A.*, 15A, (1984), 555.
24. GOUGH H.J. & SOPWITH D.G., *J. Inst., Met.*, 49, (1932), 93.
25. PELLOUX R.M.N., *Trans. ASM*, 62, (1969), 281.
26. VASUDÉVAN A.K. & BRETZ P.E., *Fat. Crack Growth Thres. Concepts*, eds.; DAVIDSON D. & SURESH S., Philadelphia, USA, (1984), 25.
27. BRADSHAW F.J. & WHEELER C., *Int. J. Fract. Mech.*, 5, (1969), 255.
28. IRVING P.E. & BEEVERS C.J., *Met. Trans.* 5, (1974), 391.
29. BEEVERS C.J. & IRVING P.E., *Effects of Chemical Environment on Fracture Processes*, (1974), 179.
30. BEEVERS C.J., *Met. Sci.*, 11, (1977), 362.
31. RUPPEN J. & McEVILY A.J., *Fat. Eng. Mat & Struct.*, 2, (1979), 63.
32. ROBINSON J.L. & BEEVERS C.J., *Met. Sci. J.*, 7, (1973), 153.
33. PETERS M., GYSLER A., & LÜTJERING G., *Met. Trans. A*, 15A, (1984), 1597.
34. GRAY III G.T. & LÜTJERING G., "Ti, Sci & Tech." 5th Int. Conf. on Ti, Munich, FRG, eds; LÜTJERING G., SWICKER U. & BUNK W., (1984), 2251.
35. MOODY N.R. & GERBERICH W.W., *Met. Trans. A*, 11A, (1980), 973.
36. MOODY N.R. & GERBERICH W.W., *Met. Trans. A*, 13A, (1982), 1055.
37. MEYN D.A., *Met. Trans.*, 3, (1972), 2302.
38. MEYN D.A., *Met. Trans.*, 2, (1971), 853.

39. PATON P.E. & SPURLING R.A., *Met. Trans. A*, 7A, (1976), 1769.
40. FORSYTH P.J.E., *Proc. Crack Prop. Symp.*, Cranfield, (1961), 76.
41. OTSUKA A., MORI K. & MIYATA T., *Eng. Fract. Mech.*, 7, (1975), 429.
42. MINAKAWA K. & McEVILY A.J., *Scripta Met.*, 15, (1981), 633.
43. WALKER N. & BEEVERS C.J., *Fat. Eng. Mat. & Struct.*, 1, (1979), 135.
44. PURUSHOTHAMAN S. & TIEN J.K., *ICSMA5*, eds.; HAASEN P., GEROLD V. & KORTORZ G., Aachen, W. Germany, (1979), 1267.
45. SURESH S. & RITCHIE R.O., *Met. Trans. A*, 13A, (1982), 1627.
46. BEEVERS C.J., BELL K., CARLSON R.L. & STARKE Jr. E.A., *Eng. Fract. Mech.*, 19, (1984), 93.
47. BROWN C.W., KING J.E., & HICKS M.A., *Met. Sci.*, 18, (1984), 374.
48. VENABLES R.A., HICKS M.A. & KING J.E., *Fat. Crack Growth Thres. Concepts*, eds.; DAVIDSON D & SURESH S., Philadelphia, USA (1984), 341.
49. DUGGAN T.V., *Fat. Thresholds*, eds.; BACKLUND J., BLOM A. & BEEVERS C.J., Stockholm, Sweden, (1981), 809.
50. HUSSEY I.W., BRYNE J. & DUGGAN T.V., *Fatigue 84*, ed. BEEVERS C.J., Birmingham, UK, (1984), 807.
51. MINAKAWA K., NEWMAN J.C. & McEVILY A.J., *Fat. Eng. Mat. & Struct.*, 6, (1983), 359.
52. ZAIKEN E. & RITCHIE R.O., *Scripta Met.*, 18, (1984), 847.
53. ZAIKEN E. & RITCHIE R.O., *Met. Trans. A*, 16A, (1985), 1467.
54. GRAY III G.T., WILLIAMS J.C. & THOMPSON A.W., *Met. Trans. A*, 14A, (1983), 421.
55. GRAY III G.T., THOMPSON A.W. & WILLIAMS J.C., *Fat. Crack Growth Thres. Concepts*, eds. DAVIDSON D.L & SURESH S., Philadelphia, USA (1984), 131.
56. GRAY III G.T., THOMPSON A.W., WILLIAMS J.C. & STONE D.H., *Fat. Thres. eds.*; BACKLUND J., BLOM A. & BEEVERS C.J., Stockholm, Sweden, (1981), 345.
57. RITCHIE R.O., *Int. Met. Rev.*, 24, (1979), 205.
58. MINAKAWA K. & McEVILY A.J., *ICSMA5* eds.; HAASEN P., GEROLD V. & KORTORZ G., Aachen, W. Germany, (1979).1145.
59. BENSON J.P. & EDMONDS D.V., *Met. Sci.*, 12, (1978), 223.
60. MASOUNAVE J. & BAILON J-P., *Scripta Met.*, 10, (1976), 165.
61. BAILON J-P., MASOUNAVE J. & LANKEIGNE J., *Scripta Met.*, 12, (1978), 607.
62. PRIDDLE E.K., *Scripta Met.*, 12, (1978), 49.
63. IRVING P.E. & BEEVERS C.J., *Mat. Sci. & Eng.*, 14, (1974), 229.
64. YUEN A., HOPKINS S.W., LEVERANT G.R. & RAU C.A., *Met. Trans.*, 5, (1974) 1833.
65. CHESNUTT J.C. & WERT J.A., *Fat. Crack Growth Thres. Concepts*, eds.; DAVIDSON D.L. & SURESH S., Philadelphia, USA, (1984), 83.
66. YODER G.R., COOLEY L.A. & CROOKER T.W., *Eng. Fract. Mech.*, 17, (1983), 185.
67. HALLIDAY M.D. & BEEVERS C.J., *J. Test Eval.*, 9, (1981), 195.
68. HICKS M.A., JEAL R.H. & BEEVERS C.J., *Fat. Eng. Mat. & Struct.*, 6, (1983), 51.
69. ASARO R.J., HERMANN L. & BAIK J.M., *Met. Trans. A*, 12A, (1981), 1133.
70. GYSLER A., LINDIGKEIT J. & LÜTJERING G., *ICSMA5* eds.; HAASEN P., GEROLD V. & KORTORZ G., Aachen, W. Germany, (1979), 1113.
71. LINKIGKEIT J., TERLINDE G., GYSLER A. & LÜTJERING G., *Acta Met.*, 27, (1979), 1717.
72. VASUDEVAN A.K., BRETZ P.E. & MILLER A.C., *Mat. Sci. & Eng.*, 64, (1984), 113.
73. SURESH S., *Met. Trans. A*, 14A, (1983), 2375.
74. SURESH S., *Met. Trans. A*, 16A, (1985), 249.
75. BILBY. B.A., CARDEW G.E. & HOWARD I.C., *Fracture 1977 (ICF4)*, ed.; TAPLIN D.M.R., Waterloo, Canada, (1977), 197.
76. CARLSON M.F. & RITCHIE R.O., *Scripta Met.*, 11, (1977), 1113.
77. CARLSON M.F. & RITCHIE R.O., *Scripta Met.*, 12, (1978), 613.
78. CHESNUTT J.C., "Ti, Sci. & Tech." 5th Int. Conf. on Ti, Munich, FRG, eds.; LÜTJERING G., SWICKER U. & BUNK W., (1984), 2227.

79. PETERS M., WELPMANN K. & DOKER H., "Ti, Sci & Tech" 5th Int Conf on Ti, Munich, FRG, eds; LÜTJERING G., ZWICKER U. & BUNK W., (1984), 2267.
80. THOMPSON A.W., WILLIAMS J.C., FRANSEN J.D. & CHESNUTT J.C., "Ti & Ti Alloys", Proc. 3rd Int. Conf. on Ti, Moscow, USSR, eds; WILLIAMS J.C. & BELOV A.F. (1976), 691.
81. BANIA P.J., BIDWELL L.R., HALL J.A., EYLON D. & CHAKRABARTI A.K., "Ti & Ti Alloys" Proc. 3rd Int. Conf. on Ti, Moscow, USSR, eds; WILLIAMS J.C. & BELOV A.F. (1976), 663.
82. EYLON D., & BANIA P.J., Met. Trans. A, 9A, (1978), 1273.
83. YODER G.R., COOLEY L.A. & CROOKER T.W., Eng. Fract. Mech., 11, (1979), 805.
84. YODER G.R., COOLEY L.A. & CROOKER T.W., Met. Trans A, 9A, (1978), 1413.
85. EYLON D., Met. Trans. A, 10A, (1979), 311.
86. YODER G.R., & EYLON D., Met. Trans. A, 10A, (1979), 1809.
87. BRETZ P.E., PETIT J.I. & VASUDEVAN A.K., Fat. Crack Growth Thres. Concepts, eds; DAVIDSON D.L. & SURESH S., Philadelphia, USA, (1984), 163.
88. PETIT J.I. & BRETZ P.E., Proc. Conf. High Strength P/M Al Alloys eds; HILDEMAN G.J. & KOCZAK M.J., AIME, (1982), 147.
89. DAVIDSON D.L. & LANKFORD J., Mat. Sci. & Eng., 74, (1985), 189.
90. ZAIKEN E. & RITCHIE R.O., Mat. Sci. & Eng., 70, (1985), 151.
91. ZAIKEN E. & RITCHIE R.O., Eng. Fract. Mech., 22, (1985), 35.
92. HORNBOKEN E. & ZUM GAHR K-H., Acta Met., 24, (1976), 581.
93. ALBRECHT J. & LÜTJERING G., Met. Sci., 15, (1981), 323.
94. LINDIGKEIT J., GYSLER A. & LÜTJERING G., Met. Trans. A, 12A, (1981), 1613.
95. RENAUD P., VIOLAN P., PETIT J. & FERTON D., Scripta Met. 16, (1982), 1311.
96. PETIT J., Fat. Crack Growth Thres. Concepts, eds; DAVIDSON D.L. & SURESH S., Philadelphia, USA, (1984), 3.
97. SURESH S. & VASUDEVAN A.K., Fat. Crack Growth Thres. Concepts, eds; DAVIDSON D.L. & SURESH S., Philadelphia, USA, (1984), 361.
98. ZEDALIS M., & FINE M.E., Scripta Met., 16, (1982), 1411.
99. LIN F-S & STARKE Jr. E.A., Mat. Sci. & Eng., 39, (1979), 27.
100. LIN F-S & STARKE Jr. E.A., Mat. Sci. & Eng., 43, (1980), 65.
101. LIN F-S & STARKE Jr. E.A., Mat. Sci. & Eng., 45, (1980), 153.
102. ZEDALIS M., FILLER L. & FINE M.E., Scripta Met., 16, (1982), 471.
103. YODER G.R., COOLEY L.A. & CROOKER T.W., Fatigue '84, ed BEEVERS C.J., Birmingham, UK, (1984), 351.
104. YODER G.R., COOLEY L.A. & CROOKER T.W., Met. Trans. A, 8A, (1977), 1737.
105. YODER G.R., COOLEY, L.A. & CROOKER T.W., J. Eng. Mat. & Tech., Trans ASME, 101, (1979), 86.
106. YODER G.R., FROES F.H. & EYLON D., Met. Trans. A, 15A, (1984), 183.
107. YODER G.R., COOLEY L.A. & CROOKER T.W., Scripta Met., 16, (1982), 1021.
108. SUZUKI H. & McEVILY A.J., Met. Trans A, 10A, (1979), 475.
109. RICE J.R., ASTM STP 415, (1967), 247.
110. BUCCI R.J., VASUDEVAN A.K., BRETZ P.E. & MALCOLM R.C., Interim Rep. to Nav. Air Systems Comm., Contract No. N00019-76-C-0258, Alcoa Labs, Alcoa Cen., PA, USA, (1980).
111. STUBBINGTON C.A. & FORSTH P.J.E., Metallurgica, 74, (1966), 15.
112. GARRETT G.G. & KNOTT J.F., Acta Met., 23 (1975), 841.
113. HIGO Y., PICKARD A.C. & KNOTT J.F., Met. Sci., 15, (1981), 233.
114. BOWLES C.Q. & BROEK D., Int. J. Fract. Mech., 8, (1972), 75.
115. LAIRD C., ASTM-STP 415, (1966), 131.
116. NIX K.J. & FLOWER H.M., Acta Met., 30, (1982), 1549.
117. MINAKAWA K., MATSUO Y. & McEVILY A.J., Met. Trans. A, 13A, (1982), 439.
118. DUTTA V.B., SURESH S. & RITCHIE R.O., Met. Trans. A, 15A, (1984), 1193.
119. TZOU J-L. & RITCHIE R.O., Scripta Met., 19, (1985), 751.
120. WASYNCZUK J.A., RITCHIE R.O. & THOMAS G., Mat. Sci. & Eng., 62, (1984), 79.
121. EWING J.A. & HUMPHREY J.C.W., Phil. Trans., A200, (1903), 241.

122. THOMPSON N., WADSWORTH N.J. & LOUAT N., *Phil. Mag.*, 1, (1956), 113.
123. FORSYTH P.J.E. & STUBBINGTON C.A., *J. Inst. Met.*, 86, (1957-58), 90.
124. COTTRELL A.H. & HULL D., *Proc. Royal. Soc.*, A242, (1957), 211.
125. NEUMANN P., *Acta Met.*, 17, (1969), 1219.
126. FINE M.E. & RITCHIE R.O., *ASTM-STP 675*, (1979), 245
127. MILLER K.J., *Fat. Eng. Mat. & Struct.*, 5, (1982), 223.
128. De Los RIOS E.R., MOHAMED H.J. & MILLER K.J., *Fat. Eng. Mat. & Struct.*, 8, (1985), 49.
129. SAUNDERS Jr. T.H. & STARKE Jr. E.A., *Met. Trans. A*, 7A, (1976), 1407.
130. LÜTJERING G., HAMAJIMA T. & GYSLER A., *Fracture 1977 (ICF4)*, ed. TAPLIN D.M.R., Waterloo, Canada, (1977), 7.
131. KUNG C.Y. & FINE M.E., *Met. Trans. A*, 10A, (1979), 603.
132. GROSSKRUETZ J.C. & SHAW G.G., *ICF2*, ed. PRATT P.L. London, (1969), 620.
133. PARTRIDGE P.G. & PEEL C.J., "Sci., Tech. & App. of Ti", 1st Int. Conf. on Ti, London, eds; JAFFEE R.T. & PROMISEL N.E., 21-24 May 1968 517.
134. WELLS C.H. & SULLIVAN C.P., *Trans. ASM*, 62, (1969), 263.
135. BENSON D.K., GROSSKRUETZ J.C. & SHAW G.G., *Met. Trans.*, 3, (1972), 1239.
136. STUBBINGTON C.A. & BOWEN A.W., *J. Mat. Sci.*, 9, (1974), 941.
137. STEELE R.K. & McEVILY A.J., *Eng. Fract. Mech.*, 8, (1976), 31.
138. BROWN C.W., PhD Thesis, Cambridge, 1981.
139. LIU S.Z., MINAKAWA K., SCHOLTES B. & McEVILY A.J., *Met. Trans. A*, 16A, (1985), 144.
140. BOWEN A.W. & STUBBINGTON C.A., "Ti., Sci. & Tech." 2nd Int. Conf. on Ti, Cambridge, Mass. USA, eds; JAFFEE R.I. & BURTE H.M. May 2-5 1972, 2097.
141. BOWEN A.W., "Ti, Sci. & Tech"., 2nd Int. Conf. on Ti, Cambridge, Mass. USA, eds; JAFFEE R.I. & BURTE H.M., May 2-5 1972, 1271.
142. NEAL D.F. & BLENKINSOP. P.A., *Acta Met.*, 24, (1976), 59.
143. RUPPEN J., BHOWAL P., EYLON D. & McEVILY A.J., *ASTM STP 675*, (1979), 47.
144. BROWN R. & SMITH G.C., *Fat. Eng. Mat. & Struct.*, 7, (1984), 229.
145. LUCAS J.J., "Ti, Sci. & Tech"., 2nd Int. Conf. on Ti, Cambridge, Mass. USA. eds; JAFFEE R.I. & BURTE H.M., May 2-5 1972, 2081.
146. LUCAS J.J. & KONIECZNY P.P., *Met. Trans.*, 2, (1971), 911.
147. De LANGE R.G., *Trans. Met. Soc. AIME*, 20, (1964), 644.
148. LANKFORD J., *Fat. Eng. Mat. & Struct.*, 5, (1982), 233.
149. LANKFORD J., *Fat. Eng. Mat. & Struct.*, 6, (1983), 15.
150. KITAGAWA H. & TAKAHASHI S., *Proc. 2nd Int. Conf. on Mech. Behaviour of Mats.*, Boston, Mass, USA, (1976), 627.
151. TAYLOR D. & KNOTT J.F., *Fat. Eng. Mat. & Struct.*, 4, (1981), 147.
152. ROMANIV O.N., SIMINKOVICH V.N. & TKACH A.N., *Fat. Thresholds*, eds; BACKLUND J., BLOM A. & BEEVERS C.J., Stockholm, Sweden, (1981), 799.
153. LANKFORD J., *Eng. Fract. Mech.*, 9, (1977), 617.
154. LANKFORD J., *Int. J. Fract.*, 16, (1980), R7.
155. NAKAI Y. & TANAKA K., *Proc. 23rd Japan. Cong. on Mat. Research*, (1980), 106.
156. SMITH R.A., *Int. J. Fract.*, 13, (1977), RCR 717.
157. TANAKA K., NAKAI Y. & YAMASHITA M., *Int. J. Fract.*, 17, (1981), 519.
158. EL HADDAD M.H., SMITH K.N. & TOPPER T.H., *Trans. ASME*, 101, (1979), 42.
159. CHAN K.S. & LANKFORD J., *Scripta Met.*, 17, (1983), 529.
160. WARD-CLOSE M., "Ti, Sci & Tech", *proc 5th Int. Conf. on Ti.*, Munnich, FRG, September 10-14, 1984, eds; LÜTJERING G, SWICKER U & BUNK W, 2318.
161. MORRIS W.L., *Met. Trans. A*, 11A, (1980), 1117.
162. MORRIS W.L., JAMES M.R. & BUCK O., *Met. Trans. A*, 12A, (1981), 57.
163. ZUREK A.K., JAMES M.R. & MORRIS W.L., *Met. Trans. A*, 14A, (1983), 1697.
164. MORRIS W.L., JAMES M.R. & BUCK O., *Eng. Fract. Mech.*, 18, (1983), 871
165. EASTABROOK J.N., *Int. J. Fracture*, 24, (1984), 1243.

166. GERDES C., GYSLER A. & LÜTJERING G., Fat. Crack Growth Thres Concepts eds; DAVIDSON D.L. & SURESH S., Philadelphia, USA, (1984), 465.
167. HICKS M.A. & BROWN C.W., Fatigue '84, ed. BEEVERS C.J., Birmingham, UK, (1984), 1337.
168. BROWN C.W. & HICKS M.A., Fat. Eng. Mat. & Struct, 6, (1983), 67.
169. HICKS M.A. HOWLAND C & BROWN C.W., The Metallurgy of Light Alloys, Loughborough, 24-26 March 1983, Inst. of Metallurgists, 252.
170. BROWN C.W. & TAYLOR D., Fat. Crack Growth Thres. Concepts, eds; DAVIDSON D.L. & SURESH S., Philadelphia, USA (1984), 433.
171. BROWN C.W. & KING J.E., Small Fatigue Cracks, eds; RITCHIE R.O. & LANKFORD J., AIME, (1986), 73.
172. TOKAJI K., OGAWA T., HARADA Y & ANDO Z., Fat. & Fract. Eng. & Struct., 9, (1986), 1.
173. HASTINGS P., KING J.E. & HICKS M.A. "Fat '87", 3rd Int. Conf. on Fat and Fat. Thres., Charlottesville, Virginia, USA, eds; RITCHIE R.O. & STARKE Jr. E.A., 28 June-3 July 1987, 251
174. BLOM A., HEDLUND A, ZHAO W. FATHULLA A., WEISS B & STICKLER R. The Behaviour of Short Fatigue Cracks, EGF Publ. #1. eds; MILLER K.J. and De Los RIOS E.R., Sheffield U.K., (1986), 37.
175. DINSDALE K., Private Communication, (1988).
176. GREGORY J.K., GYSLER A. & LÜTJERING G., Fatigue '84, ed. BEEVERS C.J., Birmingham, UK, (1984), 847.
177. KUNIO T. & YAMADA K., ASTM-STP 675, (1979), 342.
178. De Los RIOS E.R., TANG Z. & MILLER K.J., Fat. Eng. Mat. & Struct., 7, (1984), 97.
179. TAYLOR D., Fat. Eng. Mat. & Struct., 5, (1982), 305.
180. LANKFORD J., Fat. & Fract. Eng. Mat. & Struct., 8, (1985), 161.
181. WAGNER L., GREGORY J.K., GYSLER A & LUTJERING G., Small Fatigue Cracks, eds; RITCHIE R.O. & LANKFORD J., AIME, (1986), 117.
182. COX B.N. & MORRIS W.L., "Fatigue '87", 3rd Int. Conf. on Fat. & Fat. Thres., Charlottesville, Virginia, USA, eds; RITCHIE R.O. & STARKE Jr., E.A. 28 June-3rd July 1987, 241.
183. DOWLING N. ASTM-STP 637, (1978), 97.
184. HAMMOUDA M.M. & MILLER K.J., ASTM-STP 668, (1979), 703.
185. TANAKA K. & NAKAI Y., Fat. Eng. Mat. & Struct., 6, (1983), 315.
186. NEWMAN J.C., AGARD Conf. Proc. No. 328, France, (1983), 6-1.
187. McCARVER J.F. & RITCHIE R.O., Mat. Sci. & Eng., 55, (1982), 63.
188. JAMES M.R. & MORRIS W.L., Met. Trans. A, 14A, (1983), 153.
189. BU R. & STEPHENS R.I., Fat. & Fract. Eng. Mat. & Struct., 9, (1986), 35.
190. BROWN C.W. & SMITH G.C., Fat. Eng. Mat. & Struct., 7, (1984), 155.
191. EVANS W.J. & GOSTELOW C.R., Met. Trans. A, 10A, (1979), 1837.
192. STUBBINGTON C.A. & PEARSON S. RAE Tech. Report No. 76040, (1976).
193. STUBBINGTON C.A., PEARSON S. & BAKER T.S., RAE Tech. Report No. 76147, (1976).
194. EYLON D. & HALL J.A., Met. Trans. A., 8A, (1977), 981.
195. BANIA P.J. & EYLON D., Met. Trans. A, 9A, (1978), 847
196. CHESNUTT J.C., WILLIAMS J.C. & THOMPSON A.W., Fatigue '84, 2nd Int. Conf. on Fat. & Fat. Thres., ed; BEEVERS C.J., Birmingham, UK 3-4 Sept, 1984, 341.
197. RITCHIE R.O., Trans. AIME, 99, (1977), 195.
198. LEWIS J.A., Scripta Met., 18, (1984), p625.
199. KING J.E. & BROOK P., Private Communication, (1983).
200. KNOTT J.F., 'Fundamentals of Fracture Mechanics', Butterworths, London (1973).
201. SHAH R.C. & KOBAYSHI A.S., ASTM-STP 573, (1972), 3.

202. SHAH R.C. & KOBAYSHI A.S., "The Surface Crack; Physical Problems & Computational Methods", ASME, New York, (1972).
203. SHAH R.C. & KOBAYSHI A.S., Int. J. Fract. Mech., 9, (1973), 133.
204. PICKARD A.C., Proc. 2nd Int. Conf. on Numerical Methods in Fracture Mechanics, eds; OWEN D.R.J. & LUXMORE A.R., Swansea, (1980), 599.
205. TRANTINA G.G., De LORENZI H.G., & WILKENING W.W., Eng. Fract. Mech., 18, (1983), 925.
206. ROOKE D.P. & CARTWRIGHT D.J., "Compendium of Stress Intensity Factors", HMSO, London, (1976).
207. LANKFORD J., DAVIDSON D.L. & CHAN K.S., Met. Trans. A, 15A, (1984), 1579.
208. WILM A., Metallurgie, 8, (1911) 225.
209. ROSENHAIN, ARCHBUTT & HANSON, 11th Report Alloys Research Committee, NPL, (1921).
210. SANDER W. & MEISSER K.L., Zeitschrift fuer Anorganische Chemie, 154, (1926), 144.
211. DIX Jr. E.H., Trans ASM, 35, (1945), 130.
212. NICHOLSON R.B., THOMAS G. & NUTTING J., J. Inst. Met., 87, (1958), 429.
213. STALEY J.T., BROWN R.H. & SCHMIDT R., Met. Trans., 3, (1972), 191.
214. SCHRA L. & 't HART W.G.J., Eng. Fract. Mech., 17, (1983), 493.
215. REYNOLDS M.A., FITZSIMMONS P.E. & HARRIS J.G., "Aluminium Alloys in the Aircraft Industries", Proc. Symp. Turin, Italy, 1-2 October 1976, 115.
216. FITZSIMMONS P.E. "A Review of the Properties of Alcan 7010 Plate", Alcan Technical Report, August 1981.
217. WILSON R.N., Private Communication, (1986).
218. HAHN G.T., HOAGLAND R.G. & ROSENFELD A.R., Met. Trans. 3, (1972), 1189.
219. IRWIN G.R., J. Appl. Mech. (Trans AIME), 24, (1957), 361.
220. DAVIDSON D.L. & LANKFORD J., Fat. Eng. Mat. & Struct., 3, (1980), 289.
221. DUGDALE D.S., J. Mech. Phys. Sol., 8, (1960), 100.
222. HAMMOND C. & NUTTING J., Met. Sci., 11, (1977), 474.
223. POLMEAR I.J., "Light Alloys, Metallography of the Light Metals", EDWARD ARNOLD, 1987, Chapter 6.
224. DUNCUN R.M., BLENKINSOP P.A. & GOOSEY R.E., "Development of Gas Turbine Materials", Ed; MEETHAM G.W., App. Sci., London (1981), 63.
225. ROBERTS W.T., J. Less Common Metals, 4, (1962), 345.
226. BOWEN A.W., Mat. Sci. & Eng. 29, (1977), 19.
227. OGDEN H.R., MAYKUTH D.J., FINLAY W.L. & JAFFEE R.I., Trans. AIME, 197, (1953), 267.
228. CROSSLEY F.A., CAREW W.F., Trans. AIME, 209, (1957), 43.
229. EYLON D., FUJISHIRO S., POSTANS P.J. & FROES F.H., J. Met., 36, (1984), 55.
230. ROSENBERG H.W., "The Sci. & App. of Ti", 1st Int. Conf. on Ti, London, Eds; JAFFEE R.I. & PROMISEL N.E., 21-24 May, 1968, 851.
231. ANON, Met. Treat., 22, (1955), 430.
232. SHERMAN R.G. & KESSLER H.D., Trans. ASM, 48, (1956), 657.
233. HARRIS G.T., CHILD H.C. & DALTON A.L., J. Inst. Met. 88, (1959), 112.
234. IMI, IMI 550 Brochure.
235. MORTON P.H., P. Trans. Roy. Soc. Series A, 282, (1976), 401.
236. WINSTONE M.R., RAWLINGS R.D. & WERT D.R.F., J. Less Common Metals, 39, (1975), 205.
237. TAYLOR D., "The Behaviour of Short Fatigue Cracks", EGF Publication No. 1, eds; MILLER K.J. & De Los RIOS E.R., Sheffield, UK, 1986, 479.
238. SMITH C.W., PETERS W.H. & KIRBY G.C., "Analytical & Experimental Fracture Mechanics", eds; SIH G.C., & MIRABILE M., Sijthoff & Noordhoff, 1981, 699.
239. PICKARD A.C., Application of 3D Finite Element Methods to Fracture Mech. & Fatigue Life Prediction, EMAS, 1986.

## APPENDIX 1

The figure in this appendix is a plot of  $da/dN$  vs  $\Delta K$  and crack depth (a) for a surface crack tip growing in 318A. The figure can be folded out and placed over other similar plots in Chapter 8 for comparative purposes.

